Effect of Order-Disorder Phase Transition, Bond Anharmonicity and Lattice Asymmetry on the Thermoelectric Properties of Noble Metal Based Chalcogenides

A Thesis
Submitted for the Degree of

Doctor of Philosophy

by

Satya Narayan Guin

New Chemistry Unit
Jawaharlal Nehru Centre for Advanced Scientific Research
(A Deemed University)
Bangalore – 560 064

January 2017

To My Grandmother and
To the Memory of My Grandfather

DECLARATION

I hereby declare that the matter embodied in this thesis entitled "**Effect of Order-Disorder Phase Transition, Bond Anharmonicity and Lattice Asymmetry on the Thermoelectric Properties of Noble Metal Based Chalcogenides**" is the result of the research carried out by me at the New Chemistry Unit, Jawaharlal Nehru Centre for Advanced Scientific Research, Bangalore, India, under the supervision of Dr. Kanishka Biswas and it has not been submitted elsewhere for the award of any degree or diploma.

In keeping with the general practices of reporting scientific observation, due acknowledgments have been made whenever the work described is based on the findings of other investigators. Any omission which might have occurred by oversight or error in judgment is regretted.

_____

Bangalore Satya Narayan Guin

CERTIFICATE

I hereby certify that the matter embodied in this thesis entitled "**Effect of Order-Disorder Phase Transition, Bond Anharmonicity and Lattice Asymmetry on the Thermoelectric Properties of Noble Metal Based Chalcogenides**" has been carried out by Mr. Satya Narayan Guin at the New Chemistry Unit, Jawaharlal Nehru Centre for Advanced Scientific Research, Bangalore, India under my supervision and that has not been submitted elsewhere for the award of any degree or diploma.

Bangalore

Dr. Kanishka Biswas
(Research Supervisor)

Acknowledgements

First and foremost, I would like to express my sincere gratitude to my research supervisor Dr. Kanishka Biswas for enormous freedom, constant motivation and excellent guidance throughout my Ph.D. His valuable comments and instructions in scientific communications have helped me immensely. I am thankful to him for giving me an opportunity to work under his guidance.

I would like to thank Prof. C. N. R. Rao, FRS for being a constant source of inspiration throughout my Ph.D life. His presence and speeches are truly inspiring.

I would like to thank Prof. Umesh V. Waghmare, Prof. Swapan K. Pati, Prof. Ranjan Datta, Prof. Dirtha Sanyal, Prof. A. Sundaresan, Prof. Chandrabhas Narayana, Dr. Gautam Sheet, Swastika, Jaysree, Arghya, Devendra Negi, Rajaji for fruitful scientific collaborations and insightful discussions. I would also like to express my sincere gratitude to Prof. G. Mugesh (IISc, Bangalore) under whom I have worked before joining JNCASR.

I would like to thank all my course instructors: Prof. A. Sundaresan, Dr. Ranjani Viswanatha, Dr. Sebastian C. Peter, Dr. Ujjal K. Gautam, and Prof. S. Balasubramanian.

My special thanks to my labmates, the Solid State Chemistry group members: Manoj, Arindom, Ananya, Subhajit, Manisha, Sujoy, Ekashmi, Dr. P. Chithaiah, Dr. Suresh Perumal and Dr. Provas Pal for their wonderful company and scientific discussions. I also thank all the visiting students, Subhajit, Ashoke, Arnab, Sohang and Shreya who worked with me.

I would like to thank Dr. Nitesh Kumar and Mr. Somnath Ghara for helping me with Hall measurement.

I thank all the technical staff of JNCASR, especially Mr. Anil, Mr. Vasu, Mr. Kannan, Mrs. Usha, Ms. Selvi, Mr. Jagadish, Mr. Kishore, Mr. Naveen, Mr. Mune Gowda and Mr. Dileep.

I am thankful to the academic and administrative staff of JNCASR for their assistance.

I would also like to thank the Hostel staff, Mess workers and Canteen staff and Raju for keeping me well fed. I am thankful to Garden staff, Cleaning staff, Security staff, Electrical staff.

I thank all my friends, seniors and juniors at JNC and IISc: Rajkumar, Swastika, Rana da, Sumanta da, Tarak, Avijit, Debdyuti, Moumita, Sudeshna, Aloke da, Koushik da, Somnath da, Santanu, Bhowmick da, Manna da, Gaurango da, Mohini, Krishnendu, Nivedita, Dheeraj, Sandip da, Arpan da, Debu da, Sudip da, Ritesh da, Dibya, Koushik, Arpan, Jia, Saikat, Subhajit, Debdipta, Rajib, Manoj, Anaranya, CD, Jia da, Somnath, Sohini, Soumyabrata, Syamantak, Promoda, Shreedhara, Anirban, Sunita, Papri, Abhiroop, Manjeet, Shrimayee, Shreya, Anindita, Saibal da, Monodeep, Satyajit, Sourav, Swagatam, Niloyendu, Ranjan, Aritra, Debasish, Shreyan and many more. My stay in JNC would not have been wonderful and enjoyable without their presence.

I thank all my B.Sc., M.Sc. friends, and classmates. I express my sincere thanks to all my teachers, especially from Kalyani University.

Last, but not the least, my parents and family members for their for their support, love and affection. They have always believed in me, and never tied me down in any of my endeavors.

Finally, I express my sincere gratitude to all those who helped me directly or indirectly.

Satya

Preface

Thermoelectric materials can convert directly and reversibly heat into electrical energy and will play an important role in future energy management. This thesis demonstrates synthesis, structure-property correlation and thermoelectric property investigations based on I-V-VI_2 (I= Cu/Ag, V= Sb/Bi, VI= S/Se) and superionic metal chalcogenides (AgCuS). The thesis is divided into eight chapters.

Chapter 1 introduces the field of thermoelectrics and presents the different strategies for tuning of thermoelectric properties in inorganic solid. High performance state-of-art thermoelectric materials are also summarized in this chapter. At the last part, a general discussion on metal chalcogenide synthesis, detailed characterization, and thermoelectric measurements are presented.

Chapter 2 demonstrates the synthesis and thermoelectric property study of noble metal based AgCuS and it is divided into two parts. In ***Chapter 2A***, we show that a crystalline semiconducting noble metal sulfide, AgCuS, exhibits a sharp temperature-dependent reversible *p-n-p* type conduction switching, along with a colossal change in the thermopower (ΔS of $\sim$1757 μV K^{-1}) at the superionic phase transition (T $\sim$364 K). Moreover, AgCuS exhibits ultra-low thermal conductivity. We have developed a fundamental understanding of the phase transition and *p-n-p* type conduction switching in AgCuS through temperature dependent synchrotron powder X-ray diffraction, heat capacity, Raman spectroscopy, positron annihilation spectroscopy measurements and DFT-based first-principles calculations. Order- disorder phase transition and thermoelectric properties of bulk AgCuS can be tuned further by reducing the size to the nanoscale.

In ***Chapter 2B***, we present a facile, ambient and capping free solution based synthesis of AgCuS nanocrystals and their temperature-dependent thermoelectric properties. Temperature dependent Seebeck coefficient measurement indicates that the nanocrystalline AgCuS does not display *p-n-p* type conduction switching property like its

bulk counterpart. Electronic structure modulation and varying defect concentration tailor the thermoelectric properties of AgCuS nanocrystals.

Chapter 3 presents the synthesis and thermoelectric properties of *p*-type $AgSbSe_2$. $AgSbSe_2$ exhibits intrinsically low thermal conductivity due to the presence of $5s^2$ stereo-chemically active lone pair on Sb, which creates significant anharmonicity in Sb-Se bonds. We have shown that the optimum concentrations cation doping (Pb, Bi, and Cd) act as effective *p*-type dopants and substantially increase the electrical conductivity, which resulted in a large increase in the power factor in $AgSbSe_2$. With superior electronic transport and ultra-low thermal conductivity, high zT values of ~1 and ~1.15 at 680 K were achieved in $AgSb_{0.96}Pb_{0.04}Se_2$ and $AgSb_{0.98}Bi_{0.02}Se_2$. For Cd-doped sample, a maximum zT, of 1 at 640 K in $AgSb_{0.98}Cd_{0.02}Se_2$ was achieved. Our finding offers the promise to replace traditional metal tellurides by $AgSbSe_2$ for mid temperature power generation.

In ***Chapter 4***, we demonstrate a significant enhancement of the thermoelectric performance of *p*-type $AgSbSe_2$ through the creation of Sb deficiencies rather addition of any foreign cation dopant. With superior electronic transport and ultra-low thermal conductivity, a peak zT value of ~1 at 610 K was achieved for the *p*-type $AgSb_{0.9925}Se_2$ and $AgSb_{0.99}Se_2$ samples, which is comparable to metal ion doped $AgSbSe_2$.

In ***Chapter 5***, we demonstrate a design strategy that provides simultaneous enhancement of electrical transport through optimized doping, superior thermopower by the convergence of degenerate valence bands, and glass-like thermal conductivity due to the effective scattering of phonons by nanostructuring and bond anharmonicity. We show that by integrating different but synergistic concepts: (a) carrier engineering, (b) second phase endotaxial nanostructuring and (c) bond anharmonicity, we can achieve a maximum zT of ~1.1 at 635 K in *p*-type $AgSbSe_2$-ZnSe (2 mol%), which is significantly higher than that of pristine $AgSbSe_2$.

While both *n*- and *p*-type materials are essential for constructing the thermoelectric device, the available high-performance materials are generally *p*-type. In ***Chapter 6***, we present promising thermoelectric performance in halogen (Cl/Br/I) doped *n*-type bulk $AgBiSe_2$. Aliovalent halide ion doping (2-4 mol%) in the Se^{2-} sublattice of $AgBiSe_2$ significantly increases the *n*-type carrier concentration, which improves the temperature

dependent electronic transport properties. Bond anharmonicity and disordered cation sublattice effectively scatter heat carrying phonon in the high-temperature cubic phase of $AgBiSe_{1.98}X_{0.02}$ (X = Cl, Br and I). The highest thermoelectric figure of merit, *zT*, value of ~0.9 at ~810 K has been achieved for the $AgBiSe_{1.98}Cl_{0.02}$ sample, which is significant among the *n*-type metal selenide based thermoelectric materials.

Chapter 7 demonstrates the low-temperature soft chemical synthesis of kinetic cubic phases of $AgBiS_2$ and $AgBiS_{2-x}Se_x$ (x = 0.05-0.1) in the form of nanocrystals at ambient condition. The existence of fascinating order-disorder type transition in $AgBiS_2$ nanocrystals was evidenced by temperature dependent electrical conductivity, thermopower, and heat capacity measurements. We have developed a fundamental understanding of the origin of order-disorder phase transition and the associated anomalous change of thermopower in $AgBiS_2$ nanocrystals using positron annihilation spectroscopy measurement, density functional theory based first-principles calculation, and *ab-initio* molecular dynamics simulations.

Chapter 8 presents the synthesis of the non-equilibrium cubic phase of AgBiSeS nanocrystals. Rock salt nanocrystals upon thermal treatment undergo an irreversible phase transition to a low symmetry trigonal phase. The origin for such unusual finding was further investigated using temperature dependent synchrotron powder X-ray diffraction, positron annihilation spectroscopy, and first principles calculation.

Chapter 9 presents the summary of all the chapters and contribution of the thesis in solid-state chemistry and thermoelectrics.

Table of contents

Chapter 1

A brief introduction to thermoelectrics *

*This chapter also discuss about the methods and measurement details

CHAPTER 1

A brief introduction to thermoelectrics

Summary. *Significant interest has grown recently for energy production, conservation, and management due to emerging global need in more effective means of power generation. Thermoelectric materials can generate electrical energy from waste heat and could play an important role in a global energy management. Advances in thermoelectric materials development has made increased the interest in the field of chemistry, physics and materials engineering. This chapter highlights a brief introduction to thermoelectrics followed by the importance of the research and development in this field. I have discussed the main criteria for good thermoelectric materials, different strategies for tuning the thermoelectric properties and examples of state-of-the-art materials. At the last part of the chapter a general discussion on metal chalcogenide synthesis, characterization, and thermoelectric measurements are presented.*

1.1 Introduction

The emerging global need for energy production, conservation, and utilization has intensified interest in more efficient, cost-effective and pollution-free means of power generation. Enhancements to the existing energy supply must come from a variety of renewable sources including solar, wind, biomass, and others. Driven by the demand for clean and sustainable energy sources, thermoelectricity has become an important part of the research portfolio seeking to recognize new and efficient energy materials for power generation and cooling applications. The major percentage of the energy was consumed in terms of the use of coal, petroleum and gas. In general, the main share of the electricity is generated from coal, hydro and nuclear fuel (Figure 1.1(a)). On the other hand, combustions of petroleum and gas are used to run the industrial and transportation sector. After the use of this enormous amount of energy in terms of electricity or combustion process, ~65 % of the utilized energy is being lost as waste heat (Figure 1.1(b)). Thermoelectric materials are the all solid-state converters without any moving part can directly and reversibly convert heat energy into electrical energy.[1,2] Over the last two decades, there has been an escalated interest in the field of thermoelectric materials research. The application of thermoelectric materials in the industrial and defense applications are generating increased activity in this field by demanding high-performance materials. More recently, research on solar-thermoelectric is gaining attention to utilize the IR part of the solar spectrum for thermoelectric-solar power generation.[3] Novel applications of thermoelectrics are biothermal batteries to power heart pacemakers, enhanced performance of optoelectronics coupled with solid-state thermoelectric cooling, and power provision for deep-space probes via radioisotope thermoelectric generators. Efforts are already underway to replace the alternator in cars with a thermoelectric generator. Thermoelectric generators have been installed in automobiles to capture waste heat from the exhaust and to transform it into useful electrical energy for automotive electrical systems and for increased fuel efficiency.[1,2,4] The deep-space applications of NASA's *Voyager* and *Cassini* missions are using radioactive thermoelectric generators.[5] Thermoelectric refrigeration is an environmentally green method of small-scale, localized cooling in computers, infrared detectors, electronics and optoelectronics, and many other applications. In addition,

thermoelectric refrigeration applications include seat coolers for comfort. Recent utilization of Peltier coolers in relation to refrigeration of biological specimens/samples is also an emerging thermoelectric application.[1] Thus, development of low-temperature thermoelectric refrigeration devices, as well as for the development of high-temperature materials for waste heat recovery will have a broad spectrum of use in future energy management and technology.

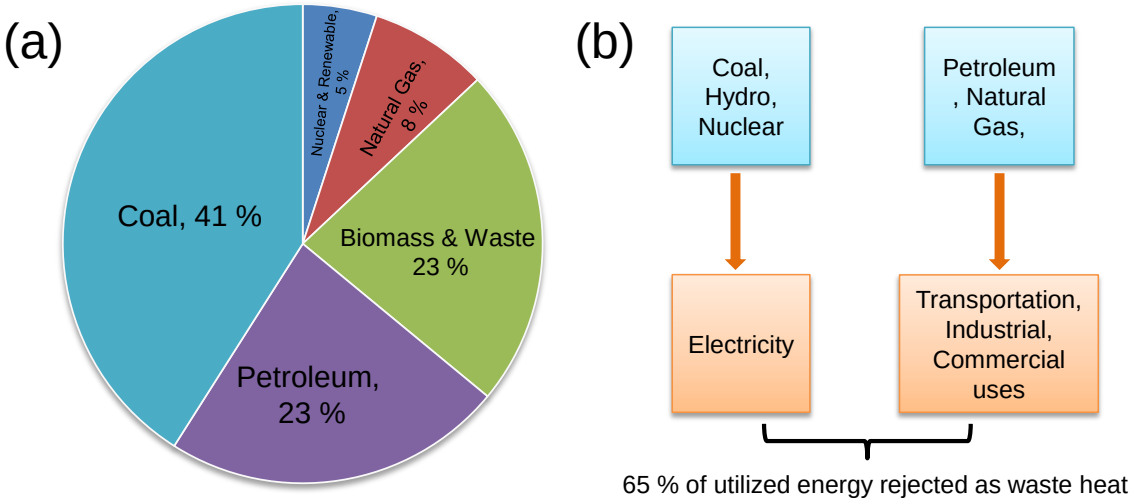

Figure 1.1 (a) Total energy consumption by type for India in the year 2012. (b) Schematic demonstrates ~65 % of the utilized energy being lost as waste heat.

1.2 History of thermoelectrics

The beginnings of this field of study can be traced back as early as 1821 when German scientist Thomas Johann Seebeck (Figure 1.2(a)) discovered an interesting experimental result that the formation of a circuit with two non-identical bismuth and copper wires, each with a different temperature, would deflect the needle of a compass. He found that increasing the temperature difference causes a greater deflection of the compass needle. This deflection was originated from an electric field as opposed to Seebeck's original hypothesis the "thermomagnetism" phenomenon.[6] The amount of the voltage difference (ΔV) produced between the dissimilar wires junctions kept at different temperatures (temperature difference is ΔT) is proportional to ΔT. The ratio of the generated voltage to the temperature difference (ΔV / ΔT) is related to an intrinsic property of the materials termed as Seebeck coefficient (S) or the thermopower (equation 1.1).[7]

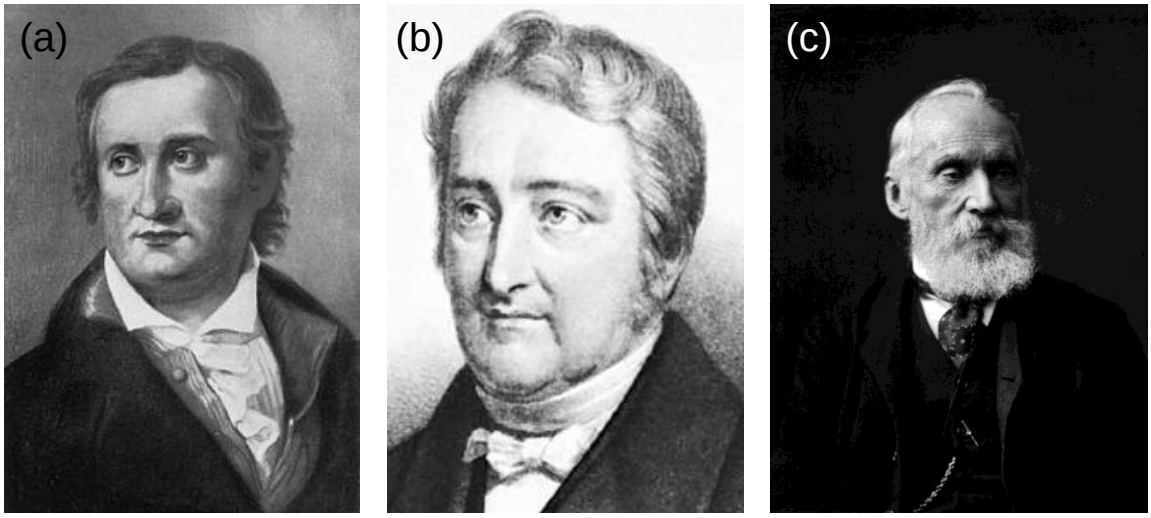

Figure 1.2 (a) Thomas Johann Seebeck (b) Jean Charles Athanase Peltier (c) William Thompson (Lord Kelvin).

$$S = \frac{\Delta V}{\Delta T} \tag{1.1}$$

Thirteen years after Seebeck made his discovery, a complementary effect was discovered by French scientist Jean Charles Athanase Peltier (Figure 1.2(b)), who observed temperature changes near the junction between dissimilar conductors when a current passed. However, he failed to explain his observation or relate the effect to the findings of Seebeck. The true nature of the Peltier effect was explained by Russian scientist Heinrich Emil Lenz in 1838. He concluded that depending upon the direction of the current flow, heat is absorbed or generated at a junction between two conductors and demonstrated this by freezing water at a bismuth-junction and melting the ice by reversing the direction of current flow. The Peltier coefficient (Π) can be described as the ratio of heat flow (Q), to current applied (I): $\Pi = \frac{Q}{T}$. In 1852, William Thompson (Lord Kelvin) (Figure 1.2(c)) able to recognize the interdependency Seebeck's and Peltier's phenomena and succeeded in proving a relationship between Seebeck and Peltier coefficient, through the Kelvin relation, $\Pi = ST$. His theory also showed that there must be a third thermoelectric effect. This effect now known as the Thomson effect consists of reversible heating or cooling when there is both flow of electric current and temperature gradient. Thus, the above discussion demonstrates that the properties discovered separately are in fact united as a single concept of thermoelectric effects.[6,8]

1.3 Thermoelectric figure of merit and efficiency

In 1909, Altenkirch analyzed the efficiency of a thermoelectric generator and derived an expression for the load resistance that yields the highest efficiency in a thermoelectric generator. The paper qualitatively showed the effect of thermal conductivity, κ, and electrical conductivity, σ, in the efficiency but does not identify a single figure of merit. In 1947, Telkes presented an extensive historical review of thermoelectric generators, including a consideration of desirable properties, but with no discussion of a single figure of merit. In describing research conducted at the Institute for Semiconductors of the Academy of Sciences of the USSR over the period from 1952 to 1955, Abram Ioffe introduced the thermoelectric figure of merit as a part of thermoelectric conversion efficiency in a thermoelectric generator.[9] The thermoelectric conversion efficiency for a material given by the following relation:[6,10][11]

$$\eta = \frac{\Delta T}{T_H} \frac{\sqrt{1+zT}-1}{\sqrt{1+zT}+\frac{T_C}{T_H}} \tag{1.2}$$

where $\Delta T/T_H$ refers the Carnot efficiency, T_H and T_C are the hot and cold side temperature and zT is the dimensionless figure of merit. The conversion efficiency is limited to a fraction of the Carnot efficiency determined by the material's dimensionless figure of merit, zT as:

$$zT = \frac{\sigma S^2}{\kappa}\, T \tag{1.3}$$

where σ is the electrical conductivity, S is the Seebeck coefficient, T is the temperature in Kelvin, κ is thermal conductivity.[1,2,5,7,10,12–15] Thermoelectric materials are evaluated in the field based on their zT values. It allows researchers to identify materials with good potential for thermoelectric applications.

The overall thermoelectric figure of merit of a p and n- type pair [$(ZT)_m$] of thermoelectric materials can be express as:[6]

$$(ZT)_m = \int_{T_C}^{T_H} \frac{(S_p - S_n)^2 .\ T}{\left[\sqrt{\rho_p . \kappa_p} + \sqrt{\rho_n . \kappa_n}\right]^2 .\ \Delta T} dT \tag{1.4}$$

where, (S_p and S_n), (ρ_p and ρ_n) and (κ_p and κ_n) represent Seebeck coefficient, electrical resistivity and total thermal conductivity of *p*-and *n*-type materials, respectively.

The thermoelectric efficiency (η) of a thermoelectric generator is defined by combining the Carnot efficiency ($\eta_c = \Delta T/T_{hot}$) and the average figure of merit $(ZT)_{m,avg}$ as shown in equation 1.5 [6]

$$\eta = \frac{\Delta T}{T_H} \frac{\sqrt{1 + (ZT)_{m,avg}} - 1}{\sqrt{1 + (ZT)_{m,avg}} + \frac{T_C}{T_H}} \tag{1.5}$$

where T_H and T_C are the hot and cold side temperature and $(ZT)_{m,avg}$ is the average figure-of-merit of a pair of thermoelectric legs. Equation 1.5 indicates that increasing efficiency requires both high $(ZT)_{m,avg}$ values and a large temperature difference across the thermoelectric materials.

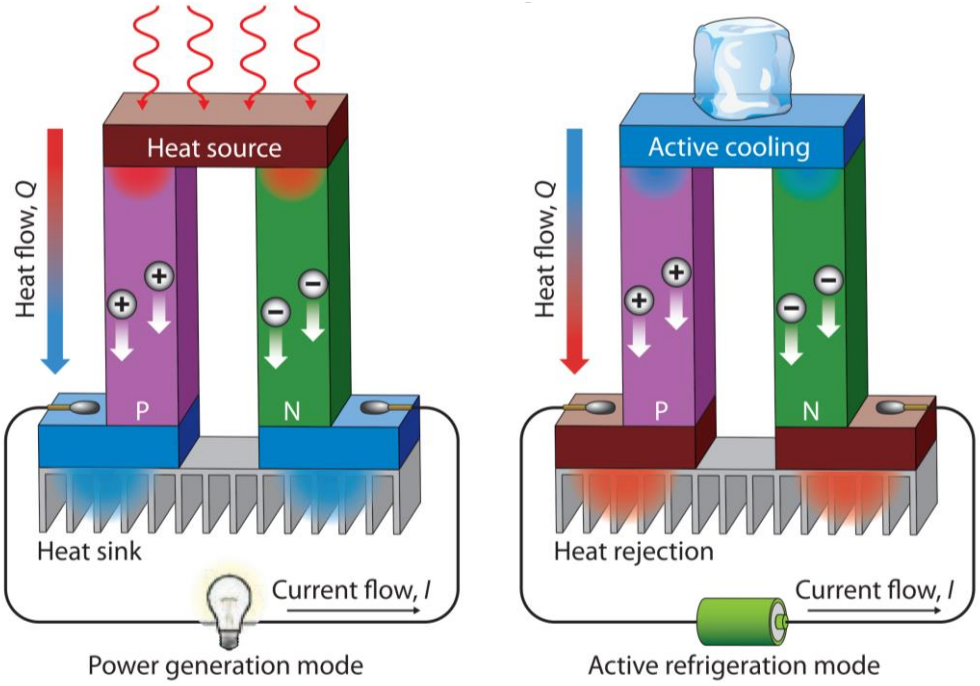

Figure 1.3 A generic diagram of a thermoelectric couple made of *n*-type and *p*-type thermoelectric materials. Power generation or refrigeration modes are possible, depending on the configuration. J. F. Li *et al.*, *NPG Asia Mater.* **2010**, *2*, 152-158 © Nature Publishing Group.

Thermoelectric devices contain many thermoelectric couples consisting of *n*-type (containing free electrons) and *p*-type (containing free holes) thermoelectric materials (Figure 1.3). A thermoelectric device comprises of an array of these couples, which are arranged electrically in series and thermally in parallel and connected through metallic

electrical contact pads.[7] Both refrigeration and power generation may be accomplished using the same module. A thermoelectric generator uses heat flow across a temperature gradient to power an electric load through the external circuit. The temperature difference provides the voltage ($V = S\Delta T$) from the Seebeck effect (Seebeck coefficient S) while the heat flow drives the electrical current, which therefore determines the power output. In a Peltier cooler, a temperature gradient is generated when the device is connected to an external d.c. power, which drives the electric current (I) and heat flow (Q), thereby cooling the top surface due to the Peltier effect ($Q = STI$).[5] In both devices, the heat rejected must be removed through a heat sink. In a thermoelectric generator, when the temperature gradient is applied, the thermally excited holes from *p*-type and electrons from *n*-type semiconductor diffuse towards cold side from hot side and generate power in an electric load connected through an external circuit. Here, temperature difference produces the voltage (equation 1) and heat flow drives the electrical current, which determines the power output. The performance of these devices depends on semiconducting materials used as *p*- and *n*-type leg. Thermoelectric solid-state energy conversion is advantageous because of compactness, quietness (no moving parts) and localized heating or cooling.

1.4 Thermoelectric parameters

Despite great advantage for waste to electricity conversion using the thermoelectric device, the fundamental challenge of designing of high-performance materials is a great challenge. To increase zT, the materials need to have either high power factor (σS^2) or low thermal conductivity (κ), or both at the same time. For high σS^2, a material need to have high electronic conductivity (σ) and high thermopower (S) value. As these transport characteristics depend on interrelated material properties, a number of parameters need to be optimized to maximize zT (Figure 1.4).[5,13,14]

1.4.1 Seebeck coefficient

The Seebeck coefficient (S), also referred to as the “thermopower”, represents the material’s ability to migrate charge carriers away from regions of high concentration. It can be thought of as the heat per carrier over temperature or more simply the entropy per

carrier. For a degenerated semiconductor with parabolic band dispersion, assuming that dopant does not change the scattering or band structure significantly, *S* is given by Mott-Jones relation:[5,13,14]

$$S = \frac{8\pi^2 k_B^2}{3eh^2} m^* T \left(\frac{\pi}{3n}\right)^{3/2} \quad (1.6)$$

where k_B is the Boltzmann constant, *e* the electron charge, *h* the Plank constant, and *m** the density of states effective mass of carriers. Temperature aside, there are two key variables in this equation: *m** and number of charge carriers *n*.

1.4.2 Electrical conductivity

Electrical conductivity (σ) is the measure of a material's ability to allow the transport of an electric charge. The electrical conductivity (σ) is related to *n* through the carrier mobility (μ) through the following expression.[5]

$$\sigma = ne\mu \quad (1.7)$$

μ relies on the additional conditions shown in equation 1.8

$$\mu = \frac{e\tau}{m^*} \quad (1.8)$$

where, τ is the relaxation time or time between carrier-carrier collisions, and *m** the carrier's effective mass.

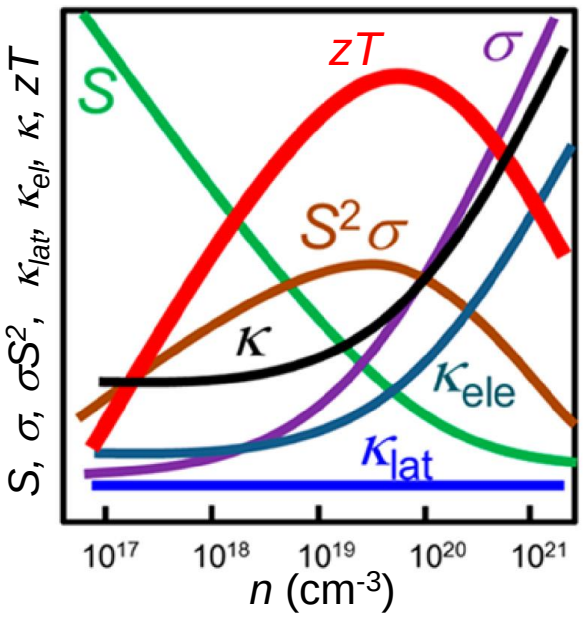

Figure 1.4 Schematic diagram showing how *zT* and its related parameters (electrical conductivity σ, Seebeck coefficient *S*, power factor $S^2\sigma$, electrical thermal conductivity κ_{ele}, lattice thermal conductivity κ_{lat}, and total thermal conductivity κ) change as a function of carrier concentration *n*. G. Tan *et al.*, *Chem. Rev.* **2016**, *116*, 12123–12149 © American Chemical Society.

From equation (1.6)-(1.8) it is clear that S and σ is highly interdependent to each other and related to several conflicting parameters. To attain large Seebeck coefficient, one should have the only single type of carrier. Mixed *n*-type and *p*-type conduction will lead to both charge carriers moving to the cold end, canceling out the induced Seebeck voltages. Apparently, high S is usually found in low n semiconductors or insulators, and with increasing n, S drops rapidly (Figure 1.4). On the contrary, to ensure a large σ, n should be as high as possible (see equation 1.6 and Figure 1.4). Only within the carrier concentration range ~10^{19}-10^{20} cm^{-3} (for most semiconductors) can the power factors be maximized by balancing S and σ.[5,14]

1.4.3 Effective mass

The effective mass of the charge carrier offers another conflict as large effective masses generate high thermopower but low carrier mobility. Physically, the effective mass m^* in a band is related to the curvature of the bands. The m^* in equation 1.6 refers to the density-of-states effective mass, which increases with flat, narrow bands with a high density of states at the Fermi surface. However, as the inertial effective mass is also related to m^*, heavy carriers will move with slower velocities, and therefore small mobility, which in turn leads to low electrical conductivity (equation 1.6).[5,13,14,16] The precise relationship between effective mass and mobility is complex, and depends on the electronic structure, scattering mechanism and anisotropy (equation 1.8). In principle, these effective mass terms can be decoupled in anisotropic crystal structures.[5] An equilibrium must be found for the effective mass (or bandwidth) for the dominant charge carrier, forming a compromise between high effective mass and high mobility. Optimum effective mass for thermoelectric is not known; good thermoelectric materials can be found within a wide range of effective masses and mobility: from low mobility, high effective mass polaron conductors (oxides, chalcogenides) to high mobility, low effective mass semiconductors (SiGe, GaAs).[5,13]

1.4.4 Thermal conductivity

Thermal conductivity, κ, is the measure of transfer of heat through a material by charge carrier and phonons. The thermal conductivity κ_{total} comprises two major components: (i) electronic contribution, electrons and holes transporting heat (κ_{el}) and (ii) lattice

contribution, phonons traveling through the lattice (κ_{lat}) and it can be express as $\kappa = \kappa_{el}+\kappa_{lat}$. The necessity of low thermal conductivity is another confliction in thermoelectric material design.[5,13,14]

1.4.4.1 Electronic thermal conductivity. The electronic term (κ_{el}) is directly related to the electrical conductivity through the Wiedemann–Franz law:[5,13,14]

$$\kappa_{el} = L\sigma T = Lne\mu T \tag{1.9}$$

where L is the Lorenz number, 2.4×10^{-8} $W\Omega K^{-2}$ for free electrons. Equation 1.9 indicate that efforts to improve zT by increasing the electrical conductivity are potentially detrimental due to increase in the thermal conductivity can be seen clearly in Figure 1.4. However, fine tuning n, can balance electrical to thermal transport (κ_{el}) and can optimise zT. The Lorenz number can vary particularly with carrier concentration. Accurate evaluation of κ_{el} is important, as κ_{lat} is often calculated as the difference between κ_{total} and κ_{el} using the experimental electrical conductivity. Ambiguity in κ_{el} happens due to mixed conduction, which introduces the bipolar term into the thermal conductivity. As this term is not considered into the Wiedemann-Franz law, the standard computation of κ_{lat} erroneously takes account of bipolar thermal conduction. This results in a perceived increase in κ_{lat} at high temperatures for low band gap materials like Bi_2Te_3 and PbTe.

1.4.4.2 Lattice thermal conductivity. In solids, the interaction between atoms results in displacements from their equilibrium positions, which generates a set of vibrational waves with various wavelengths, so-called phonons. Phonons are heat carriers that propagate through the lattice, contributing to the lattice thermal conductivity κ_{lat}.[14] As an extension of the early work of Schlöhmann, and more recently by Slack, Klemens, Julian, and Toberer focusing on acoustic phonons has shown that the influence on κ_{lat} of the average mass, M, the elastic constants via the mean speed of sound, v_m, and the Grüneisen parameter, γ, the average volume per atom, V, and the number of atoms per primitive unit cell, N, can be written as:[16]

$$\kappa_{lat} \sim \frac{M v_m^3}{T V^{\frac{2}{3}} \gamma^2}\left(\frac{1}{N^{1/3}}\right) \tag{1.10}$$

Materials possessing low sound velocities, high Grüneisen parameter value and short phonon mean free path will have favorably low κ_{lat}. Increasing N in a material intuitively

creates a more tortuous transport path for phonons, ultimately reducing κ_{lat} by increasing phonon scattering opportunities and slowing short-wavelength phonons. As *N* becomes very large, *i.e.,* a completely amorphous material, the speed of sound becomes the most important characteristic and the thermal conductivity approaches a constant value, leads to the concept of a minimum thermal conductivity, κ_{min}. However, glasses are poor thermoelectric because of the absence of needed 'electron-crystal' properties, which essential for electrical transport (σ). They also have lower mobility compared to crystalline semiconductors, due to increased electron scattering and lower effective masses because of broader bands. Good thermoelectric materials are therefore crystalline materials that manage to scatter phonons without significantly interrupting the electrical conductivity. The heat flow is carried by a spectrum of phonons with widely varying wavelengths and mean free paths (from less than 1 nm to greater than 10 μm), creating a need for phonon scattering agents at a variety of length scales.

1.5 Advanced approaches for high-performance thermoelectric materials

Thermoelectrics have always been a materials design problem involving complicated tuning of structure-property relationships in inorganic solids through principles of solid-state chemistry. Slack and thereafter Mahan has described the chemical characteristics of the good thermoelectric material.[6,7,17] A potential material should be narrow-bandgap semiconductor (e.g., $E_G \approx 10k_BT$ or ≈ 0.25 eV at 300 K) with high carrier mobility.[7] In semiconductors, the *S* and σ (power factor part of *zT*) depend on the doping level and chemical composition. In addition, the lattice thermal conductivity of the material must be low. Therefore, to design a high-performance thermoelectric material optimization of these properties are essential. The complex relationships among the parameter make the approach of tuning carrier concentration alone difficult to enhance *zT*.[5] However, over the past few decades, significant progress has been made in the thermoelectric field to enhance the power factor and reduce thermal conductivity. In the following section, I will discuss the different strategies to improve thermoelectric properties of inorganic solids.

1.5.1 Enhancement of Seebeck coefficient

The product (σS^2) is a purely electronic property, dominated by the details of the electronic structure and of the scattering mechanisms.[18] Therefore, band structure engineering has been used to enhance σS^2. The well-known approaches in this regard are (i) distortions of the electronic density of states (DOS) near the Fermi energy by the formation of the resonant level and (ii) convergence of electronic valleys by decreasing the energy offsets between light and heavy valence bands.[13,18,19]

1.5.1.1 Resonant levels. The concept of resonant levels was first proposed in metals in 1950s.[14,20,21] Resonant levels originate from the coupling between electrons of a dilute impurity with those of the conduction or the valence band of the host solid. This creates an excess density of states near the resonant energy and can give rise to improved m^* and increase the thermoelectric figure of merit due to enhancement in Seebeck coefficient.[14] Electronic transport properties of semiconductor generally follow Boltzmann theory. According to this, the Seebeck coefficient strongly depends on energy derivative of carrier density ($n(E)$) and mobility (μ) via Mott relation (equation 1.11), in which slight changes in the DOS can alter the S value.[13,18,22]

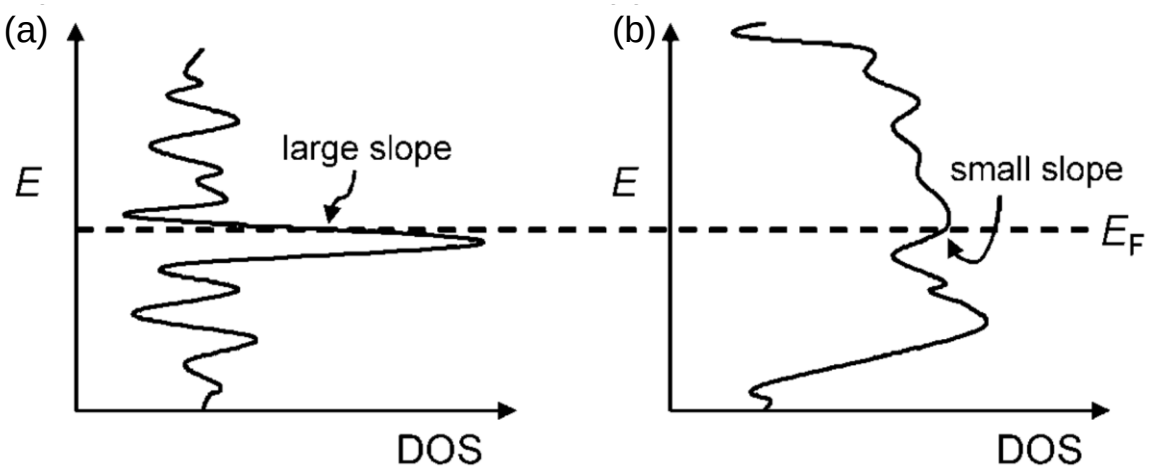

Figure 1.5 Hypothetical density of state (DOS) with (a) a large slope (d lnσ(E)/dE) and (b) a small slope near E_F. J. R. Sootsman, *et al.*, *Angew. Chem. Int. Ed.* **2009**, *48*, 8616–8639 © WILEY-VCH Verlag GmbH & Co.

$$S = \frac{\pi^2}{3}\frac{k_B}{q}\,k_BT\left\{\frac{d[ln(\sigma(E))]}{dE}\right\}_{E=E_F} = \frac{\pi^2}{3}\frac{k_B}{q}\,k_BT\left\{\frac{1}{n}\frac{dn(E)}{dE}+\frac{1}{\mu}\frac{d\mu(E)}{dE}\right\}_{E=E_F} \quad (1.11)$$

Here, $\sigma(E)$ is the electronic conductivity determined as a function of the band filling or Fermi energy, E_F; [$\sigma(E) = n(E)q\mu(E)$]; $n(E)$ [$n(E) = g(E)f(E)$], the carrier density at the energy level, E [q is the carrier charge, and $\mu(E)$ is the mobility as a function of energy, $f(E)$ is the Fermi function, $g(E)$ is density of state]. When electronic scattering is independent of energy, $\sigma(E)$ is just proportional to the density of states (DOS) at E. Figure 1.5, shows two hypothetical DOS diagrams. In Figure 1.5(a) the DOS varies rapidly near E_F and in Figure 1.5(b) it does not. Based on the above expression it is clear that the system with rapid changing DOS near E_F is expected to have large thermopower.

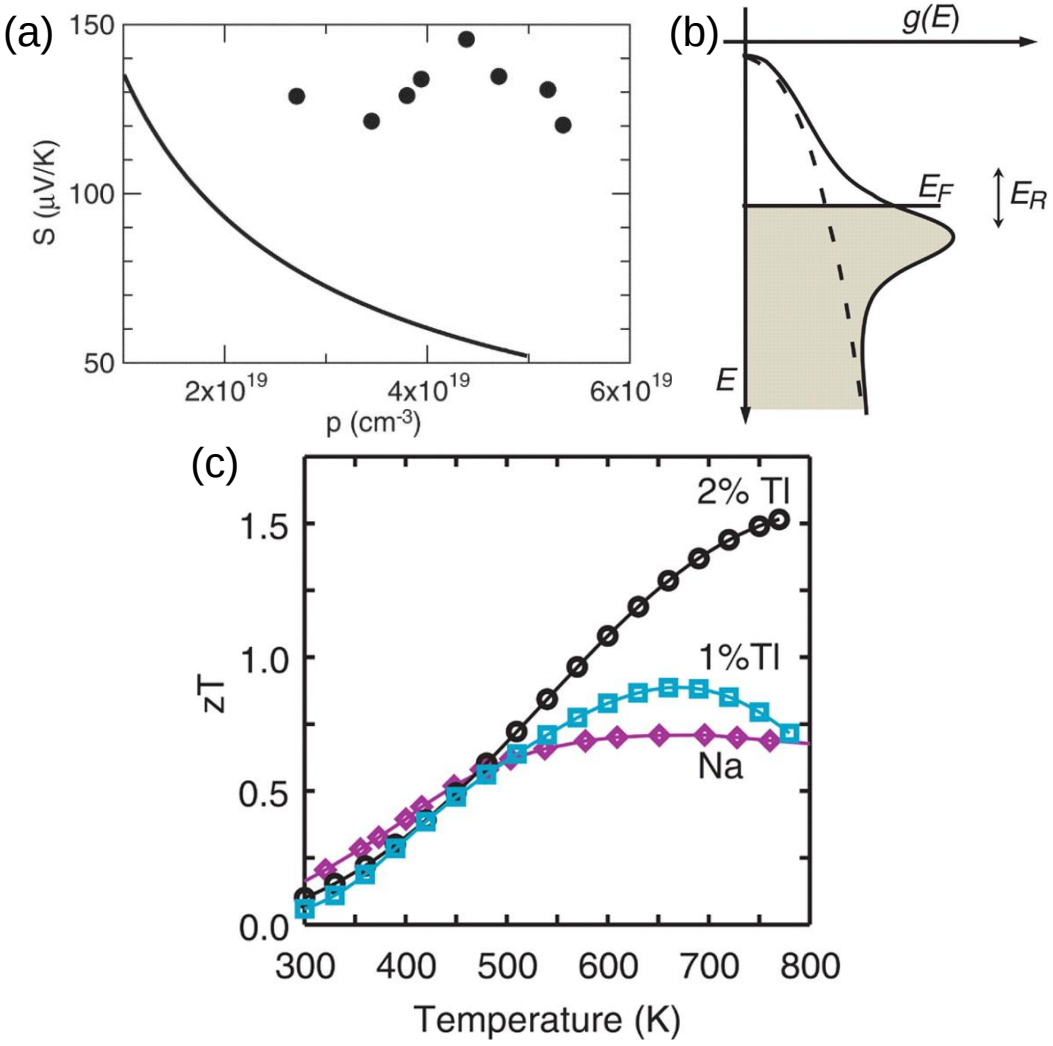

Figure 1.6 (a) Pisarenko relation of Seebeck coefficient versus hole concentration for PbTe (solid line) at 300 K compared to the results on Tl-PbTe sample. Significantly large *S* value in Tl-doped PbTe confirmed the presence of resonance level. (b) The formation of Tl resonant state (solid line) on PbTe DOS (dashed line). (c) The temperature dependent *ZT* values for $Tl_{0.02}Pb_{0.98}Te$ (black circles) and $Tl_{0.01}Pb_{0.99}Te$ (blue squares) compared to that of a reference sample of Na-PbTe (purple diamonds). J. P. Heremans *et al.*, *Science* **2008**, *321*, 554–557 © AAAS.

Mahan and Sofo theoretically suggested the possibilities of the formation of the resonant states, from the localized impurity energy level, near to E_F of the semiconductors.[18,22,23] Hereman, *et al*. demonstrated experimentally that Tl-doped PbTe shows increased effective mass and significantly high Seebeck coefficient value by resonant level formation (Figure 1.6(a,b)). The DOS distortion results in a z*T* as high as 1.6 at 773K (Figure 1.6(c)).[22] The concept of resonant levels has been recently extended to *p*-type SnTe, which is an analogue of PbTe.[24,25]

1.5.1.2 Band convergence. Multiple pockets in valence or conduction band extreme give rise to high Seebeck coefficient. Multiple degenerate valleys (separate pockets of Fermi surface with the same energy) have the effect of producing large effective mass (m^*) without explicitly reducing μ as shown in equation 1.12.[26] Hence, when the system is heavily doped, the overall effective mass can be enhanced through carrier injection to more valleys, thus resulted in high power factor. Tuning of the energy offsets between light and heavy valence bands is also effective to increase the Seebeck coefficient.

$$m^* = N_v^{2/3} m_b^* \tag{1.12}$$

where m_b^* is band mass of single valley and N_v is valley degeneracy. Thus, it is clear that a large valley degeneracy is good for thermoelectric materials.[6,8,13,14,26] Convergence of many charges carrying electronic band valleys can occur in high-symmetry crystal structures (such as PbTe and $(Bi,Sb)_2Te_3$) if the Fermi surface forms isolated pockets at low symmetry points.[26] The widely used thermoelectric material $(Bi,Sb)_2Te_3$ has significant valley degeneracy, with $N_v = 6$ in both the conduction and valence bands.[8,26] PbTe with its rock salt structure has N_V of 4 and 12 at the L and Σ points of the valence band, respectively.[14,26,27] Other good thermoelectric materials, such as SiGe alloys, $CoSb_3$, Mg_2Si, and half-Heusler alloy, also feature $N_V > 1$.[14]

Pei *et al.* have demonstrated the band convergence in doped $PbTe_{1-x}Se_x$ alloys, in that case, the effective N_V becomes larger than 12, leading to an extraordinarily high *zT* value of ~1.8 at about 850 K, as shown in Figure 1.7.[26] Alloying Se reduces the energy difference between the L and Σ bands of the PbTe making the two bands effectively converged and results increase in m^*. A similar result was also observed upon proper alloying with specific elements (for example, Mg,[28] Cd,[29] Sr,[30]) in PbTe. Recently, the concept of band convergence has been extended to *p*-type SnTe.[31–34]

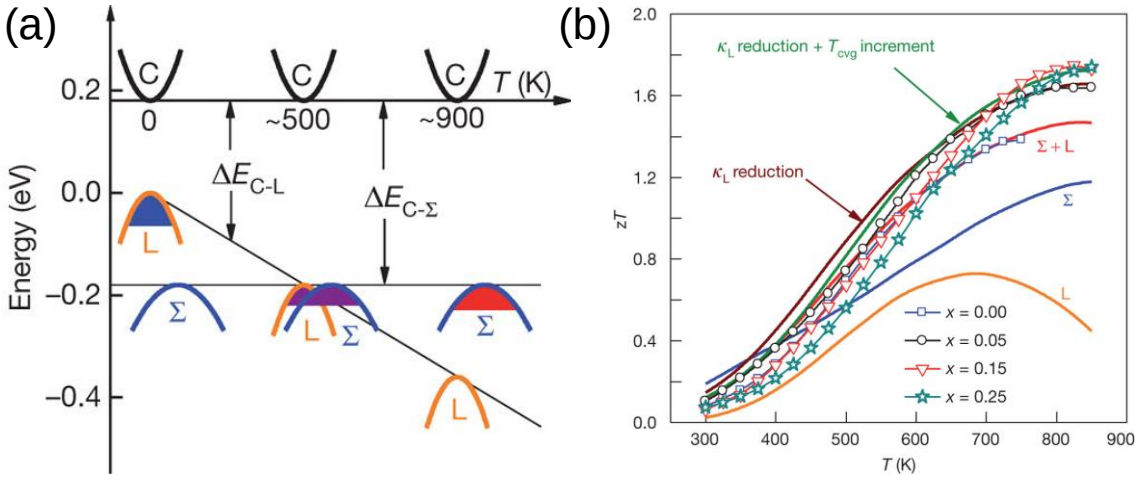

Figure 1.7 (a) Relative energy of the valence bands in $PbTe_{0.85}Se_{0.15}$. At, 500 K the two valence bands converge, resulting in transport contributions from both the L and Σ bands. (b) Temperature dependence of the *zT* of *p*-$PbTe_{1-x}Se_x$ materials doped with 2 atom % Na. Y. Pei *et al., Nature* **2011**, *473*, 66–69 © Nature Publishing Group.

1.5.2 Reduction of lattice thermal conductivity

1.5.2.1 Extrinsic approaches. An effective technique to increase the figure of merit (*zT*) is to manipulate the lattice part of thermal conductivity as this is the only parameter not determined by the electronic structure of the material (Figure 1.4).[13] All other material parameters, such as electrical conductivity and Seebeck coefficient, are correlative with the electronic structure of the material and thus, in most cases, cannot be optimized independently.[13] Above Debye temperature, κ_{lat} primarily depends on phonon mean free path; that means materials with higher phonon- phonon scattering will show lower value of κ_{lat}.[5] Phonon waves can be scattered at crystal defects (*e.g.*, point defects, dislocations, interfaces, precipitates, etc.), giving rise to a reduction of κ_{lat}. Creation of atomic point defects formed by elemental substitution can significantly scatter the short-wavelength phonons. For example, solid solutions of $PbTe_{1-x}Se_x$ and $Pb_{1-x}Sn_xTe$ have the lower thermal conductivity than that of pure PbTe (Figure 1.8(a)). The solid solution will provide an environment of mass fluctuation throughout the crystal lattice (*i.e.* disorder) which induces strong phonon scattering and results in significantly lower thermal conductivity. Nanoscale precipitates by second-phase nucleation and growth in bulk materials can significantly scatter the mid- and long-wavelength phonons and reduce the lattice thermal conductivity further lower (Figure 1.8(b)).[13,14,35,36] Calculations predict

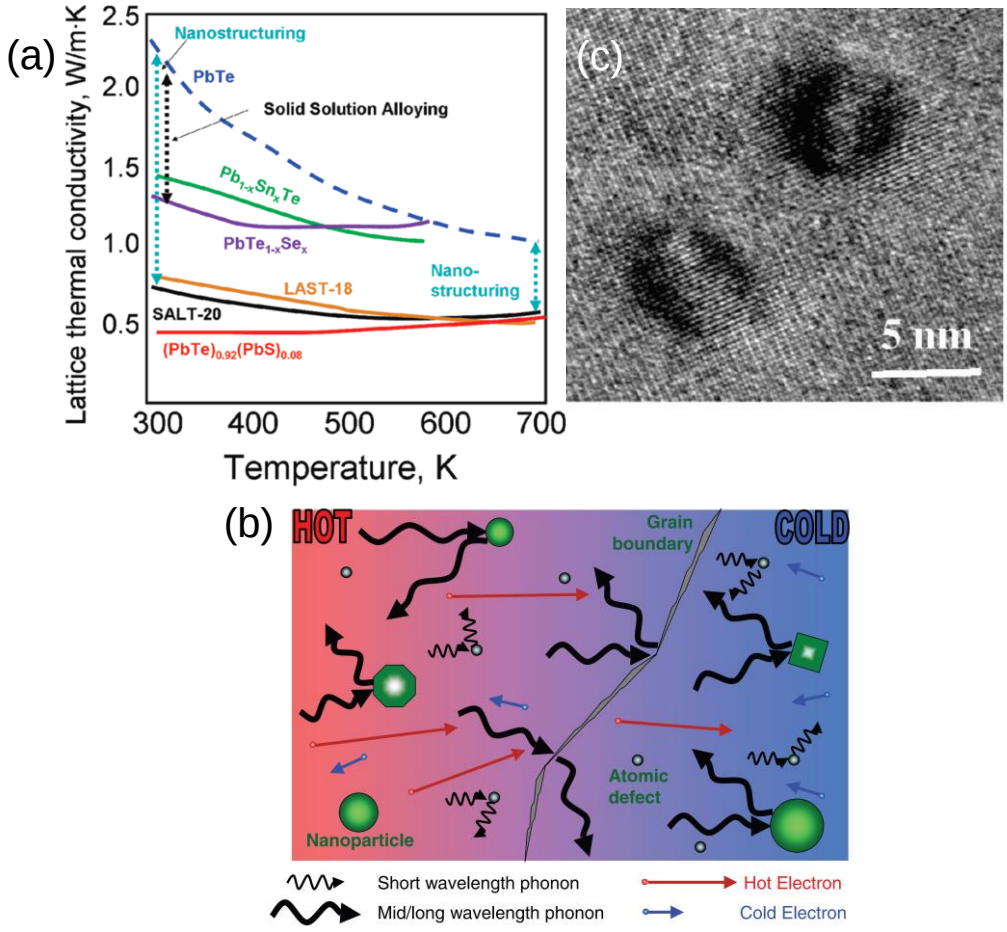

Figure 1.8 (a) Lattice thermal conductivity (κ_{lat}) as a function of temperature for various PbTe-based alloys and nanostructured samples. (b) Schematic diagram illustrating various phonon scattering mechanisms within a thermoelectric material, along with electronic transport of hot and cold electrons. (c) High-resolution transmission electron microscopy of a LAST-18 sample. Panel (a), (c) from M. G. Kanatzidis, *Chem. Mater*. 2010, *22*, 648–659 © American Chemical Society and (b) from C. J. Vineis *et al.*, *Adv. Mater*. 2010, *22*, 3970–3980 © WILEY-VCH Verlag GmbH & Co.

that to make the scattering effective, the geometric length of the nanoscaled defects should be small enough, typically on the order of several to dozens of nanometers, and the nanostructures should be uniformly distributed for maximal interface density over a large material volume. This phenomenon was first observed in a high-performance thermoelectric system, so-called LAST-m (lead antimony silver telluride).[37] The thermal conductivity at room temperature has been reduced from 2.0-2.5 W /mK for PbTe to 0.5-0.8 W /mK for LAST-m (Figure 1.8(a)). The very low lattice thermal conductivity of the LAST system was attributed to the spontaneous and ubiquitous nanoscale precipitation of second phases in the PbTe matrix (Figure 1.8(c)). After this observation, nanostructures were also observed in LASTT ($Ag(Pb_{1-x}Sn_x)_mSbTe_{2+m}$)[38] and SALT ($NaPb_mSbTe_{2+m}$)[39].

The nanostructuring approach has been successfully applied to numerous thermoelectric materials with a great reduction of lattice thermal conductivity.[36,40–46] The presence of mesoscale grains are effective for scattering of long-wavelength phonons. When point defects, nanostructuring, and mesoscale structuring are integrated into a single material, it is known as all-scale hierarchical architecture and with this strategy, it is possible to achieve the highest phonon scattering.[14,15,44]

Slack has proposed an interesting idea to achieve high zT and is referred to as the "phonon glass electron crystal" (PGEC) approach.[6] A PGEC material features cages in its crystal structure inside which massive atoms can reside. These big atoms are small enough relative to the cage to rattle. This situation produces a phonon damping that can result in significant reduction of the lattice thermal conductivity. In the PGEC picture, a glass-like thermal conductivity can in principle coexist with charge carriers of high mobility. The PGEC approach has inspired a significant amount of new research and has led to significant increases in zT for several compounds such as the multiple filled skutterudites and clathrates.[47–50]

1.5.2.2 Intrinsic low thermal conductivity. The intrinsically low thermal conductivity means the complicated approaches to reduce thermal conductivity can be avoided. In some special class of materials, low thermal conductivity can be found intrinsically. Low κ_{lat} arise from an anharmonic and anisotropic bonding,[16,51] lattice vibrations,[52] liquid-like behaviour of ions in crystal lattice,[53] large molecular weight,[13,54] complex crystal structure,[55] lone-pair electrons,[56,57] resonance bonding[58] etc. The presence of these characteristics in a crystal lattice results in enhanced phonon-phonon scattering, which reduces κ_{lat}.

In real material all bonding are anharmonic in nature and the degree of anharmonicity varies largely from material to material. Anharmonicity means the asymmetry in the ability of an atom to vibrate harmonically around its position. Asymmetry in vibration implies that the atom to move along certain directions of the lattice without causing large repulsions in its environment and destabilization of the entire structure.[16,59,60] Ideal perfectly harmonic bonds in one-dimension are schematically illustrated in Figure 1.9. The potential energy to which an atom is subjected is proportional to its displacement from the equilibrium position, and the

proportionality constant is called the spring constant or stiffness. In the anharmonic case, the spring stiffness varies with increasing atom displacement, which has pronounced effects when two phonons run into each other, as shown in Figure 1.9. The presence of the first phonon then changes the spring constant values for the second phonon, which thus runs into a medium with modified elastic properties. High anharmonicity, therefore, results in enhanced phonon–phonon scattering, which reduces the lattice thermal conductivity.[60]

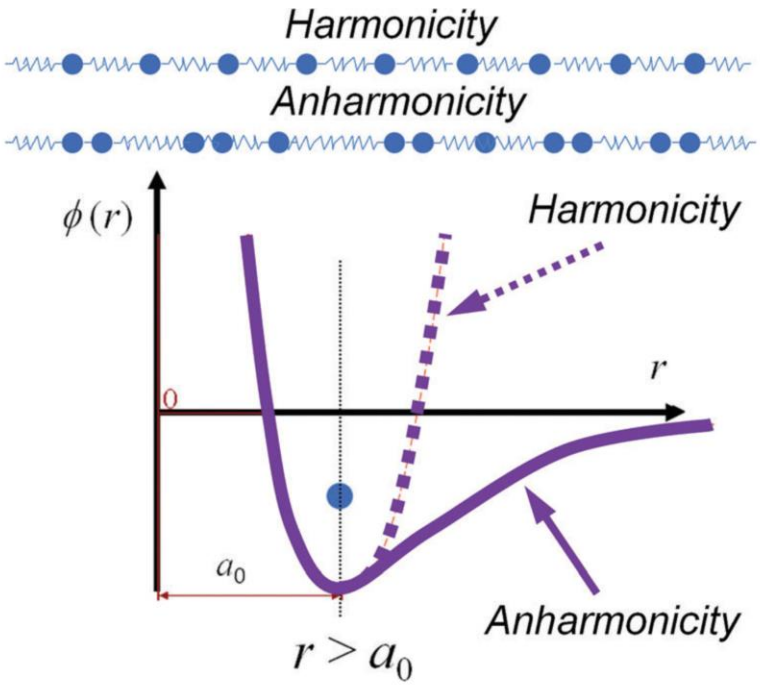

Figure 1.9 Schematic representations of harmonicity and anharmonicity (ϕ (r), a_0 and r are the potential energy, lattice parameter and distance between two adjacent atoms, respectively); anharmonicity is the deviation from a linear relationship between displacement and restoring force. L.-D. Zhao *et al.*, *Energy Environ. Sci.* **2016**, *9*, 3044–3060 © 2012 Royal Society of Chemistry.

1.6 State-of-art thermoelectric materials

1.6.1 Criteria for a good thermoelectric material

To maximize the thermoelectric figure of merit (zT) of a material, a large Seebeck coefficient, high electrical conductivity, and low thermal conductivity are required. As these transport characteristics depend on interrelated material properties, a number of parameters need to be optimized to maximize zT. Ideally, a good thermoelectric material should have low thermal conductivity (property of glass), high electrical conductivity

(property of metal) and large Seebeck (property of semiconductor). The challenge lies in the field to optimize all these important properties to achieve high thermoelectric performances. Figure 1.10 shows the major milestones achieved for *zT* over the past several decades as a function of both year and temperature. In the following part, I shall briefly discuss state of art thermoelectric materials.

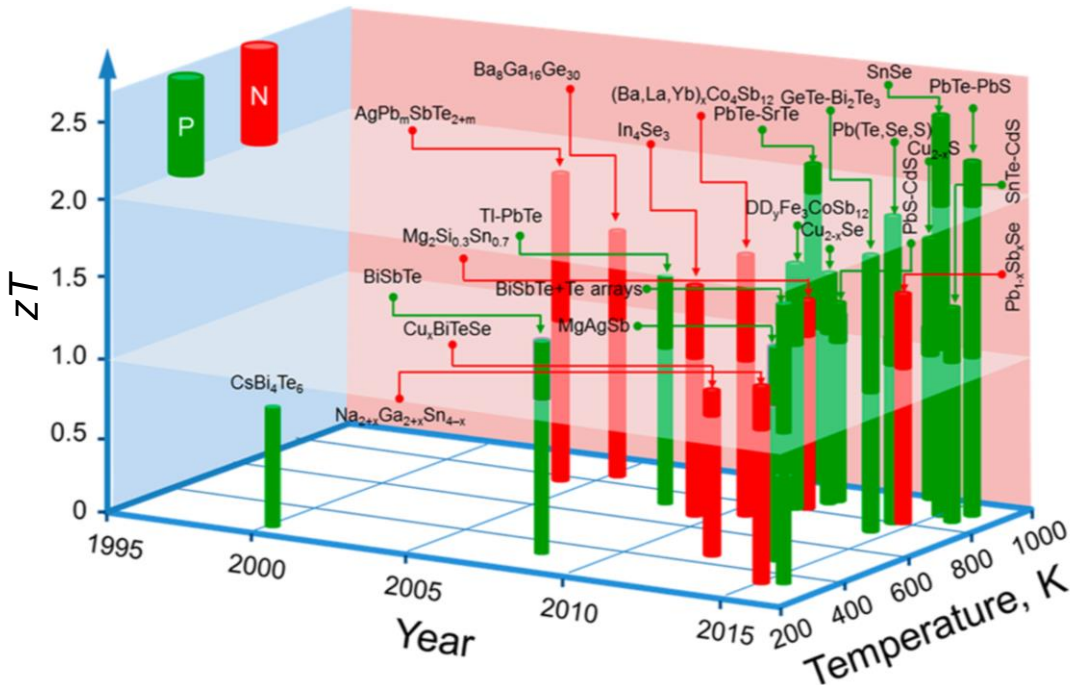

Figure 1.10 Current state-of-the-art bulk thermoelectric materials: the thermoelectric figure-of-merit *zT* as a function of temperature and year illustrating important milestones. Green cylinders represent the *p*-type materials, while red cylinders represent the *n*-type ones. G. Tan *et al.*, *Chem. Rev.* **2016**, *116*, 12123–12149 © American Chemical Society.

1.6.2 Bismuth telluride

Bismuth telluride (Bi_2Te_3), a narrow-gap semiconductor with an indirect band gap of ~0.15 eV, is well-known for its distinct layered crystal structure and excellent thermoelectric properties.[61,62] H. Julian Goldsmid in 1954 first inspected Bi_2Te_3 as an effective material for thermoelectric refrigeration.[62] Bi_2Te_3 crystallizes in a rhombohedral layered structure (space group *R-3m*) with five atoms in one unit cell. The lattice parameters of Bi_2Te_3 are a =0.4384 nm and c =3.045 nm.[63]The structure is formed by quintuple layers of Te(1)-Bi-Te(2)-Bi-Te(1) stacked by van der Waals interactions along the crystallographic *c*-axis. This weak binding between the Te layers accounts for

the ease of cleavage along the plane perpendicular to the *c*-axis and the anisotropic thermal and electrical transport properties of Bi_2Te_3. The material prepared by ball milling followed by hot pressing shows a peak value zT~1.4 at 100 °C (see Figure 1.11 (b)).[64] The enhancement of zT arises due to reduction of the lattice thermal conductivity while maintaining a comparable power factor to that of the bulk *p*-type $Bi_{0.5}Sb_{1.5}Te_3$. This material is called "nanobulk" $Bi_{2-x}Sb_xTe_3$ and it is a single-phase material made of nanograins and micrograins (Figure 1.11(c)). The device made up with nanostructured Bi_2Te_3 has shown superior thermoelectric efficiency than that of the device from commercially available *p*-type Bi_2Te_3. Recently, promising thermoelectric performance has been achieved in nanostructured Bi_2Te_3, Sb_2Te_3 and their alloys synthesized by bottom-up solution based microwave assisted synthesis.[65] Formation of dense dislocation arrays at low-energy grain boundaries by liquid-phase compaction in $Bi_{0.5}Sb_{1.5}Te_3$ effectively scatter mid-frequency phonons, resulting in a substantially lower thermal conductivity (Figure 1.12(b,c)). Full-spectrum phonon scattering with minimal charge carrier scattering significantly improved the zT to 1.86 at 320 K (Figure 1.12(d)).[66]

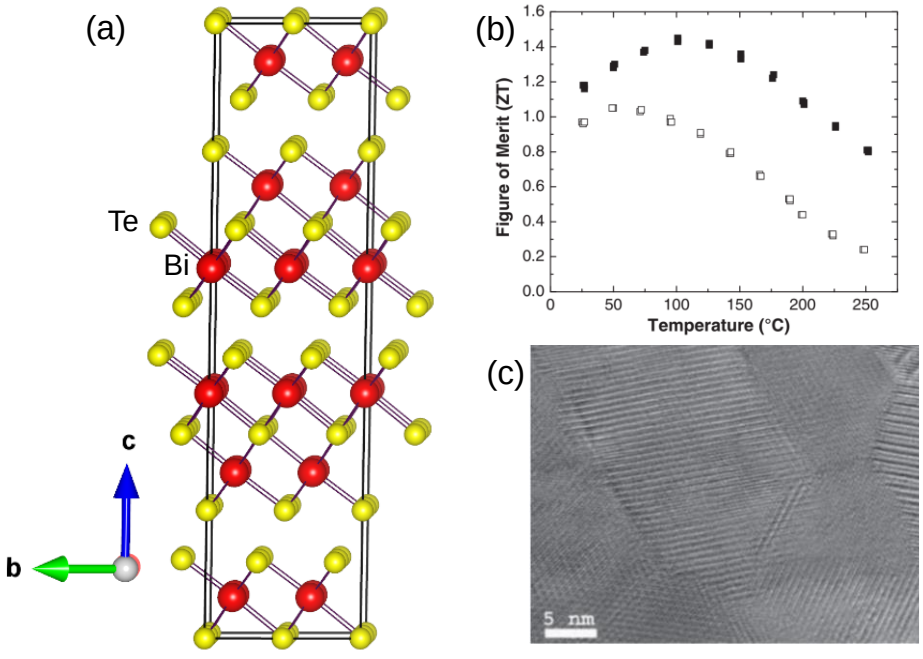

Figure 1.11 (a) Crystal structure of Bi_2Te_3. (b) Temperature dependent *ZT (~zT)* of hot pressed nanostructured and market-based ingot bismuth antimony telluride. (c) Transmission electron microscope (TEM) image showing nanocrystalline grain of high-performance bismuth antimony telluride. (b) and (c) from B. Poudel *et al. Science* **2008**, *320*, 634–638 © AAAS.

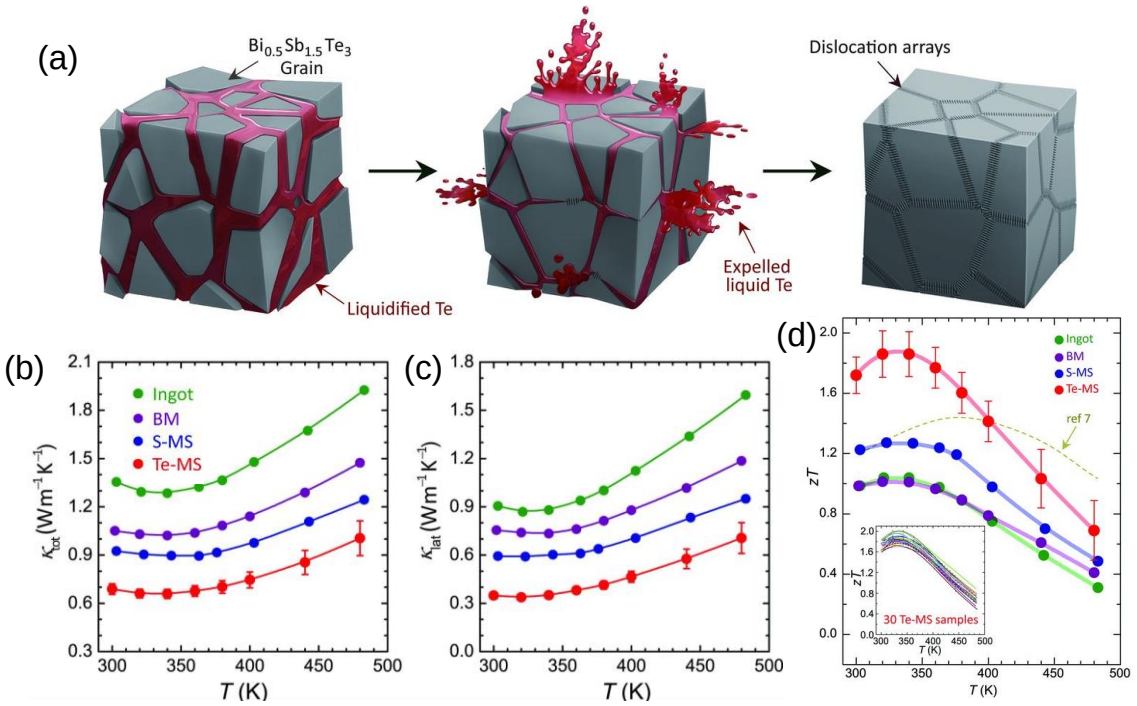

Figure 1.12 (a) Schematic illustration showing the generation of dislocation arrays during the liquid-phase compaction process. The Te liquid (red) between the $Bi_{0.5}Sb_{1.5}Te_3$ grains flows out during the compacting process and facilitates the formation of dislocation arrays embedded in low-energy grain boundaries Temperature dependences of total (b) and lattice (c) thermal conductivity (κ_{tot} and κ_{lat}) for all samples. (d) The figure of merit (zT) as a function of temperature for $Bi_{0.5}Sb_{1.5}Te_3$ alloys. S. Il. Kim *et al.*, *Science* **2015**, *348*, 109–114 © AAAS.

1.6.3 $CsBi_4Te_6$

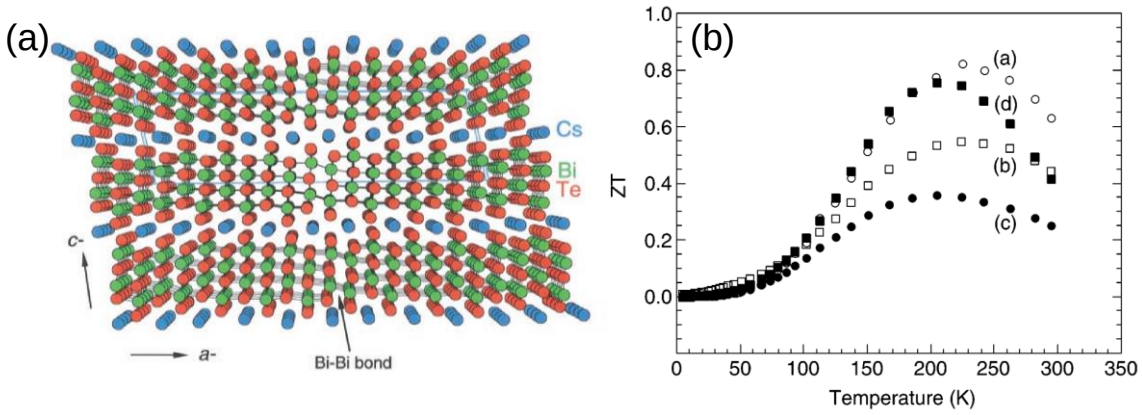

Figure 1.13 (a) The structure of $CsBi_4Te_6$ looking down the crystallographic b axis. The Bi-Bi bond is indicated by the arrow. (b) Variable-temperature ZT (~zT) for (a) 0.05% SbI_3-doped $CsBi_4Te_6$ and for comparison the estimated zT's for (b) 0.06% Sb, (c) 0.3% BiI_3, and (d) 0.1% Bi-doped sample. Panel (a) and (b) from D.-Y. Chung *et al.*, *Science* **2000**, *287*, 1024–2027 © AAAS and D.-Y. Chung *et al.*, *J. Am. Chem. Soc.* **2004**, *126*, 6414–6428 © American Chemical Society respectively.

$CsBi_4Te_6$ is a potential material for low-temperature thermoelectric applications. It was first synthesized by Kanatzidis and coworkers in the year 2000.[67] $CsBi_4Te_6$ crystallizes in the space group *C2/m*, has a layered anisotropic structure composed of anionic $[Bi_4Te_6]$ slabs alternating with layers of Cs^+ ions. The $[Bi_4Te_6]$ slabs are align parallel to b axis and are linked via Bi-Bi bonds (Figure 1.13(a)). The presence of Bi-Bi bonds in the structure is responsible for a narrow energy gap (~0.1 eV), nearly half compared to that of Bi_2Te_3.[67][68] The narrower band gap is responsible for the maximum *zT* value in $CsBi_4Te_6$ being at lower temperature than that of Bi_2Te_3. $CsBi_4Te_6$ is sensitive to doping, in fact very low doping levels can affect the charge-transport properties. A *zT* value of 0.8 at 225 K was obtained for 0.06% SbI_3-doped $CsBi_4Te_6$ (Figure 1.13(b)). Various other doping have also been explored in this compound thereafter by the same group. For example, 0.3% BiI_3, 0.1% Bi, and 0.06% Sb-doped $CsBi_4Te_6$ exhibited significantly high power factors at 150 K which is 30-40 K below the temperature compared to that of the 0.05% SbI_3- doped $CsBi_4Te_6$.[68]

1.6.4 Lead telluride

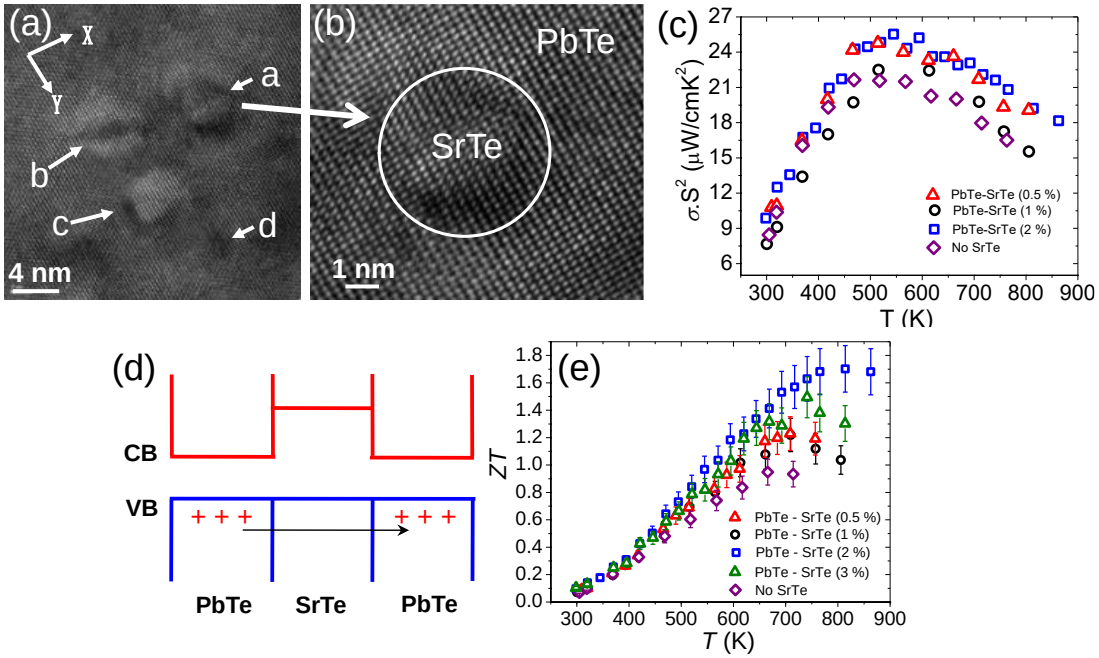

Figure 1.14 (a) High-resolution TEM phase contrast image of several endotaxial nanocrystals of SrTe in the PbTe matrix. Arrows indicate presence of SrTe. (b) Enlarged image of a particle depicting a coherent (with elastic strain) boundary between precipitate and matrix. (c) Power factor (σS^2) of PbTe–SrTe samples doped with 1% Na_2Te and a controlled sample containing no SrTe. (d) Schematic representation of the alignment of the valence band (VB) and conduction band (CB) energies of SrTe precipitates in the PbTe matrix at 300 K. (e) *ZT* (~*zT*) as a function of temperature for PbTe–SrTe samples doped with 1% Na_2Te. K. Biswas *et al. Nat. Chem.* **2011**, *3*, 160–166 © Nature Publishing Group.

PbTe is the most efficient thermoelectric material for mid-range temperature (600–800 K) applications. It crystallizes in the NaCl crystal structure with Pb atoms occupying the cation sites and Te forming the anionic sub-lattice. It is a narrow band gap semiconductor (~0.32 eV) and can be doped either *n*- or *p*-type with appropriate dopants. Significant enhancement of the Seebeck coefficient was achieved by introducing resonant level in the valence band of PbTe by doping 2 mol% thallium (Tl), resulted doubling of *zT* to 1.5 at 773 K (Figure 1.6(c)).[22] Highly doped *p*-type Na-doped $PbTe_{1-x}Se_x$ also exhibit high-performance thermoelectric properties (*zT* ~1.8 at 850 K) arising from convergence of the multiple valence bands (Figure 1.7(b)).[26]

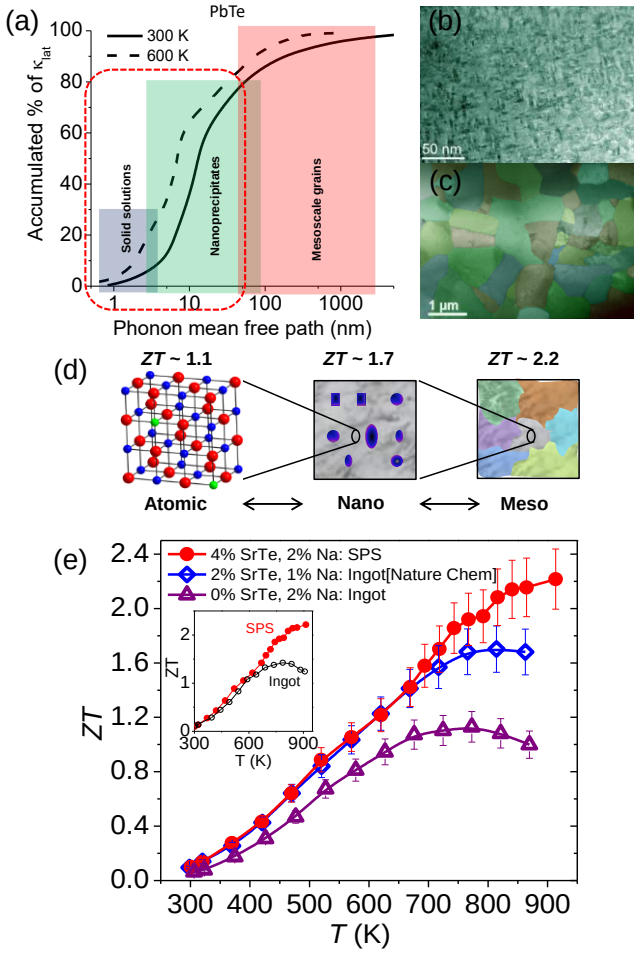

Figure 1.15 (a) Contributions of phonons with different mean free paths to the cumulative κ_{lat} value for PbTe. (b) and (c) Low and medium magnification TEM images shows the micro and nanostructures in spark-plasma-sintered PbTe–SrTe doped with Na respectively. (d) Maximum achievable *ZT* (~*zT*) values for the respective length scales: the atomic scale (alloy the nanoscale (PbTe matrix, grey; SrTe nanocrystals, blue) to the mesoscale (grain-boundary scattering). (e) Temperature dependent *zT* for an ingot (atomic scale), endotaxial nanostructuted PbTe (atomic plus nanoscale) and spark-plasma-sintered PbTe (atomic + nano + mesoscale). K. Biswas, *et al.*, *Nature*, **2012**, *489*, 414–418 © Nature Publishing Group.

Nanoscale inclusions in bulk materials can dramatically suppress the lattice thermal conductivity (κ_{lat}) by scattering the longer wavelength heat-carrying phonons, as shown first time in the case of $AgPb_mSbTe_{m+2}$.[37] In all these cases, however, the power factor ($S^2\sigma$) is also reduced because the nano-inclusions increase carrier scattering which in turn adversely affects the carrier mobility. Biswas and coworkers have observed that by embedding endotaxial SrTe nanocrystals at concentration as low as 2% in *p*-type bulk PbTe the heat flow can be greatly inhibited without affecting the carrier mobility, thereby allowing a large power factor to be maintained, as shown in Figure 1.14(a-c).[41] The insensitivity of carrier scattering was attributed to valence band alignment of SrTe and PbTe allowing facile hole transport (Figure 1.14(d)). The crystallographic alignment of SrTe and PbTe lattices and associated strain at interfaces decouples phonon and hole transport leading to a *zT* of 1.7 at ~ 800 K (Figure 1.14(e)).[41]

In 2012, Biswas and Kanatzidis have demonstrated a substantial suppression of lattice thermal conductivity at high temperature in the PbTe-SrTe system that led to a record high *zT* of ~2.2 at 915 K in spark plasma sintered-processed samples (Figure 1.15).[15] This is the result of introducing phonon scattering at all-length scales in a hierarchical fashion from atomic scale doping and endotaxial nanostructuring to mesoscale grain boundary engineering (Figure 1.15). With this new advance in the maximum *zT*, average *zT* values of ~1.2 and ~1.7 were obtained for non-segmented and segmented thermoelectric devices respectively (segmentation with BiSbTe, *zT* ~ 1.2 at 350 K). Considering a cold side temperature of 350 K and hot side 950 K for such devices waste heat conversion efficiencies respectively of ~16.5 and ~20 % were predicted.[15]

1.6.5 Tin selenide

SnSe is a layered material, adopt a orthorhombic crystal structure, which can be derived from a three-dimensional distortion of the NaCl structure (Figure 1.16).[51] At high temperature the low symmetry *Pnma* phase undergoes a displacive phase transition to a high symmetry *Cmcm* phase. The two-atom-thick SnSe slabs are folded up and create a zig zag accordion-like projection along the crystallographic b axis. In both the structures these identical layers are weakly bound (van der Waals interaction) and resulting in an anisotropic layered structure (Figure 1.16).[51,69] Zhao and Kanatzidis have investigated

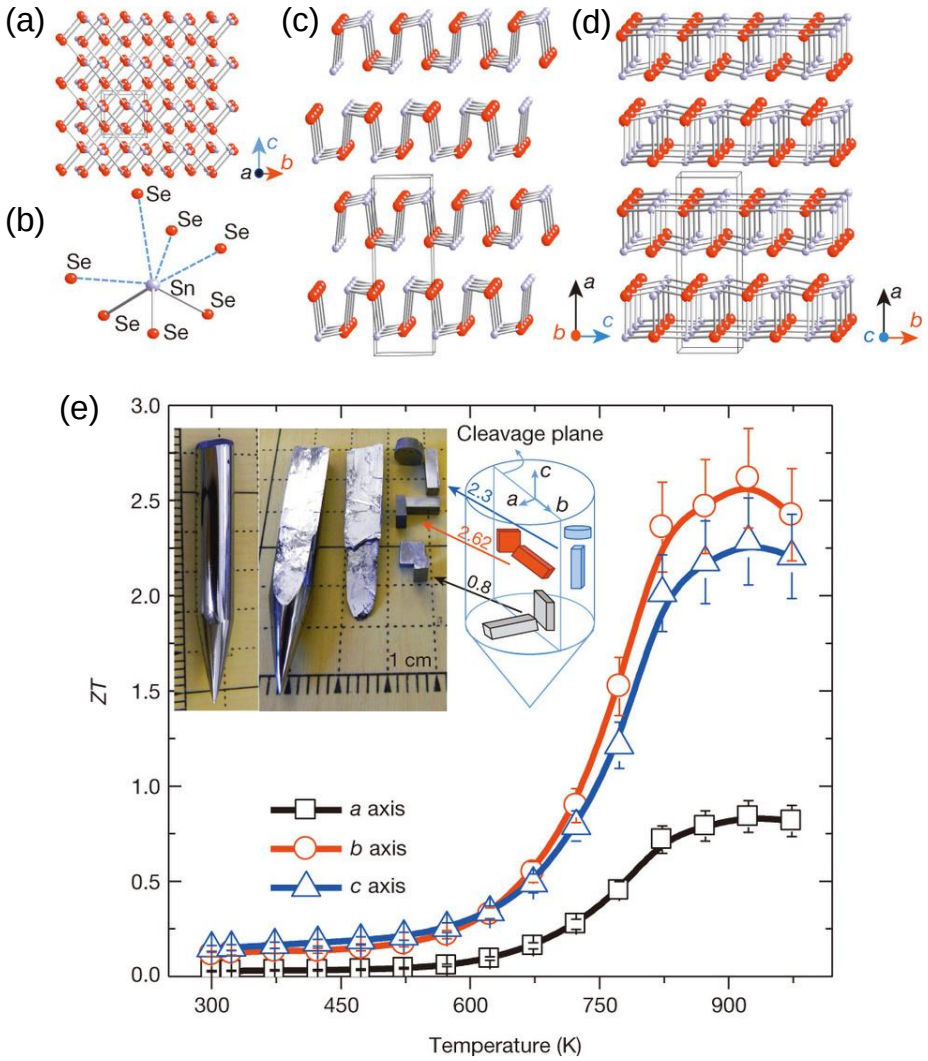

Figure 1.16 (a) Crystal structure of SnSe along the crystallographic *a* axis: grey, Sn atoms; red, Se atoms. (b) Highly distorted $SnSe_7$ coordination polyhedron with three short and four long Sn–Se bonds. (c) Structure along the *b* axis. (d) Structure along the *c* axis. (e) *ZT* (~*zT*) values along different axial directions; the *ZT* measurement uncertainty is about 15% (error bars). Inset images: left, a typical crystal; right, a crystal cleaved along the (l00) plane, and specimens cut along the three axes and corresponding measurement directions. Inset diagram, how crystals were cut for directional measurements; *ZT* values are shown on the blue, red and grey arrows; colours represent specimens oriented in different directions. L.-D. Zhao *et al.*, *Nature* **2014**, *508*, 373–377 © Nature Publishing Group.

the thermoelectric properties of single crystalline SnSe at different crystallographic direction. They are able to achieve a record high *zT* of 2.6 at 923 K due to moderate power factor and ultra-low thermal conductivity, measured along the *b* axis in SnSe crystals without addition of any impurities or other optimization (Figure 1.16(e)).[51] Thereafter investigations on the thermoelectric properties of SnSe has gained a

significant attention.[70][71] Recently, it has been shown that excellent average *zT* value can be obtained in Na-doped *p*-type SnSe single crystal due to increase in the σ value.[72]

1.6.6 Skutterudites

Skutterudites are one of the promising classes of compounds for thermoelectric power generation. They crystallize in cubic $CoAs_3$-type structure with the space group $Im\bar{3}$. The structure is composed of eight corner-shared XY_6 (X=Co, Rh, Ir; Y=P, As, Sb) octahedra. Linked octahedra gives rise to a void at the center of the $(XY_6)_8$ cluster, where the void space occupies a body-centered position of the cubic lattice. This void is large enough to accommodate large metal atoms to form filled skutterudites.[73] Since the void-filling atoms can act as electron donors or acceptors, partially filling the void space of skutterudites can lead to an optimum electron concentration. At the same time, these atoms can also act as strong phonon-scattering centers to greatly reduce the lattice thermal conductivity. The "rattling" effect of these void-filling atoms has resulted in improvements in the thermoelectric properties of skutterudite. High *zT* values of partially filled skutterudites with a small amount of Ni doping for Co, $Ba_{0.30}Ni_{0.05}Co_{3.95}Sb_{12}$ (*zT* ~1.25 at 900 K) were reported.[74] Further improvement in the *zT* was achieved by filling up multiple atom in the void of $CoSb_3$.[48]

1.6.7 Half Heusler compounds

Another class of compounds of considerable interest as potential thermoelectric materials for high-temperature applications is the Half-Heusler (HH) compounds denoted as MNiSn (M=Ti, Hf, Zr). HH phases have the MgAgAs crystal structure, which consists of three filled interpenetrating face-centered cubic lattice sublattices and one vacant sublattice. The general formula is XYZ, where X and Y are transition metals and Z is a main-group element.[75] Another advantage of these compounds is their high melting points of 1370-1573 K as well as their chemical stability with essentially zero sublimation at temperatures near 1273 K. The Heusler intermetallic compounds with fully filled sublattices are metals (full-Heusler alloys), whereas the vacant Ni atom sites in half-Heusler compounds give rise to narrow bands resulting in *d*-orbital hybridization and substantial semiconducting character of the compounds. Sakurada and Shutoh

reported a zT value ~1.4 at 700 K for *n*-type $(Zr_{0.5}Hf_{0.5})_{0.5}Ti_{0.5}NiSn_{1-y}Sb_y$.[76] Recently, Fu *et al.* has reported a zT of 1.5 in *p*-type $FeNb_{1-x}Hf_xSb$.[77]

1.7 Synthesis

1.7.1 Sealed tube method

Evacuated quartz tubes are used when the products or reactants are sensitive to air or water or are volatile. Majority of chalcogenides to date has been synthesized by sealed tube reactions in vacuum (10^{-3} -10^{-5} Torr) either by employing high-temperature melt cooling or alkali metal polychalcogenide fluxs A_2Q_n (Q= S, Se, Te) at low temperature. Chalcogens generally have low boiling temperature and hence evacuated tube is necessary to prevent boiling off and being lost from the reaction vessel. In high-temperature method, appropriate quantities of elemental metals and chalcogens are heated above the melting point of desired compounds in vacuum-sealed tubes, followed by cooling the reaction mixture at different cooling rates depending on the reaction conditions. Products of the reactions are thermodynamically/kinetically stable polycrystalline ingots or single crystals.[78,79]

1.7.2 Solvothermal method

The solvothermal method involves heating the reactants and solvent in a closed vessel, called autoclave. An autoclave is usually constructed from thick stainless steel to withstand the high pressures, and is fitted with safety valves; it may be lined with non-reactive materials such as teflon. The pressure generated in the vessel due to the solvent vapors elevates the boiling point of the solvent. Typically, solvothermal methods make use of various organic solvents such as ethanol, toluene, long chain organic molecule (oleic acid, octadecene, oleylamine) and water. This method has been widely used to synthesize zeolites, inorganic open-framework structures, and other solid materials. In the past few years, solvothermal synthesis has emerged to become the chosen method to synthesize nanocrystals of inorganic materials. By employing a metal salt, elemental Te/Se/S and a reducing agent, it is possible to produce metal chalcogenide nanocrystals. Control over size is rendered possible by the slow release of sulfide or selenide ions.[79,80]

1.7.3 Schlenk line method

The Schlenk line (also vacuum gas manifold) techniques are useful to work with air-sensitive compounds. It consists of a duplex of glass tubes with several ports connected side-by-side, which together is called a manifold. One manifold is connected to a source of purified inert gas (Ar, N_2), while the other is connected to a vacuum pump. The inert-gas line is vented through an oil bubbler. A liquid nitrogen or dry-ice/acetone cold trap generally use in the connector line of pump and manifold to prevent the contamination of the vacuum pump oil from solvent vapors and gaseous reaction products. Special stopcocks or Teflon taps allow vacuum or inert gas to be selected without the need for placing the sample on a separate line.

1.8 Characterizations

Following characterization techniques are used in the present thesis.

1.8.1 Powder X-ray diffraction (PXRD)

Powder X-ray diffraction is the most commonly used technique in solid state inorganic chemistry and has many uses from analysis and assessing phase purity to determining the structure. In this thesis, both lab source X- ray and synchrotron X-ray have been used for structural characterization. In the laboratory, X-rays are generated in a cathode tube. In this technique, a tungsten filament was heated to produce electrons and electron beam was then accelerated towards an anode by applying a voltage (~30-40 kV). When electrons have sufficient energy to dislodge inner shell electrons of the target material, characteristic X-ray spectra are produced. These spectra consist of several components, the most common being Kα and Kβ. Kα consists, in part, of Kα_1 and Kα_2. Kα_1 has a slightly shorter wavelength and twice intensity than Kα_2. The specific wavelengths are characteristic of the target material (Cu, Fe, Mo, Cr). Cu is the most common target material use for laboratory X-ray. To produce monochromatic X-rays, it is required filtering out Kβ radiation by foils or crystal monochromators. For Cu radiation, a sheet of Ni foil is a very effective filter, but it is difficult to remove Kα_2 from Kα_1 because of close wavelength. The filtering process in laboratory X-ray leads to a reduction in intensity and hence it is difficult to detect low-intensity peaks in laboratory X-ray

diffraction. In addition, it is difficult to distinguish peak splitting when peaks appear closely. These limitations can be ruled out in synchrotron X- ray. Synchrotron radiation is emitted when charged particles such as electrons, traveling at relativistic speeds, are forced to change direction on passing through a magnetic field. To generate synchrotron radiation, electrons or positrons are accelerated to speeds close to that of light and circulate in ultra-high vacuum tubes or storage rings, guided by arrays of magnets.

X-ray diffraction obeys Bragg's law, which states that constructive interference would occur if the path difference between the x-rays scattered from parallel planes were an integer number of the wavelength of radiation. If the planes of atoms, separated by a distance d, make an angle θ with the incident beam, then the path difference would be $2d\sin\theta$. So, for constructive interference, the Braggs law must be satisfied

$$i.e. \qquad n\lambda = 2d\sin\theta \qquad n = 1, 2, 3, \ldots\ldots \tag{1.13}$$

λ= wavelength of the x-ray radiation

In this thesis, room-temperature and high-temperature powder X-ray diffraction experiments on the samples are carried out using Bruker D8 Advance diffractometer using Cu-Kα radiation having wavelength 1.5406 Å. Powder or precipitates of the sample were placed on a glass plate sample holder during measurement. To understand the structural evolution we have also used temperature dependent synchrotron X-ray diffraction measurements under N_2 atm at BL-18B (Indian beamline), Photon Factory, KEK, Tsukuba, Japan. The wavelength of X-ray and temperature ranges for the measurement have been given in the experimental part of the respective chapters. The energy of the beam was set by Si(111) double crystal monochromator, which was cross-checked with Si (640b NIST) standard. All the measurements were carried out in Bragg-Brentano geometry with a divergence slit (300 μm), an anti-scattering slit (350 μm), and a receiving slit (300 μm). High-temperature measurements were carried out with Anton Paar DHS1100 heat cell.

1.8.2 Transmission electron microscopy (TEM)

TEM is one of the important tools in material science for characterization of the microscopic structure of materials. A TEM image represents a two-dimensional projection of a three-dimensional object. TEM operates on the same basic principles as the light microscope, however, uses electrons as "light source" that makes it possible to

get a resolution of about thousand times better than a visible light microscope. Instead of glass lenses focusing the light in the light microscope, the TEM uses electromagnetic lenses to focus the electrons into a very thin beam. The electron beam then travels through the specimen you want to study. When the electron beam passes through an ultrathin specimen, it gets absorbed or diffracted through the specimen. Some of the electrons are scattered and disappear from the beam depending on the density of the material present on the focused region. A "shadow image" is formed by the interaction of the electrons transmitted through the specimen focused onto a fluorescent screen or a photographic film or by a sensor such as a charge-coupled device (CCD). TEM study allows to focus electron beam to any part of specimen and electron diffraction data from a different area of the specimen can give us more details about the accurate local structure of the sample.

TEM samples for the solid state materials were prepared by conventional mechanical and tripod polishing. Large electron transparent area was obtained by subsequent Ar ion milling in the precision ion polishing system (PIPS) with the ion energy of 4.5 eV and beam angle of 7 deg. The thickness was restricted to 40-50 μm. Bright field imaging, Diffraction pattern, HRTEM imaging is carried out in aberration corrected FEI TITAN3™ 80–300kV transmission electron microscope. For nanocrystals, TEM samples were prepared by drop casting very dilute well-dispersed sample solution (solvent: water or organic solvent: hexane, toluene, ethanol) onto a carbon-coated grid (Cu grid). The grid was then dried under IR lamp to evaporate the solvent before imaging. TEM imaging was performed using JEOL (JEM3010) TEM microscope, operating at 300 kV and FEI TECNAI G^2 T20 operating at 200 kV.

1.8.3 Field emission scanning electron microscopy (FESEM)

Like TEM microscope, FESEM microscope also uses electrons as a light source. The electrons are liberated by a field emission source. The object is scanned by electrons according to a zig-zag pattern. Within the high vacuum column, the primary electrons are finely focused to produce a narrow scan beam which then bombards on the surface of the sample. As a result, secondary electrons are emitted from the sample. By scanning the sample and collecting the secondary electrons that are emitted using a detector, an image displaying the topography of the surface is created. This technique is useful for looking at

particle size, crystal morphology, magnetic domains, and surface defects. Using backscattered electrons (BSE) detection mode in FESEM it is possible to obtain compositional maps of a sample, as heavy elements (high atomic number) backscatter electrons more strongly than light elements (low atomic number), and thus appear brighter in the image.

Samples for FESEM imaging has been prepared by drop casting very dilute well-dispersed sample solution (solvent: water or organic solvent: hexane, toluene, ethanol) onto an alumina or silicon wafer. Before imaging, the sample was then dried under IR lamp to evaporate the solvent. FESEM imaging was performed using a NOVA NANO SEM 600 (FEI) microscope operated at 15 kV.

1.8.4 Energy dispersive X-ray analysis (EDX)

EDX is an analytical technique used for the elemental or compositional analysis of a sample. EDX makes use of the X-ray spectrum emitted by a solid sample bombarded with a focused beam of electrons to obtain elemental analysis. For EDX analysis an X-ray detector integrated with the FESEM or TEM instrument, which detects and converts X-ray into electronic signals. Qualitative analysis involves the identification of the lines in the spectrum and quantitative for each element in the sample involves measurement of x-ray intensities. We have performed EDX analysis with EDX Genesis instrument attached to the FESEM column. The STEM-EDX technique has been used for elemental mapping.

1.8.5 X-ray photoelectron spectroscopy (XPS)

XPS is a surface analytical technique, which measures the elemental composition, empirical formula, chemical state and electronic state of the elements in a material. The technique is based on Einstein's idea about the photoelectric effect. The sample analysis is conducted in ultrahigh vacuum chamber (~10^{-10} torr) to prevent contamination of the surface and aid an accurate analysis of the sample. When an X-ray beam directs to the sample surface, the energy of the X-ray photon is absorbed completely by the core electron of an atom. The ionizing radiation is usually a monochromatic X-ray (Mg Kα, 1254 eV, or Al Kα, 1487 eV)**.** If the photon energy, E_{photon}, is large enough, the core electron will then escape from the atom and emit out of the surface. The emitted electron

with the kinetic energy of $E_{kinetic}$ is referred to as the photoelectron. The binding energy, $E_{binding}$ of the core electron is given by the Einstein relationship:

$$E_{photon} = E_{binding} + E_{kinetic} + \phi \quad (1.14)$$

$$E_{binding} = E_{photon} - (E_{kinetic} + \phi)$$

where ϕ is the work function of the spectrometer, about few eV(~ 4-5 eV). $E_{kinetic}$ is determined by means of a high-resolution electron spectrometer. Since core electrons are close to the nucleus and have the binding energies characteristic of the certain chemical environment, XPS allow determining the atomic compositions of a sample or the chemical state of a certain element. On a modern instrument, the detection limits for most of the elements are in the parts per thousand range. However, using special condition parts per million (ppm) level detection is possible.

XPS measurements were performed with a Mg-Kα (1253.6 eV) X-ray source with a relative composition detection better than 0.1% on an Omicron Nanotechnology spectrometer.

1.8.6 Inductively coupled plasma atomic emission spectroscopy (ICP-AES)

ICP-AES is an analytical technique used to determine the elemental composition of a sample. An ICP-AES system composed of two basic parts: (i) the inductively coupled plasma source and (ii) the atomic emission spectrometry detector. This technique is based on Atomic Emission Spectroscopy. First, a stable, high-temperature plasma of about 7000 - 8000K is generated by an intense electromagnetic field, created using a high power radio frequency signal flowing in the coil. Argon gas is generally used to create the plasma. Sample introduced into the ICP should be liquid form. For solid samples, the sample should be dissolved completely in Millipore water in acidic medium (2-5%). The sample solution is introduced into the nebulizer chamber into the central channel of the plasma. The sample solution is quickly vaporized at central channel due to very high temperature (~8000 K). Therefore, molecule breaks up into individual elements as free atoms. The collisional excitation within the plasma imparts additional energy to the atoms, promoting them to excited states. In addition, sufficient energy is often available to convert the atoms to ions and subsequently promote the ions to excited states. Both the atomic and ionic excited state species may then relax to the ground state via the emission of a photon. Every element has its own characteristics emission spectrum and hence

element type is determined based on the wavelength of the photons. The concentration of each element is determined based on the intensity of photons.

In this thesis, we have used Perkin Elmer optima 7000 DV ICP-OES machine to determine the elemental concentration in our samples. Samples were dissolved in 2-5% (V/V) aqua regia (HNO_3: HCl = 1: 3)/ water solution, and different elemental concentrations were measured against high purity is known standards.

1.8.7 Optical band gap

In this thesis, diffuse reflectance method has been used for the determination of band gap of the solid powder material. Diffuse reflectance is an excellent sampling tool for powdered or crystalline materials. When radiation is directed onto the surface of a solid sample, two types of reflection can occur specular reflection and diffuse reflection. The specular component is the radiation that reflects directly off the sample surface according to the normal reflection law; angle of reflection equals the angle of incidence. Diffuse reflection is the radiation that penetrates into the sample and then emerges at all angles after suffering multiple reflections and refractions by the sample particles. A diffuse reflection accessory is designed so the diffusely reflected energy is optimized and the specular component is minimized. The optical system collects the scattered radiation and directs it to the detector. In 1931, Kubelka and Munk derived a theory of diffuse reflection and the function is given by equation 1.15

$$f(R) = \frac{(1-R)^2}{2R} = \frac{\alpha}{\Lambda} \tag{1.15}$$

where R is the absolute reflectance of the sample, α and Λ are the absorption and scattering coefficients. The Kubelka-Munk theory predicts a linear relationship between spectral intensity and sample concentration under conditions of constant scattering coefficient and infinite sample dilution. Therefore, the sample must be ground uniformly fine size and sample thickness should be low (~3 mm) if quantitatively valid measurements are desired. Using diffuse reflection spectroscopy, samples can be analyzed either directly or as dispersions in nonabsorbing matrices (*e.g.* alkali halides such as KBr) for qualitative analysis. It eliminates the time-consuming process of pressing pellets for transmission measurements. Apart from this, it has several other

advantages: (i) Very high sensitivity (ppm levels) (ii) Ability to analyze most nonreflective materials (iii) Ability to analyze irregular surfaces or coatings.

In this thesis, to probe optical energy gap of the synthesized compounds, diffuse reflectance measurements were performed on finely ground powders at room temperature. The spectra were recorded using a Perkin-Elmer Lambda 900, UV/Vis/NIR spectrometer.

1.8.8 Differential scanning calorimetry (DSC)

DSC is a thermoanalytical technique in which difference in the amount of heat released or absorbed by a sample is compared with that of an inert reference material during a programmed change of temperature. The sample and reference are maintained at the same temperature during heating and temperature are monitored with a thermocouple. The temperatures of the sample and reference remain same until some thermal event, such as melting, decomposition or change in crystal structure, occurs, in which case the sample temperature either lags behind (if the change is endothermic) or leads (if the change is exothermic) the reference temperature. The extra heat input to the sample (or to the reference if the sample undergoes an exothermic change) required in order to maintain this balance is measured and thus change in enthalpy measured directly.[81]

We have performed DSC measurement using an NETZSCH DSC 200F3 instrument with a heating/cooling rate of 20 K/ min in N_2 atmosphere. The temperature ranges for the measurement has been given in the relevant chapters.

1.8.9 Raman spectroscopy

Raman spectroscopy is a spectroscopic technique for structural characterization of inorganic or organic samples. This technique is based on inelastic scattering of monochromatic light. A change in the molecular polarizability with respect to the vibrational coordinate corresponding to the rovibronic state is required for a molecule to exhibit a Raman effect. Normally a laser source such as Nd: YAG with a fixed wavelength of 532 nm, an argon ion laser at 514 nm or a He–Ne laser at 633 nm a laser use for the light source. During the irradiation process, the photons of the laser light interacts with molecular vibrations, phonons or other excitations in the system and the molecule is promoted to a much higher energy state. This results in the molecule being in a so-called virtual energy state for a short period of time and then relax back, giving

either Rayleigh scatter with exactly the same energy and wavelength as the incident light (the molecule returns to its initial vibrational state). A very small amount of the scattered light (~10^{-6} times the incident light intensity) is shifted in energy either lower (Stokes) or higher (anti-Stokes) energy than the incident photon due to interactions between the incident electromagnetic waves and the vibrational energy levels of the molecules. In Raman scattering, Stokes lines are more intense than anti-Stokes because only molecules that are vibrationally excited before irradiation can give anti-Stokes line. Therefore, in Raman spectroscopy, only Stokes line is normally measured. Raman spectra are plotted with respect to the frequency of light such that the Rayleigh band (frequency of laser) lies at 0 cm^{-1}. Plotting the intensity of this "shifted" light versus frequency results in a Raman spectrum of the sample.

In this thesis, room temperature and temperature dependent Raman spectroscopic measurement were carried out on pellet shaped samples with an LABRAMHR spectrometer. The excitation wavelength of the laser was 514 nm. All the high-temperature measurements were carried out under N_2 gas flow.

1.8.10 Positron annihilation spectroscopy (PAS)

PAS is a nondestructive nuclear solid state technique commonly used for defects and voids study in materials. It is a powerful technique to study open volume defects like dislocation, agglomerates, and vacancies at ppm concentration. Positrons (e^+) is an antiparticle of the electron (e^-) having exactly equal rest-mass of the electron (511 keV) but with a positive charge. One can obtain positrons from the β^+ decay of radioactive isotopes such as ^{22}Na, ^{64}Cu, and ^{58}Co. In the present experiments, ^{22}NaCl has been used as positron source. Positrons injected from a radioactive source get thermalized within 1-10 ps and annihilate with a nearby electron inside the material, normally (379 out of 380 cases) emitting two exactly opposite 511 keV gamma rays, in the center of mass frame. The positron lifetime is inversely proportional to the electron density at the annihilation site. Hence by measuring the positron lifetime (sub nano-second) one can study the electron density distribution in the studied material. Naturally, the lifetime of positrons annihilated at defects is larger compared to the annihilation of positron in the bulk of the material, since the electron density is lower at such defects and positrons survive relatively longer time before annihilation. Therefore, the measured positron lifetime at

defects indicates the nature and type of the open volume and the corresponding intensity (weight of that particular lifetime in the overall spectrum) represents the relative abundance of such defect sites in the studied material.

The other PAS technique is to measure the Doppler broadening of the electron-positron annihilated γ-ray (511 keV) line shape (DBEPARL) with a high purity germanium (HPGe) detectors. The basic concept is that although before annihilation positrons are thermalized but the electron has some energy and the corresponding momentum is p_{el}. Thus the electron-positron pair has some momentum which is translated as a Doppler shift to the 511 keV γ-rays by an amount ($\pm \Delta E = p_L c/2$) in the laboratory frame; where p_L is the component of p_{el} along the direction of measurement. Contributions from all possible p_{el}s are convoluted in the DBEPARL spectrum which looks like an inverted parabola with the centroid at 511 keV ($p_{el} = 0$). The region close to the centroid is formed due to positron annihilation with very low momentum electrons. In the open volume defects, it is more probable for a positron to find a nearly free electron ($p_{el} \sim 0$), the wave function of which are spatially extended. The core electron wave functions are localized and do not span inside the open volumes. Therefore, a more sharpened DBEPARL spectrum represents sample with high concentration of open volume defects. The wing region of DBEPARL spectrum (away from centroid with a higher value of p_L) carries the information about the annihilation of positrons with the core electrons (which are element specific). De-convolution of DBEPARL spectrum is not straightforward thus ambiguous and in general, a simple methodology is adopted to understand the element specific changes in the wing region of the spectrum. Area-normalized DBEPARL spectrum of a high purity material, either Al, Si single crystal or a single crystal of the respective material is recorded in the same detector assembly. The ratio of counts at each energy is taken and the so-called “ratio curve” is formed. The peak and dip positions in this ratio curve represent more or less annihilation (respectively) with the electrons of nearby momentum region. The Compton continuum of 1276 keV gamma ray, simultaneously emitted with a positron from the ^{22}Na radioactive source, enhances the background counts in the wing region of the spectrum and thereby blurred the peak or dip shapes as well as positions. Two HPGe detector in coincidence successfully suppresses this Compton continuum and the chemical sensitivity of ratio curves with high

precision can be achieved. In general, defects modify the local electronic configuration and hence, an intimate relationship is found between PAS parameters (PAL and DBEPARL) and electronic properties of a material.[82][83]

The experimental details about the positron annihilation spectroscopy have been given in the relevant chapters.

1.8.11 Hall effect

Measurement of the hall effect gives an important source of information about the conduction type, especially in semiconductors. From conductivity measurement, it is not possible to separate the number of current carriers, *n*, from their mobility, μ. Combined hall and conductivity measurement enable the separation of *n* and μ. If a current of *I* amperes flows through a solid in one direction and a magnetic field *B* oersteds is applied at right angle to the direction of current flow, a potential difference is developed across the sample in the direction perpendicular to *B* and *I*. This is because the magnetic field causes the electrons to follow curved paths and therefore one side of the material becomes depleted in electrons compare to other side. The unequal electron concentration across the sample causes an electric field to build by until an equilibrium situation is reached where the tendency for electrons to deflect is balanced by the Hall potential acting in the opposite direction. Hall coefficient (R_H), charge carrier density (*n*), and carrier mobility (μ) for a material can be calculated using following equations,

$$\rho_H = \frac{R \times L \times T}{W} \tag{1.16}$$

$$R_H = \frac{R \times T}{B} \times 10^8 \, cm^3/C \tag{1.17}$$

$$n = \frac{1}{R_H \times e} \, cm^{-3} \tag{1.18}$$

$$\mu = \frac{\sigma}{n \times e} \tag{1.19}$$

ρ_H is the measured Hall resistivity [Ω·m]; *R* is the Hall resistance (Ω); *L*, *W*, *T* are the dimensions of the sample (cm), respectively. *n* is the charge carrier density (cm^{-3}); $e = 1.6 \times 10^{-19}$ C, σ and μ are the conductivity and carrier mobility.[81][84]

In this thesis hall measurement has been done in using an ECOPIA HMS 3000 system and also using PPMS (Physical Property Measurement System, Quantum Design,

USA) with a variable magnetic field up to 5 Tesla.

1.9 Thermoelectric measurements

1.9.1 Electronic transport

The power factor of the *zT* expression depends on the product of the Seebeck coefficient and the electrical conductivity. The Seebeck coefficient is the ratio of a resulting electric field gradient to an applied temperature gradient. In a typical measurement, the temperature is varied around a constant average temperature and the slope of the voltage (V) *vs.* temperature difference (ΔT) curve gives the Seebeck coefficient (the slope method) or just $V/\Delta T$ is measured (single point measurement). Either a specific temperature difference is stabilized before each measurement (steady-state), which takes longer, or measurements are conducted continuously while the temperature difference is varied slowly (quasi- steady-state). Little difference was found between steady-state and quasi-steady-state measurements when good thermal and electrical contact is ensured. The employed temperature difference should be kept small, but too small will lead to decreased accuracy. Usually, 4-20 K (or 2-10 K) is appropriate for the full temperature span.[85]

In the present thesis, temperature dependent Seebeck coefficient measurement has been done using the most popular commercial instruments ULVAC ZEM 3 RIKO using off-axis 4-point geometry under low-pressure helium (He) atmosphere (Figure 1.17(a)). In the off-axis, 4-point geometry, the thermocouples, and voltage leads are pressed against the sides of the sample (Figure 1.17(b)). The instrument uses slope method to extract the Seebeck coefficient from steady-state measurements. In the slope method, the measured raw data is corrected for constant offset voltages by using the slope of several (ΔT, V) points for extracting the Seebeck coefficient. The typical sample for measurement has a rectangular shape with the dimensions of 2 mm × 2 mm × 8 mm and ΔT values 5, 10, 15 K have been used in the measurement. The error in the measurement is ~5%. In a typical measurement, the sample is set in a vertical position between the upper and lower electrode blocks in the heating furnace. For temperature dependent measurement, the sample was first heated to a specified temperature using an infrared (IR) furnace.

Thereafter a temperature gradient across the sample was created by heating the lower part of it by a heater. Seebeck coefficient is measured by measuring the upper and lower temperatures T_1 and T_2 with the thermocouples pressed against the side of the sample, followed by measurement of voltage (ΔV) between the same wires on one side of the thermocouple.[86]

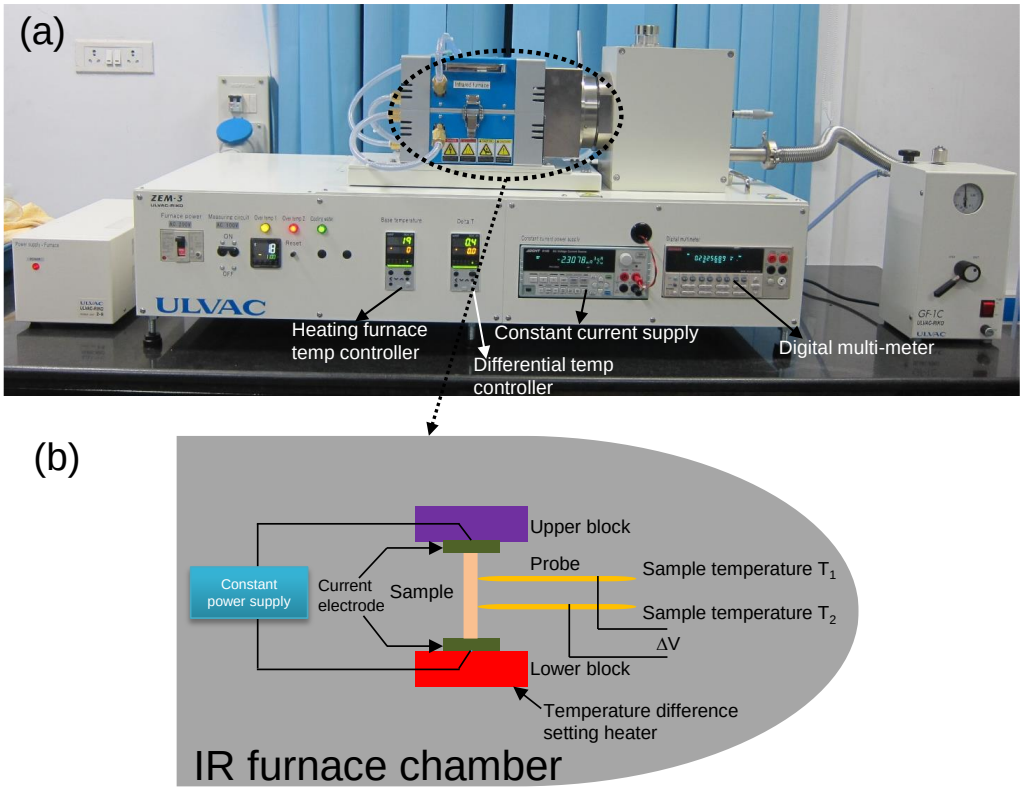

Figure 1.17 (a) Photograph of ULVAC ZEM 3 RIKO instrument (b) Schematic representation of sample chamber in ULVAC ZEM 3 RIKO.

The electrical conductivity, σ is measured using the four-probe method. Temperature dependent σ has been measured concurrently during Seebeck measurement in ULVAC ZEM 3 RIKO. For the measurement, a constant current I is applied to both ends of the sample to measure the voltage V between the thermocouple. By knowing resistance of sample, R ($R = V/I$), we can calculate σ from resistivity (ρ) of the sample using following equations:

$$\rho = R \times \frac{A}{l} \tag{1.20}$$

$$\sigma = \frac{1}{\rho} \tag{1.21}$$

where *A* is sample cross section and *l* is the distance between probes.

1.9.2 Thermal transport

The flash diffusivity method most frequently is used for the determination of thermal conductivity (κ_{total}) of material. Non-contact, non-destructive, easy sample preparation, applicability for a wide range of diffusivity values with excellent accuracy and reproducibility makes this method more advantageous than direct method. In the flash diffusivity method, the thermal conductivity is calculated as $\kappa_{total} = DC_p\rho$, where D is thermal diffusivity, ρ is density, and C_p is the constant pressure heat capacity. In this method, the sample is mounted on a carrier system, which is located in a furnace. After the sample reaches a predetermined temperature, a short heat pulse from a pulsed laser is applied to one side of a thin sample, resulting in homogeneous heating. The relative temperature increase on the rear face of the sample is then measured as a function of time by an IR detector. The temperature will rise to a maximum, after which it will decay. The time for the temperature to increase to half-maximum, $t_{1/2}$, is used to calculated the thermal diffusivity using equation 1.22

$$D = 0.1388 \times \frac{l^2}{t_{1/2}} \tag{1.22}$$

where D is thermal diffusivity in cm^2/sec, l is the thickness.[87]

In this thesis, temperature dependent thermal transport measurement has been done using the most popular NETZSCH LFA-457 instrument in N_2 atmosphere (Figure 1.18(a)). Coins with ~8 mm diameter and ~2 mm thickness were used for all the measurements. The samples were coated with a thin layer of graphite (~5 μm) in order to enhance the absorption of laser energy and emission of IR radiation to the detector. It also increases the signal to noise ratio. The error for the κ_{total} measurement is ~5%. The samples were placed inside SiC sample holder to mount on carrier system (Figure 1.18(c)). A Nd-Glass pulsed laser source of wavelength 1054 nm has been used for all the measurement. To measure the increased temperature on the rear face of the sample a liquid N_2 cooled InSb IR detector has been used. The density (ρ) was determined using the dimensions and mass of the sample and C_p, was derived indirectly using a standard

sample (pyroceram). The thermal diffusivity data were analyzed using a Cowan model with pulse correction to account for heat losses on the sample faces.

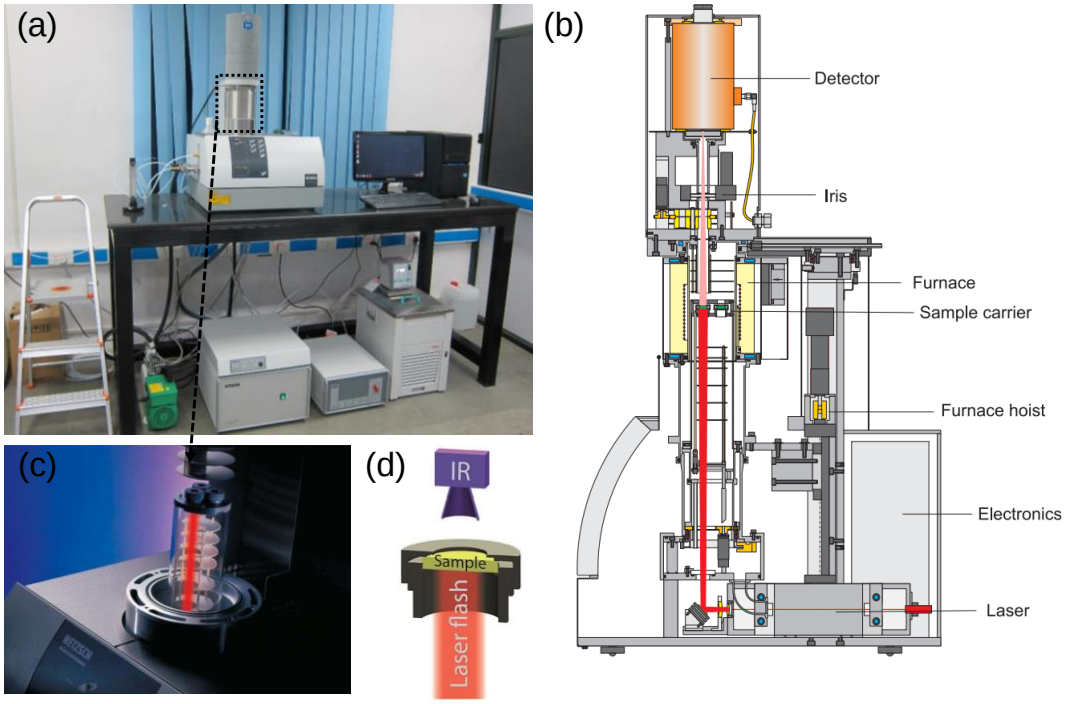

Figure 1.18 (a) Photograph of NETZSCH LFA-457 instrument. In (b) diffident component of the instrument. (c) and (d) show schematic of a short laser pulse is applied to the bottom of a sample (shown in a sample holder) and the resulting temperature rise on the top is monitored with an IR detector[85].

1.10 Motivation of the thesis

The global need for sustainable energy inspires a growing interest in the thermoelectric research. In the past two decades, there has been a rapid growth and several exciting conceptual and performance breakthroughs in thermoelectric research. This was achieved through greater theoretical understanding, the power of synthetic solid-state chemistry in its ability to deliver new materials, new processing techniques and state-of-the-art measurements. All these together keep promises to advance further. New concepts make it possible to invent new strategies on how to decouple the strong interrelation of thermoelectric transport parameters. As there are no theoretical or thermodynamic limits to the maximum value of zT, much higher performance can be anticipated for the next generation of thermoelectric devices. In addition, significant focus needs for the development of *n*-type and lead and tellurium free thermoelectric materials. In this context, many materials yet to be investigated, and therefore, any strategy that balances

or decouples thermoelectric parameters would be useful for the development of new materials. In the following chapters we will focus on the (a) decoupled electronic and phonon transport in super-ionic noble metal chalcogenides, (b) effect of lone pair and aliovalent doping on the thermoelectric performance of Te- free metal chalcogenides and (c) stabilization of kinetic phases of noble metal chalcogenides and effect of order-disordered transitions on their thermoelectric properties.

References

[1] T. M. Tritt, *Annu. Rev. Mater. Res.* **2011**, *41*, 433–448.

[2] A. Shakouri, *Annu. Rev. Mater. Res.* **2011**, *41*, 399–431.

[3] D. Kraemer, B. Poudel, H. Feng, J. C. Caylor, B. Yu, X. Yan, Y. Ma, X. Wang, D. Wang, A. Muto, et al., *Nat. Mater.* **2011**, *10*, 532–538.

[4] L. E. Bell, *Science* **2008**, *321*, 1457–61.

[5] G. J. Snyder, E. S. Toberer, *Nat. Mater.* **2008**, *7*, 105–114.

[6] D. M. Rowe, *CRC Handbook of Thermoelectrics*, CRC Press, Boca Raton, **1995**.

[7] T. M. Tritt, M. A. Subramanian, *MRS Bull.* **2006**, *31*, 188–198.

[8] H. J. Goldsmid, *Thermoelectric Refrigeration*, Springer, **1964**.

[9] D. Nemir, J. Beck, *J. Electron. Mater.* **2010**, *39*, 1897–1901.

[10] D. Kraemer, J. Sui, K. McEnaney, H. Zhao, Q. Jie, Z. F. Ren, G. Chen, *Energy Environ. Sci.* **2015**, *0*, 1–10.

[11] J. F. Li, W. S. Liu, L. D. Zhao, M. Zhou, *NPG Asia Mater.* **2010**, *2*, 152–158.

[12] M. S. Dresselhaus, G. Chen, M. Y. Tang, R. Yang, H. Lee, D. Wang, Z. Ren, J. P. Fleurial, P. Gogna, *Adv. Mater.* **2007**, *19*, 1043–1053.

[13] J. R. Sootsman, D. Y. Chung, M. G. Kanatzidis, *Angew. Chemie - Int. Ed.* **2009**, *48*, 8616–8639.

[14] G. Tan, L.-D. Zhao, M. G. Kanatzidis, *Chem. Rev.* **2016**, *116*, 12123–12149.

[15] K. Biswas, J. He, I. D. Blum, C.-I. Wu, T. P. Hogan, D. N. Seidman, V. P. Dravid, M. G. Kanatzidis, *Nature* **2012**, *489*, 414–418.

[16] W. G. Zeier, A. Zevalkink, Z. M. Gibbs, G. Hautier, M. G. Kanatzidis, G. J. Snyder, *Angew. Chemie - Int. Ed.* **2016**, *55*, 6826–6841.

[17] G. D. Mahan, in *MRS Proc.*, Cambridge Univ Press, **1998**, p. 459.

[18] J. P. Heremans, B. Wiendlocha, A. M. Chamoire, *Energy Environ. Sci.* **2012**, *5*, 5510–5530.

[19] Y. Pei, H. Wang, G. J. Snyder, *Adv. Mater.* **2012**, *24*, 6125–6135.

[20] J. Korringa, A. N. Gerritsen, *Physica* **1953**, *19*, 457–507.

[21] J. Friedel, *Can. J. Phys.* **1956**, *34*, 1190–1211.

[22] J. P. Heremans, V. Jovovic, E. S. Toberer, A. Saramat, K. Kurosaki, A. Charoenphakdee, S. Yamanaka, G. J. Snyder, *Science* **2008**, *321*, 554–557.

[23] G. D. Mahan, J. O. Sofo, *Proc. Natl. Acad. Sci. U. S. A.* **1996**, *93*, 7436–7439.

[24] Q. Zhang, B. Liao, Y. Lan, K. Lukas, W. Liu, K. Esfarjani, C. Opeil, D. Broido, G. Chen, Z. Ren, *Proc. Natl. Acad. Sci.* **2013**, *110*, 13261–13266.

[25] A. Banik, K. Biswas, *J. Mater. Chem. A* **2014**, *2*, 9620–9625.

[26] Y. Pei, X. Shi, A. LaLonde, H. Wang, L. Chen, G. J. Snyder, *Nature* **2011**, *473*, 66–69.

[27] I. A. Ravich, Y. I., Efimova, B. A. Smirnov, *Semiconducting Lead Chalcogenides*, Springer, **1970**.

[28] L. D. Zhao, H. J. Wu, S. Q. Hao, C. I. Wu, X. Y. Zhou, K. Biswas, J. Q. He, T. P. Hogan, C. Uher, C. Wolverton, et al., *Energy Environ. Sci.* **2013**, *6*, 3346–3355.

[29] Y. Pei, A. D. LaLonde, N. A. Heinz, G. J. Snyder, *Adv. Energy Mater.* **2012**, *2*, 670–675.

[30] G. Tan, F. Shi, S. Hao, L.-D. Zhao, H. Chi, X. Zhang, C. Uher, C. Wolverton, V. P. Dravid, M. G. Kanatzidis, *Nat. Commun.* **2016**, *7*, 12167.

[31] A. Banik, U. S. Shenoy, S. Anand, U. V Waghmare, K. Biswas, *Chem. Mater.* **2015**, *27*, 581–587.

[32] G. Tan, F. Shi, S. Hao, H. Chi, T. P. Bailey, L. D. Zhao, C. Uher, C. Wolverton, V. P. Dravid, M. G. Kanatzidis, *J. Am. Chem. Soc.* **2015**, *137*, 11507–11516.

[33] G. Tan, F. Shi, J. W. Doak, H. Sun, L.-D. Zhao, P. Wang, C. Uher, C. Wolverton, V. P. Dravid, M. G. Kanatzidis, *Energy Environ. Sci.* **2015**, *8*, 267–277.

[34] A. Banik, U. S. Shenoy, S. Saha, U. V Waghmare, K. Biswas, *J. Am. Chem. Soc.* **2016**, *138*, 13068–13075.

[35] C. J. Vineis, A. Shakouri, A. Majumdar, M. G. Kanatzidis, *Adv. Mater.* **2010**, *22*, 3970–3980.

[36] M. G. Kanatzidis, *Chem. Mater.* **2010**, *22*, 648–659.

[37] K. F. Hsu, S. Loo, F. Guo, W. Chen, J. S. Dyck, *Science* **2004**, *303*, 818–821.

[38] J. Androulakis, K. F. Hsu, R. Pcionek, H. Kong, C. Uher, J. J. D'Angelo, A. Downey, T. Hogan, M. G. Kanatzidis, *Adv. Mater.* **2006**, *18*, 1170–1173.

[39] P. F. P. Poudeu, J. D'Angelo, A. D. Downey, J. L. Short, T. P. Hogan, M. G. Kanatzidis, *Angew. Chemie Int. Ed.* **2006**, *45*, 3835–3839.

[40] K. Ahn, K. Biswas, J. He, I. Chung, V. Dravid, M. G. Kanatzidis, *Energy Environ.*

Sci. **2013**, *6*, 1529.

[41] K. Biswas, J. He, Q. Zhang, G. Wang, C. Uher, V. P. Dravid, M. G. Kanatzidis, *Nat. Chem.* **2011**, *3*, 160–166.

[42] L. D. Zhao, S. Hao, S. H. Lo, C. I. Wu, X. Zhou, Y. Lee, H. Li, K. Biswas, T. P. Hogan, C. Uher, et al., *J. Am. Chem. Soc.* **2013**, *135*, 7364–7370.

[43] J. He, M. G. Kanatzidis, V. P. Dravid, *Mater. Today* **2013**, *16*, 166–176.

[44] L.-D. Zhao, V. P. Dravid, M. G. Kanatzidis, *Energy Environ. Sci.* **2014**, *7*, 251–268.

[45] G. Tan, L. D. Zhao, F. Shi, J. W. Doak, S. H. Lo, H. Sun, C. Wolverton, V. P. Dravid, C. Uher, M. G. Kanatzidis, *J. Am. Chem. Soc.* **2014**, *136*, 7006–7017.

[46] A. Banik, B. Vishal, S. Perumal, R. Datta, K. Biswas, *Energy Environ. Sci.* **2016**, *9*, 2011–2019.

[47] D. T. Morelli, G. P. Meisner, B. Chen, S. Hu, C. Uher, *Phys. Rev. B* **1997**, *56*, 7376.

[48] X. Shi, J. Yang, J. R. Salvador, M. Chi, J. Y. Cho, H. Wang, S. Bai, J. Yang, W. Zhang, L. Chen, *J. Am. Chem. Soc.* **2011**, *133*, 7837–7846.

[49] A. Saramat, G. Svensson, A. E. C. Palmqvist, C. Stiewe, E. Mueller, D. Platzek, S. G. K. Williams, D. M. Rowe, J. D. Bryan, G. D. Stucky, *J. Appl. Phys.* **2006**, *99*, 23708.

[50] B. C. Sales, *MRS Bull.* **1998**, *23*, 15–21.

[51] L.-D. Zhao, S.-H. Lo, Y. Zhang, H. Sun, G. Tan, C. Uher, C. Wolverton, V. P. Dravid, M. G. Kanatzidis, *Nature* **2014**, *508*, 373–377.

[52] S. K. Saha, *Phys. Rev. B* **2015**, *92*, 41202.

[53] H. Liu, X. Shi, F. Xu, L. Zhang, W. Zhang, L. Chen, Q. Li, C. Uher, T. Day, G. J. Snyder, *Nat. Mater.* **2012**, *11*, 422–425.

[54] E. S. Toberer, A. F. May, G. J. Snyder, *Chem. Mater.* **2010**, *22*, 624–634.

[55] K. Kurosaki, A. Kosuga, H. Muta, M. Uno, S. Yamanaka, *Appl. Phys. Lett.* **2005**, *87*.

[56] M. D. Nielsen, V. Ozolins, J. P. Heremans, *Energy Environ. Sci.* **2013**, *6*, 570–578.

[57] E. J. Skoug, D. T. Morelli, *Phys. Rev. Lett.* **2011**, *107*, 235901.

[58] S. Lee, K. Esfarjani, T. Luo, J. Zhou, Z. Tian, G. Chen, *Nat. Commun.* **2014**, *5*,

3525.

[59] J. P. Heremans, *Nat. Phys.* **2015**, *11*, 990–991.

[60] L.-D. Zhao, C. Chang, G. Tan, M. G. Kanatzidis, *Energy Environ. Sci.* **2016**, *9*, 3044–3060.

[61] M. Zebarjadi, K. Esfarjani, M. S. Dresselhaus, Z. F. Ren, G. Chen, *Energy Environ. Sci.* **2012**, *5*, 5147–5162.

[62] G. S. Nolas, J. Sharp, J. Goldsmid, *Thermoelectrics: Basic Principles and New Materials Developments*, Springer Science & Business Media, **2013**.

[63] D. Teweldebrhan, V. Goyal, A. A. Balandin, *Nano Lett.* **2010**, *10*, 1209–1218.

[64] B. Poudel, Q. Hao, Y. Ma, Y. Lan, A. Minnich, B. Yu, X. Yan, D. Wang, A. Muto, D. Vashaee, et al., *Science* **2008**, *320*, 634–638.

[65] R. J. Mehta, Y. Zhang, C. Karthik, B. Singh, R. W. Siegel, T. Borca-Tasciuc, G. Ramanath, *Nat. Mater.* **2012**, *11*, 233–240.

[66] S. Il Kim, K. H. Lee, H. A. Mun, H. S. Kim, S. W. Hwang, J. W. Roh, D. J. Yang, W. H. Shin, X. S. Li, Y. H. Lee, et al., *Science* **2015**, *348*, 109–114.

[67] D.-Y. Chung, T. Hogan, P. Brazis, M. Rocci-lane, C. Kannewurf, M. Bastea, C. Uher, M. G. Kanatzidis, *Science* **2000**, *287*, 1024–2027.

[68] D. Y. Chung, T. P. Hogan, M. Rocci-Lane, P. Brazis, J. R. Ireland, C. R. Kannewurf, M. Bastea, C. Uher, M. G. Kanatzidis, *J. Am. Chem. Soc.* **2004**, *126*, 6414–6428.

[69] F. Q. Wang, S. Zhang, J. Yu, Q. Wang, *Nanoscale* **2015**, *7*, 15962–15970.

[70] S. Sassi, C. Candolfi, J.-B. Vaney, V. Ohorodniichuk, P. Masschelein, A. Dauscher, B. Lenoir, *Mater. Today Proc.* **2015**, *2*, 690–698.

[71] T.-R. Wei, G. Tan, X. Zhang, C.-F. Wu, J.-F. Li, V. P. Dravid, G. J. Snyder, M. G. Kanatzidis, *J. Am. Chem. Soc.* **2016**, *138*, 8875–8882.

[72] L.-D. Zhao, G. Tan, S. Hao, J. He, Y. Pei, H. Chi, H. Wang, S. Gong, H. Xu, V. P. Dravid, et al., *Science* **2016**, *351*, 141–144.

[73] G. S. Nolas, D. T. Morelli, T. M. Tritt, *Annu. Rev. Mater. Sci.* **1999**, *29*, 89–116.

[74] X. Tang, Q. Zhang, L. Chen, T. Goto, T. Hirai, *J. Appl. Phys.* **2005**, *97*, 3712.

[75] T. Graf, C. Felser, S. S. P. Parkin, *Prog. Solid State Chem.* **2011**, *39*, 1–50.

[76] S. Sakurada, N. Shutoh, *Appl. Phys. Lett.* **2005**, *86*, 82105.

[77] C. Fu, S. Bai, Y. Liu, Y. Tang, L. Chen, X. Zhao, T. Zhu, *Nat. Commun.* **2015**, *6*, 8144.

[78] C. N. R. Rao, K. Biswas, *Essentials of Inorganic Materials Synthesis*, John Wiley & Sons, **2015**.

[79] L. E. Smart, E. A. Moore, *Solid State Chemistry: An Introduction*, CRC Press, **2012**.

[80] C. N. R. Rao, P. J. Thomas, G. U. Kulkarni, *Nanocrystals*, Springer, **2007**.

[81] A. West, *Solid State Chemistry and Its Applications, 2nd Edition, Student Edition*, **2014**.

[82] A. N. Singh, *Appl. Spectrosc. Rev.* **2016**, *51*, 359–378.

[83] C. Hautojarvi, P. Corbel, *Positron Spectroscopy of Solids*, IOS Press: Amsterdam, The Netherlands, **1995**.

[84] Quantum Design, *Physical Property Measurement System Manual*, **n.d.**

[85] K. A. Borup, J. de Boor, H. Wang, F. Drymiotis, F. Gascoin, X. Shi, L. Chen, M. I. Fedorov, E. Müller, B. B. Iversen, et al., *Energy Environ. Sci.* **2015**, *8*, 423–435.

[86] ULVAC ZEM3 RIKO, *Seebeck-Coefficient and Eleectric-Resistance-Measuring-System Manual*, **2012**.

[87] NETZSCH, *Operating Instructions LFA 457 Microflash*, **2012**.

Chapter 2

The effect of order-disorder phase transitions and electronic structure modulation on the thermoelectric properties of AgCuS *

Chapter 2A: *Temperature dependent reversible p-n-p type conduction switching with colossal change in thermopower of semiconducting bulk AgCuS*[1]

Chapter 2B: *Tailoring of p-n-p type conduction switching and thermoelectric properties of AgCuS by size reduction to nanoscale*[2]

*Publication based on this work: (1) *J. Am. Chem. Soc.*, **2014,** *136,* 12712; (2) *Chem. Sci.* **2016,** *7,* 534.

CHAPTER 2A

Temperature dependent reversible *p-n-p* type conduction switching with colossal change in thermopower of semiconducting bulk AgCuS

Summary. *Copper and silver based chalcogenides, chalco-halides, and halides form a unique class of semiconductors, as they display mixed ionic and electronic conduction in their superionic phase. These compounds are composed of softly coupled cationic and anionic substructures and undergo a transition to a superionic phase displaying changes in the substructure of their mobile ions with varying temperature. Here, we show that a crystalline semiconducting noble metal sulfide, AgCuS, exhibits a sharp temperature-dependent reversible p-n-p type conduction switching, along with a colossal change in the thermopower (ΔS of ~1757 $\mu V\ K^{-1}$) at the superionic phase transition (T of ~364 K). In addition, its thermal conductivity is ultra-low in 300-550 K range giving AgCuS the ability to maintain temperature gradients. We have developed fundamental understanding of the phase transition and p-n-p type conduction switching in AgCuS through temperature dependent synchrotron powder X-ray diffraction, heat capacity, Raman spectroscopy, and positron annihilation spectroscopy measurements. First-principles calculations show that this rare combination of properties originates from an effective decoupling of electrical conduction and phonon transport associated with electronic states of the rigid sulfur sublattice and soft vibrations of the disordered cation sublattices, respectively. Temperature dependent p-n-p type conduction switching makes AgCuS an ideal material for diode or transistor devices that operate reversibly on temperature or voltage changes near room temperature.*

2A.1 Introduction

Structural phase transformation is a common phenomenon in materials that is of fundamental interest to solid-state inorganic chemistry.[1–3] Besides structural rearrangement, such a phase transformation can also involve changes in electronic or spin configurations, bringing in novel physical properties, such as superconductivity,[4] superionic conduction,[5,6] optical storage,[7] photoelectronic effect,[8] giant magnetocaloric effect[9] and thermoelectricity.[10–12] Switching of a material's property by external stimuli is interesting because of the fundamental science of bistability and nonlinearity, as well as of its possible technological applications.[13,14] Design and control of the changes in physical properties associated with a phase transition have been key to the development of modern functional materials.[15] Among various inorganic materials, semiconductors have been versatile in their use in transistors, non-volatile memory devices, electrochemical energy storage devices, resistive switching devices, thermoelectric energy conversion, and sensor applications.[16–20] Silver and copper chalcogenides, chalco-halides, and halides form a special class of semiconductors, as they typically exhibit mixed ionic and electronic conduction in their superionic phases.[5,6,17] These compounds are made of weakly coupled cationic and anionic substructures and undergo a transition to a superionic phase with changes in the substructure of mobile ions.[5,21] Their electronic and phonon spectra can thus be modulated due to the sudden change in the ionic mobility or in the covalent interactions within the anionic substructure.[13,16,22,23] For example, $Ag_{10}Te_4Br_3$ is capable of switching its electrical conduction induced by a change of temperature and, hence, can be used as a switch.[17] The formation of *p*-*n* or *p*-*n*-*p* junctions can be induced in such mixed ionic-electronic conductors simply by altering external electrochemical potential or temperature gradients.[14,17,24] Silver and copper based chalcogenides are also recognized as good candidates for metal-insulator-metal type non-volatile memory devices.[16,25]

Silver copper sulfide, AgCuS, is a polymorphous semiconductor that exhibits fascinating phase transitions as a function of temperature due to changes in the cationic mobility. The existence of four different polymorphs of AgCuS has been reported. [26,27] At room temperature, AgCuS crystallizes in the orthorhombic phase, *β*-AgCuS (*Cmc2₁*; *a* = 4.06 Å, *b* = 6.66 Å, *c* = 7.99 Å).[27] This room temperature structure consists of distort-

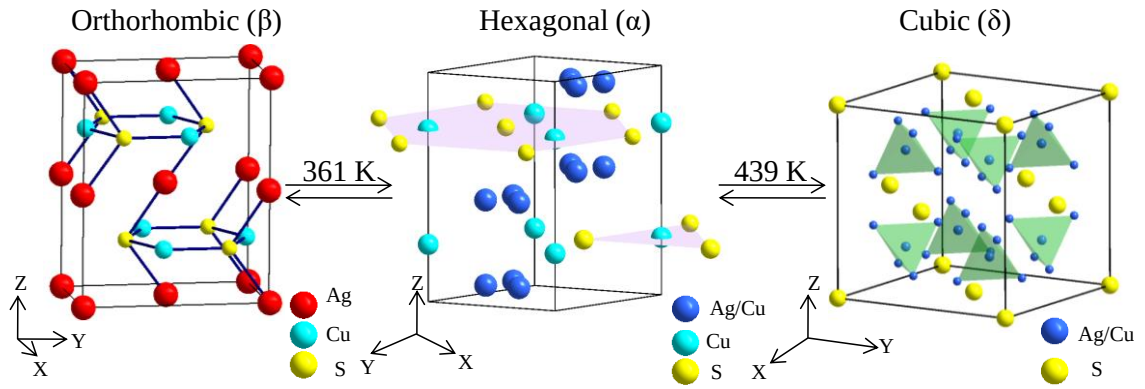

Figure 2A.1 (a) Temperature dependent crystal structural evaluation of AgCuS. In hexagonal phase, Ag and Cu are partially disordered in 12k position. In cubic structure, Ag and Cu are disordered in 8c and 32f positions.

ed hexagonal close packing (*hcp*) of sulfur atoms and three coordinated Cu atoms that lie in the *hcp* sulfur layer (Figure 2A.1). Ag atoms form loosely packed face-centered-cubic (*fcc*) layers that alternate with those of CuS, and each bonded to two sulfur atoms having a near-linear geometry (Figure 2A.1).[26] Below 120K, γ polymorph of AgCuS crystallizes in $Pmc2_1$ space group, which is a slightly distorted form of the room-temperature structure.[26] Two more structural phase transitions have been reported at higher temperatures, at 361 K (β- α) and 439 K (α- δ), respectively. Superionic α and δ phases are reported to crystallize in the hexagonal ($P6_3/mmc$; $a = b$ = 4.1389 Å, c= 7.0817 Å) and the cubic structure ($Fm\bar{3}m$; a = 5.9863 Å), respectively (Figure 2A.1).[27–29] In the high-temperature superionic α phase, sulfur atoms preserve the *hcp* sublattice, while Ag and Cu atoms are partially disordered. The second high-temperature superionic δ phase is constituted of a rigid *fcc* lattice of sulfur atoms, in which cations are randomly distributed at tetrahedral and octahedral interstitial sites (Figure 2A.1).[26]

In this chapter, we present a temperature-dependent reversible *p-n-p* type conduction switching along with a colossal change in the thermopower (ΔS of ~1757 μV K^{-1}) at the superionic phase transition (T of ~364 K) in the crystalline ingot of AgCuS. AgCuS also exhibits ultra-low thermal conductivity (0.5-0.7 W/mK) in the temperature range of 300-550 K. Temperature dependent Raman spectroscopy shows a clear variation in Raman spectra during the phase transition temperature and existence of Cu-S bond during (β-α) phase transition. First-principles density functional theoretical calculations reveal the existence of semi-metallic intermediate states(constituting of hybridized Cu- S

orbital) with Fermi level cutting into the conduction band that overlaps with valence band during the orthorhombic (β) to hexagonal (α) phase transition, which is responsible for the observed *p-n-p* type conduction switching in AgCuS. We show that electronic states of the rigid sulfur sublattice are primarily responsible for electronic charge transport, whereas phonon spectrum suggests that disordering and soft vibrations of Ag and Cu atoms are responsible for the observed low thermal conductivity. Thus, an effective decoupling of electronic and phonon transport is evident in AgCuS.

2A.2 Methods

2A.2.1 Synthesis

The following elements were purchased from Alfa Aesar and used for the synthesis without further purification. Elemental silver (Ag, 99.999%, metal basis), elemental copper (Cu, 99.9999%, metal basis), and elemental sulfur (S, 99.999%).

Ingot (~7 g) of AgCuS has been synthesized by mixing appropriate ratios of high-purity starting materials of Ag (3.6938 g, 0.03424 mol), Cu (2.1761 g, 0.03424 mol), and S (1.0978 g, 0.03424 mol) in quartz tube. The tubes were sealed under high vacuum (~10^{-5} Torr) and slowly heated to 773 K over 12 h, then heated to 1223 K in 5 h, soaked for 24 h, and subsequently, air quenched to room temperature. For electrical transport and thermal transport measurements, the sample was cut and polished. In the inset of Figure 2A.2(a), we have shown a photograph of "as synthesized" high quality ingot of AgCuS with bar and coin shaped sample obtained after cutting and polishing the ingot. Bar-shaped sample is used for electrical transport measurement, whereas coin shaped sample is used for thermal conductivity measurement.

2A.2.2 Characterizations

Room temperature powder X-ray diffraction of the sample was recorded using a Cu Kα (λ = 1.5406 Å) radiation on a Bruker D8 diffractometer. Temperature-dependent X-ray diffraction measurements under N_2 flow were carried out with X-ray beam of E = 12.42 keV and λ = 0.998 Å, at BL-18B (Indian beamline), Photon Factory, KEK, Tsukuba, Japan. DSC data and specific heat were measured using a Netzsch DSC 200F3 instrument. To probe optical energy gap of these compounds, optical diffuse reflectance

measurement was performed on finely ground powder using a Perkin Elmer Lambda 900, UV/vis/NIR spectrometer. Temperature-dependent Raman spectroscopy measurements were carried out with a LABRAM HR spectrometer. The positron annihilation lifetimes have been measured with a fast-fast coincidence assembly consisting of two constant fraction differential discriminators (Fast ComTech; Model number: 7029A). Detailed discussions on all the characterizations have been given in the introduction part of the thesis (page 31).

2A.2.3 Thermoelectric measurements

Seebeck coefficient and electrical conductivity were measured under helium atmosphere by ULVAC-RIKO ZEM-3 instrument from 290 to 550 K. Thermal diffusivity, *D*, was directly measured in the range of 290-550 K by laser flash diffusivity method in a Netzsch LFA-457 under N_2 atmosphere. The total thermal conductivity, κ_{total}, was calculated using the formula, $\kappa_{total} = DC_p\rho$, where ρ is the density of the sample, measured using sample dimension and mass. Detailed discussions on the thermoelectric measurements have been given in the introduction part of the thesis (page 41).

2A.2.4 Positron annihilation spectroscopy

The positron annihilation lifetimes have been measured with a fast-fast coincidence assembly consisting of two constant fraction differential discriminators (Fast ComTech; Model number: 7029A). The detectors are 25 mm-long × 25 mm tapered to 13 mm diameter (truncated conical) BaF_2 scintillators optically coupled to Philips XP2020Q photomultiplier tubes having a time resolution (full width at half-maximum, fwhm) of ~200 ps. For the present positron annihilation studies, a 10 μCi ^{22}Na source of positrons (enclosed between ~1.5 μm thin nickel foils) has been sandwiched between two identical samples. A total of 1.5 × 107 coincidence counts has been recorded. Computer program PATFIT-88 has been used along with necessary source corrections to evaluate all the measured positron lifetime spectra. Source component has been evaluated by measuring positron lifetime spectrum of 99.9999% pure Al sample. For the Doppler broadening measurement, a HPGe detector (Efficiency, 12%; Type, PGC 1216sp of DSG, Germany) having energy resolution of 1.15 at 514 keV of ^{85}Sr has been used. To heat the sample, an oven type furnace (30-600 °C with ±2 °C at the sample site) has been attached to the

system. For each temperature, about 2×10^7 counts have been recorded in a dual ADC based multiparameter data acquisition system (MPA-3 of FAST ComTec., Germany). The Doppler broadening spectra have been analyzed by evaluating the S-parameter defined by the ratio of the counts in the central area of the 511 keV photopeak ($|511 \text{ keV} - E\gamma| \leq 0.85$ keV) and the total area of the photo peak ($|511 \text{ keV} - E\gamma| \leq 4.25$ keV).

2A.2.5 Electronic structure and phonon dispersion

This part has been done in collaboration with Prof. Umesh V. Waghmare's group in JNCASR. Density functional theory based first principles calculations of the orthorhombic, hexagonal, and cubic phases of AgCuS were carried out with a general gradient approximation (GGA(PBE))[30] method as implemented in Quantum Espresso package.[31] On-site electron correlations of d-electrons of Ag and Cu atoms, modeled with Hubbard U parameter (5 eV) following earlier work on this material,[26] are tested to give a reasonable band gap of the orthorhombic structure of AgCuS. The plane-wave basis was truncated with energy cutoffs of 40 and 480 Ry in the representation of wave functions and density, respectively, and $6 \times 4 \times 3$ (orthorhombic), $6 \times 6 \times 3$ (hexagonal), and $4 \times 4 \times 4$ (cubic) k-meshes are used to sample Brillouin zone integration. To model partial (in hexagonal phase) and mixed (in cubic phase) occupancy at Cu and Ag sites, we fix the atomic configuration to maintain the symmetry of the crystal in the calculation of electronic structure. To understand the structural stability, we have determined complete phonon dispersion using density-functional perturbation theory (DFPT).[32] To study the orthorhombic to hexagonal phase transition, we have used a 12 atom supercell by considering that the [100] axis of orthorhombic structure transforms to [110] axis of the hexagonal structure. Cell parameter of the simulation box is taken to be the average of the experimental cell parameter of the orthorhombic structure and that of the supercell of the hexagonal structure. We have employed Nudged Elastic Band (NEB) based transformation path simulation with 28 intermediate snapshots.[31] NEB is used to search minimum energy pathway and the transition state configuration at the saddle point for a chemical reaction with known initial and final states. To find the minimum energy path, NEB uses a set of images generated by linear interpolation between the given initial and final states. Each "image" corresponds to the specific geometry of atoms/ ions of the

system along this (guessed) reaction path. NEB minimizes the energy of such string of images to achieve minimum energy path for the reaction.

2A.3 Results and discussion

High quality crystalline ingot of AgCuS (inset of Figure 2A.2(a)) was prepared by the melting reaction of elemental Ag, Cu, and S inside vacuum-sealed quartz tubes. Room temperature powder X-ray diffraction (PXRD) pattern (Figure 2A.2(a)) measured in in-house X-ray diffractometer (Cu Kα; λ = 1.5406 Å) of the as-synthesized samples could be indexed on the room temperature orthorhombic β-AgCuS phase (space group, $Cmc2_1$) with no other impurity phase being observed within the detection limits of powder XRD. In order to understand the structural evolution with temperature, we have performed tem-

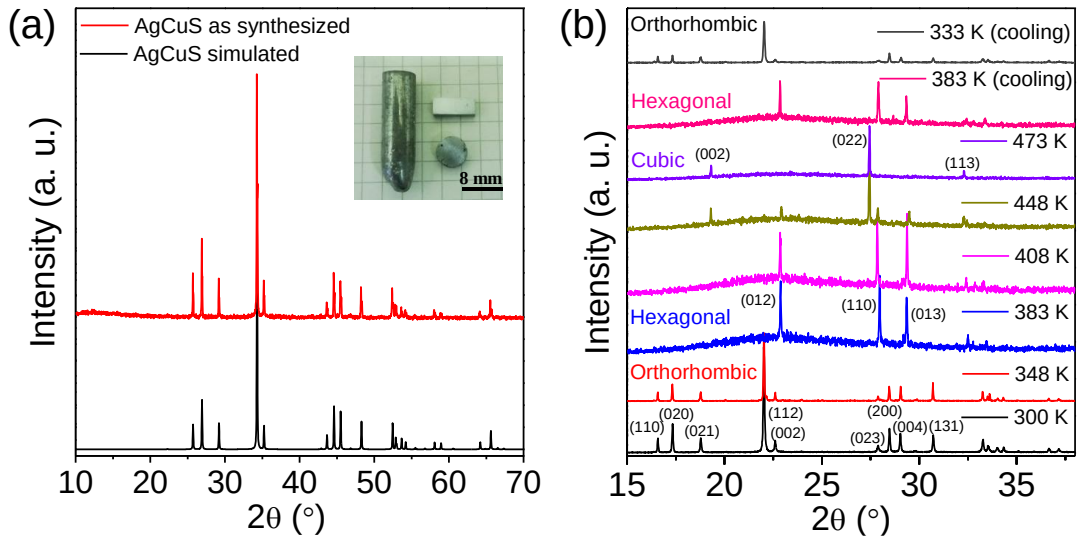

Figure 2A.2 (a) Powder XRD pattern measured at lab source (Cu Kα; λ = 1.5406 Å) of room temperature phase of AgCuS with simulated pattern; inset is showing a photograph of the as-synthesized ingot. Bar- and coin-shaped samples used for transport measurement. (b) Temperature dependent (300-473 K) heating/cooling cycle synchrotron (E = 12.42 keV and λ = 0.998 Å) powder X-ray diffraction patterns of AgCuS.

perature dependent (300-473 K) heating/cooling cycle synchrotron PXRD (E = 12.42 keV and λ = 0.998 Å) of AgCuS and plotted the data in Figure 2A.2(b). Temperature dependent PXRD data clearly shows a structural transition from orthorhombic (β) to hexagonal (α) phase around 365 K.[27] With further increase of the temperature, hexagonal (α) phase transforms to a mixture of hexagonal (α) and cubic phases (δ) and then to pure cubic phase (δ) on further heating to 473 K. The phase transformation is rev-

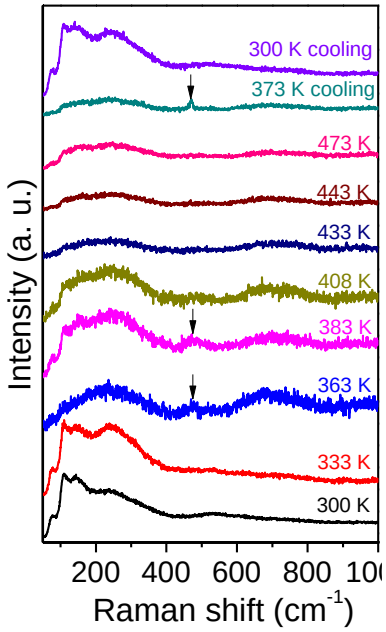

Figure 2A.3 Temperature dependent (300-473) heating/cooling cycle Raman spectra of AgCuS. Black arrow indicates the characteristic Raman peak for Cu-S vibration.

ersible in nature as confirmed by the cooling cycle PXRD data (Figure 2A.2(b)). We have observed a prominent background in the PXRD patterns of high temperature hexagonal and cubic phases, but the similar background was not present in the case of room temperature orthorhombic phase (Figure 2A.2(b)).[27] Hexagonal and cubic phases are the high-temperature superionic phases, in which Ag/Cu atoms are disordered, resulted in glass-like behavior, which will be discussed in the later part of the paper. The glassy behavior of the cation sublattice at high temperature gives rise to a prominent background in PXRD patterns for the hexagonal and cubic phases.

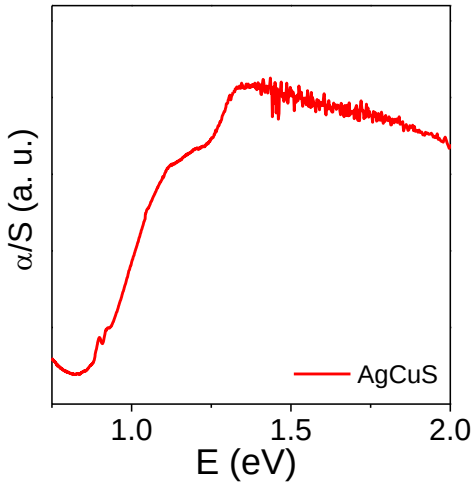

Figure 2A.4 Optical absorption spectra of *β*-AgCuS.

In Figure 2A.3, we show the temperature dependent Raman spectra of AgCuS, which shows a clear variation in Raman spectra during the phase transition temperature, which we will discuss in detail in the later part of this chapter. The spectroscopically measured band gap of the bulk β-AgCuS is ~0.9 eV, which is typical of a narrow band gap semiconductor (Figure 2A.4).

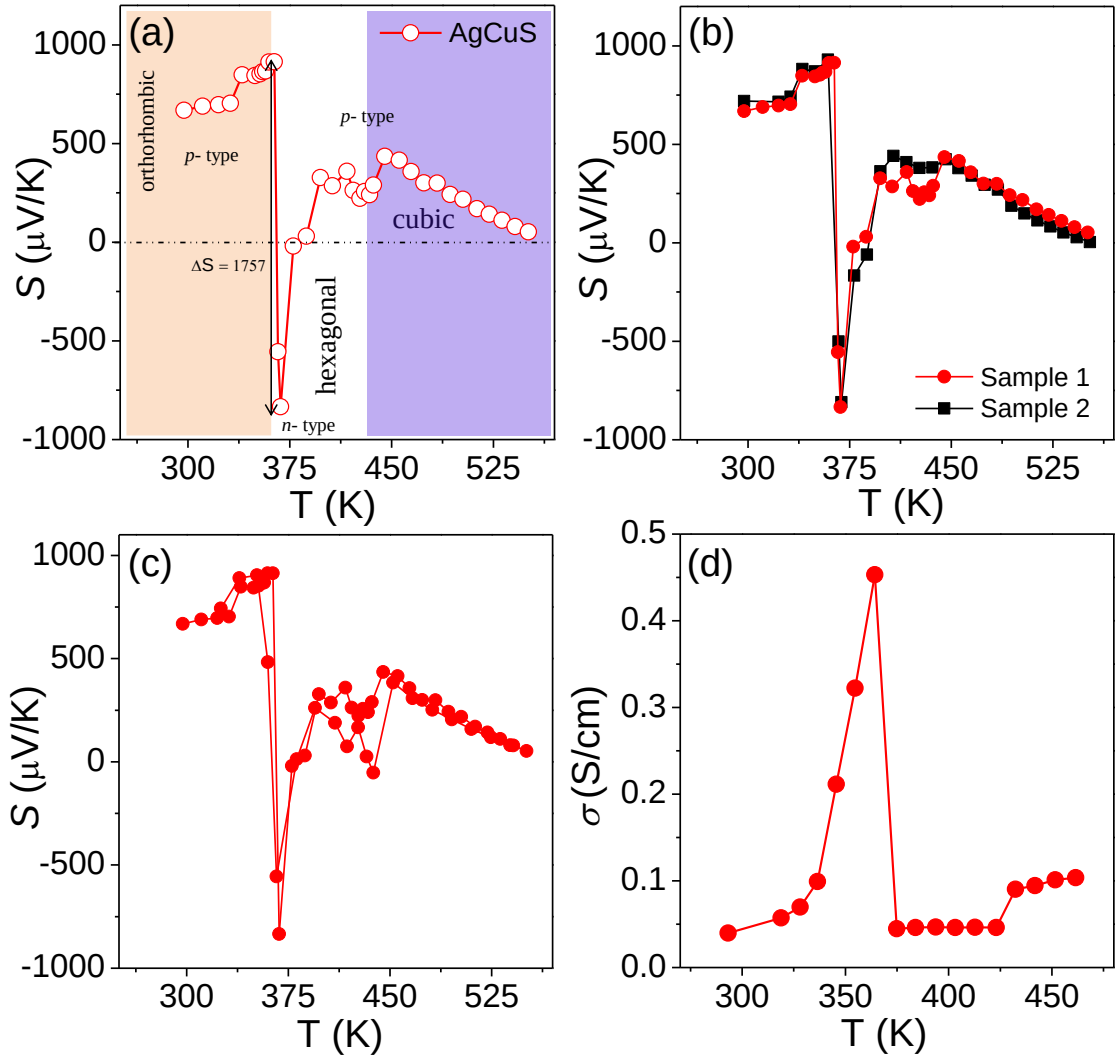

Figure 2A.5 Temperature dependent (a) thermopower of AgCuS, (b) thermopower of different samples of AgCuS. (c) Heating and cooling cycle of the thermopower and (d) Temperature dependent electrical conductivity of AgCuS.

Temperature dependent thermopower (*S*) data of AgCuS has been presented in Figure 2A.5. At room temperature, the sign of thermopower is positive, which indicates *p*-type conduction in the orthorhombic β-AgCuS phase. The *S* value of ~665 μV K^{-1} is measured at room temperature, which increases to ~917 μV K^{-1} at 364 K. A colossal

change in thermopower (ΔS = 1757 μV K^{-1}) along with a switch from *p* to *n*-type conduction is observed during orthorhombic to hexagonal (β-α) superionic phase transition (Figure 2A.5(a)). The thermopower changes from ~917 to about -840 μV K^{-1} at 367 K. Upon further increase in temperature, it reverts to 30 μV K^{-1} and *p*-type conduction at 385 K. The *p*-*n*-*p* conduction switching is reversible and reproducible in AgCuS (Figure 2A.5(b) and (c)). The colossal change in the magnitude of thermopower in AgCuS (ΔS = 1757 μV K^{-1}) is indeed sharper and higher than that of $AgBiSe_2$ (ΔS ~730 μV K^{-1}) and $Ag_{10}Te_4Br_3$ (ΔS ~1400 μV K^{-1}).[15,17] More importantly, this property of AgCuS is more readily usable in a device,[14] as the temperature of its transition (T of ~360) is closer to room temperature compared to that of $AgBiSe_2$ (T of ~560) and $Ag_{10}Te_4Br_3$ (T of ~380 K). We observe a slight dip in temperature dependent *S* during the hexagonal to cubic (α-δ) phase transition at 430 K (Figure 2A.5(a)). Temperature dependent electrical conductivity (σ) shows a sharp increase during the (β-α) transition (~364 K), while the increase in σ during the (α-δ) transition (~430 K) is not very significant (Figure 2A.5(d)). Anomalous behavior of temperature dependent σ during (β-α) transition can be understood by further theoretical calculation of electronic band structure along the transition path, which we will discuss in the later part of the chapter.

Figure 2A.6(a) represents the temperature-dependent specific heat (C_p) of AgCuS measured by DSC, which shows two phase transitions above the room temperature. A λ-shaped peak is observed at 380 K, which corresponds to the orthorhombic to hexagonal phase (β-α) transition. Such a λ- transition denotes an order-disorder transition, associated with partial disordering of Ag/Cu in the rigid sulfur sublattice during the first superionic phase transition. A broad peak centered at ~430 K corresponds to the hexagonal to cubic (α-δ) phase transition. An additional peak with a maximum at ~408 K is associated with the low-temperature boundary of the two-phase hexagonal-cubic region,[27] which is consistent with the temperature dependent PXRD results. In the β-α phase transition, C_p was dramatically high (λ-transition), while at the α-δ phase transition, C_p shows a broad peak with a low value. Peak centered at ~430 K (α-δ transition) is broad due to the fact that initially hexagonal (α) phase transforms to a mixture of hexagonal (α) and cubic phases (δ), and then to a pure cubic phase (δ) on increasing the temperature above ~430 K. In the high temperature hexagonal (α) phase, sulfur atoms form the *hcp* sublattice, wh-

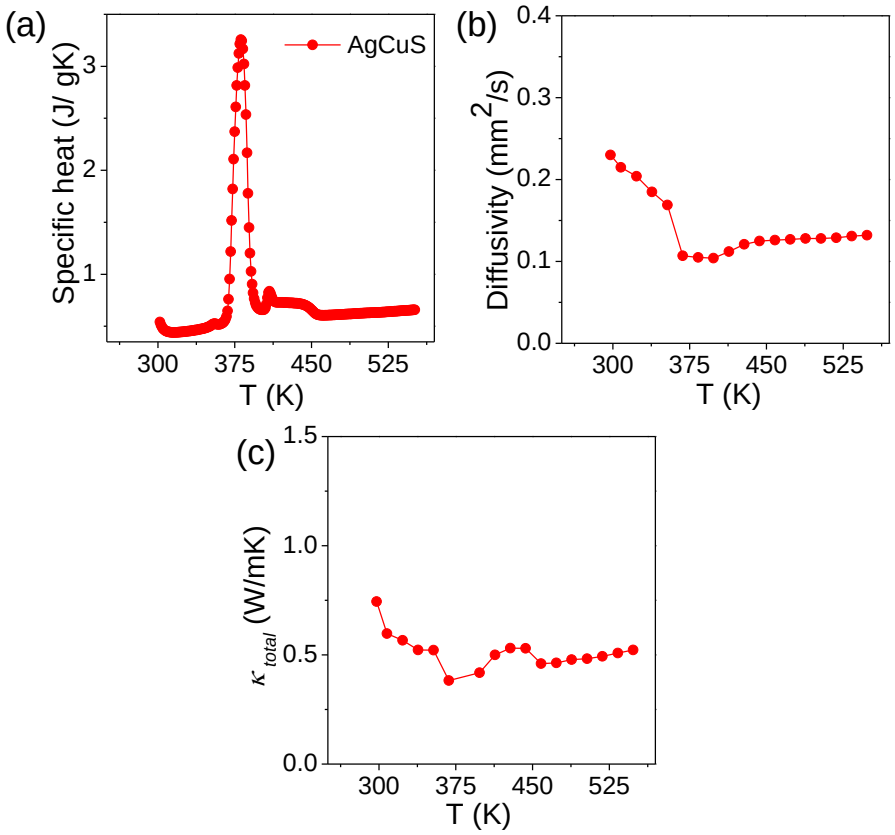

Figure 2A.6 Temperature dependent (a) specific heat, (b) thermal diffusivity, and (c) total thermal conductivity of AgCuS.

ile the Ag atoms are fully disordered and Cu atoms are in the partially disordered state (Figure 2A.1). The second high temperature cubic (δ) phase is constituted of a rigid *fcc* lattice of sulfur atoms, in which Ag and Cu atoms are completely disordered and distributed at tetrahedral and octahedral interstitial sites (Figure 2A.1). During first superionic transition (β-α), the Ag atom gets fully disordered, while 75% Cu atoms reside in ordered position (Figure 2A.1),[27] resulting in a dramatic change in the temperature dependent C_p due to onset of order- disorder transition. At the second superionic transition (α-δ), Cu atoms gets fully disordered along with the Ag atoms which are already in disordered state in the hexagonal phase (α) and the transition occurs from a partially disordered (existing disordered) state (α) to fully disordered state (δ), giving rise to less dramatic change in C_p compared to the (β-α) transition. The (β-α) transition occurs from an ordered state to a partially disordered state with a drastic volume change of 2.3%, while the (α-δ) transition occurs from a partially disordered state to fully disordered state with a volume change of 0.6%.[27] The above discussion suffices as an

explanation as to why the anomalies in the different measurements (thermopower and C_p) are generally dramatic and sharp during the (β-α) transition compared to those of (α-δ) transition.

In addition to the spectacular change in thermopower with a conduction switching, AgCuS exhibits low thermal diffusivity and thermal conductivity in 300-550 K temperature range, which is important to maintaining temperature gradients in devices. Temperature dependent total thermal conductivity, κ_{total}, displayed in Figure 2A.6(c), was estimated using the formula $\kappa_{total} = DC_p\rho$, where D is the thermal diffusivity (Figure 2A.6(b)), C_p is the specific heat, and ρ is the density of the sample. The density of the pellets was ~98% of the theoretical density. We have observed a sharp decrease in the temperature dependent diffusivity at orthorhombic (β) to hexagonal (α) phase transition around 368 K, while during hexagonal (α) to cubic (δ) transition, no significant anomaly has been observed (see Figure 2A.6(b)). At room temperature, the measured value of κ_{total} is ~0.7 W m^{-1} K^{-1}. With an increase in temperature, a pronounced peak in κ_{total} (~1.98 $Wm^{-1}K^{-1}$) is observed at ~384 K, which is due to the abrupt change in the C_p during the β-α phase transition and κ_{total} of ~0.50 W m^{-1} K^{-1} is measured just after the transition. We observe a decrease in the thermal conductivity from ~0.53 W m^{-1} K^{-1} to ~0.45 W m^{-1} K^{-1} during (α-δ) phase transition, which then increases to a value of ~0.52 W m^{-1} K^{-1} at 550 K. As electrical conductivity of the undoped pristine AgCuS is quite low (Figure 2A.5(d)), the lattice thermal conductivity ($\kappa_{lat} = \kappa_{total} - L\sigma T$, where σ is electrical conductivity and L is the Lorentz number) is essentially the same as κ_{total} in AgCuS. Low thermal conductivity over a broad temperature range is achieved in AgCuS, which is possibly due to effective scattering of phonons by the loosely bound and mobile Cu and Ag ions in the rigid sulfur sublattice.

Temperature dependent Raman spectroscopy is a well-known technique to understand the structural change during phase transition. Room temperature Raman spectrum of orthorhombic (β) AgCuS shows a broad peak around 240 cm^{-1}, which is assigned to Ag-S bond vibration (Figure 2A.3).[33,34] Other low energy peaks below 150 cm^{-1} are due to the lattice vibration of Ag/Cu,[35] which is later indicated by detailed phonon dispersion calculations. With increasing the temperature to the (β-α) transition temperature (363 K), peaks associated with Ag lattice vibration completely disappear as

the Ag atoms begin to disorder in the hexagonal (α) phase. At (β-α) transition temperature (363 K), interestingly a peak appears at 474 cm^{-1}, which is assigned to Cu-S bond vibration.[34] This result indicates that at the *p-n-p* type conduction switching temperature (363 K), Cu-S bonds remain intact, whereas Ag atoms become disordered. We will show later through electronic band structure calculation that hybridized Cu-S orbital contributes to the semimetallic intermediate state during (β-α) phase transition, which is responsible for *p-n-p* type conduction switching in AgCuS. In the hexagonal phase (α), 75% of Cu atoms are ordered, which form the Cu-S bond, whereas the remaining (25%) Cu atoms are in the disordered state along with Ag. With further increasing the temperature to 383 K (just above the phase transition), a broad Raman band centered at 240 cm^{-1} reappears which was present in the room temperature orthorhombic (β), indicating the reappearance of weak Ag-S interaction. When AgCuS completely transforms into cubic (δ) phase, Ag/Cu are in the fully disordered state, so the macroscopic polarizability disappears, and no Raman peaks are observed. A similar observation has been reported for $AgBiSe_2$ nanocrystals.[15] In the present case, the phase transition is reversible, which is confirmed by taking the Raman spectra on cooling cycle (see Figure 2A.3).

To understand the origin of the conduction type in orthorhombic β-AgCuS at room temperature, we have performed positron annihilation spectroscopy of AgCuS. The lifetime of the positron determines the type and relative concentration of defects/vacancies.[15,36] Fitting of positron annihilation spectrum (see Figure 2A.7(a)) at room temperature yields three lifetime values, 154 ± 2 ps with (24 ± 1)% intensity, 272 ± 1 ps with (70 ± 1)% intensity and a very long component of 1568 ± 200 ps with (6 ± 0.2)% intensity. The shortest lifetime component is the free annihilation of positron, while the intermediate component is due to positron annihilation at the defect site which is here the Ag vacancy.[15,37] The long lifetime component originates from the formation of positronium at the sample surface or at the large voids inside the sample.[37] Moreover, density functional theoretical calculation also confirms that the formation energy of Ag vacancy is lowest among the other possible defects in AgCuS sample (Table 2A.1). These results clearly indicate that the Ag vacancy is indeed responsible for *p*-type

conduction in β- AgCuS at room temperature and Ag vacancy can possibly act as an effective path for the movement of Ag atoms in the high-temperature superionic phases.

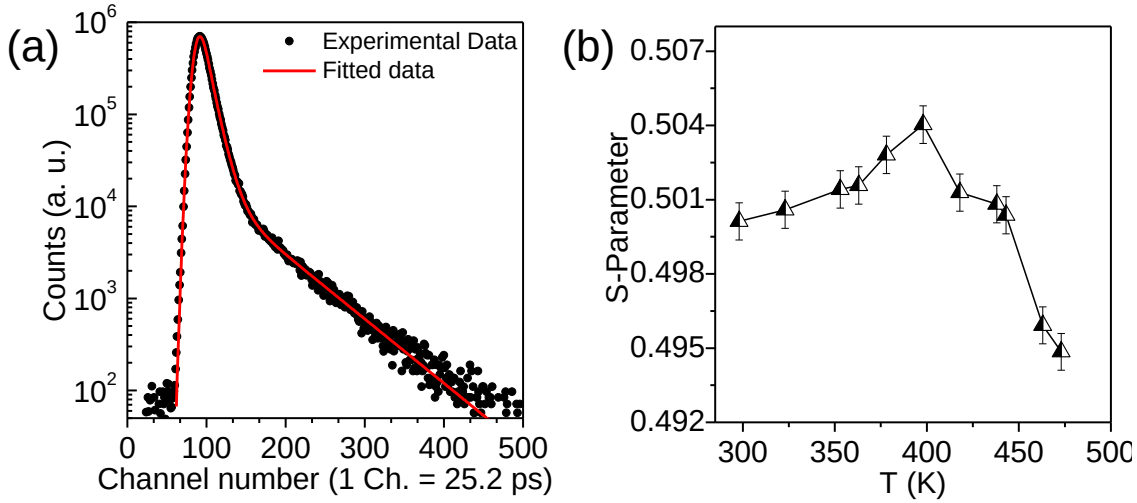

Figure 2A.7 (a) The positron annihilation lifetime spectrum for the AgCuS sample at room temperature. Solid red line shows the fitting for the determination of positron lifetime components. (b) Temperature dependent Doppler broadening S-parameter of AgCuS.

Table 2A.1 Formation Energy (E_f^v, eV/fu) of defect in β-AgCuS.

V_{Ag} (eV/fu)	V_{Cu} (eV/fu)	V_S (eV/fu)
0.585	0.876	1.322

Temperature dependent Doppler broadening of the annihilation radiation reflects the momentum distribution of annihilating electrons, which has provided further evidence of *p*-*n*-*p* type conduction switching in AgCuS during the (β-α) transition. The Doppler broadening spectra have been analyzed by evaluating the shape (S) parameter defined by the ratio of the counts in the central area of the annihilation photopeak and the total area of the photopeak. Figure 2A.7(b) represents the temperature dependent Doppler broadening S-parameter for AgCuS. The S-parameter represents the ratio between the positrons annihilation with lower momentum electrons with the higher momentum electrons. During orthorhombic (β) to hexagonal (α) phase transformation, the onset of S-parameter starts at ~360 K and it reaches a maximum at ~385 K, indicating most abundant valence electrons (majority carrier for *n*-type conduction), which is also consistent with the electronic band structure calculations discussed in later section. After passing the maximum at 385K, S-parameter decreases, indicating the conduction type changes back to *p*-type. S-parameter falls sharply after passing the (α-δ) phase transition

temperature (~440 K). Similar type behavior in temperature dependent S-parameter has been observed in the $AgBiSe_2$ nanocrystals.[15]

To further understand the origin of the significant change in the thermopower with *p-n-p* type conduction switching and low thermal conductivity, we determine electronic and phonon spectra of AgCuS from first-principles. Phonon dispersion of the orthorhombic *β*-AgCuS phase exhibits a gap that separates high energy modes originating from sulfur sublattice and low energy modes largely involving the Ag/Cu sublattices (Figure 2A.8). This stems from the large mass contrast between the cations and anion in AgCuS. A large number of phonon modes have frequencies below 50 cm^{-1}, which are expected to be strongly influenced by anharmonicity and be sensitive to variation in temperature or the other fields. Three of the calculated phonon modes (at M_1, S, and M_3 point) of *β*-AgCuS have weak imaginary frequencies in the acoustic branch. M_1 mode involves a shear type deformation in the xy direction indicating a cell distortion occurring at low temperature. The instability (S) is related to Ag atoms, which indicates restricted shear or "flow" in the y-direction. The third instability (M_3) is a transverse acoustic mode with displacements along y-direction. These instabilities are rather weak and do not quite lower the energy of the structure (as has been verified through explicit simulations of the energetics of distortions given by these modes), but suggest a shallow/flat energy landscape.

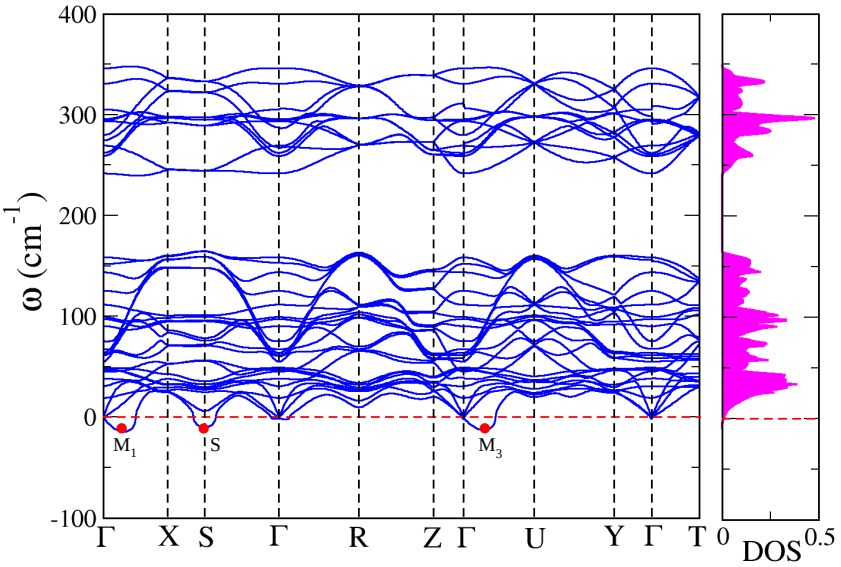

Figure 2A.8 Phonon dispersion plot and phonon density of state of orthorhombic *β*-AgCuS.

The presence of a large number of low energy phonon modes and those related to shear deformation indicate that AgCuS is a soft material, and should possess low thermal conductivity (which depends on the square of the group velocity of these modes). At higher temperatures, dynamics and renormalization of these cationic low energy phonon modes are relevant ("restricted shear") to the phase transformation and structural disorder observed experimentally. These low-frequency shear modes will soften further at higher temperature and lead to flow of cations or liquid-like behavior. While sulfur atoms form a rigid high symmetry hexagonal lattice with void spaces, Ag/Cu atoms are relatively free to move by hopping between the vacant sites within the sulfur sublattice. A similar phenomenon has been studied in superionic Cu_2Se and Cu_2S with rigid anion and liquid like cation lattices.[6,12,38] Such liquid-like behavior of the sublattice of heavy cations leads to effective phonon scattering, thereby reducing thermal conductivity in AgCuS.

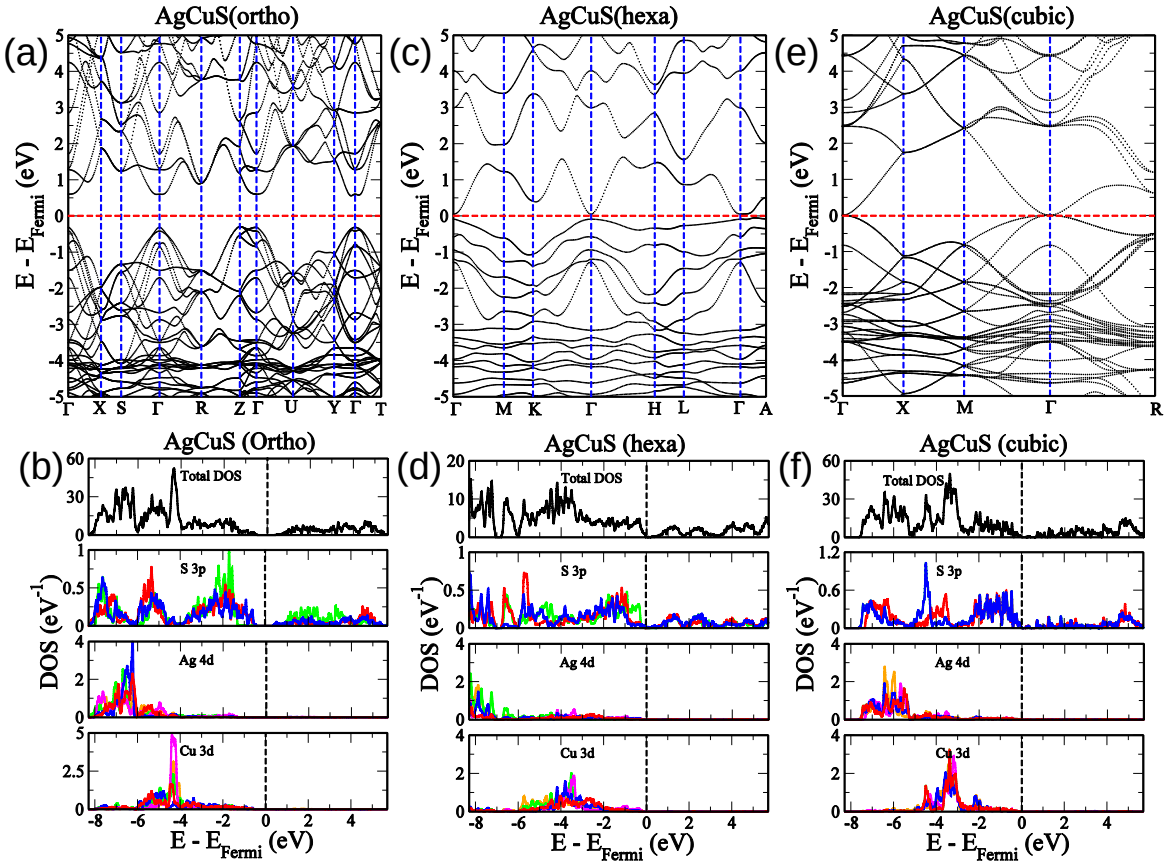

Figure 2A.9 Electronic band structure and density of state (total and atom projected) of (a and b) orthorhombic, (c and d) hexagonal, and (e and f) cubic phase of AgCuS. (Color code) S 3*p* orbitals: red line is p_x, blue line is p_y and, green line is p_z. Ag 4*d* and Cu 3*d* orbitals: red line is d_{xy}, magenta line is d_{yz}, green line is d_{zx}, orange line is d_{z^2} and blue line is $d_{x^2-y^2}$.

In Figure 2A.9, we show the electronic structure and partial density of states (PDOS) of the observed phases of AgCuS. The theoretically estimated band gap of the orthorhombic *β*-AgCuS phase is ~0.92 eV (Figure 2A.9(a)), which is close to the observed value. The degeneracy between valence band maxima at Z and Γ points in *β*-AgCuS allows coexistence of holes in two distinct valleys (pockets) leading to a high *p*-type thermopower. Analysis of the PDOS shows that the electronic states in the 2 eV window of valence band maximum are constituted solely of sulfur *p* orbitals (Figure 2A.9(b)). Interestingly, in this energy window, p_x and p_y orbitals of sulfur create the frontier states, whereas p_z orbitals are slightly lower in energy (~1 eV lower than E_F), as clearly evident in Figure 2A.9(b). A strong covalency within the planar framework of sulfur and copper ions is essentially responsible for the electronic conduction. Orbitals of Ag atoms are positioned much deeper in energy and are unlikely to contribute to the electronic conduction.

Electronic structure of the hexagonal phase shows a narrow band gap of ~0.14 eV (Figure 2A.9(c)), with a strong electron-hole asymmetry responsible for its high thermopower. Hole carriers have much higher effective mass (m_h*) than that of electron carriers (m_e*) (Figure 2A.9(c)). The structure of sulfur sublattice involves a chain-like formation along the *z*-direction, and its signature is evident in the PDOS (Figure 2A.9(d)), where p_z orbitals of sulfur constitute the valence states within 1 eV below E_F. The states at the valence band maximum at (0,0,0.6) are responsible for electrical conduction by holes along the chains of sulfur atoms. Quantum confinement of holes in the hexagonal sulfur sublattice along one dimension (*z*) leads to a high effective mass of valence band (flat band) and a large Seebeck coefficient.

The switching associated with *p-n-p* type conduction during the orthorhombic to hexagonal phase (*β*-*α*) transition can be understood from the electronic structure of AgCuS along the transition path, which we determine using a nudged elastic band technique.[31] The energy barrier of this transformation is 0.6 eV. Evolution of partial density of states along the transition path shows the existence of semimetallic intermediate states (i10, i12, i14, and i18) near the energy barrier or the transition state of the phase transformation (Figure 2A.10(a)). Due to atomic movement involved in disordering of the cationic sublattices, there are changes in bonding reflected in mixing

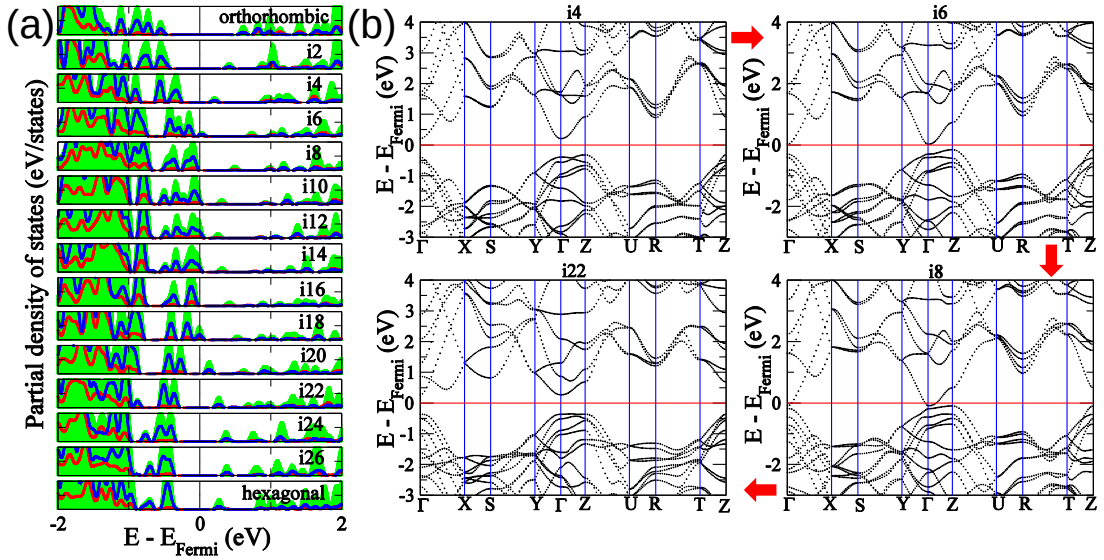

Figure 2A.10 (a) Partial density of states of AgCuS along the minimum energy path of orthorhombic to hexagonal phase transformation as predicted by NEB calculation. Green, red, and blue colors in (a) represent the partial density of states of S 3p, Ag 4d, and Cu 3d, respectively. (b) Electronic band structures of intermediate (i) states during orthorhombic to hexagonal phase transformation.

between the states in valence and conduction bands. This results in downward and upward shifts in the conduction and valence bands, respectively (see Figure 2A.10(a)), and in overlapping valence and conduction bands in a small energy interval near the gap, and hence the semimetallic state. Electronic structure of the intermediate states (Figure 2A.10(b)) clearly shows that the Fermi level first initially moves into the conduction band (i6 and i8, Figure 10b), and a gap opens up again with a shift (i22, Figure 10b) of the conduction band to higher energy, as the transition proceeds from orthorhombic to hexagonal phase. The *n*-type carriers of the intermediate semimetallic state are responsible for the *p*-*n*-*p* type conduction switching during the (β-α) transition. Unlike the orthorhombic or hexagonal phases where the states near Fermi energy are dominated by sulfur orbitals, the contribution from hybridized Cu-S orbitals to the overlapping valence and conduction band gives rise to the semimetallic character (and *n*-type conduction) of the intermediate structure. While the existence of a semimetallic intermediate state was suggested to be responsible for the *p*-*n*-*p* conduction switching reported earlier in $AgBiSe_2$ nanocrystals[15] and $Ag_{10}Te_4Br_3$,[17] our work establishes this unambiguously in AgCuS. The existence of semimetallic states during the (β-α) transition resulted in sharp increase in the temperature dependent electrical conductivity at 364 K (Figure 2A.5(d)). Finally, our calculated electronic structure of the cubic δ-AgCuS (Figure 2A.9(e)) clearly

shows a vanishing band gap. The disorder in cation sublattices and anharmonicity of the associated soft modes lead to strong phonon scattering, and hence an ultralow thermal conductivity of the cubic phase.

2A.4 Conclusions

In conclusion, temperature driven *p-n-p* conduction switching with a colossal change in thermopower has been observed in a single compound, AgCuS, which is free of expensive and less abundant Se/Te. Temperature dependent synchrotron powder X-ray diffraction, heat capacity, positron annihilation spectroscopy and Raman spectroscopy of AgCuS clearly explain the phase transition behavior and provide fundamental insight into the *p-n-p* type conduction switching. Ag vacancy is responsible for *p*-type conduction in β-AgCuS at room temperature and acts as an effective path for the movement of Ag atoms during (β-α) phase transition, whereas Cu-S bonds remain intact. An intermediate semimetallic state, constituting of hybridized Cu-S orbitals, arises from reshuffling of electronic orbitals contributing to valence and conduction bands during the orthorhombic to hexagonal phase transition, which is responsible for the *p-n-p* conduction switching in AgCuS. Temperature dependent Doppler broadening of positron annihilation indicates that semimetallic intermediate state contributes more conduction electron during the (β-α) transition, which essentially leads to *p-n-p* type conduction switching. Electronic density of states and phonon dispersion reveal that the rigid sulfur sublattice is primarily responsible for the electronic charge transport, whereas soft vibrations and mobility of Ag/Cu ions are responsible for the ultralow thermal conductivity. Such decoupling of electronic and phonon transport leads to a unique combination of temperature dependent *p-n-p* conduction switching and ultralow thermal conductivity in AgCuS near room temperature, opening up a new class of temperature controlled diode or transistor devices based on a single compound.

References

[1] C. N. R. Rao, J. Gopalakrishnan, *New Directions in Solid State Chemistry*, Cambridge University Press, **1997**.

[2] C. N. R. Rao, *Acc. Chem. Res.* **1984**, *17*, 83–89.

[3] A. West, *Solid State Chemistry and Its Applications, 2nd Edition, Student Edition*, **2014**.

[4] E. Coronado, C. Martí-Gastaldo, E. Navarro-Moratalla, A. Ribera, S. J. Blundell, P. J. Baker, *Nat. Chem.* **2010**, *2*, 1031–1036.

[5] D. A. Keen, *J. Phys. Condens. Matter* **2002**, *14*, R819–R857.

[6] H. Liu, X. Shi, F. Xu, L. Zhang, W. Zhang, L. Chen, Q. Li, C. Uher, T. Day, G. J. Snyder, *Nat. Mater.* **2012**, *11*, 422–425.

[7] S.-I. Ohkoshi, Y. Tsunobuchi, T. Matsuda, K. Hashimoto, A. Namai, F. Hakoe, H. Tokoro, *Nat. Chem.* **2010**, *2*, 539–545.

[8] Q. Zhang, Y. Liu, X. Bu, T. Wu, P. Feng, *Angew. Chemie - Int. Ed.* **2008**, *47*, 113–116.

[9] J. Liu, T. Gottschall, K. P. Skokov, J. D. Moore, O. Gutfleisch, *Nat. Mater.* **2012**, *11*, 620–6.

[10] S. N. Guin, V. Srihari, K. Biswas, *J. Mater. Chem. A* **2015**, *3*, 648–655.

[11] L.-D. Zhao, S.-H. Lo, Y. Zhang, H. Sun, G. Tan, C. Uher, C. Wolverton, V. P. Dravid, M. G. Kanatzidis, *Nature* **2014**, *508*, 373–7.

[12] Y. He, T. Day, T. Zhang, H. Liu, X. Shi, L. Chen, G. J. Snyder, *Adv. Mater.* **2014**, *26*, 3974–3978.

[13] S. Lange, T. Nilges, *Chem. Mater.* **2006**, *18*, 2538–2544.

[14] J. Janek, *Nat. Mater.* **2009**, *8*, 88–89.

[15] C. Xiao, X. Qin, J. Zhang, R. An, J. Xu, K. Li, B. Cao, J. Yang, B. Ye, Y. Xie, *J. Am. Chem. Soc.* **2012**, *134*, 18460–18466.

[16] K. Terabe, T. Hasegawa, T. Nakayama, M. Aono, *Nature* **2005**, *433*, 47–50.

[17] T. Nilges, S. Lange, M. Bawohl, J. M. Deckwart, M. Janssen, H.-D. Wiemhöfer, R. Decourt, B. Chevalier, J. Vannahme, H. Eckert, et al., *Nat. Mater.* **2009**, *8*, 101–108.

[18] R. Waser, M. Aono, *Nat. Mater.* **2007**, *6*, 833–40.

[19] K. Biswas, J. He, I. D. Blum, C.-I. Wu, T. P. Hogan, D. N. Seidman, V. P. Dravid, M. G. Kanatzidis, *Nature* **2012**, *489*, 414–8.

[20] S. N. Guin, A. Chatterjee, D. S. Negi, R. Datta, K. Biswas, *Energy Environ. Sci.* **2013**, *6*, 2603–2608.

[21] T. a Miller, J. S. Wittenberg, H. Wen, S. Connor, Y. Cui, a M. Lindenberg, *Nat. Commun.* **2013**, *4*, 1369.

[22] O. Osters, M. Bawohl, J. L. Bobet, B. Chevalier, R. Decourt, T. Nilges, *Solid State Sci.* **2011**, *13*, 944–947.

[23] T. Nilges, S. Nilges, A. Pfitzner, T. Doert, P. Bo, **2004**, 806–812.

[24] S. Ishiwata, Y. Shiomi, J. S. Lee, M. S. Bahramy, T. Suzuki, M. Uchida, R. Arita, Y. Taguchi, Y. Tokura, *Nat. Mater.* **2013**, *12*, 512–7.

[25] J. Maier, *Nat. Mater.* **2005**, *4*, 805–815.

[26] D. Santamaria-Perez, A. Morales-Garcia, D. Martinez-Garcia, B. Garcia-Domene, C. Mühle, M. Jansen, *Inorg. Chem.* **2013**, *52*, 355–361.

[27] D. M. Trots, A. Senyshyn, D. A. Mikhailova, M. Knapp, C. Baehtz, M. Hoelzel, H. Fuess, *J. Phys. Condens. Matter* **2007**, *19*, 136204.

[28] S. Djurle, *Acta Chem. Scand.* **1958**, *12*, 1427–1436.

[29] B. J. Skinner, *Econ. Geol.* **1966**, *61*, 1–26.

[30] J. P. Perdew, K. Burke, M. Ernzerhof, *Phys. Rev. Lett.* **1996**, *77*, 3865–3868.

[31] P. Giannozzi, S. Baroni, N. Bonini, M. Calandra, R. Car, C. Cavazzoni, D. Ceresoli, G. L. Chiarotti, M. Cococcioni, I. Dabo, et al., *J. Phys. Condens. Matter* **2009**, *21*, 395502.

[32] S. Baroni, S. De Gironcoli, A. Dal Corso, P. Giannozzi, *Rev. Mod. Phys.* **2001**, *73*, 515–562.

[33] A. Milekhin, L. Sveshnikova, T. Duda, N. Surovtsev, S. Adichtchev, D. R. T. Zahn, *Chinese J. Phys.* **2011**, *49*, 63–70.

[34] B. Minceva-Sukarova, M. Najdoski, I. Grozdanov, C. J. Chunnilall, *J. Mol. Struct.* **1997**, *410–411*, 267–270.

[35] M. Ishii, H. Wada, *Mater. Res. Bull.* **1993**, *28*, 1269–1276.

[36] A. Sarkar, M. Chakrabarti, S. K. Ray, D. Bhowmick, D. Sanyal, *J. Phys. Condens. Matter* **2011**, *23*, 155801.

[37] R. Krause-Rehberg, H. S. Leipner, *Positron Annihilation in Semiconductors*, **1999**.

[38] L. W. Wang, *Phys. Rev. Lett.* **2012**, *108*, 85703.

CHAPTER 2B

Tailoring of *p-n-p* type conduction switching and thermoelectric properties of AgCuS by size reduction to nanoscale

Summary. *This chapter presents a facile, ambient and capping agent-free solution based synthesis of AgCuS nanocrystals and their temperature-dependent (300-550 K) thermoelectric properties. AgCuS is known to show fascinating p-n-p type conduction switching in its bulk polycrystalline form. Temperature dependent synchrotron powder X-ray diffraction, heat capacity and Raman spectroscopy measurements indicate the observation of two superionic phase transitions, from a room temperature ordered orthorhombic (β) to a partially disordered hexagonal (α) phase at 365 K and from the hexagonal (α) to a fully disordered cubic (δ) phase at 439 K, in nanocrystalline AgCuS. The size reduction to the nanoscale resulted in a large variation in the thermoelectric properties compared to its bulk counterpart. Temperature dependent Seebeck coefficient measurements indicate that the nanocrystalline AgCuS does not display the p-n-p type conduction switching property like its bulk form, but remains p-type throughout the measured temperature range due to the presence of excess localized Ag vacancies. Also, nanocrystalline AgCuS exhibits a wider electronic band gap (1.2 eV) compared to that of the bulk AgCuS (0.9 eV), which is not sufficient to close the band gap to form a semimetallic intermediate state during the orthorhombic to hexagonal superionic phase transition. The present study demonstrates that ambient solution phase synthesis and size reduction to the nanoscale can tailor the order-disorder phase transition, the band gap, and the electronic conduction properties in superionic compounds, which will not only enrich solid-state inorganic chemistry but also open a new avenue to design multifunctional materials.*

2B.1 Introduction

The temperature-driven *p-n-p* type conduction switching and thermoelectric properties of the noble metal based chalcogenides are highly sensitive to the order-disorder phase transition, evolution of the electronic structures during the phase transition and the carrier type of the material.[1,2] Substitution of foreign cations or anions can modulate the electronic structure and carrier transport in a material, which may tune the phase transition temperature. Thus, anion substituted $Ag_{10}Te_4Br_{2.8}I_{0.2}$ shows a shift of the *p-n-p* conduction switching temperature towards room temperature, but the change in the Seebeck coefficient was smaller than that of pristine $Ag_{10}Te_4Br_3$.[3] $AgBiSe_2$ shows *p-n-p* type conduction switching in its nanocrystalline form,[4] but its bulk counterpart does not exhibit such conduction type switching.[5,6] Thus, the particle or grain size has an important role in the conduction switching property, as the electronic band gap of a material is highly sensitive to the crystallite size. Hence, it would be interesting to study the effect of the dimensionality of the material on the conduction switching property and the phase transition temperature[7] of inorganic materials.

In Chapter 2A we have shown that bulk polycrystalline AgCuS exhibits a reversible *p-n-p* type conduction switching along with a colossal change in its Seebeck value (ΔS of ~1757 μV K^{-1}) at T ~364 K during the first superionic (β-α) phase transition.[8] It should be noted that previous research has been solely focused on the bulk AgCuS synthesized by solid state reaction at high temperature,[2,8] but there is no report on the investigation of the thermoelectric properties and order-disorder phase transition of AgCuS in its nanocrystalline form.

Herein, we present a facile and room temperature solution based synthesis for capping free AgCuS nanocrystals and investigate their temperature dependent (300-550 K) structural phase transition and thermoelectric properties. The synthesis process is very simple and effective with a high yield (90%). Temperature dependent synchrotron powder X-ray diffraction, Raman spectroscopy and heat capacity measurement indicates the observation of two superionic phase transitions, from a room temperature ordered orthorhombic (β) to a partially disordered hexagonal (α) at 365 K and from the hexagonal phase (α) to a fully disordered cubic phase (δ) at 439 K, in nanocrystalline

AgCuS. A sharp decrease of the Seebeck coefficient value from 783 μV K^{-1} at 360 K to 418 μV K^{-1} at 367 K is observed during the orthorhombic to hexagonal (β-α) phase transition in AgCuS nanocrystals obtained after 30 min reaction. We found that, unlike its bulk counterpart, nanocrystalline AgCuS does not exhibit *p-n-p* type conduction switching during the first superionic phase transition. Nanocrystalline AgCuS exhibits a higher electronic band gap (1.2 eV) compared to that of its bulk counterpart (0.9 eV) and the Raman spectroscopy shows the absence of Cu-S bond vibration during the (β- α) transition, which collectively disfavor the creation of a semimetallic intermediate electronic state during the orthorhombic (β) to hexagonal (α) phase transition, which was responsible for the *p-n-p* type conduction switching in bulk AgCuS.[8] Furthermore, temperature dependent positron annihilation spectroscopy indicates that the Ag vacancy is responsible for the *p*-type conduction and the localized nature of Ag vacancies in AgCuS nanocrystals disfavors the macroscopic movement of Ag/Cu during the order-disorder phase transition, which was responsible for the *p-n-p* type conduction switching in bulk AgCuS.[8]

2B.2 Methods

2B.2.1 Synthesis

Materials Copper (II) nitrate trihydrate (Alfa Aesar, 99%), silver(I) nitrate (Sigma-Aldrich, 99%), sulfur powder (Alfa Aesar, 99.999%) and sodium borohydride (Aldrich, 98%), and tetraethylene glycol (Sigma-Aldrich, 99%) were used for synthesis without further purification.

Capping agent free AgCuS nanocrystals were synthesized using a bottom-up wet chemical method. At first, silver nitrate (100 mg, 0.59 mmol), copper nitrate (142.2 mg, 0.59 mmol), sulfur powder (18.9 mg, 0.59 mmol) and tetraethylene glycol (15 ml) were placed in a round bottom flask, then the reaction mixture was sonicated for 15 minutes to get a well-dispersed solution. $NaBH_4$ (66.8 mg, 1.76 mmol) was added to the reaction mixture with stirring at room temperature (300 K) under N_2 atm. By variation of the reaction time, we were able to synthesize nanocrystals of different sizes. Nanocrystals of 40 nm and 120 nm were synthesized with a reaction time of 30 min and 12 hours

respectively. After the reaction, the black colored product was isolated by centrifugation. The AgCuS nanocrystal powder was washed several times with ethanol to remove surface adsorbed tetraethylene glycol and was finally dried under a vacuum at 60 C for 2 h. The yield of the reaction is 90%.

2B.2.2 Characterizations

Room temperature powder X-ray diffraction of the sample was recorded using a Cu Kα (λ = 1.5406 Å) radiation on a Bruker D8 diffractometer. Temperature-dependent X-ray diffraction measurements under N_2 flow were carried out with X-ray beam of λ = 1.0279 Å, at BL-18B (Indian beamline), Photon Factory, KEK, Tsukuba, Japan. DSC and TGA data were measured by Netzsch DSC 200F3 and TGA/DSC 2 STAR instrument respectively. FESEM imaging has been performed using a NOVA NANO SEM 600 (FEI, Germany). TEM experiment has been done using a JEOL (JEM3010) and also using a FEI TECNAI G^2 T20 instrument. EDX elemental mapping was performed during STEM imaging. ICP-AES measurements were carried out using a Perkin-Elmer Optima 7000DV instrument. To probe optical energy gap optical diffuse reflectance measurement was performed on finely ground powder using a Perkin Elmer Lambda 900, UV/vis/NIR spectrometer. A Bruker IFS 66v/S spectrometer was used for recording the FTIR spectra. XPS measurements were performed with a Mg- Kα (1253.6 eV) X-ray source on an Omicron nanotechnology instrument. Temperature dependent Raman spectroscopy measurements were carried out with a LABRAM HR spectrometer. Room temperature carrier concentration has been derived from the Hall coefficient measurement using a PPMS. Elaborative discussions on all the characterizations techniques have been given in the introduction part of the thesis (page 31).

2B.2.3 Positron annihilation spectroscopy

Positron annihilation lifetime has been measured with a fast- fast coincidence assembly consisting of two constant fraction differential discriminators (Fast ComTech Model number 7029A). The detectors are 25 mm-long 25 mm tapered to 13 mm diameter cylindrical BaF2 scintillators optically coupled to Philips XP2020Q photomultiplier tubes. The resolving time (full width at half maximum, FWHM), of the present fast–fast coincidence assembly is 220 ps. For the present positron annihilation measurement, a 10 μCi ^{22}Na source of positrons (enclosed between 1.5 μm thin nickel foils) has been

sandwiched between two identical and plane faced pellet type AgCuS nanocrystalline samples. The measured positron annihilation lifetime spectrum has been analyzed by computer program PATFIT-88.[9] The source component[10] has been evaluated by measuring a positron lifetime spectrum of 99.9999% pure Al and properly subtracted from the sample spectrum. For the Doppler broadening of the positron annihilation radiation (DBPAR) measurement, a HPGe detector (efficiency: 12%; type: PGC 1216sp of DSG, Germany) with an energy resolution of 1.1 keV at 514 keV of 85Sr has been used for the detection of the 511 keV γ-ray. The DBAR spectrum has been recorded in a dual ADC based- multiparameter data acquisition system (MPA-3 of FAST ComTec, Germany). For the temperature dependent DBPAR measurement, the source sample sandwich has been placed inside a furnace (30-600 ^{0}C with $\pm$2 ^{0}C at the sample site).[11] For each temperature, about 107 counts have been recorded in a dual ADC based multiparameter data acquisition system (MPA-3 of FAST ComTec., Germany). The Doppler broadening of the annihilation 511 keV γ-ray spectrum has been analyzed by evaluating the conventional line-shape parameters (S-parameters). The S-parameter is calculated as the ratio of the counts in the central area of the 511 keV photopeak (|511 keV - Eγ| $\leq$ 0.85 keV) and the total area of the photo peak (|511 keV - Eγ| $\leq$ 4.25 keV).[11] The S-parameter represents the fraction of positrons annihilating with the lower momentum electrons with respect to the total electrons annihilated.

2B.2.4 Thermoelectric measurements

Seebeck coefficient and electrical conductivity were measured using a ULVAC-RIKO ZEM-3 instrument under helium atmosphere from room temperature to ~550 K. Elaborative discussions on the thermoelectric measurements have been given in the introduction part of the thesis (page 41).

2B.3 Results and discussion

Capping agent free nanocrystals of AgCuS were synthesized using a simple and room temperature wet chemical synthesis method. Nitrate salts of Ag^+ and Cu^+ were used as the metal precursors, and the sulfur powder was used as a sulfur source. $NaBH_4$ was used for the reduction of the metal nitrate salts. Tetraethylene glycol (TEG) was used as the solve-

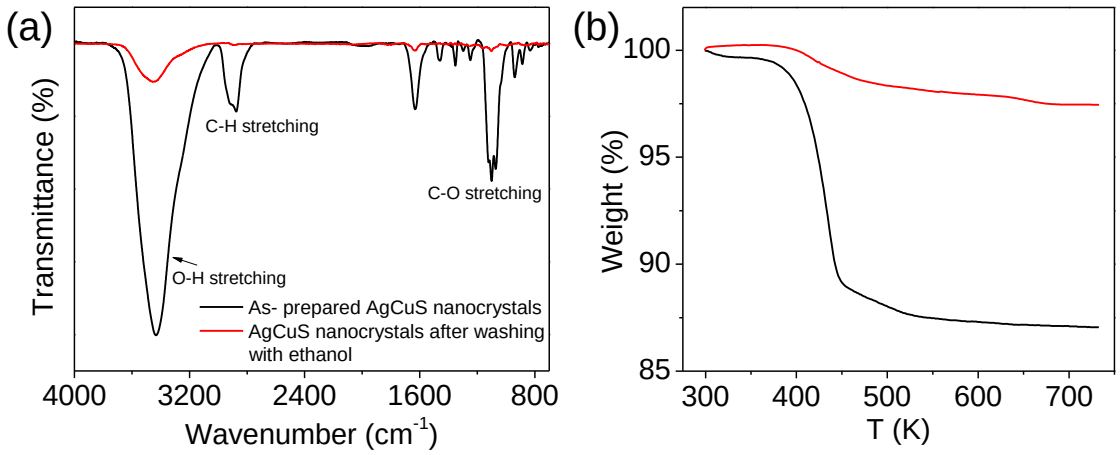

Figure 2B.1 (a) FTIR spectra and (b) TGA curve of AgCuS nanocrystals (40 nm), before and after washing with ethanol.

nt. TEG is a short chain aliphatic organic compound which contains two hydroxyl groups (-OH group) on the terminal carbon. Due to the presence of two terminal -OH groups, it can adsorb on the reactive surface of the as-synthesized nanocrystal. In order to remove the surface adsorbed TEG, we have repeatedly washed the sample with ethanol (TEG is soluble in ethanol) and finally dried it under vacuum at 60 ^{0}C for 2 h. FTIR and TGA measurements have been used to probe the removal of the TEG after washing with ethanol (Figure 2B.1). The presence of strong peaks in the FTIR spectra due to the vibration of -O-H, C-H and C-O bonds in the synthesized AgCuS nanocrystals indicates the presence of TEG in the sample (Figure 2B.1(a)). However, a significant reduction of the peak intensities was observed after washing with ethanol, indicating most of the TEG was removed from the sample (Figure 2B.1(a)). TGA measurements also confirm the removal of surface adsorbed TEG from the as-synthesized sample as the weight loss decreases from 12% to 1.5% in the as-synthesized and ethanol-treated samples, respectively (Figure 2B.1(b)). The AgCuS nanocrystals were characterized using powder X-ray diffraction (XRD), X-ray photoelectron spectroscopy (XPS), energy dispersive X-ray analysis (EDX), inductively coupled plasma atomic emission spectroscopy (ICP-AES), scanning and transmission electron microscopy (FESEM/TEM), and selected area electron diffraction analysis (SAED).

Room temperature PXRD (Cu K_α, λ = 1.5406 Å) of the as-synthesized nanocrystals could be indexed based on the orthorhombic β-AgCuS phase (space group, $Cmc2_1$) (Figure 2B.2(a)). In order to understand the structural evolution with temperature,

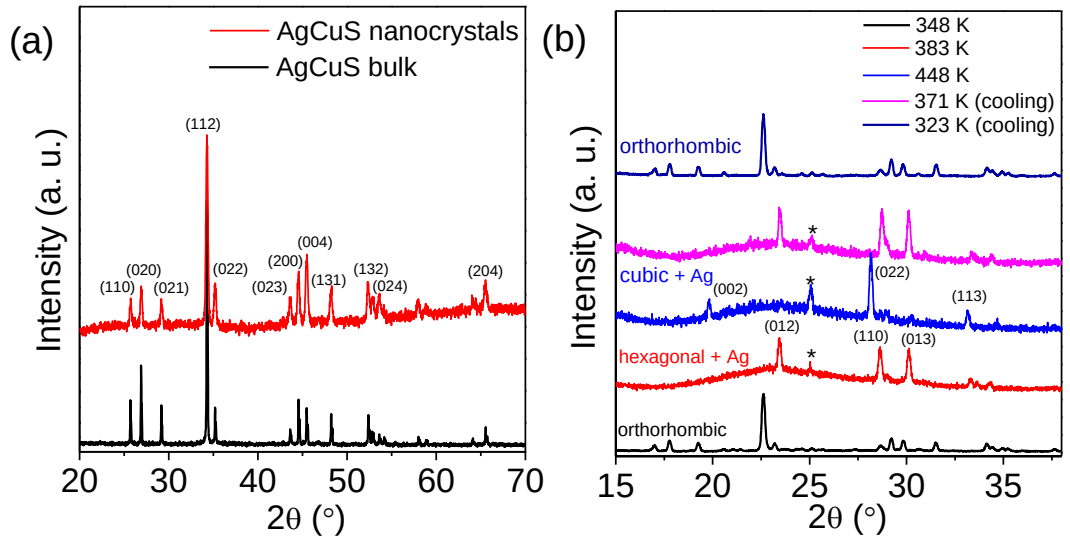

Figure 2B.2 (a) Powder XRD pattern of AgCuS nanocrystals (obtained after 30 min of reaction) measured at lab source (Cu Kα; λ = 1.5406 Å). The powder XRD pattern of bulk AgCuS was given for comparison.13 (b) Temperature dependent (300-448 K) heating/cooling cycle synchrotron (λ = 1.0279 Å) powder X-ray diffraction patterns of AgCuS nanocrystals obtained after 30 min of reaction

we have performed high temperature (300-448 K) heating/cooling cycle synchrotron powder XRD (λ = 1.0279 Å) of the AgCuS nanocrystals (obtained after 30 min of reaction) (Figure 2B.2(b)). Temperature dependent PXRD data shows a clear structural phase transition from room temperature orthorhombic (β) to the hexagonal (α) phase around 365 K. With further heating the hexagonal (α) phase transforms to the cubic phase (δ). The phase transformation is reversible in nature as confirmed by the cooling cycle PXRD data. Interestingly, we have observed the appearance of a little metallic Ag phase (* marked in Figure 2B.2(b)) along with the α- and δ-AgCuS phase on heating the β-AgCuS nanocrystalline sample, which then disappeared on cooling back to the orthorhombic β-AgCuS. This was not observed in the case of the bulk AgCuS sample,[8] which I shall discuss in later part of this chapter.

FESEM images of the as-synthesized sample indicate that AgCuS nanoparticles are agglomerated in nature. The absence of an additional capping agent during the synthesis results in the agglomeration of the AgCuS nanoparticles. The FESEM image indicates the average particle size of the nanocrystals obtained after 30 min of the reaction is 40 nm (Figure 2B.3(a)). The average particle size of the nanocrystals obtained after 12 h of reaction is 120 nm (Figure 2B.3(b)) and particles becomes more agglomerated and interconnected with increasing reaction time. EDX analysis indicates

the presence of Ag, Cu, and S in the proper ratios (insets of Figure 2B.3). ICP-AES measurements also indicate the composition of nanocrystals to be $Ag_{0.97}CuS_{0.98}$, which is close to the nominal composition.

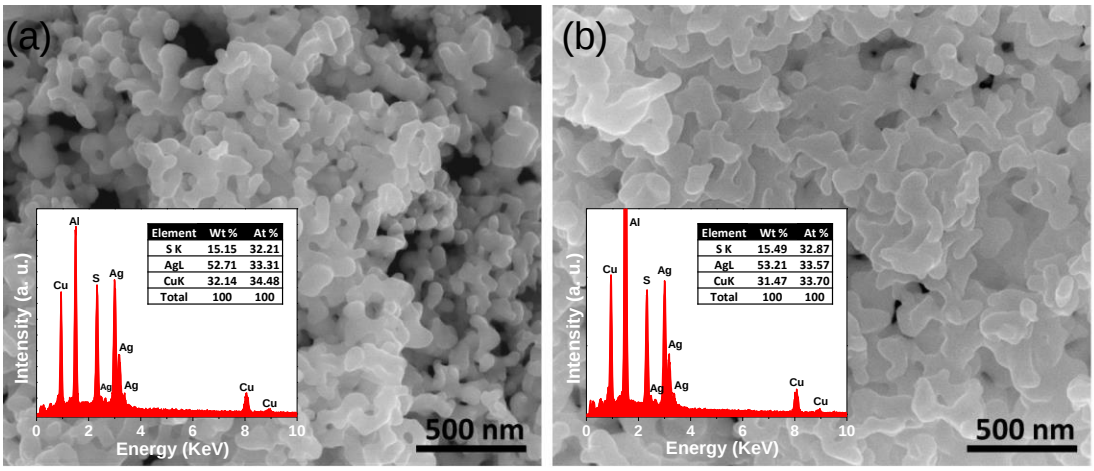

Figure 2B.3 FESEM images of nanocrystalline AgCuS obtained after the reaction times of (a) 30 min and (b) 12 h, respectively. Insets in (a) and (b) show EDX spectra of respective nanocrystal with elemental percentage.

The TEM image of the AgCuS nanocrystals obtained after 30 min of reaction also indicates the agglomerated nature of the particles (Figure 2B.4(a)). The SAED pattern taken from a particle indicates a single crystalline nature of the AgCuS nanocrystal (inset of Figure 2B.4(a)). The high-resolution TEM (HRTEM) image shows a clear lattice spacing of 2.6 Å corresponding to the (112) inter-planar distance of orthorhombic AgCuS (Figure 2B.4(b)). Additionally, the STEM-EDX compositional mapping over the group of nanocrystals indicates the single-phase homogeneity of the AgCuS nanocrystals (Figure 2B.4(c)).

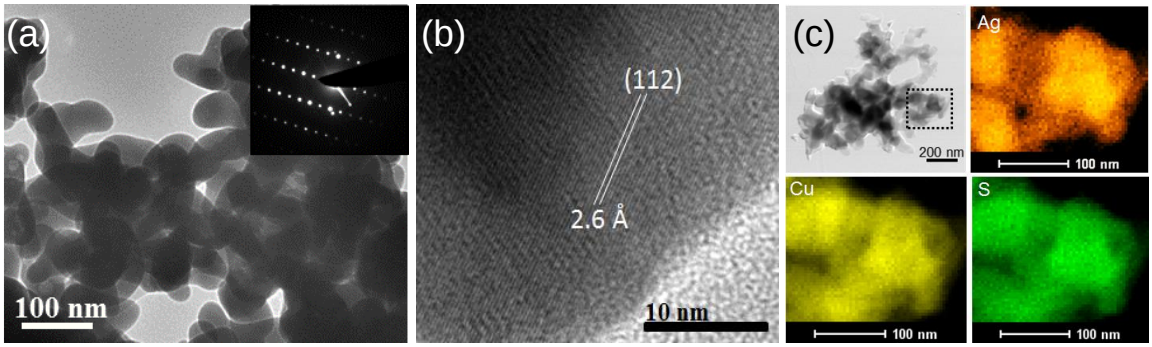

Figure 2B.4 (a) TEM image and inset in (a) shows the SAED pattern, (b) HRTEM image of AgCuS nanocrystals (30 min reaction). (c) STEM image and STEM-EDX compositional mapping over a group of nanocrystals (from the highlighted portion of the STEM image).

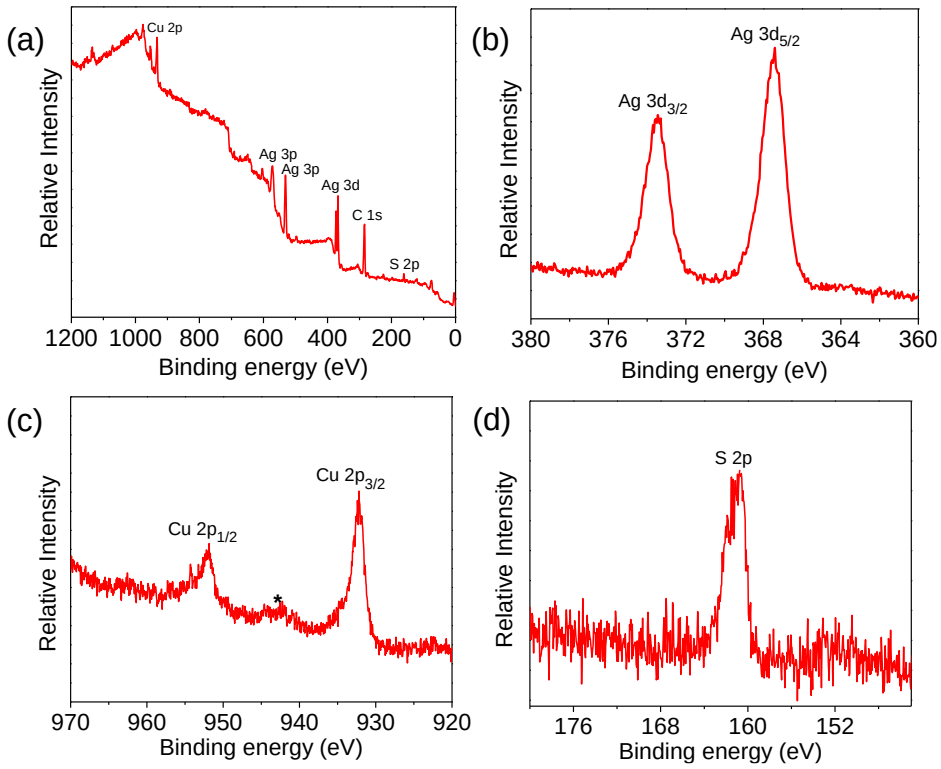

Figure 2B.5 XPS spectra of AgCuS nanocrystals (30 min reaction) (a) XPS survey scan (b) Ag 3d, (c) Cu 2p and (d) S 2p spectra. An additional peak (* marked) in Cu 2p was due to presence of small amount of Cu(II).

In order to further confirm the presence of the relevant elements and their oxidation states, we have performed XPS of the nanocrystalline AgCuS (Figure 2B.5). The presence of two strong peaks at 373.5 eV and 367.4 eV in the XPS is due to Ag(I) $3d_{3/2}$ and Ag(I) $3d_{5/2}$, respectively (Figure 2B.5(b)). The peaks at 952 eV and 932.2 eV correspond to Cu(I) $2p_{1/2}$ and Cu(I) $2p_{3/2}$ respectively (Figure 2B.5(c)). An additional small peak centered at 942.6 eV was evidenced, which is due to the presence of Cu(II). As the synthesized nanocrystals are capping free, surface oxidation of the AgCuS nanocrystals resulted in the formation of a minor amount of the more stable Cu(II), which was otherwise not detected by PXRD. A peak located at 161 eV is due to S 2p (Figure 2B.5(d)).

The temperature-dependent specific heat (C_p) of nanocrystalline AgCuS obtained after 30 min of the reaction was measured using a differential scanning calorimetry (DSC) technique and demonstrates two phase transitions above room temperature (Figure 2B.6). A λ-shaped peak centered at 375 K corresponds to the phase transition from the

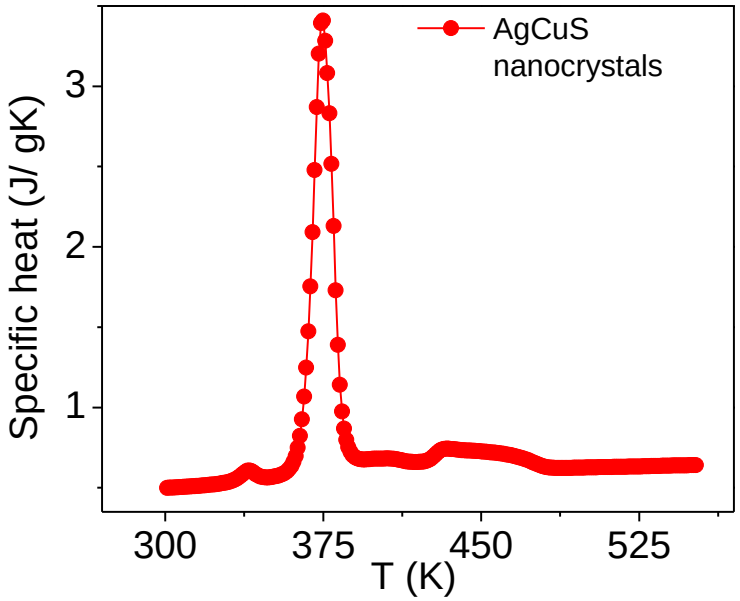

Figure 2B.6 Temperature dependent specific heat (C_p) of nanocrystalline AgCuS obtained after 30 min of reaction.

ordered orthorhombic (β) to the partially disordered hexagonal (α) phase. A broad peak centered at 445 K corresponds to the phase transition from the partially disordered hexagonal (α) to the fully disordered cubic (δ) phase. A similar observation has also been evidenced in the bulk AgCuS sample.[8] However, the additional peak at 408 K corresponding to the phase boundary of the biphasic hexagonal-cubic region was present for the bulk AgCuS sample,[8] which is absent in the case of the nanocrystalline AgCuS sample. This indicates that the hexagonal (α) phase transforms to the cubic (δ) phase without passing through a mixture of hexagonal (α) + cubic (δ) phases in the present nanocrystalline AgCuS sample, which is consistent with the temperature dependent PXRD data (Figure 2B.2(b)). The (β-α) transition takes place from an ordered state to a partially disordered state (onset of order-disorder transition) with a significant change in volume of 2.3%, while the (α-δ) transition occurs from a partially disordered state to a fully disordered state with a volume change of 0.6%.[12] The above discussion explains why the anomalies in the different measurements (Seebeck and C_p) are generally dramatic and sharp during the (β-α) transition compared to that of an (α-δ) transition.

In Figure 2B.7(a) we present room temperature Raman spectrum of nanocrystalline AgCuS (obtained after 30 min of reaction) which is compared with its bulk counterpart. All of the peaks in the Raman spectrum of the nanocrystalline sample

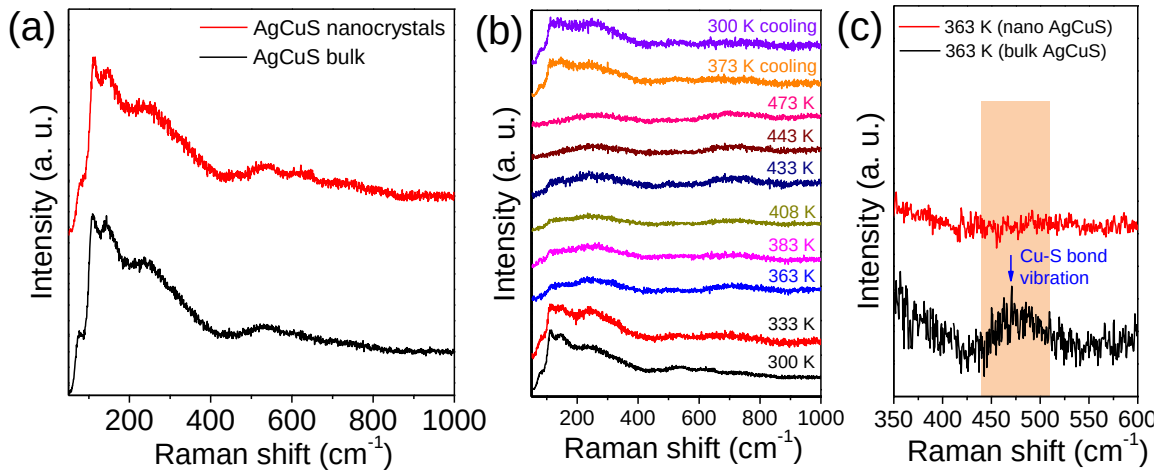

Figure 2B.7 (a) Room temperature Raman spectra of nanocrystalline AgCuS (obtained after 30 min of reaction) compared with that of the previously reported bulk AgCuS sample.[8] (b) Temperature dependent Raman spectra of nanocrystalline AgCuS (obtained after 30 min of reaction). (c) Raman spectra of bulk and nanocrystalline AgCuS (30 min reaction), in the range of 350-600 cm^{-1}, indicating the absence of Cu-S bond vibration in nanocrystalline sample during orthorhombic (β) to hexagonal phase (α) transition.

are matching with that of bulk AgCuS. A broad peak at 240 cm^{-1} can be assigned to the Ag-S bond vibration.[8,13,14] The peaks below 150 cm^{-1} can be assigned to Ag/Cu lattice vibration.[8,15] Temperature dependent Raman spectra of nanocrystalline AgCuS were presented in Figure 2B.7(b). During the (β-α) transition temperature (363 K), the peaks associated with the Ag lattice vibration completely disappear as the Ag atoms begin to disorder in the hexagonal (α) phase. However, the most interesting observation is that the peak associated with the Cu-S bond vibration at 474 cm^{-1} is absent in the nanocrystalline AgCuS during the (β-α) transition, which was present in the bulk AgCuS sample (Figure 2B.7(c)). In case of bulk AgCuS, using density functional theory (DFT) based calculations, we have shown that the Cu-S hybridized orbital plays a crucial role in the *p-n-p* type conduction switching as it contributes to the semimetallic intermediate state during the (β-α) transition.[8] The absence of the Cu-S bond vibration results in a significant change in the conduction property of the nanocrystalline AgCuS, which will be discussed in a later part of the chapter. Further increasing the temperature to 443 K, the cubic (δ) phase does not show any Raman signal due to the absence of macroscopic polarizability as the Ag/Cu are fully disordered.[8] The phase transitions are reversible in nature, which is confirmed by taking the Raman spectra on cooling.

In order to measure their thermoelectric properties, the AgCuS nanocrystals were pressed into a rectangular bar (2 × 2 × 8 mm^3) using an AIMIL die-press at 60 kN m^{-2}

pressure. The bar was sealed in a quartz tube under vacuum (10^{-5} Torr) and then sintered for 3 h at 573 K, which is above the upper limit of the thermoelectric measurement temperature. We could achieve a density of ~94%, which is really good as the present nanoparticles do not contain any capping agents.

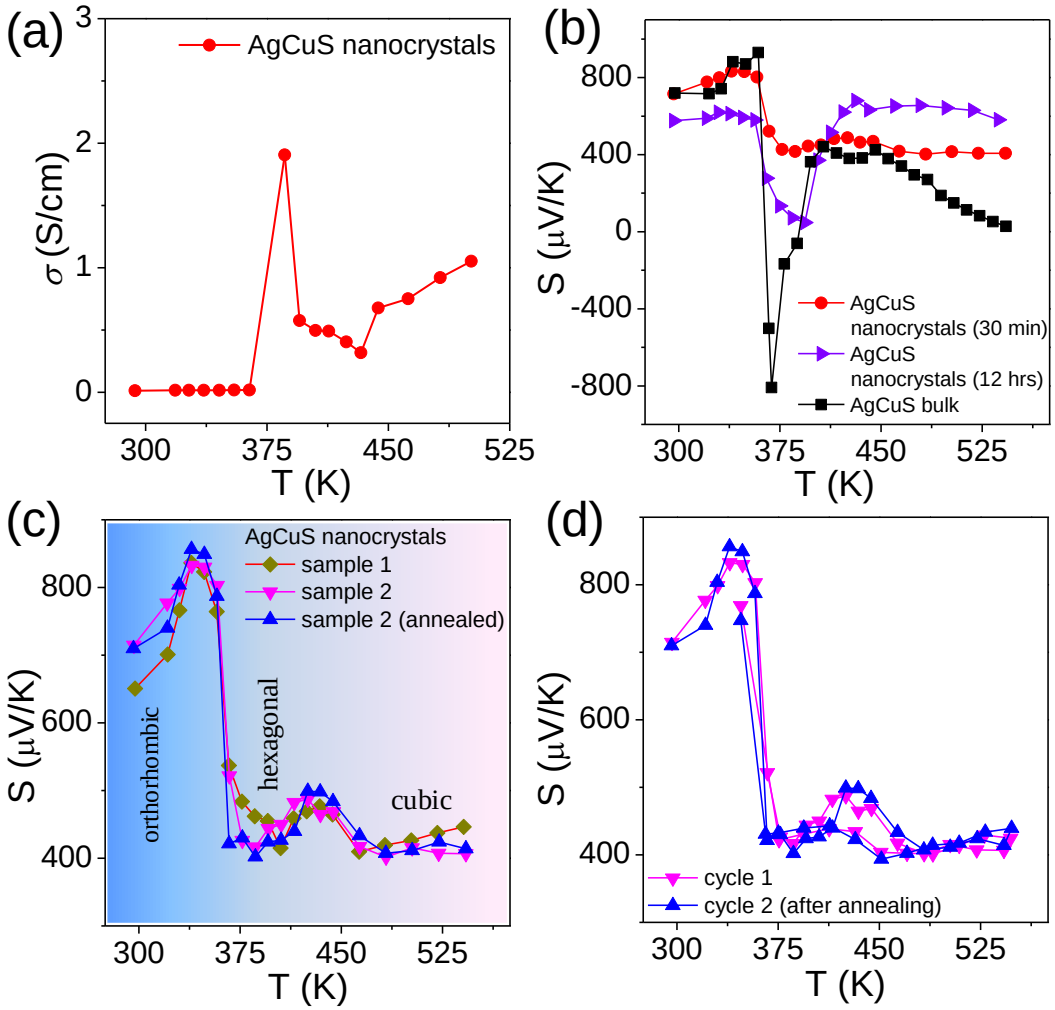

Figure 2B.8 Temperature dependent (a) electrical conductivity (σ) of AgCuS nanocrystals obtained after 30 min of reaction. (b) Seebeck coefficients (S) of AgCuS nanocrystals obtained after 30 min and 12 h of reaction, which are compared to that of their bulk counterpart.[8] (c) Seebeck coefficients (S) of different batches of nanocrystalline AgCuS samples (30 min of reaction) show the reproducibility and temperature stability. (d) Two cycle heating cooling Seebeck coefficient data for nanocrystalline AgCuS.

In Figure 2B.8, we present the temperature dependent thermoelectric properties for nanocrystalline AgCuS. Temperature dependent electrical conductivity (σ) indicates a sharp anomaly during the (β-α) transition (361 K); while the increase in σ during the (α-δ) transition (433 K) is not very significant (Figure 2B.8(a)). The trend of temperature dependent σ in the case of nanocrystalline AgCuS (obtained after 30 min of reaction) is

quite similar to that for the bulk AgCuS.[8] However, the value of σ for the nanocrystalline sample is higher compared to that of bulk AgCuS, which is due to the higher carrier concentration in the nanocrystalline phase (n_{nano} = 2.6 × 10^{15} cm^{-3} at 300 K) than in its bulk counterpart (n_{bulk} = 1.3 × 10^{15} cm^{-3} at 300 K). Higher *p*-type carrier concentration in the nanocrystalline AgCuS sample is due to the formation of more Ag vacancies in the nanoscale, which act as a *p*-type dopant and inject more positively charged holes into the nanocrystalline sample.

Nanocrystalline AgCuS (obtained after 30 min of reaction) shows a positive sign Seebeck coefficient (*S*) in the temperature 300-550 K range, indicating *p*-type conduction (Figure 2B.8(b)). An *S* value of ~710 μV K^{-1} is measured at room temperature, which increases to ~855 μV K^{-1} at 350 K. A sharp decrease in *S* from ~783 μV K^{-1} at 360 K to ~418 μV K^{-1} at 367 K is observed during the orthorhombic to hexagonal (β-α) phase transition Figure 2B.8(b). The decrease in *S* during the (β-α) phase transition temperature is consistent with the sharp increases in σ at 361 K. We have compared the temperature dependent *S* data of the AgCuS nanocrystals to the previously reported bulk AgCuS in Figure 2B.8(b).[8] Bulk AgCuS is known to show reversible *p*-*n*-*p* type conduction switching with a large change in the Seebeck coefficient (ΔS = ~1757 μV K^{-1}) during the orthorhombic to hexagonal (β-α) phase transition.[2,8] Interestingly, we have not observed any *p*-*n*-*p* type conduction switching after the size reduction to the nanoscale in AgCuS. We observe a slight dip in temperature dependent *S* during the hexagonal to cubic (α-δ) phase transition at 437 K (Figure 2B.8(b)). Measurements on the different batches of samples and an annealed sample reproduced a similar trend in the temperature dependent *S* data for AgCuS nanocrystals (Figure 2B.8(c)). Heating-cooling cycle *S* measurements indicate the reversibility of the phase transition (Figure 2B.8(d)). The repeated heating-cooling cycle measurements on the same sample after annealing (573 K for 12 h) also show the reversibility of the transition and hence confirm the temperature stability of the thermoelectric properties above the phase transition temperature. It must be mentioned that the heating-cooling cycle Seebeck data shows small hysteresis during the (β-α) and (α-δ) phase transitions (Figure 2B.8(d)). Superionic phase transitions in AgCuS involve a change in volume of 2.3% and 0.6% during the β-α and α-δ phase transitions,

respectively.[12] The phase transitions in AgCuS are first order type as the volume (V) is the first derivative of Gibbs free energy (G), $\left(\frac{\partial G}{\partial P}\right)_T = V$, where, P is pressure and T is temperature. First order phase transitions are generally associated with a hysteresis due to the change in volume during the transition.[16,17] A change in volume during the phase transition might result in the small hysteresis in the temperature dependent Seebeck data. Thus, the bump on the heating cycle transformed to a small dip on cooling during the (α-δ) phase transition (Figure 2B.8(d)). We have also performed the temperature dependent S measurement on the nanocrystals obtained after 12 h of reaction. Larger sized (120 nm) nanocrystalline AgCuS also shows p-type conduction in the 300-550 K range, but interestingly during the phase transition (β-α) the S value decreases to a much lower value (133 μV K^{-1} at 374 K) than that for the smaller nanocrystals (40 nm) obtained after 30 min of reaction (Figure 2B.8(b)). S vs. T data of the different particle sized AgCuS nanocrystals indicate that with increasing reaction time (*i.e.* increasing particle size) the conduction properties of the system are moving towards the conduction properties of bulk AgCuS.

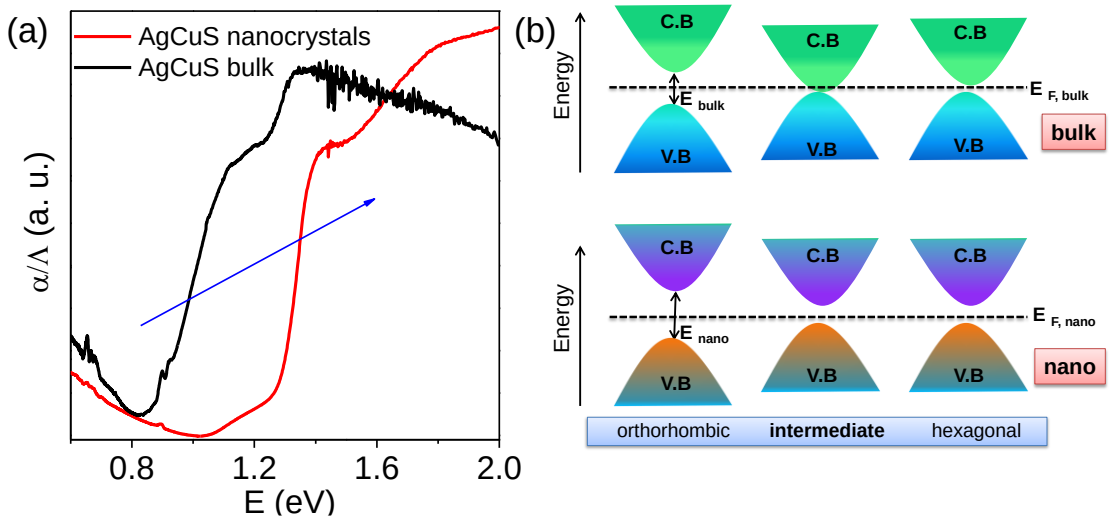

Figure 2B.9 Room temperature optical absorption spectra of as synthesized AgCuS nanocrystals (obtained after 30 min of reaction) compared with the bulk AgCuS.[8] (b) Schematic representation of changes of the band gap of bulk and nanocrystalline AgCuS during orthorhombic (β) to hexagonal (α) phase transition.

In order to understand the thermoelectric properties of the AgCuS nanocrystals, we have performed optical band gap and temperature dependent positron annihilation spectroscopy measurements. Structural phase transformation in solids can result in a decrease of the electronic band gap and hence sometimes creates a semimetallic

intermediate state where the Fermi level can reshuffle from the valence to the conduction band, thus giving rise to a conduction switching property.[2,4,8,18] Previously, first principle density functional theoretical calculations on the electronic structure of bulk AgCuS showed that closing of the band gap occurred during the orthorhombic (β) to hexagonal phase (α) transition. This caused the formation of an intermediate semimetallic state, which was responsible for the *p-n-p* conduction switching in bulk AgCuS. The spectroscopically measured band gap of the nanocrystalline AgCuS (obtained after 30 min of reaction) is 1.2 eV at room temperature (Figure 2B.9(a)), which is higher comparatively than that of the bulk AgCuS (0.9 eV). We believe that the increase in the band gap is one of the primary reasons for the absence of conduction type switching in nanocrystalline AgCuS. The higher electronic band gap in nanocrystalline AgCuS compared to that of its bulk counterpart is not sufficient for closing of the gap between the conduction and valence band (*i.e.* formation of semimetallic electronic state) during the orthorhombic (β) to hexagonal (α) phase transition. Figure 2B.9(b) represents a schematic of changes of the band gap of bulk and nanocrystalline AgCuS during the first phase transition.

Positron annihilation spectroscopy is a powerful technique for the detection of vacancies or defect types in solids. In Figure 2B.10(a), we present a room temperature positron annihilation lifetime spectrum of the nanocrystalline AgCuS (obtained after 30 min of reaction). The annihilation lifetime spectrum for the nanocrystalline AgCuS sample (variance of fit < 1 per channel) yields three lifetime components (Table 2B.1), which are similar to those previously reported for bulk AgCuS.[8] The shortest lifetime component (τ_1) has been assigned to the free annihilation of positrons,[19] while the intermediate lifetime component (τ_2) is due to the annihilation of positrons in the defect site, mainly the Ag vacancy.[2,8] The long lifetime component (τ_3) originates from the formation of positronium at the sample surface or in the large voids inside the sample.[19] Since the nanocrystal size (40 nm) is less than the positron diffusion length, the positrons are mainly trapped in the vacancy-like defects at the surfaces/grain boundaries. Here the grain surface is enriched with Ag vacancy type defects, thus τ_1 is an admixture with the positron lifetime in Ag mono-vacancy type defects present at the grain boundaries. The intermediate lifetime component is due to the trapping of positrons in Ag vacancy

clusters. Positron annihilation lifetime measurements on the nanocrystalline AgCuS clearly show that the nanocrystalline surface is enriched with Ag vacancy-like defects and defect clusters. This finding indicates that Ag vacancies are indeed responsible for the *p*-type conduction in nanocrystalline AgCuS.

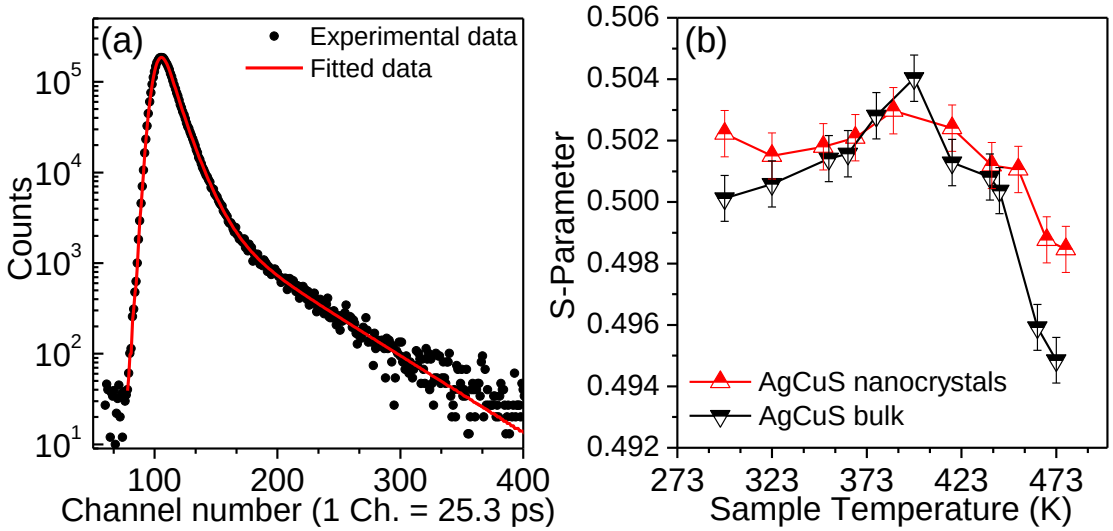

Figure 2B.10 (a) Room temperature positron annihilation lifetime spectrum for the AgCuS nanocrystals (obtained after 30 min of reaction). Solid red line shows the fitting for the determination of positron life time components (b) Temperature dependent Doppler broadening S-parameter of nanocrystalline AgCuS (30 min of reaction) with bulk AgCuS.[8]

Table 2B.1 Positron lifetime components of AgCuS nanocrystals.

τ_1 (ps)	I_1 (%)	τ_2 (ps)	I_2 (%)	τ_3 (ps)	I_3 (%)
182 ± 3	42 ± 1	312 ± 2	52 ± 1	1342 ± 150	6 ± 0.2

Temperature dependent Doppler broadening of the annihilation radiation indicates the momentum distribution of annihilating electrons, which provides important fundamental insight into the temperature dependent thermoelectric properties of the nanocrystalline AgCuS during the (β-α) transition. The Doppler broadening spectra have been analyzed by evaluating the S-parameter defined by the ratio of the counts in the central area of the annihilation photo-peak and the total area of the photo-peak. In Figure 2B.10(b), we present the temperature dependent S-parameter curve for nanocrystalline AgCuS (40 nm) obtained after 30 min of reaction. In the nanocrystalline AgCuS, the variation of the S-parameter with temperature is almost flat (within error limit) during the (β-α) transition and beyond 450 K the fall off of S-parameter is shallow. In the case of

the bulk AgCuS,[8] during the (β-α) transition, onset of the S-parameter starts at 360 K and it reaches a maximum at 385 K, then it falls rapidly compared to that of the nanocrystalline sample. The nanocrystalline AgCuS sample is enriched with Ag vacancy like defects and Ag vacancy clusters, but the rise of the S-parameter with temperature in the temperature interval of 273 K to 393 K is significantly absent. This result indicates that the Ag vacancy is less diffusive in the nanocrystalline AgCuS compared to that of its bulk counterpart at high temperatures. Movement of Ag/Cu atoms during the (β-α) transition occurs through the Ag vacancy. Thus, migration of the Ag vacancy is essential for phase transformation. The large grain size in the bulk crystals results in long-range periodicity in the crystal lattice, hence Ag vacancies are delocalized in nature, which essentially favors the *p*-*n*-*p* type conduction switching in bulk AgCuS. However, in the AgCuS nanocrystals, due to low periodicity of the crystal lattice (*i.e.* due to smaller size), the Ag vacancy is localized in nature, which demands creation of more Ag vacancies during the (β-α) transition. This resulted in the leaching out of the Ag from the AgCuS nanocrystals followed by the segregation at the surface or grain boundaries. Ag leaching from the AgCuS nanocrystals injects more positively charged carriers, which makes the AgCuS nanocrystal *p*-type throughout the measured temperature range. Temperature dependent PXRD data also shows the appearance of the Ag peak along with the hexagonal (α) and cubic (δ) AgCuS phases on heating from orthorhombic (β) AgCuS nanocrystals (Figure 2B.2(b)). Previous electronic structure calculations on the bulk AgCuS during the (β-α) transition indicated that the contribution from hybridized Cu-S orbitals to the overlapping valence and conduction band gave rise to the semimetallic character of the intermediate structure that was responsible for the *p*-*n*-*p* type conduction switching. Although the signature of Cu-S bond vibration was present in the Raman spectra of the bulk AgCuS during the (β-α) transition, the Raman spectra of nanocrystalline AgCuS does not show any Cu-S bond vibration during the (β-α) transition. This result also indicates the absence of a semimetallic intermediate electronic state during the (β-α) transition in nanocrystalline AgCuS.

2B.4 Conclusions

In conclusion, nanocrystalline AgCuS was synthesized for the first time by a simple capping free solution phase reaction at room temperature. Temperature dependent synchrotron powder X-ray diffraction, heat capacity (C_p) and Raman spectroscopy measurements clearly indicate that the nanocrystalline sample undergoes two distinct order-disorder phase transitions at high temperatures. A superionic order-disorder phase transition tailors the thermoelectric properties in AgCuS nanocrystals and the fundamental understanding was developed based on temperature dependent Raman spectroscopy, positron annihilation spectroscopy, and optical absorption experiments. Size reduction to the nano-dimension resulted in the vanishing of *p*-*n*-*p* conduction switching in AgCuS due to the following combined reasons: (a) higher band gap of AgCuS nanocrystals than that of the bulk counterpart, which is not appropriate for the creation of a semimetallic electronic state and the shifting of the Fermi level in the conduction band during the first order–disorder phase transition, (b) absence of hybridized Cu-S states during the (β-α) transition, which were otherwise responsible for the creation of an intermediate semimetallic state, (c) high surface to volume ratio in nanocrystalline AgCuS, which gives rise to the formation of more Ag vacancies and increases the *p*-type carrier concentration and (d) Ag leaching from AgCuS nanocrystals at elevated temperature injects more positively charged carriers into the system, which makes the AgCuS nanocrystal *p*-type throughout the measured temperature range. Our findings demonstrated that the *p*-*n*-*p* type conduction switching and thermoelectric properties of the bulk noble metal based chalcogenides could be tuned by reducing the crystallite size to the nanometer scale. The discovery of an order-disorder phase transition in nanoscale materials and its effect on the electronic structure can bring novel phenomena with unusual properties.

References

[1] J. Janek, *Nat. Mater.* **2009**, *8*, 88–89.

[2] S. N. Guin, K. Biswas, *Phys. Chem. Chem. Phys.* **2015**, *17*, 10316–10325.

[3] O. Osters, M. Bawohl, J. L. Bobet, B. Chevalier, R. Decourt, T. Nilges, *Solid State Sci.* **2011**, *13*, 944–947.

[4] C. Xiao, X. Qin, J. Zhang, R. An, J. Xu, K. Li, B. Cao, J. Yang, B. Ye, Y. Xie, *J. Am. Chem. Soc.* **2012**, *134*, 18460–18466.

[5] S. N. Guin, V. Srihari, K. Biswas, *J. Mater. Chem. A* **2015**, *3*, 648–655.

[6] L. Pan, D. Bérardan, N. Dragoe, *J. Am. Chem. Soc.* **2013**, *135*, 4914–4917.

[7] J. B. Rivest, L.-K. Fong, P. K. Jain, M. F. Toney, A. P. Alivisatos, *J. Phys. Chem. Lett* **2011**, *2*, 2402–2406.

[8] S. N. Guin, J. Pan, A. Bhowmik, D. Sanyal, U. V. Waghmare, K. Biswas, *J. Am. Chem. Soc.* **2014**, *136*, 12712–12720.

[9] M. Kirkegaard, P. Pedersen, N. J. Eldrup, *Rep. Riso Natl. Lab* **1989**.

[10] C. Hautojarvi, P. Corbel, *Positron Spectroscopy of Solids*, IOS Press: Amsterdam, The Netherlands, **1995**.

[11] M. Chakrabarti, A. Sarkar, S. Chattapadhayay, D. Sanyal, A. K. Pradhan, R. Bhattacharya, D. Banerjee, *Solid State Commun.* **2003**, *128*, 321–324.

[12] D. M. Trots, A. Senyshyn, D. A. Mikhailova, M. Knapp, C. Baehtz, M. Hoelzel, H. Fuess, *J. Phys. Condens. Matter* **2007**, *19*, 136204.

[13] A. Milekhin, L. Sveshnikova, T. Duda, N. Surovtsev, S. Adichtchev, D. R. T. Zahn, *Chinese J. Phys.* **2011**, *49*, 63–70.

[14] B. Minceva-Sukarova, M. Najdoski, I. Grozdanov, C. J. Chunnilall, *J. Mol. Struct.* **1997**, *410–411*, 267–270.

[15] M. Ishii, H. Wada, *Mater. Res. Bull.* **1993**, *28*, 1269–1276.

[16] C. N. R. Rao, J. Gopalakrishnan, *New Directions in Solid State Chemistry*, Cambridge University Press, **1997**.

[17] C. N. R. Rao, *Acc. Chem. Res.* **1984**, *17*, 83–89.

[18] T. Nilges, S. Lange, M. Bawohl, J. M. Deckwart, M. Janssen, H.-D. Wiemhöfer, R. Decourt, B. Chevalier, J. Vannahme, H. Eckert, et al., *Nat. Mater.* **2009**, *8*, 101–108.

[19] R. Krause-Rehberg, H. S. Leipner, *Positron Annihilation in Semiconductors*, **1999**.

Chapter 3

Ultra-low thermal conductivity and high thermoelectric performance in *p*- type cation doped $AgSbSe_2$ *

*Publications based on this chapter: (1) *Energy Environ. Sci.* **2013,** *6*, 2603; (2) *RSC Advances* **2014,** *4*, 11811.

CHAPTER 3

Ultra-low thermal conductivity and high thermoelectric performance in *p*- type cation doped $AgSbSe_2$

Summary. *Thermoelectric materials can convert directly and reversibly waste heat into electrical energy and will play a significant role in future energy management. The main challenge in this field is to develop highly efficient, stable and inexpensive solid-state materials. Leading high-performance thermoelectric materials such as* Bi_2Te_3*, PbTe, and* $AgSbTe_2$ *are mainly based on tellurium, which is extremely scarce in the Earth crust. Hence, the Te price is likely to rise sharply if Te-based thermoelectric materials reach mass markets. Given that Te is 5000% more rare than Se and 500% more expensive, there is a compelling need to utilize tellurium free, earth abundant thermoelectrics, which can still achieve high zT performance.* $AgSbSe_2$*, a homologue of* $AgSbTe_2$*, containing earth-abundant elements has attracted our attention for thermoelectric investigation due to its intrinsically low thermal conductivity. In the present chapter, we show that the optimum concentrations cation doping (Pb, Bi, and Cd) act as effective p-type dopants and substantially increase the electrical conductivity, which results in a large increase in the power factor. With superior electronic transport and ultra-low thermal conductivity, high zT values of ~1 and ~1.15 at 680 K were achieved in* $AgSb_{0.96}Pb_{0.04}Se_2$ *and* $AgSb_{0.98}Bi_{0.02}Se_2$*. A maximum zT, of ~1 at 640 K was achieved for* $AgSb_{0.98}Cd_{0.02}Se_2$*.*

3.1 Introduction

Driven by the demand for clean and sustainable energy sources, thermoelectricity has become an important part of the research portfolio seeking to recognize new and efficient energy materials for power generation and cooling applications.[1–8] Beyond the traditional thermoelectric materials based on PbTe and Bi_2Te_3, the I-V-VI_2 (where I = Cu, Ag, Au or alkali metal; V = As, Sb, Bi; and VI = Se, Te) chalcogenides have emerged for their intrinsically low κ_{lat} due to the strong anharmonicity in the bonding.[9,10] Fifty-five years ago, Rosi *et al.* recognized $AgSbTe_2$, a typical member of the I-V-VI_2 family, to be an efficient *p*-type thermoelectric material with a zT of ~1.3 at 720 K.[11] In recent years, $AgSbTe_2$ has been studied repeatedly to improve its performance further by the optimization of the carrier concentration through doping with various elements.[12–16] Interestingly, GeTe (TAGS)[17] and PbTe rich alloys with AgSbTe (LAST-m)[18] showed extraordinary zT values of ~1.5 at 750 K and ~1.8 at 800 K, respectively.

Leading high-performance thermoelectric materials are mainly based on tellurium, which is extremely scarce in the Earth crust.[19] Hence, Te price is likely to rise sharply if Te-based thermoelectric materials reach mass markets. Therefore, it would be desirable to develop alternative materials, which minimize the use of rare and toxic elements such as Te and involve cheaper and more abundant elements. Attractive alternatives are $AgBiSe_2$ and $AgSbSe_2$ because Se is less expensive, has a longer-term price stability, and is 50 times more abundant than Te. Recent theoretical and experimental studies on a series of cubic bulk I-V-VI_2 compounds (where I = Cu, Ag, Au; V = As, Sb, Bi; and VI = S, Se, Te) have shown that the lone pair on the group V element plays an important role in deforming the lattice vibrations, which results intrinsically low κ_{lat} in these compounds.[9,10] Valence electronic configuration of Group V element in I-V-VI_2 compounds is ns^2np^3, where only np^3 electrons are involved in the bond formation with group VI element valence electrons, while the ns^2 electrons of group V element remain as a lone pair. The electrostatic repulsion between the stereochemically active lone pair of group V element and the valence bonding charge of the chalcogen atom results in strong anharmonicity in the bonding arrangement. Recently, zT values as high as ~1 at 773 K have been achieved in *n*-type Nb-doped bulk $AgBiSe_2$ synthesized by

a solid state reaction.[20] Solution-grown nanocrystalline $AgBiSe_2$ also exhibits a high zT of ~1.5 at 700 K with interesting *p-n-p* type conduction.[21] *n*-type $BiAgSeS_{1-x}Cl_x$ has also shown promising thermoelectric performance due to its low thermal conductivity.[22,23]

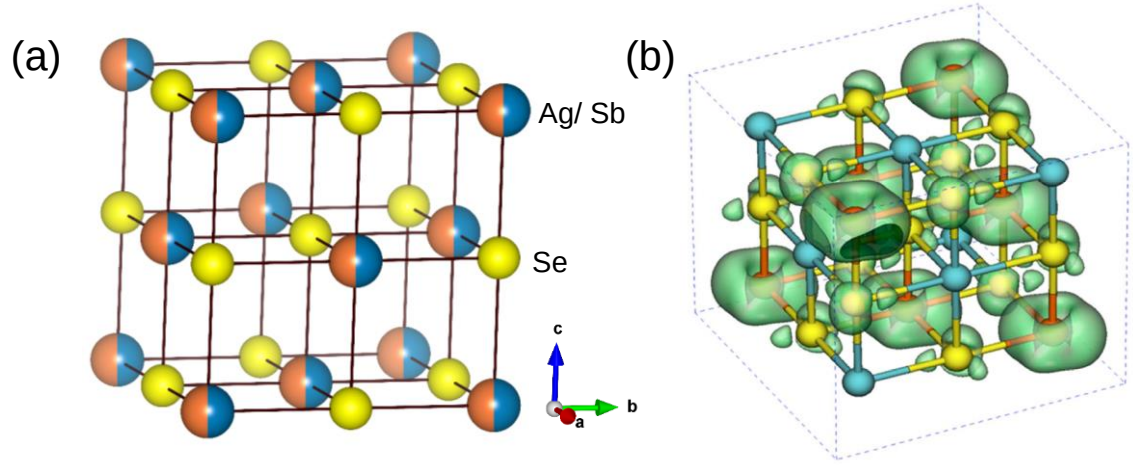

Figure 3.1 (a) Crystal structure of cubic rock salt $AgSbSe_2$ with disordered Ag/Sb positions. (b) Schematic representation of the presence of stereochemically active lone pair on Sb atom. Color code: Ag- light blue; Sb- orange; Se- yellow.[10]

$AgSbSe_2$, a homologue of $AgSbTe_2$ containing earth-abundant elements, has attracted our attention for thermoelectric investigation.[9,10] At room temperature, $AgSbSe_2$ crystallizes in a cubic rock salt structure (space group, $Fm\bar{3}m$) with disordered Ag and Sb positions (Figure 3.1(a)). The presence of stereochemically active $5s^2$ lone pair on Sb atom results in strong anharmonicity in the Sb-Se bond ((Figure 3.1(b)).[10,24] Grüneisen parameter (γ) is a direct measurement of anharmonicity. The compounds with a high degree of anharmonicity in bonding exhibit high γ value. Theoretical investigations by Heremans and co-workers showed that the γ value is higher in the case of $AgSbSe_2$ (γ = 3.4) compared to those of $AgSbTe_2$ (γ = 2.3) and $AgBiSe_2$ (γ = 2.5).[10] $AgSbSe_2$ possess the lowest lattice thermal conductivity among all the I-V-VI_2 compounds in 10-300 K range.[10] In addition to low thermal conductivity, $AgSbSe_2$ is a narrow band gap semiconductor with a favorable valence band structure composed of 12 half-pockets located at the X-point of the Brillouin zone.[12,14,25] Thermoelectric performance of $AgSbSe_2$ can, therefore, be enhanced significantly by the convergence of many valleys through proper carrier engineering.[8,26]

In this chapter, we present the synthesis and promising thermoelectric properties of high-quality bulk crystalline ingots of *p*-type bulk $AgSbSe_2$ doped with 2-4 mol% of

Pb, Bi, and Cd. We show that the optimum concentration of cation doping acts as an effective *p*-type dopant and substantially increases the electrical conductivity, which results in a large increase in the power factor (σS^2) of $AgSbSe_2$ over a broad temperature range. The large thermopower in this system was achieved due to the broad valence band maximum and multi-peak valence band structure of $AgSbSe_2$.[12] We could achieve a maximum zT of ~1 at 610 K in the case of the $AgSb_{0.96}Pb_{0.04}Se_2$ crystalline ingot due to its high power factor and ultra-low thermal conductivity. With optimum Bi doping, the zT of *p*-type $AgSbSe_2$ can reach ~1.15 at 680 K, which is 190% higher than that of pristine $AgSbSe_2$. Additionally, we further investigated the effect of Cd doping to validate our result on Pb-doped $AgSbSe_2$. Cd-doped samples also show large thermopower and improved electrical conductivity, which resulted in a significant improvement in the power factor (σS^2) over a broad temperature range. With this high σS^2 and ultra-low κ_{lat} values, we could achieve a maximum zT of ~1 at 640 K in the case of $AgSb_{0.98}Cd_{0.02}Se_2$ sample.

3.2 Methods

3.2.1 Synthesis

Elemental silver (Ag, 99.9%, metal basis, Alfa Aesar), elemental antimony (Sb, 99.9999%, metal basis), elemental bismuth (Bi, 99.999 %, Alfa Aesar), elemental cadmium (Cd, 99.9 %, Sigma-Aldrich) and elemental selenium (Se, 99.999%, metal basis, Alfa Aesar) were used for synthesis without further purification.

Pristine $AgSbSe_2$ and nominally doped $AgSb_{1-x}Pb_xSe_2$ (x = 0.02, 0.04), $AgSb_{1-x}Bi_xSe_2$ (x = 0.02, 0.04) and $AgSb_{1-x}Cd_xSe_2$ (x = 0-0.06) bulk ingots (9 g) were synthesized by adding appropriate ratios of high purity starting materials of Ag, Sb, Pb/Bi/Cd and Se in the fused-silica tubes (10 mm diameter). The tubes were sealed under high vacuum (10^{-5} Torr) and slowly heated up to 673 K over 12 h, then to 1123 K over 4 h, soaked for 10 h, and subsequently cooled to room temperature. In Figure 3.2(a), we show a typical photograph of the "as-synthesized" high-quality $AgSbSe_2$ ingot. Bar and coin shaped samples (Figure 3.2(b)) obtained after cutting and polishing of such ingots, which were used for electrical and thermal transport measurements, respectively.

3.2.2 Characterizations

Powder XRD for all the samples was recorded using Cu Kα (λ = 1.5406 Å) radiation on a Bruker D8 diffractometer. To probe the optical energy gap of these compounds, optical diffuse reflectance measurements were performed on finely ground powders using a Perkin Elmer Lambda 900, UV-vis/NIR spectrometer at room temperature. TEM imaging was performed using an aberration corrected FEI TITAN3TM 80-300 kV transmission electron microscope operating at 300 kV. Room temperature carrier concentration has been derived from Hall coefficient measurements using a PPMS. Detailed discussions on all the characterizations have been given in the introduction part of the thesis (page 31).

3.2.3 Thermoelectric measurements

Seebeck coefficient and electrical conductivity were measured under helium atmosphere by ULVAC-RIKO ZEM-3 instrument in 300-723 K temperature range. Thermal diffusivity, *D*, was directly measured by laser flash diffusivity method in a Netzsch LFA-457 under N_2 atmosphere range of 300-725 K. The total thermal conductivity, κ_{total}, of the samples was estimated to be in the temperature using the formula, $\kappa_{total} = DC_p\rho$, where *D* is the thermal diffusivity, C_p is the specific heat and ρ is the density of the sample. The thermal and electrical transport properties were measured along the same direction of the sample. Detailed discussions on thermoelectric measurements have been given in the introduction part of the thesis (page 41).

3.3 Results and discussion

Powder X-ray diffraction patterns (XRD) of the $AgSbSe_2$, $AgSb_{1-x}Pb_xSe_2$ (x = 0.02, 0.04) and $AgSb_{1-x}Bi_xSe_2$ (x = 0.02, 0.04) samples could be indexed on the cubic $AgSbSe_2$ structure (space group, $Fm\bar{3}m$) with no other impurity phase observed within the detection limits of powder XRD (Figure 3.2(b)). The observed linear expansion in the lattice parameter follow Vegard's law for the $AgSb_{1-x}Pb_xSe_2$ (x = 0.02, 0.04) and $AgSb_{1-x}Bi_xSe_2$ (x = 0.02, 0.04) samples, with increasing Pb or Bi concentrations (Figure 3.1(c) and (d)). The ionic radii of Bi and Pb are larger than that of Sb. As bigger Pb or Bi is introduced in the place of smaller Sb, the unit cell undergoes a systematic expansion,

leading to an increase in the lattice parameter. This gradual expansion of lattice parameter indicates an isomorphic substitution of the smaller Sb position by bigger Pb or Bi.

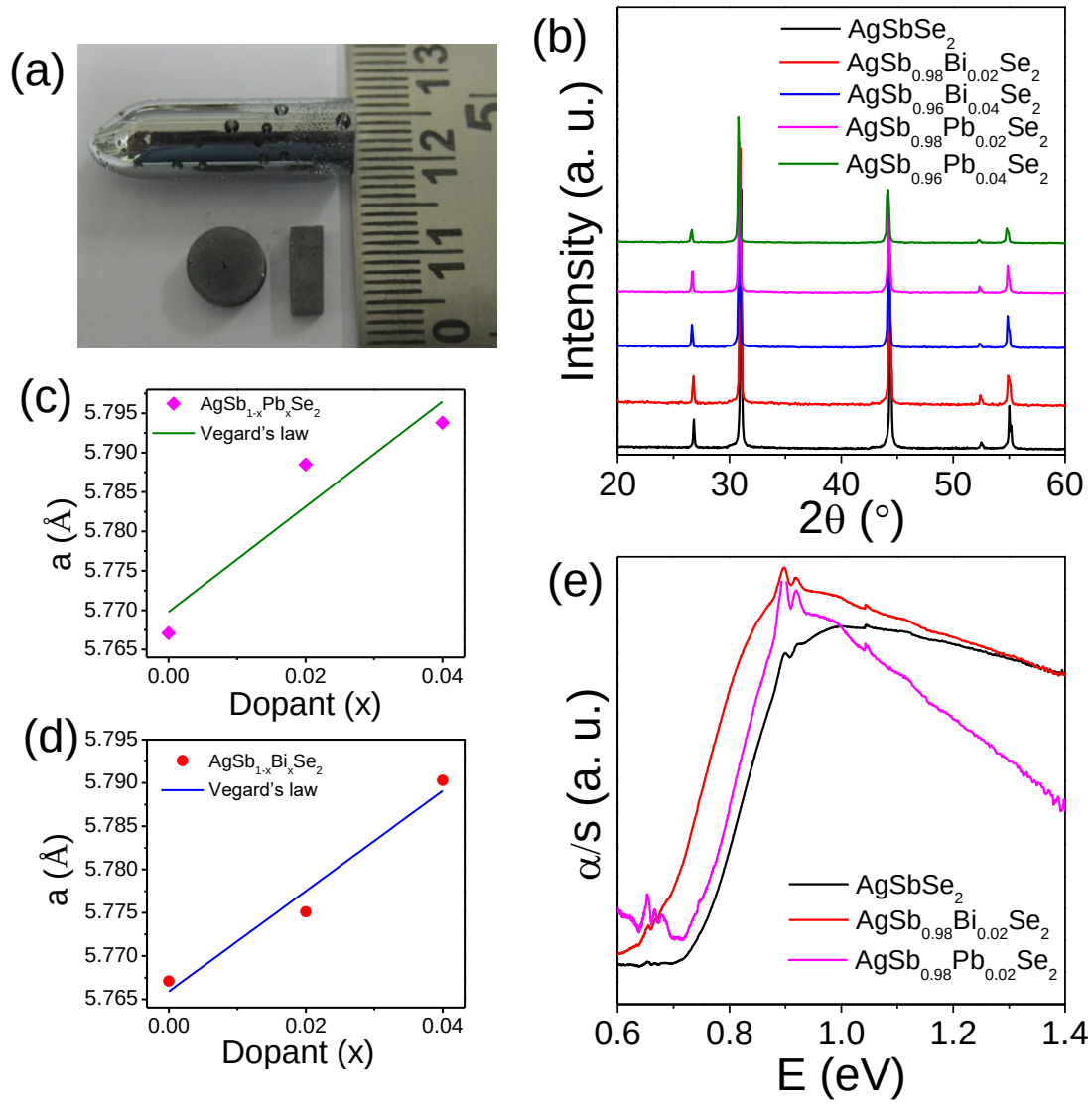

Figure 3.2 (a) Photograph of the as-synthesized ingot. Bar- and coin-shaped samples are used for electrical and thermal transport measurements, respectively. (b) Powder XRD patterns of pristine $AgSbSe_2$ and Pb or Bi doped $AgSbSe_2$ samples. (c) & (d) Lattice parameter vs. Pb or Bi concentrations in $AgSb_{1-x}(Pb/ Bi)_xSe_2$ (x = 0.02, 0.04) and the solid line indicates Vegard's law for a solid solution. (e) Electronic absorption spectra of $AgSbSe_2$ and 2 mol% Pb and Bi doped $AgSbSe_2$.

The spectroscopically measured optical band gap of the bulk $AgSbSe_2$ is 0.7 eV, which is typical of a narrow band gap semiconductor (Figure 3.2(e)). The systematic decrease in the band gaps of $AgSb_{0.98}Pb_{0.02}Se_2$ and $AgSb_{0.98}Bi_{0.02}Se_2$, compared to pristine $AgSbSe_2$, supports the successful substitution of Pb or Bi in the Sb sublattice of

$AgSbSe_2$. The absorption edge is not sharp and is suggestive of an indirect gap. This is consistent with the previous electronic structure calculations for $AgSbSe_2$.[12]

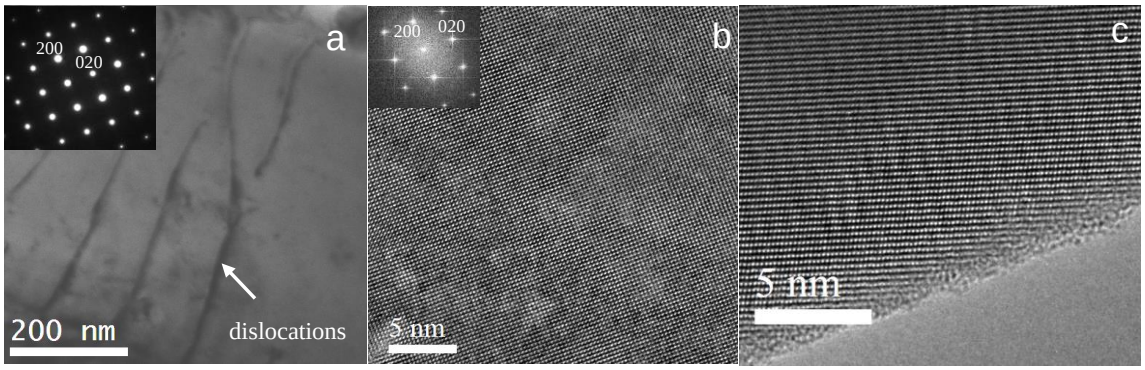

Figure 3.3 (a) Low magnification TEM image of $AgSb_{0.98}Pb_{0.02}Se_2$; inset in (a) shows the electron diffraction pattern. High resolution TEM images of (b) $AgSb_{0.98}Pb_{0.02}Se_2$ and (c) $AgSb_{0.98}Bi_{0.02}Se_2$ samples. Inset in (b) shows the corresponding pattern obtained by a Fourier transformation.

In order to understand the nanoscale architecture of the Pb/Bi-doped $AgSbSe_2$, we have performed a transmission electron microscopy (TEM) investigation (Figure 3.3). Figure 3.3(a) shows the low magnification TEM image of the $AgSb_{0.98}Pb_{0.02}Se_2$ sample. Although we have observed the presence of dislocations and grain boundaries, we have not observed the presence of nanoprecipitates in the sample. This result suggests the solid solution nature of the samples, which also supports the XRD and band gap results. The electron diffraction pattern (inset, Figure 3. 3(a) and (b)) confirms the single phase $AgSbSe_2$ with space group, $Fm\bar{3}m$. Figure 3.3(b) and (c) show the high resolution TEM images of $AgSb_{0.98}Pb_{0.02}Se_2$ and $AgSb_{0.98}Bi_{0.02}Se_2$ samples.

The temperature dependent electronic transport properties of $AgSbSe_2$ and solid solution $AgSb_{1-x}Pb_xSe_2$ (x = 0.02, 0.04) samples over a 290-723 K range are presented in Figure 3.4. Figure 3.4(a) shows the temperature-dependent electrical conductivity (σ) of pristine $AgSbSe_2$ and $AgSb_{1-x}Pb_xSe_2$ (x = 0.02, 0.04) samples. The room temperature σ value measured for the pristine sample is ~4.5 S cm^{-1}. A systematic rise of σ at room temperature is observed with increasing Pb doping concentrations from 0 to 4 mol%. Typically, the room temperature σ for the $AgSb_{0.96}Pb_{0.04}Se_2$ sample was ~61 S cm^{-1}, which remains almost the same up to 600 K and then decreases to ~16 S cm^{-1} at 705 K.

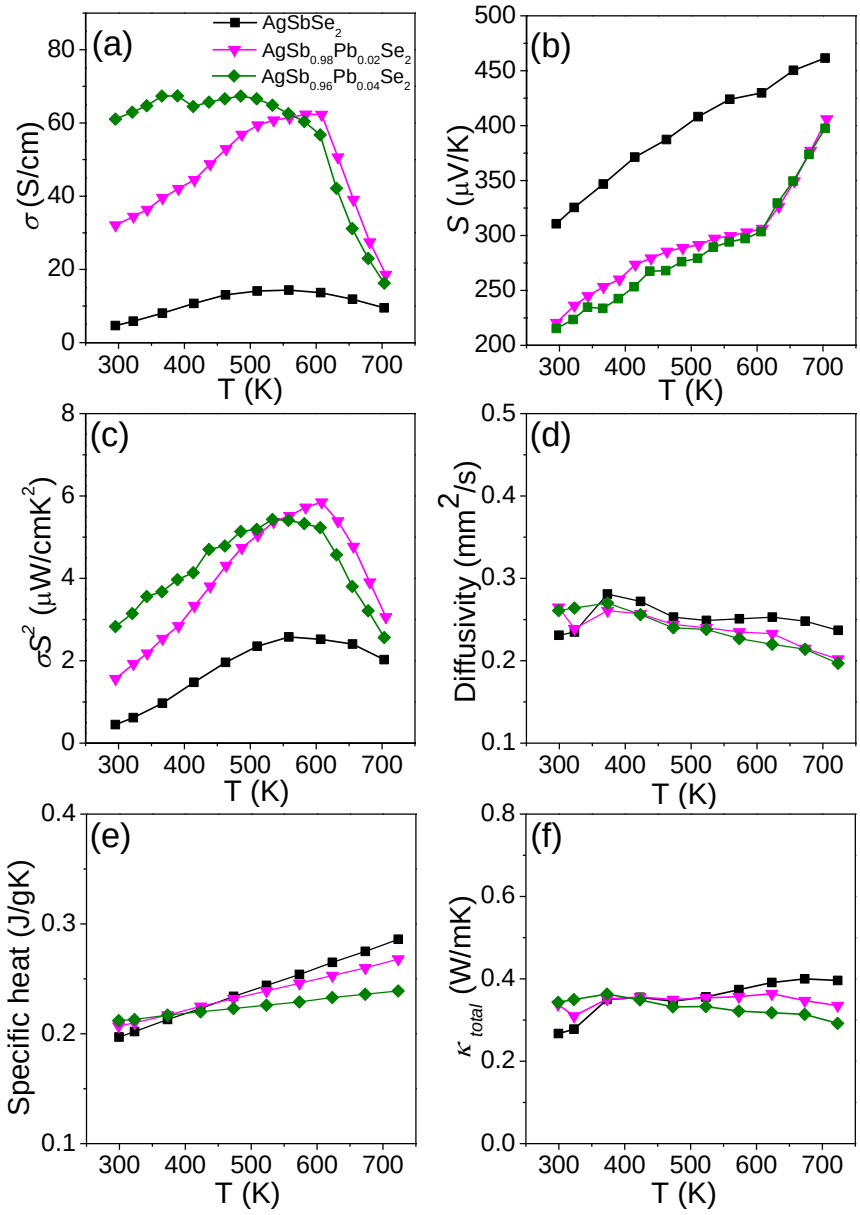

Figure 3.4 Temperature dependent (a) electrical conductivity (σ), (b) Seebeck coefficient (S), (c) power factor (σS^2), (d) thermal diffusivity, (e) specific heat and (f) total thermal conductivity (κ_{total}) of $AgSb_{1-x}Pb_xSe_2$ (x = 0.02, 0.04) and pristine $AgSbSe_2$.

The Hall coefficient, R_H, at room temperature is positive for pristine and Pb-doped samples, which indicates *p*-type conduction in this system. Assuming parabolic bands and a single band conduction process at 300 K, we estimated the carrier concentration, n, from the formula: $n = 1/eR_H$, where e is the electronic charge. The measured carrier concentrations are 5×10^{18} and 3×10^{19} carriers per cm^3 for the pristine $AgSbSe_2$ and $AgSb_{0.96}Pb_{0.04}Se_2$, respectively (Table 3.1). An increase in the hole concentration in Pb-doped samples indicates that the Pb^{2+} is doped on the Sb^{3+} cation

sublattice and, from simple valence counting, contributes one *p*-type carrier. The room-temperature hole mobility, defined as $\mu = \sigma/ne$, for pristine $AgSbSe_2$ and $AgSb_{0.96}Pb_{0.04}Se_2$ samples is ~7 and ~13 $cm^2 V^{-1} s^{-1}$, respectively (Table 3.1). A low hole mobility indicates the presence of heavy holes, resulting from the flat valence band maximum of $AgSbSe_2$. [12]

Table 3.1 Carrier concentration (n), electrical conductivity (σ) and carrier mobility (μ) of pristine $AgSbSe_2$, selected Pb and Bi-doped $AgSbSe_2$ samples at room temperature.

Sample	n (cm^{-3})	σ (S cm^{-1})	μ ($cm^2 V^{-1} s^{-1}$)
$AgSbSe_2$	5×10^{18}	5	7
$AgSb_{0.98}Pb_{0.02}Se_2$	3×10^{19}	61	13
$AgSb_{0.98}Bi_{0.02}Se_2$	1.5×10^{19}	51	22

Figure 3.4(b) shows the temperature dependent Seebeck coefficient (S) of $AgSbSe_2$ and Pb-doped $AgSbSe_2$. A positive value of S confirms the *p*-type conduction in the system. The room temperature S value measured for pristine $AgSbSe_2$ was ~310 $\mu V K^{-1}$, which linearly increases to ~461 $\mu V K^{-1}$ at 705 K. The flat valence band maximum and multipeak valence band structure result in a large positive thermopower in this compound.[12] In the case of $AgSb_{0.98}Pb_{0.02}Se_2$ and $AgSb_{0.96}Pb_{0.04}Se_2$ samples, the room temperature S values are ~220 and ~215 $\mu V K^{-1}$, respectively, which increase to ~405 and ~400 $\mu V K^{-1}$, respectively at 705 K. The high S values in this compound may be due to the high density of state effective mass (m^*). Assuming a single parabolic band model with acoustic phonon scattering, we have estimated the m^* according to the following equation (3.1-3.3) using the measured S and Hall carrier concentration (n):[14,16,22]

$$m^* = \frac{h^2}{2k_B T}\left[\frac{n}{4\pi F_{1/2}(\eta)}\right]^{2/3} \tag{3.1}$$

$$S = \frac{k_B}{e}\left(\frac{2F_1(\eta)}{F_0(\eta)} - \eta\right) \tag{3.2}$$

$$F_n(\eta) = \int_0^\infty \frac{x^n}{1 + e^{x-\eta}}\,dx \tag{3.3}$$

where, η is the reduced Fermi energy, $F_n(\eta)$ is the nth order Fermi integral, k_B is the
where, η is the reduced Fermi energy, $F_n(\eta)$ is the nth order Fermi integral, k_B is the

Boltzmann constant, e is the electron charge, *h* is the Planck constant. The reduced Fermi energy was extracted based on fitting the respective Seebeck data.[22,27,28] The calculation gives an m^* of $1.2m_0$ and $1.8m_0$ for pristine $AgSbSe_2$ and $AgSb_{0.98}Pb_{0.02}Se_2$, respectively. Similar m^* values of $1.7\pm0.2m_0$ were obtained by Jovovic and Heremans in the case of $AgSbTe_2$ with a similar *p*-type carrier density, 3×10^{19} carriers per cm^3.[14] Wojciechowski *et al.* also obtained a high m^* of $2.7m_0$ for $AgSbTe_2$ with the carrier density of 5×10^{19} carriers per cm^3.[29] Optimum Pb doping in $AgSbSe_2$ increases the number of *p*-type carriers markedly (Table 3.1). We speculate that at high temperatures, high-density carriers resulted from heavy doping may be redistributed in the multiple degenerate valence bands, thus giving rise to the effective convergence of bands.[8,26] An increase in the population of carriers in the multiple flat valence bands at high temperature produces higher m^*, which in turn results in an increase in *S* above 600 K (Figure 3.4(b)), as *S* is directly related to m^* by equation (3.4).[1–3,8]

$$S = \frac{8\pi^2 k_B^2}{3eh^2} m^* T \left(\frac{\pi}{3n}\right)^{3/2} \quad (3.4)$$

We have already observed that these compounds have a low hole mobility, which is due to the presence of heavy holes (Table 3.1). The probable increase in m^* at high temperatures further decreases the hole mobility, thus resulting in a decrease in σ (Figure 3.3(a)) above 600 K for Pb-doped samples.

Power factor (σS^2) values for $AgSb_{1-x}Pb_xSe_2$ (x = 0.02, 0.04) samples are significantly higher than that of the pristine $AgSbSe_2$ (Figure 3.4(c)). Typically, the room temperature σS^2 value is ~1.6 μW cm^{-1} K^{-2} for the 2 mol% Pb doped sample. This value rises to a maximum of ~5.9 μW cm^{-1} K^{-2} at about 610 K and falls to ~3.1 μW cm^{-1} K^{-2} at 710 K.

The total thermal conductivity, κ_{total}, of the samples was estimated to be in the temperature range of 300-725 K using the formula, $\kappa_{total} = DC_p\rho$, where *D* is the thermal diffusivity (Figure 3.4(d)), C_p is the specific heat (Figure 3.3(e)) and ρ is the density of the sample. At room temperature, a typical κ_{total} value of ~0.35 W m^{-1} K^{-1} was observed for the $AgSb_{0.96}Pb_{0.04}Se_2$ sample, which remains almost the same throughout the 300-725 K range (Figure 3.4(f)). The lattice thermal conductivity, κ_{lat}, was obtained after subtracting the electronic part, κ_{el} from the κtotal and is plotted in Figure 3.4(e). The ele-

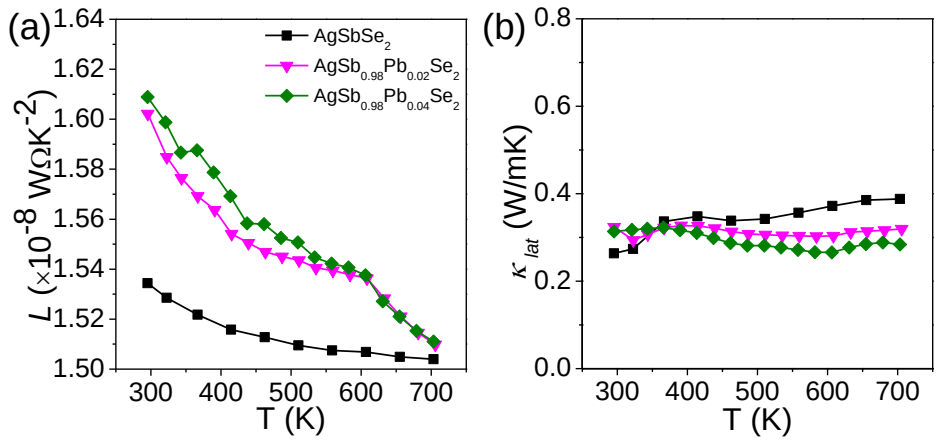

Figure 3.5 (a) Calculated Lorenz numbers for pristine and $AgSb_{1-x}Pb_xSe_2$ (x= 0.02, 0.04) samples. (b) Temperature dependent lattice thermal conductivity (κ_{lat}) of $AgSb_{1-x}Pb_xSe_2$ (x= 0.02, 0.04) and pristine $AgSbSe_2$.

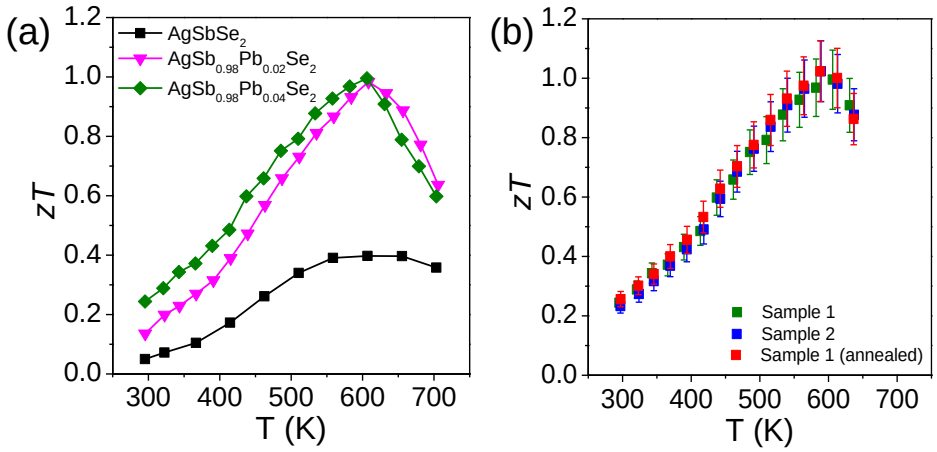

Figure 3.6 (a) Thermoelectric figure of merit (zT) of $AgSb_{1-x}Pb_xSe_2$ (x = 0.02, 0.04) and pristine $AgSbSe_2$. (b) zT (with 10% error bar) obtained on multiple $AgSb_{0.96}Pb_{0.04}Se_2$ samples with same nominal composition obtained from different synthesis. Annealed (673 K for 15 h) samples also show similar zT, which confirms the thermal stability at high temperature.

ctronic thermal conductivities, $\kappa_{el} = L\sigma T$, were extracted based on fitting of the respective Seebeck values which estimate the reduced chemical potential from which the Lorentz number, L, can be obtained (Figure 3.5(a)), as explained in detail previously.[27,28] This assumes a parabolic band model and energy independent scattering time. We measured κ_{lat} values of ~0.36-0.4 W m^{-1} K^{-1} over the 300-700 K temperature range for pristine $AgSbSe_2$, which are indeed similar to the experimentally obtained κ_{lat} values of $AgSbSe_2$ in the 10-300 K temperature range.[10] $AgSb_{0.96}Pb_{0.04}Se_2$ sample exhibits a κ_{lat} value of ~0.3 W m^{-1} K^{-1} at room temperature, which remains almost the same in the 300-725 K range (Figure 3.5(b)). The extremely low κ_{lat} value observed in

this system is due to two possible reasons: (a) the high degree of anharmonicity of the Sb-Se bonds that gives rise to strong phonon-phonon interactions and (b) effective phonon scattering by the highly disordered Ag/Sb lattice.

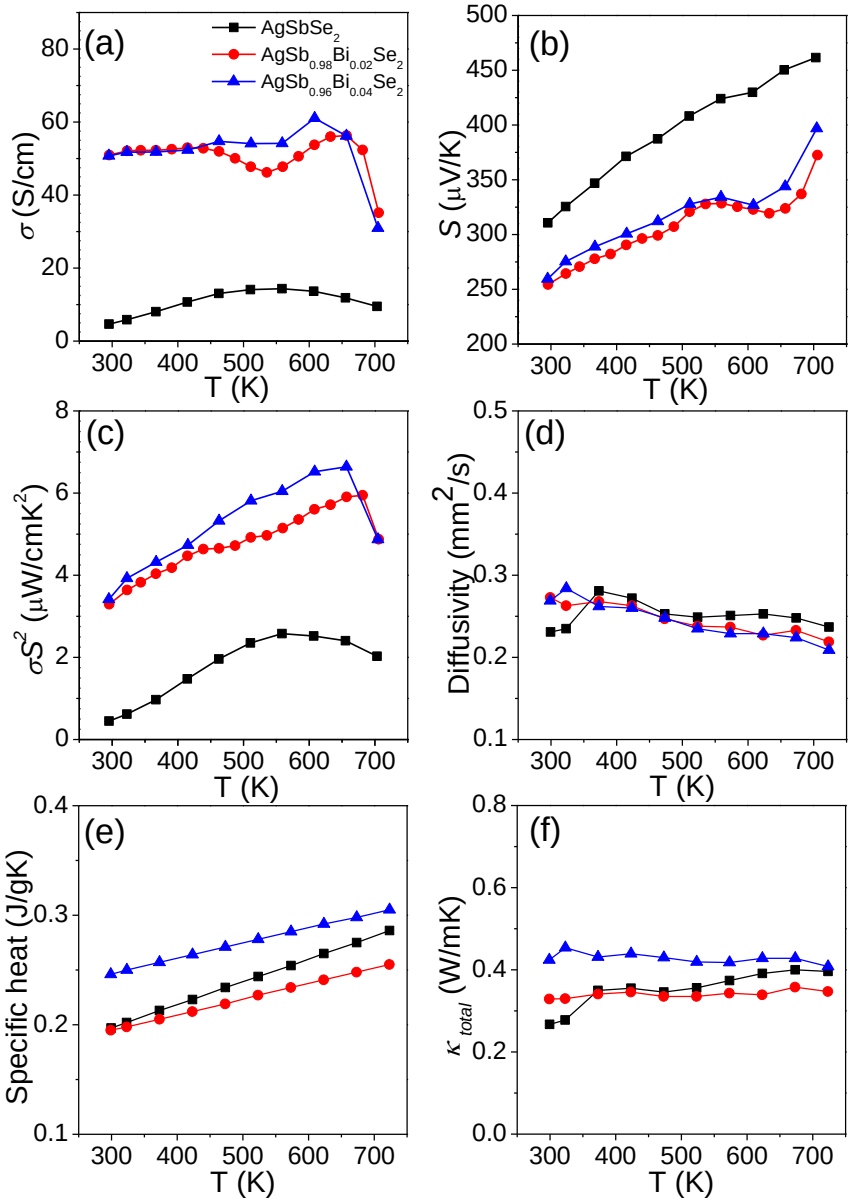

Figure 3.7 Temperature dependent (a) electrical conductivity (σ), (b) Seebeck coefficient (S), (c) power factor (σS^2), (d) thermal diffusivity, (e) specific heat and (f) total thermal conductivity (κ_{total}) of $AgSb_{1-x}Bi_xSe_2$ (x = 0.02, 0.04) and pristine $AgSbSe_2$.

Figure 3.6 presents the zT values of pristine $AgSbSe_2$ and samples doped with 2-4 mol% Pb. The maximum zT achieved is ~1 at 610 K for both 2% and 4% Pb-doped samples, which is 150 % higher compared to pristine $AgSbSe_2$. We have checked the

reproducibility and thermal stability of through different sample *zT* vs T measurement (see Figure 3.6(b)).

We have also measured the electronic and thermal transport properties of $AgSb_{1-x}Bi_xSe_2$ (x = 0.02, 0.04) samples in the 300-725 K range (Figure 3.7). Typically, the room temperature σ for the $AgSb_{0.98}Bi_{0.02}Se_2$ sample was 51 S cm^{-1} which remains almost the same up to 655 K, then decreases to ~35 S cm^{-1} at 705 K (Figure 3.7(a)). The Hall coefficient, R_H, is positive for Bi-doped samples, indicating they are *p*-type carriers. The carrier concentration estimated from R_H is 1.5×10^{19} carriers/cm^3 for $AgSb_{0.98}Bi_{0.02}Se_2$ (Table 3.1). The sign of *S* is also positive, which confirms the hole conduction (Figure 3.7(b)). Typically, the room temperature *S* for the $AgSb_{0.98}Bi_{0.02}Se_2$ sample was ~254 μVK^{-1}, which reaches ~373 μV K^{-1} at 705 K. The density of state effective mass (m^*) of the $AgSb_{0.98}Bi_{0.02}Se_2$ sample was calculated to be $1.6m_0$ using equation (3.1-3.3). The highest room temperature σS^2 value of ~3.4 μW cm^{-1} K^{-2} was achieved for the 4% Bi-doped sample, which rises to ~6.7 μW cm^{-1} K^{-2} at 660 K and then decreases to ~4.9 μW cm^{-1} K^{-2} at 705 K (Figure 3.7(c)). Power factors of $AgSb_{1-x}Bi_xSe_2$ samples are generally superior compared to $AgSb_{1-x}Pb_xSe_2$ samples. We have also observed ultra-low κ_{total} and κ_{lat} values in the case of $AgSb_{1-x}Bi_xSe_2$ samples, similar to $AgSb_{1-x}Pb_xSe_2$ (Figure 3.7(f) and Figure 3.8(b)). A typical room temperature value of κ_{total} ~0.32 W m^{-1} K^{-1} was observed for the $AgSb_{0.98}Bi_{0.02}Se_2$ sample, which remains almost the same throughout the 300-725 K range (Figure 3.7(f)).

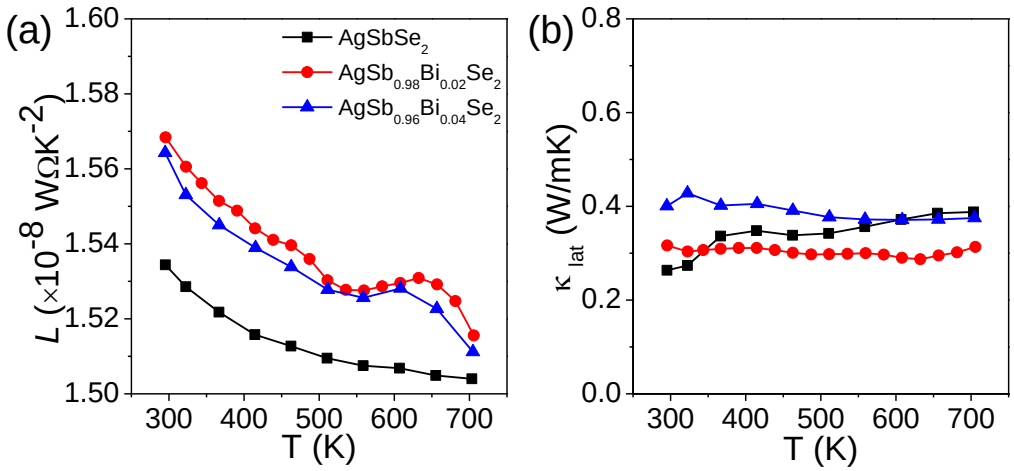

Figure 3.8 (a) Calculated Lorenz numbers for pristine and $AgSb_{1-x}Bi_xSe_2$ (x= 0.02, 0.04) samples. (b) Temperature dependent lattice thermal conductivity (κ_{lat}) of $AgSb_{1-x}Bi_xSe_2$ (x= 0.02, 0.04) and pristine $AgSbSe_2$.

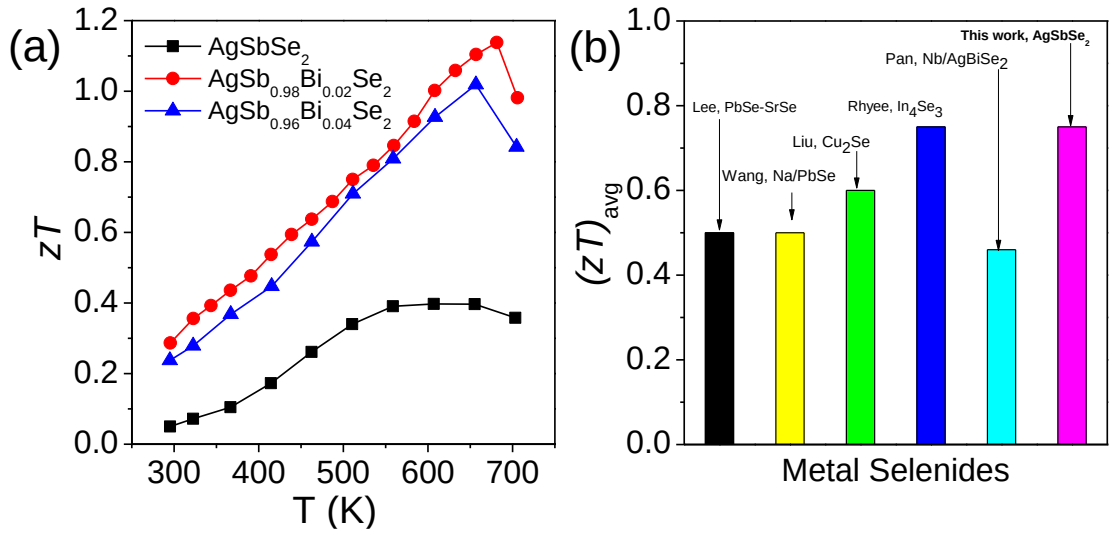

Figure 3.9 (a) Thermoelectric figure of merit (*zT*) of $AgSb_{1-x}Bi_xSe_2$ (x = 0.02, 0.04) and pristine $AgSbSe_2$. (b) Average *zT* of the present $AgSb_{0.98}Bi_{0.02}Se_2$ and leading polycrystalline metal selenides reported in literature, considering a hot side temperature of 690 K and cold side temperature of 350 K.

From the electrical and thermal transport measurements, we have estimated the *zT* of $AgSb_{1-x}Bi_xSe_2$ (x = 0.02, 0.04) samples in 300-710 K range (Figure 3.9(a)). The maximum *zT* achieved is ~1.15 at 685 K for the 2 mol% Bi-doped sample, which is 190 % higher compared to the pristine $AgSbSe_2$ sample. With this advance in the maximum *zT* value of this Te-free material, we can expect an average *zT* value of ~0.75 (considering a hot side temperature of 690 K and cold side temperature of 350 K), which is comparable or higher than leading metal selenide based thermoelectric systems reported recently in the literature (Figure 3.9(b)).[20,30–33]

To validate our cation doping concept on $AgSbSe_2$, we have further studied the effect of Cd doping on Sb^{3+} site of $AgSbSe_2$. We found a significant improvement in the electronic transport in $AgSb_{1-x}Cd_xSe_2$ (x = 0.02-0.06) compared to that of pristine $AgSbSe_2$, resulting in a high thermoelectric performance. We have chosen Cd^{2+} as an effective hole donor because the crystal ionic radius of Sb^{3+} (90 pm) matches closer with that of Cd^{2+} (109 pm) as compared to that of Pb^{2+} (137 pm) dopant.[34] We show that the 2-4 mol% of Cd acts as an effective *p*-type dopant and substantially increases the electrical conductivity in $AgSbSe_2$.

Powder X-ray diffraction (XRD) patterns of the $AgSb_{1-x}Cd_xSe_2$ (x = 0-0.04) samples are presented in Figure 3.10(a). XRD peaks of $AgSb_{1-x}Cd_xSe_2$ (x = 0-0.04) samples could be indexed based on the pure cubic $AgSbSe_2$ structure (space group,

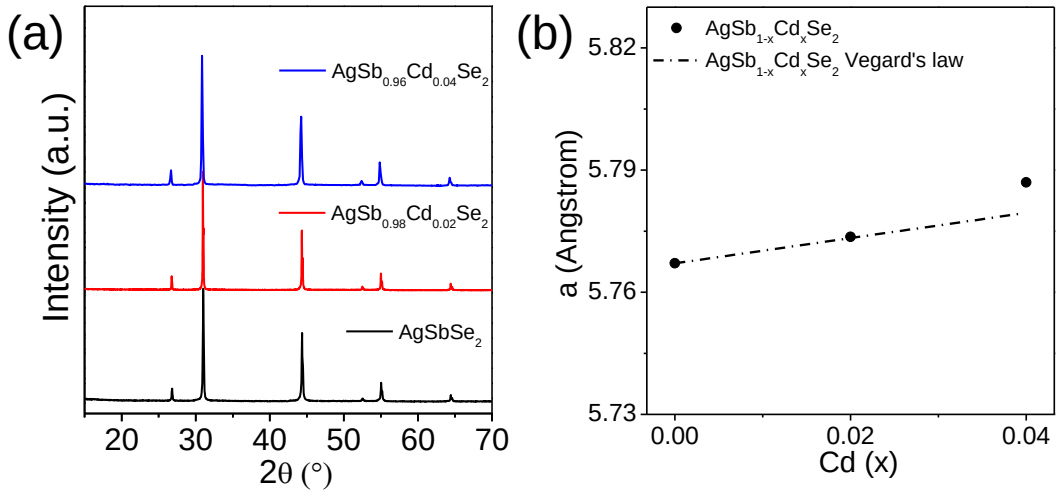

Figure 3.10 (a) Powder XRD patterns of $AgSb_{1-x}Cd_xSe_2$ (x = 0-0.04). (b) Lattice parameter (a) *vs.* Cd concentrations in $AgSb_{1-x}Cd_xSe_2$ (x = 0-0.04) and dotted black line indicates the Vegard's law for solid solution.

Fm$\bar{3}$*m*). Systematic peak shift towards lower angle and linear expansion in the lattice parameter with increasing Cd concentration indicate the Vegard's law for the solid solution in $AgSb_{1-x}Cd_xSe_2$ (x = 0-0.04) samples (Figure 3.10(b)). This gradual expansion of lattice parameter indicates an isomorphic substitution of Cd^{2+} ion in Sb^{3+} position in $AgSbSe_2$.

The temperature dependent transport properties of pristine $AgSbSe_2$ and $AgSb_{1-x}Cd_xSe_2$ (x = 0.02-0.06) samples over 290-640 K range are presented in Figure 3.11. Figure 3.11(a) shows the temperature dependent σ of pristine $AgSbSe_2$ and $AgSb_{1-x}Cd_xSe_2$ (x = 0.02-0.06) samples. Room temperature σ value increases with increasing Cd doping concentration from 0 to 4 mol% and then the σ falls with a further increase in Cd concentration to 6 mol%. Typically, the room temperature σ for $AgSb_{0.98}Cd_{0.02}Se_2$ sample was ~33 Scm^{-1}, which slightly increases to ~54 S cm^{-1} at 640 K. The additional solid solution mass fluctuations and point defects scatter the hole carriers significantly in the case of 6 mol % Cd-doped $AgSbSe_2$ sample, thereby decreasing the σ value compared to that of 2-4 mol% Cd-doped samples. Room temperature Hall measurement indicates positive sign of Hall coefficients, R_H, for Cd-doped samples, which indicate *p*-type conduction. The measured carrier concentrations value for $AgSb_{0.98}Cd_{0.02}Se_2$ is 3.8 × 10^{19} carriers/ cm^3. An increase in the hole concentration in Cd-doped sample indicates that the Cd^{2+} dopes on the Sb^{3+} cation sublattice and, from the simple valence *e* counting

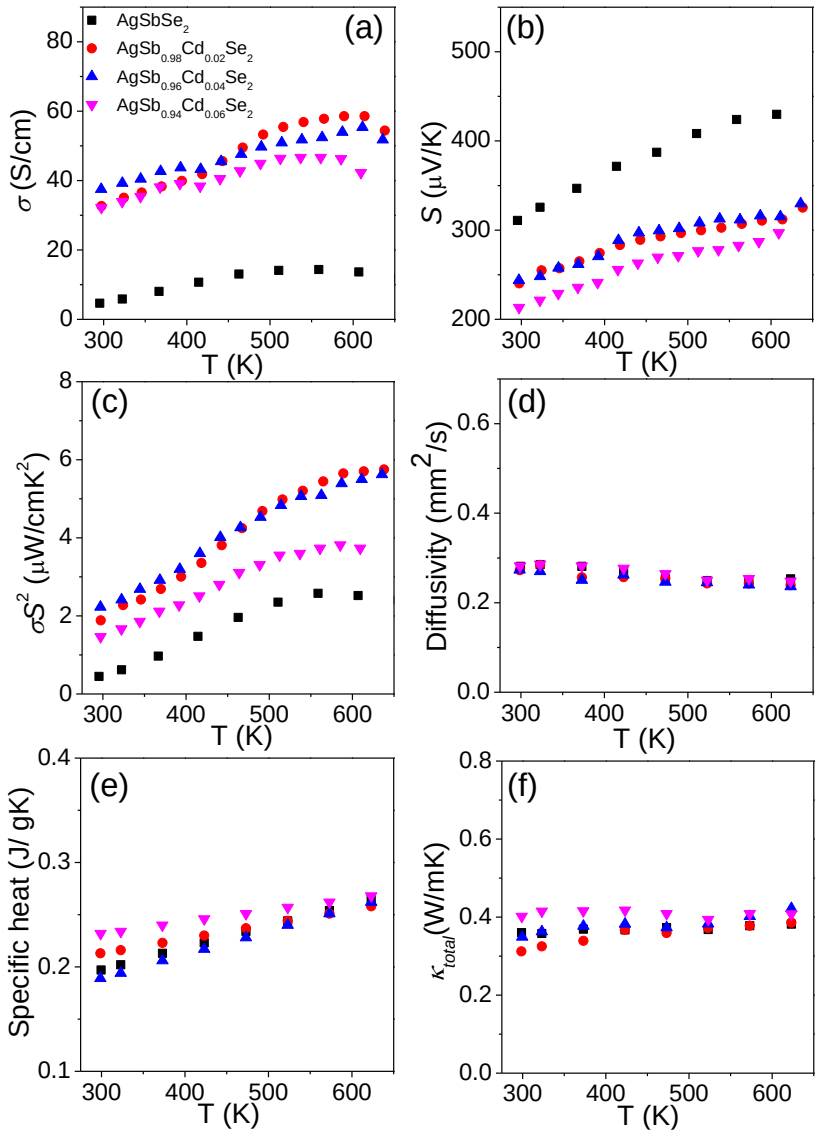

Figure 3.11 Temperature dependent (a) electrical conductivity (σ), (b) Seebeck coefficient (S), (c) power factor (σS^2), (d) thermal diffusivity, (e) specific heat and (f) total thermal conductivity (κ_{total}) of $AgSb_{1-x}Cd_xSe_2$ (x = 0-0.06).

contributes one extra *p*-type carrier. The room temperature hole mobility, $\mu = \sigma/ne$, for $AgSb_{0.98}Cd_{0.02}Se_2$ samples is ~6 $cm^2 V^{-1} s^{-1}$. The relatively low hole mobility than pristine sample indicates the presence of heavy holes, resulting from the flat valence band of $AgSbSe_2$.[12] Similar result was also observed for Pb^{2+} doped $AgSbSe_2$.

All the $AgSb_{1-x}Cd_xSe_2$ (x = 0.02-0.06) samples shows positive sign of *S*, confirms the *p*-type conduction in system (Figure 3.11(b)). In case of $AgSb_{0.98}Cd_{0.02}Se_2$, the room temperature *S* value is ~242 $\mu V K^{-1}$, which increases to ~325 $\mu V K^{-1}$ at 640 K. The density of state effective mass (m^*) of the $AgSb_{0.98}Cd_{0.02}Se_2$ sample was calculated to be

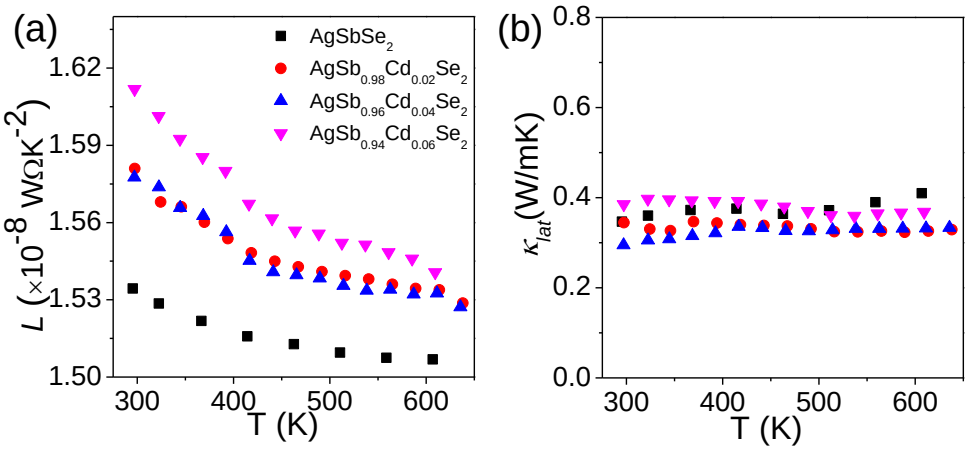

Figure 3.12 Temperature dependent (a) calculated Lorenz numbers and (b) lattice thermal conductivity (κ_{lat}) of $AgSb_{1-x}Cd_xSe_2$ (x = 0-0.06).

2.3m_0 using equation (3.1-3.3). High density of states effective mass (m^*) is responsible for the high thermopower values in $AgSb_{1-x}Cd_xSe_2$ (x = 0.02-0.06). Similar m^* values (1.2-1.8m_0) have also been observed in Pb doped $AgSbSe_2$.

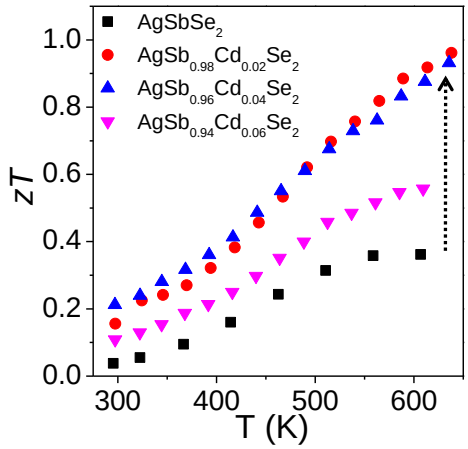

Figure 3.13 Temperature-dependent thermoelectric figure of merit (zT) of $AgSb_{1-x}Cd_xSe_2$ (x = 0-0.06) samples. Dotted arrow indicates the significant enchantment in zT in Cd-doped samples compared to pristine $AgSbSe_2$.

Improved electronic transport in Cd-doped samples result in superior σS^2 value in the measured temperature range (290-640 K). Typically, at room temperature $AgSb_{0.98}Cd_{0.02}Se_2$ sample shows a σS^2 value ~1.9 μW cm^{-1} K^{-2}, which rises to a maximum of 5.7 μW cm^{-1} K^{-2} at 640 K (Figure 3.11(c)). Similar high values of σS^2 have also been measured in Pb and Bi-doped $AgSbSe_2$. Enhanced electrical transport in $AgSb_{1-x}Cd_xSe_2$ samples resulted in significantly higher σS^2 compared to that of pristine $AgSbSe_2$.

Cd-doped $AgSbSe_2$ also exhibits ultra-low thermal conductivity like Pb and Bi-doped samples (Figure 3.11(f)). At room temperature, $AgSb_{0.98}Cd_{0.02}Se_2$ sample shows a κ_{total} and κ_{lat} value of ~0.36 W m^{-1} K^{-1} and 0.34 W m^{-1} K^{-1} respectively, which remains almost same throughout 300-650 K range (Figure 3.11(f) and 3.12(b)).

Figure 3.13 presents the *zT* values $AgSb_{1-x}Cd_xSe_2$ (x = 0-0.06). The highest *zT* value of ~1 at 640 K was achieved for $AgSb_{0.98}Cd_{0.02}Se_2$. The measured *zT* value of $AgSb_{1-x}Cd_xSe_2$ is indeed comparable to Pb doped $AgSbSe_2$ system. Thus, the Cd doping in $AgSbSe_2$ validate our result on the thermoelectric property of Pb doped $AgSbSe_2$.

3.4 Conclusions

High quality crystalline ingots of *p*-type $AgSbSe_2$, $AgSb_{1-x}Pb_xSe_2$ (x = 0.02, 0.04), $AgSb_{1-x}Bi_xSe_2$ (x = 0.02, 0.04) and $AgSb_{1-x}Cd_xSe_2$ (x = 0-0.06) were grown by simple melting of elemental metal and chalcogen followed by quenching to room temperature. The hole concentrations in $AgSbSe_2$ could be optimized by doping of a small amount of Pb, Bi, and Cd to achieve superior electrical conductivity compared to the pristine sample. The broad valence band maximum and multi-peak valence band structure resulted in a large thermopower in $AgSbSe_2$. A high degree of anharmonicity in the Sb-Se bond and effective phonon scattering by the highly disordered Ag/Sb lattice gives rise to an ultra-low κ_{lat}. Peak *zT* values of ~1 and ~1.15 were achieved in $AgSb_{0.96}Pb_{0.04}Se_2$ and $AgSb_{0.98}Bi_{0.02}Se_2$ samples, which are 150% and 190% higher than that of pristine $AgSbSe_2$, respectively. Furthermore, a peak *zT* value of ~1 was achieved in $AgSb_{0.98}Cd_{0.02}Se_2$, which indeed validate our result on the thermoelectric property of cation doped $AgSbSe_2$. With this excellent thermoelectric performance, *p*-type $AgSbSe_2$, consisting of earth abundant Se, offers a promise to replace traditional metal tellurides constituting expensive and scarce Te. The best $(zT)_{avg}$ found for our system is also in line with other leading metal selenide based thermoelectric materials in the mid-temperature range (350-700 K).

References

[1] G. Tan, L.-D. Zhao, M. G. Kanatzidis, *Chem. Rev.* **2016**, *116*, 12123–12149.

[2] J. R. Sootsman, D. Y. Chung, M. G. Kanatzidis, *Angew. Chemie - Int. Ed.* **2009**, *48*, 8616–8639.

[3] G. J. Snyder, E. S. Toberer, *Nat. Mater.* **2008**, *7*, 105–114.

[4] W. G. Zeier, A. Zevalkink, Z. M. Gibbs, G. Hautier, M. G. Kanatzidis, G. J. Snyder, *Angew. Chemie - Int. Ed.* **2016**, *55*, 6826–6841.

[5] L.-D. Zhao, V. P. Dravid, M. G. Kanatzidis, *Energy Environ. Sci.* **2014**, *7*, 251–268.

[6] G. Chen, M. S. Dresselhaus, G. Dresselhaus, J.-P. Fleurial, T. Caillat, *Int. Mater. Rev.* **2003**, *48*, 45–66.

[7] M. Zebarjadi, K. Esfarjani, M. S. Dresselhaus, Z. F. Ren, G. Chen, *Energy Environ. Sci.* **2012**, *5*, 5147–5162.

[8] Y. Pei, H. Wang, G. J. Snyder, *Adv. Mater.* **2012**, *24*, 6125–6135.

[9] D. T. Morelli, V. Jovovic, J. P. Heremans, *Phys. Rev. Lett.* **2008**, *101*, 16–19.

[10] M. D. Nielsen, V. Ozolins, J. P. Heremans, *Energy Environ. Sci.* **2013**, *6*, 570–578.

[11] F. D. Rosi, E. F. Hockings, N. E. Lindenblad, *RCA Rev.* **1961**, *22*, 82–121.

[12] K. Hoang, S. D. Mahanti, J. R. Salvador, M. G. Kanatzidis, *Phys. Rev. Lett.* **2007**, *99*, 156403.

[13] V. Jovovic, J. P. Heremans, *J. Electron. Mater.* **2009**, *38*, 1504–1509.

[14] V. Jovovic, J. P. Heremans, *Phys. Rev. B* **2008**, *77*, 245204.

[15] B. Du, H. Li, J. Xu, X. Tang, C. Uher, *Chem. Mater.* **2010**, *22*, 5521–5527.

[16] K. T. Wojciechowski, M. Schmidt, *Phys. Rev. B - Condens. Matter Mater. Phys.* **2009**, *79*, 184202.

[17] S. H. Yang, T. J. Zhu, T. Sun, J. He, S. N. Zhang, X. B. Zhao, *Nanotechnology* **2008**, *19*, 245707.

[18] K. F. Hsu, S. Loo, F. Guo, W. Chen, J. S. Dyck, *Science* **2004**, *303*, 818–821.

[19] Z. Hu, S. Gao, *Chem. Geol.* **2008**, *253*, 205–221.

[20] L. Pan, D. Bérardan, N. Dragoe, *J. Am. Chem. Soc.* **2013**, *135*, 4914–4917.

[21] C. Xiao, X. Qin, J. Zhang, R. An, J. Xu, K. Li, B. Cao, J. Yang, B. Ye, Y. Xie, *J. Am. Chem. Soc.* **2012**, *134*, 18460–18466.

[22] Y.-L. Pei, H. Wu, J. Sui, J. Li, D. Berardan, C. Barreteau, L. Pan, N. Dragoe, W.-S. Liu, J. He, et al., *Energy Environ. Sci.* **2013**, *6*, 1750.

[23] D. Wu, Y. Pei, Z. Wang, H. Wu, L. Huang, L. D. Zhao, J. He, *Adv. Funct. Mater.* **2014**, *24*, 7763–7771.

[24] S. Geller, J. H. Wernick, *Acta Crystallogr.* **1959**, *12*, 46–54.

[25] K. Wojciechowski, M. Schmidt, J. Tobola, M. Koza, A. Olech, R. Zybala, *J. Electron. Mater.* **2010**, *39*, 2053–2058.

[26] Y. Pei, X. Shi, A. LaLonde, H. Wang, L. Chen, G. J. Snyder, *Nature* **2011**, *473*, 66–69.

[27] L. D. Zhao, S. H. Lo, J. He, H. Li, K. Biswas, J. Androulakis, C. I. Wu, T. P. Hogan, D. Y. Chung, V. P. Dravid, et al., *J. Am. Chem. Soc.* **2011**, *133*, 20476–20487.

[28] J. Androulakis, I. Todorov, J. He, D. Y. Chung, V. Dravid, M. Kanatzidis, *J. Am. Chem. Soc.* **2011**, *133*, 10920–10927.

[29] K. Wojciechowski, J. Tobola, M. Schmidt, R. Zybala, *J. Phys. Chem. Solids* **2008**, *69*, 2748–2755.

[30] Y. Lee, S. Lo, J. Androulakis, C. Wu, L. Zhao, D. Chung, *J. Am. Chem. Soc.* **2013**, *135*, 5152–5160.

[31] H. Wang, Y. Pei, A. D. Lalonde, G. J. Snyder, *Adv. Mater.* **2011**, *23*, 1366–1370.

[32] H. Liu, X. Shi, F. Xu, L. Zhang, W. Zhang, L. Chen, Q. Li, C. Uher, T. Day, G. J. Snyder, *Nat. Mater.* **2012**, *11*, 422–425.

[33] J.-S. Rhyee, K. H. Lee, S. M. Lee, E. Cho, S. Il Kim, E. Lee, Y. S. Kwon, J. H. Shim, G. Kotliar, *Nature* **2009**, *459*, 965–968.

[34] R. D. Shannon, *Acta Crystallogr. Sect. A* **1976**, *32*, 751–767.

Chapter 4

Effect of Sb deficiency on the thermoelectric properties of *p*-type $AgSbSe_2$ *

*Publication based on this work: *J. Mater. Chem. C* **2015,** *3*, 10415.

CHAPTER 4

Effect of Sb deficiency on the thermoelectric properties of *p*-type $AgSbSe_2$

Summary. *Previously thermoelectric performance of $AgSbSe_2$ has been improved by doping of monovalent (M^+) and divalent (M^{2+}) cations in the Sb sublattice. Here, we present a significant enhancement of the thermoelectric performance of p-type nonstoichiometric $AgSbSe_2$ through Sb deficiencies. Sb deficiencies markedly increase the carrier concentration in $AgSbSe_2$ without the addition of any foreign dopant, which in turn enhances electrical conductivity in the 300-610 K temperature range. Enhancement in the electrical transport results in a remarkable improvement in the power factor (σS^2) values up to ~6.94 $\mu W\ cm^{-1}\ K^{-2}$ at 610 K in $AgSb_{1-x}Se_2$. Notably, we have achieved a nearly constant σS^2 value of ~6 $\mu W\ cm^{-1}\ K^{-2}$ in the 400-610 K temperature range in Sb deficient samples. Additionally, $AgSbSe_2$ exhibits ultra-low thermal conductivity due to phonon scattering because of bond anharmonicity and a disordered cation sublattice. With superior electronic transport and ultra-low thermal conductivity, a peak zT value of ~1 at 610 K was achieved for the $AgSb_{0.9925}Se_2$ and $AgSb_{0.99}Se_2$ samples. A maximum thermoelectric conversion efficiency (η_{max}) of ~8% was calculated by considering a virtual thermoelectric module consisting of the present p-type $AgSb_{1-x}Se_2$ and n-type $AgBiSe_{2-x}Cl_x$, by maintaining a temperature difference of ΔT = 400 K.*

4.1 Introduction

Although $AgSbSe_2$ has favorable valence band structure, but electrical conductivity of the pristine sample is low, which results in a poor thermoelectric performance.[1–3] Density functional theory based calculations of electronic structure of $AgSbSe_2$ by Mahanti and coworkers indicated that the strongly hybridized state of Sb *p* and that of Se show significant contribution near the Fermi level in the density of states (DOS) of $AgSbSe_2$.[2] Thus, in order to improve the electrical conductivity of $AgSbSe_2$, either a divalent (Pb^{2+}, Cd^{2+}, Zn^{2+}, Mg^{2+}, Ba^{2+}, Sn^{2+}) or a monovalent cation (Na^{+}) have been earlier doped into the Sb^{3+} site.[3–8] Divalent (M^{2+}) or monovalent (M^{+}) cation dope the Sb^{3+} sublattice, and from simple valence counting, contribute one or two extra *p*-type carrier(s), respectively (Table 1), thus enhances the carrier concentration and electrical conductivity of $AgSbSe_2$.

The rational introduction of appropriate vacancies in material has been realized to be an effective strategy to tune the electron and phonon transport. This strategy has been successfully applied to tune the thermoelectric performance of BiCuSeO, InTe, Cu_2Se, Cu_2S.[9–13] In contrast to M^{2+}/ M^{+} doping in $AgSbSe_2$, if one can create Sb deficiency (*i.e.* $AgSb_{1-x}Se_2$), then three extra *p*-type carriers can be generated per Sb deficiency (Table 4.1), which will possibly enhance the electrical conductivity without the addition of any foreign dopant. Although the effect of cation doping on the thermoelectric properties of $AgSbSe_2$ has been studied, an investigation into the effect of nonstoichiometry or cation deficiency has not been carried out to date.

Table 4.1 From simple valence calculation, number(s) of hole(s) expected for per cation substitution or deficiency in the Sb^{3+} position in $AgSbSe_2$

Sample	Number of expected holes per substitution in the Sb position
$AgSb_{1-x}M_xSe_2$ (M^{2+} = divalent cation; x = mol%)	1
$AgSb_{1-x}M_xSe_2$ (M^{2+} = monovalent cation; x = mol%)	2
$AgSb_{1-x}Se_2$ (Sb^{3+} trivalent cation deficiency; x = mol%)	3

In this chapter, we present the effect of Sb deficiency [$AgSb_{1-x}Se_2$; x = 0-3 mol%] on the thermoelectric properties of *p*-type $AgSbSe_2$. We have shown that the hole transport in $AgSbSe_2$ can be significantly tuned by controlling the Sb stoichiometry without the addition of any foreign dopant. The *p* orbital of Sb shows a significant contribution near the Fermi level in the DOS of $AgSbSe_2$,[2] and thus creation of Sb deficiencies can result in the tuning of the Fermi level. Our experimental results demonstrate that a small amount of Sb deficiencies markedly increases the hole concentrations, which indeed enhances the electrical conductivity up to ~90 S cm^{-1} from 4.5 S cm^{-1} (for the pristine sample) at room temperature. Although there is a slight decrease in the Seebeck coefficient for Sb deficient samples, the large increase in σ results in an improved power factor ($S^2\sigma$) over a wide temperature range (300-620 K). With this enhanced power factor and ultra-low thermal conductivity (~0.4 W m^{-1} K^{-1}), a maximum zT of ~1 at 610 K has been achieved in the $AgSb_{0.9925}Se_2$ and $AgSb_{0.9925}Se_2$ samples. A maximum theoretical thermoelectric efficiency (η_{max}) of ~8% was calculated by considering a virtual thermoelectric module consisting of the present *p*-type $AgSb_{1-x}Se_2$ and *n*-type $AgBiSe_2$,[14] by maintaining the temperature difference of ΔT = 400 K.

4.2 Methods

4.2.1 Synthesis

Elements silver (Ag, 99.9999%, metal basis), elemental antimony (Sb, 99.9999%, metal basis), and elemental selenium (Se, 99.999%, metal basis) were purchased from Alfa Aesar and used for synthesis without further purification.

Ingots (~7 g) of $AgSb_{1-x}Se_2$ (x = 0-3 mol%) were synthesized by mixing appropriate ratios of high-purity Ag, Sb, and Se in quartz tubes. The tubes were flame sealed under a high vacuum (~10^{-5} Torr) and slowly heated up to 673 K for 12 h, then heated up to 1123 K in 4 h, soaked for 10 h, and subsequently, air quenched to room temperature. The air quenched samples were then annealed at 600 K for 10 h.

4.2.2 Characterizations

Powder XRD for all the samples was recorded using Cu Kα (λ = 1.5406 Å) radiation on a Bruker D8 diffractometer. FESEM-BSE imaging experiment was performed using

NOVA NANO SEM 600 (FEI, Germany). To probe the optical energy gap of these compounds, optical diffuse reflectance measurements were performed on finely ground powders using a Perkin Elmer Lambda 900, UV-vis/NIR spectrometer at room temperature. Room temperature carrier concentration has been derived from Hall coefficient measurements using a PPMS. Detailed discussions on all the characterizations have been given in the introduction part of the thesis (page 31).

4.2.3 Thermoelectric measurements

Seebeck coefficient and electrical conductivity were measured under helium atmosphere by ULVAC-RIKO ZEM-3 instrument from room temperature to ~623 K. Thermal diffusivity, *D*, was directly measured by laser flash diffusivity method in a Netzsch LFA-457 under N_2 atmosphere from room temperature to 623 K. The total thermal conductivity, κ_{total}, was calculated using the formula, $\kappa_{total} = DC_p\rho$, where D is thermal diffusivity, C_p is specific heat and ρ is the density of the sample. The longer direction coincides with the direction in which the thermal conductivity was measured. Detailed discussions on thermoelectric measurements have been given in the introduction part of the thesis (page 41).

4.2.4 Thermoelectric efficiency (η) calculations

The overall thermoelectric figure of merit of a *p* and *n*- type pair [$(ZT)_m$] of thermoelectric materials was theoretically calculated from the equation (1)[15]

$$(ZT)_m = \int_{T_C}^{T_H} \frac{(S_p - S_n)^2 \,.\, T}{[\sqrt{\rho_p . \kappa_p} + \sqrt{\rho_n . \kappa_n}]^2 .\ \Delta T} dT \qquad (4.1)$$

where, (S_p and S_n), (ρ_p and ρ_n) and (κ_p and κ_n) represent Seebeck coefficient, electrical resistivity and total thermal conductivity of *p*-and *n*-type materials, respectively. The theoretical conversion efficiency of the aforementioned pair of materials was calculated from the equation (2)[15]

$$\eta = \frac{\Delta T}{T_H} \frac{\sqrt{1 + (ZT)_{m,avg}} - 1}{\sqrt{1 + (ZT)_{m,avg}} + \frac{T_C}{T_H}} \qquad (4.2)$$

where $\Delta T/T_H$ refers the Carnot efficiency, T_H and T_C are the hot and cold side temperature and $(ZT)_{m,avg}$ is the average figure-of-merit of a pair of thermoelectric legs.

4.3 Results and discussion

4.3.1 Structural and optical characterizations

Powder X-ray diffraction (XRD) patterns of pristine $AgSbSe_2$ and non-stoichiometric [$AgSb_{1-x}Se_2$ (x = 0.5-3 mol%)] samples have been presented in Figure 4.1(a). In all the cases, PXRD patterns could be index based on cubic $AgSbSe_2$ (space group $Fm\bar{3}m$). No impurity peaks were observed within the detection limit of the PXRD, which indicates that Sb deficiency in the sample does not create any new second phase. For further confirmation, we have performed field emission scanning electron microscopy (FESEM) via back-scattered electron (BSE) imaging of the $AgSb_{0.9925}Se_2$ sample (see Figure 4.1(b)). The BSE image is uniform and shows no contrast difference, which confirms the absence of second phase segregation.

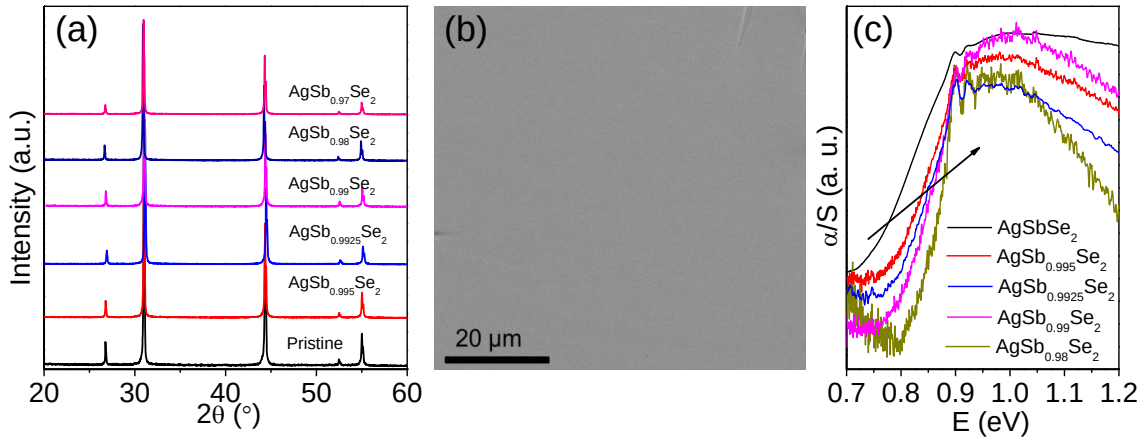

Figure 4.1 (a) Powder XRD patterns (b) FESEM-backscattered electron (BSE) image of $AgSb_{0.9925}Se_2$ sample and (c) optical absorption spectra of $AgSb_{1-x}Se_2$ (x = 0–2 mol%) at room temperature.

The optical absorption spectra of the selected samples are shown in Figure 4.1(c). Measured band gaps for all the Sb deficient samples are slightly higher than that of pristine $AgSbSe_2$. We observed an increase in the *p*-type carrier concentration with increasing the concentration of Sb deficiencies (see the later part of the chapter), which indicates the shift of the Fermi level to deeper inside the valence band. Moving of the Fermi level inside the valence band probably gives rise to a slight increase in the band gap for Sb deficient samples.

4.3.2 Thermoelectric properties

Temperature dependent electrical conductivity (σ) of pristine and Sb deficient samples are presented in Figure 4.2(a). We have observed a large increase in the σ value in all the Sb deficient samples compared to that of pristine $AgSbSe_2$. σ shows a weak temperature dependence with an increase of temperature. The highest room temperature σ is to be ~86 S cm^{-1} for $AgSb_{0.9925}Se_2$, which reaches a value of ~70 S cm^{-1} at 610 K. The measured carrier concentration (n_h) and carrier mobility (μ) for selected samples are presented in Table 4.2. Sb deficient samples show significantly higher hole concentrations (n_h) compared to that of the pristine sample.

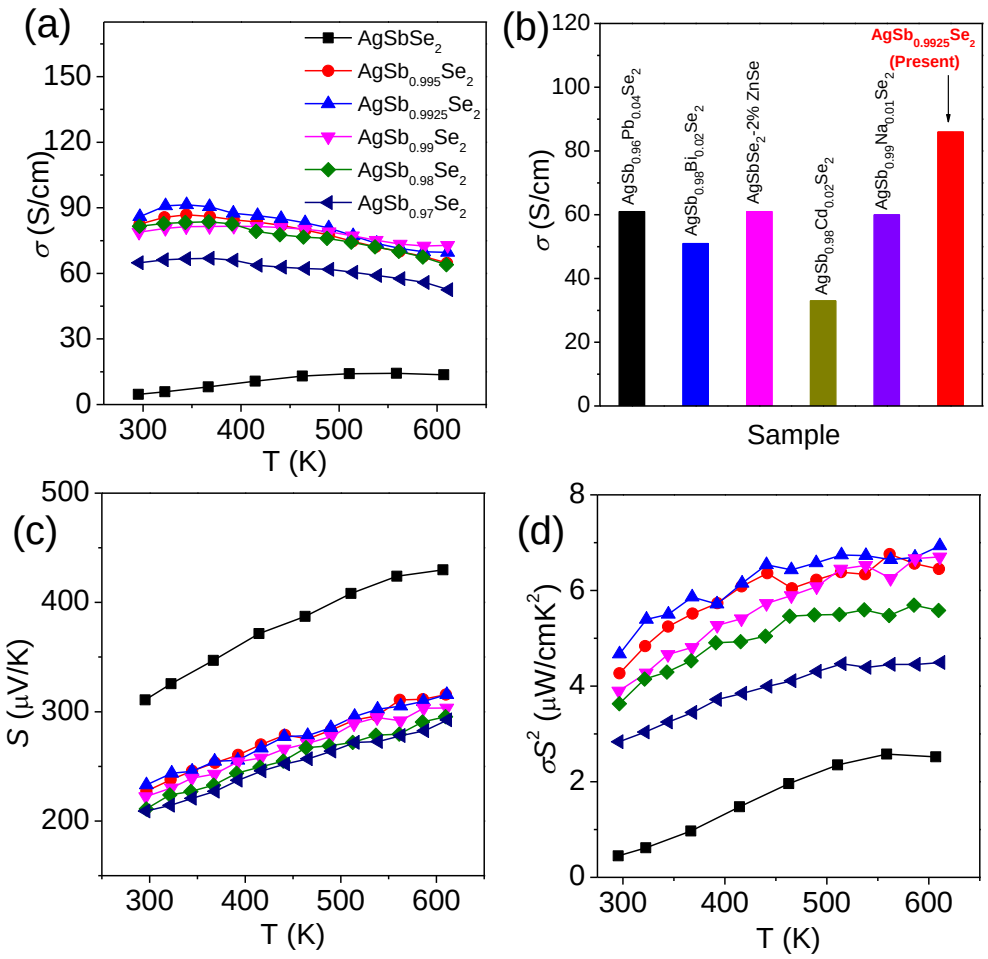

Figure 4.2 (a) Temperature dependent electrical conductivity (σ) of $AgSb_{1-x}Se_2$ (x = 0–3 mol%) samples. (b) Room temperature σ of $AgSb_{0.9925}Se_2$ compared with that of different cation doped $AgSbSe_2$;[3–5,7,8] Temperature dependent (c) Seebeck coefficient (S) and (d) power factor (σS^2) of $AgSb_{1-x}Se_2$ (x = 0-3 mol%) samples.

The Sb deficient samples show higher σ values compared to those of previously reported divalent (M^{2+} = Pb^{2+}, Zn^{2+}, Cd^{2+}) or monovalent (M^{+} = Na^{+}) cation doped $AgSbSe_2$ (Figure 4.2(b)).[3–5] When a divalent M^{2+} cation is substituted in the Sb^{3+} position, then for each substitution it contributes one extra hole (Table 4.1), which is calculated from the simple valence counting chemistry. Similarly, for monovalent M^{+} cation doping, each substitution in place of Sb^{3+} contributes two extra holes (Table 4.1). In the present case, each Sb vacancy gives rise to three extra holes as Sb is trivalent (Table 4.1), thus the required Sb deficiency concentration is three times less compared to the doping concentration of the M^{2+} cation. For example, optimized doping concentration for Zn^{2+}/Cd^{2+} in $AgSbSe_2$ was 2 mol%,[4,5] whereas optimized Sb deficiency concentration is 0.75 mol% which is approximately three times less than M^{2+} doping concentration. Notably, Sb deficient samples show higher carrier mobility compared to the cation doped samples,[3–5] which is probably due to the absence of a foreign dopant in the present $AgSb_{1-x}Se_2$ samples.

Table 4.2 Room temperature carrier concentration (n_h), electrical conductivity (σ) and carrier mobility (μ) of selected $AgSb_{1-x}Se_2$ samples.

Sample	n_h (cm^{-3})	μ ($cm^2\ V^{-1}\ s^{-1}$)	m^*/m_0
$AgSbSe_2$	5×10^{18}	7	1.2
$AgSb_{0.9925}Se_2$	1.98×10^{19}	17	1.46
$AgSb_{0.99}Se_2$	2.8×10^{19}	17.5	1.68
$AgSb_{0.97}Se_2$	6.93×10^{19}	5.8	2.74

In Figure 4.2(c), we represent temperature dependent Seebeck coefficient (S) of $AgSb_{1-x}Se_2$ (x = 0-3 mol%) samples. The positive sign of S indicates p-type conduction in all the samples, which agrees well with the Hall coefficient data. All the Sb deficient samples show slightly lower Seebeck values compared to that of the pristine sample, which is due to a higher carrier concentration of Sb deficient samples compared to that of pristine $AgSbSe_2$. Typically, the $AgSb_{0.9925}Se_2$ samples show an S value of ~233 $\mu V\ K^{-1}$ at room temperature, which increases with the increasing the temperature and reaches a value of ~316 $\mu V\ K^{-1}$ at 610 K. We have estimated effective mass (m^*) of the carriers in $AgSb_{1-x}Se_2$ (x = 0-3 mol%) using measured S and Hall carrier concentration (n_h) at room

temperature (Table 4.2). Although the accurate calculation of m^* requires consideration of the non-parabolic band and multiple band model, the present calculation of m^* considers only single parabolic band for simplicity. The equations used for estimation of m^* have been given in chapter 3 (see page 110). The increased population of carriers in the multiple flat valence band valleys of the Sb deficient sample produces high m^* in $AgSb_{1-x}Se_2$ samples (Table 4.2). The calculated m^* values are comparable to the observed value for the divalent and monovalent cation doped $AgSbSe_2$.[3–8]

From the measured σ and S, we have estimated the temperature dependent power factors (σS^2) for all the samples (Figure 4.2(d)). The combination of improved σ and moderate Seebeck coefficient resulted in an enhancement in the σS^2 value for all the Sb deficient samples. Typically, the $AgSb_{0.9925}Se_2$ sample shows a σS^2 value of ~4.7 μW cm^{-1} K^{-2} at room temperature which reaches a value of ~6.94 μW cm^{-1} K^{-2} at 610 K. All the Sb deficient samples show reasonably constant power factors over the measured temperature.

Temperature dependent thermal conductivities of all $AgSb_{1-x}Se_2$ (x = 0-3 mol%) samples are presented in Figure 4.3. Total thermal conductivity, κ_{total}, values of $AgSb_{1-x}Se_2$ (x = 0-3 mol%) samples were estimated over the 300-623 K temperature range using the formula, $\kappa_{total} = DC_p\rho$, where D is thermal diffusivity (Figure 4.3(a)), C_p is specific heat (Figure 4.3(b)) and ρ is the density of the sample. The density of the pellets used for the measurement was in the range of ~97% of the theoretical density. All the samples show ultra-low thermal conductivity in the 300-623 K temperature range (Figure 4.3(c)). At room temperature, a κ_{total} value of ~0.44 W m^{-1} K^{-1} was measured for $AgSb_{0.9925}Se_2$, which remains nearly constant throughout the measured temperature range. Temperature dependent lattice thermal conductivity, κ_{lat}, values were obtained by subtracting the electronic thermal conductivity, κ_{el}, from the κ_{total}. The κ_{el} were estimated using the Wiedemann-Franz law, $\kappa_{el} = L\sigma T$; where, L is Lorenz number, σ is electrical conductivity and T is temperature. Temperature dependent L values (Figure 4.3(d)) were extracted based on the fitting of the respective temperature-dependent S values that estimate the reduced chemical potential.[3] The κ_{lat} value for the $AgSb_{0.9925}Se_2$ sample at room temperature is ~0.40 W m^{-1} K^{-1}, which remains nearly constant throughout

measured temperature range (Figure 4.3(e)). Similar κ_{lat} values were observed in the case of cation doped $AgSbSe_2$.[3–8] Highly anharmonic Sb-Se bonds and disordered cation sublattice contribute to phonon scattering processes, which give rise to low κ_{lat} in $AgSb_{1-x}Se_2$.

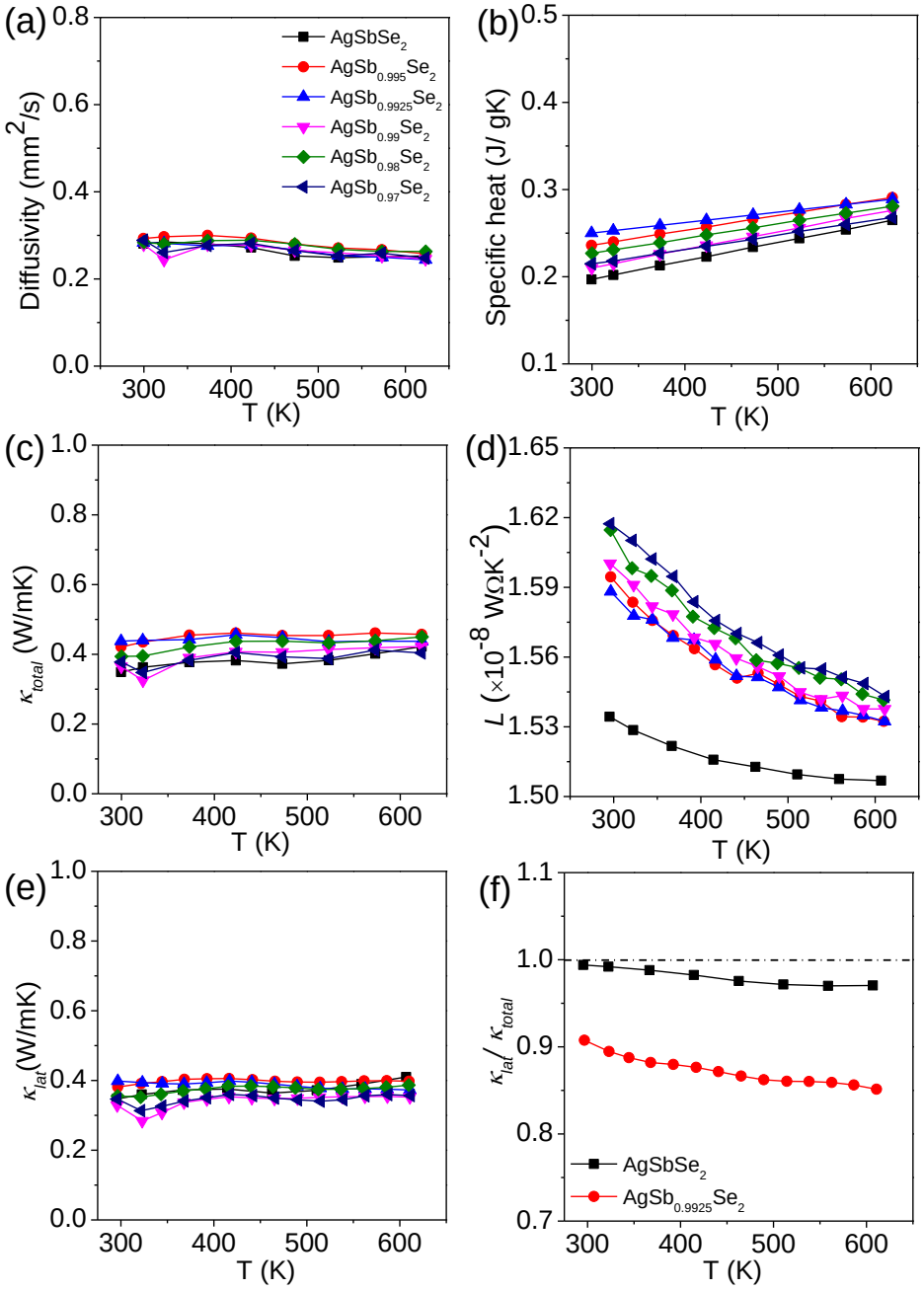

Figure 4.3 Temperature dependent (a) thermal diffusivity, (b) specific heat capacity, (c) total thermal conductivity (κ_{total}) (d) Lorenz number, (e) lattice thermal conductivity (κ_{lat}) of $AgSb_{1-x}Se_2$ (x = 0-3 mol%) samples. (f) Temperature dependent $\kappa_{lat}/\kappa_{total}$ of $AgSbSe_2$ and $AgSb_{0.9925}Se_2$ samples.

In order to find out the contribution of κ_{lat} in κ_{total}, we have calculated the ratio of κ_{lat} and κ_{total} as a function of temperature for the pristine and $AgSb_{0.9925}Se_2$ sample (Figure 4.3(f)). The major portion of heat conduction in the pristine sample takes place through phonon transport, because of low electrical conductivity. However, for the $AgSb_{0.9925}Se_2$ sample, the phonon contribution to the total thermal conductivity is ~90% in the 300-610 K temperature range, even though there was a significant increase in electrical conductivity. Thus, κ_{total} in the $AgSbSe_2$ system is intrinsically dominated by heat conduction through lattice vibrations.

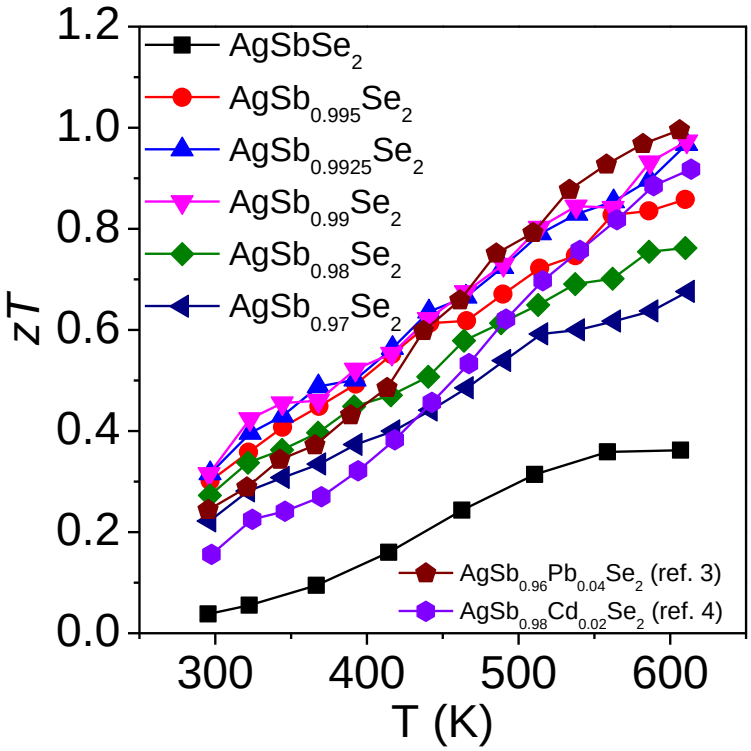

Figure 4.4 Temperature dependent thermoelectric figure merit (zT) of $AgSb_{1-x}Se_2$ (x = 0-3 mol%) samples compared with previously reported Pb and Cd doped $AgSbSe_2$.[3,4]

Temperature dependent thermoelectric figure of merits (zT) of all $AgSb_{1-x}Se_2$ (x = 0-3 mol%) samples are estimated from the measured electrical and thermal transport data. In Figure 4.4 we present the zT values of $AgSb_{1-x}Se_2$ (x = 0-3 mol%) samples. We also compare the present zT vs. T data with those of the previously reported high-performance Pb and Cd-doped $AgSbSe_2$ samples (Figure 4.4).[3,4] The highest zT value measured in the present case is indeed comparable to that of the monovalent or divalent cation doped $AgSbSe_2$.[3–8] Enhanced electrical transport due to Sb deficiencies and ultralow thermal

conductivity due to bond anharmonicity and disordered cation sublattice resulted in a superior performance in Sb deficient samples compared to pristine $AgSbSe_2$. The maximum zT ~1 at 610 K was achieved for both the $AgSb_{0.9925}Se_2$ and $AgSb_{0.99}Se_2$ samples without the use of any foreign dopant. Notably, we have achieved ~170% improvement in zT in Sb deficient sample compared to that of pristine $AgSbSe_2$.

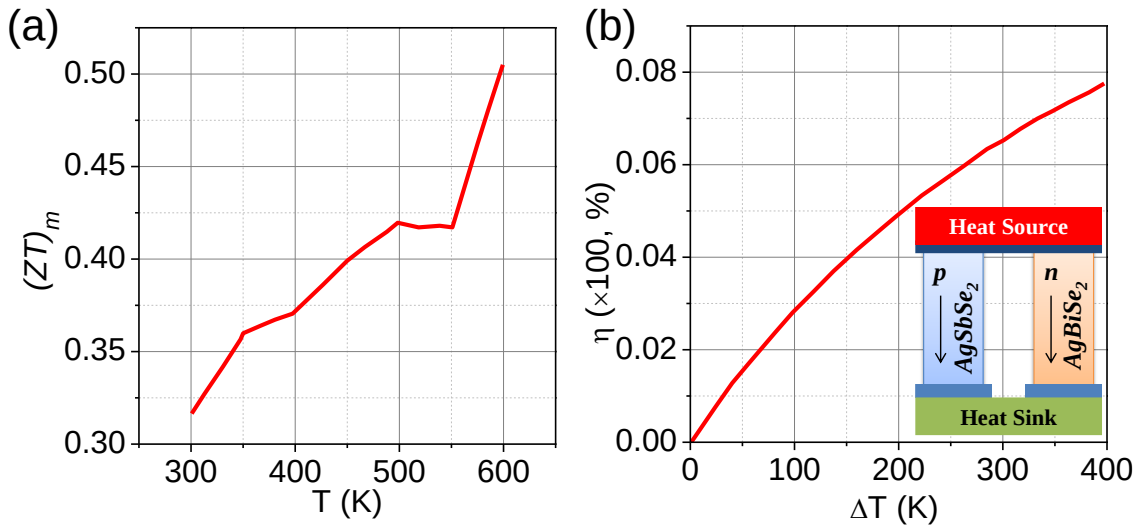

Figure 4.5 (a) The overall theoretical thermoelectric figure of merit [$(ZT)_m$] of a *p* and *n*-type pair, considering present $AgSb_{0.9925}Se_2$ as *p*-type leg and previously reported $AgBiSe_{1.98}Cl_{0.02}$ as *n*-type leg. (b) Theoretical thermoelectric energy conversion efficiency (η) as a function of temperature difference (ΔT) for thermoelectric devices considering $AgSb_{0.9925}Se_2$ and $AgBiSe_{1.98}Cl_{0.02}$[14] as *p*-type and *n*-type material, respectively. Inset in panel (b) represent schematic of a typical thermoelectric module.

The overall thermoelectric figure of merit of a *p* and *n*-type pair, [$(ZT)_m$], was theoretically calculated using equation (4.1) (see Experimental section), considering the present $AgSb_{0.9925}Se_2$ and $AgBiSe_{1.98}Cl_{0.02}$ as *p*-type and *n*-type materials, respectively (Figure 4.5(a)). We have chosen $AgBiSe_{1.98}Cl_{0.02}$ as *n*-type, as this material also belongs to the I-V-VI_2 class.[14] A maximum $(ZT)_m$ value of 0.53 at 600 K was calculated for the above mentioned theoretical module. To calculate the theoretical efficiency (η) of this pair, first we have calculated the $(ZT)_{m,avg}$ from the $(ZT)_m$ considering a hot side temperature of 600 K and cold side temperature of 300 K. A $(ZT)_{m,avg}$ of ~0.45 was estimated. A maximum conversion efficiency (η_{max}) of ~8% was calculated theoretically by fixing the cold side temperature to 300 K by maintaining a temperature difference of ΔT = 400 K (Figure 4.5(b)). The present theoretical η_{max} value is comparable to that of

the market-based metal telluride thermoelectric generator for mid-temperature applications.

4.4 Conclusions

In conclusion, we have demonstrated a new way to control the *p*-type carrier concentrations in high-quality crystalline ingots of $AgSbSe_2$ without the addition of any foreign dopant. We have shown that Sb deficiency can play a crucial role in tuning the electronic transport properties of $AgSbSe_2$. From simple valence counting, each Sb deficiency creates three extra holes in $AgSbSe_2$, which results in an improved carrier concentration, thus giving rise to enhanced electronic conductivity. The combination of improved electrical conductivity and reasonable Seebeck coefficient leads to high and constant power factor values in the 300-610 K temperature range. A highly anharmonic Sb-Se bond and disordered Ag/Sb sublattice significantly scatter the heat-carrying phonons, thus resulting in ultra-low κ_{lat}. Improved electronic transport and low thermal conductivity provided a maximum zT value of ~1 at 610 K for both the Sb deficient $AgSb_{0.9925}Se_2$ and $AgSb_{0.99}Se_2$ samples. A maximum thermoelectric conversion efficiency (η_{max}) of ~8% was estimated theoretically by considering $AgSb_{1-x}Se_2$ and $AgBiSe_{2-x}Cl_x$ as *p*-type and *n*-type materials, respectively, which shows the potential for the use of this class of materials in mid-temperature power generation applications.

References

[1] V. Jovovic, J. P. Heremans, *Phys. Rev. B* **2008**, *77*, 245204.

[2] K. Hoang, S. D. Mahanti, J. R. Salvador, M. G. Kanatzidis, *Phys. Rev. Lett.* **2007**, *99*, 156403.

[3] S. N. Guin, A. Chatterjee, D. S. Negi, R. Datta, K. Biswas, *Energy Environ. Sci.* **2013**, *6*, 2603–2608.

[4] S. N. Guin, A. Chatterjee, K. Biswas, *RSC Adv.* **2014**, *4*, 11811–11815.

[5] S. N. Guin, D. S. Negi, R. Datta, K. Biswas, *J. Mater. Chem. A* **2014**, *2*, 4324–4331.

[6] Z. Liu, J. Shuai, H. Geng, J. Mao, Y. Feng, X. Zhao, X. Meng, R. He, W. Cai, J. Sui, *ACS Appl. Mater. Interfaces* **2015**, *7*, 23047–23055.

[7] D. Li, X. Y. Qin, T. H. Zou, J. Zhang, B. J. Ren, C. J. Song, Y. F. Liu, L. Wang, H. X. Xin, J. C. Li, *J. Alloys Compd.* **2015**, *635*, 87–91.

[8] S. Cai, Z. Liu, J. Sun, R. Li, W. Fei, J. Sui, *Dalt. Trans.* **2015**, *44*, 1046–1051.

[9] Y. Liu, L. Zhao, Y. Liu, J. Lan, W. Xu, F. Li, B. Zhang, *J. Am. Chem. Soc.* **2011**, *133*, 20112–20115.

[10] Z. Li, C. Xiao, S. Fan, Y. Deng, W. Zhang, B. Ye, Y. Xie, *J. Am. Chem. Soc.* **2015**, *137*, 6587–6593.

[11] M. K. Jana, K. Pal, U. V. Waghmare, K. Biswas, *Angew. Chemie - Int. Ed.* **2016**, *55*, 7792–7796.

[12] H. Liu, X. Shi, F. Xu, L. Zhang, W. Zhang, L. Chen, Q. Li, C. Uher, T. Day, G. J. Snyder, *Nat. Mater.* **2012**, *11*, 422–425.

[13] Y. He, T. Day, T. Zhang, H. Liu, X. Shi, L. Chen, G. J. Snyder, *Adv. Mater.* **2014**, *26*, 3974–3978.

[14] S. N. Guin, V. Srihari, K. Biswas, *J. Mater. Chem. A* **2015**, *3*, 648–655.

[15] D. M. Rowe, *CRC Handbook of Thermoelectrics*, **1995**.

Chapter 5

Nanostructuring, carrier engineering and bond anharmonicity synergistically boost the thermoelectric performance of *p*- type $AgSbSe_2$–ZnSe *

*Publication based on this work: *J. Mater. Chem. A* **2014,** *2,* 4324.

CHAPTER 5

Nanostructuring, carrier engineering and bond anharmonicity synergistically boost the thermoelectric performance of *p*- type $AgSbSe_2$ – ZnSe

Summary. *Simultaneous tailoring of interdependent thermoelectric parameters, i.e. electrical conductivity, thermopower and thermal conductivity, to improve the thermoelectric figure of merit is the utmost challenge in this field. Herein, we show that by integrating different but synergistic concepts: (a) carrier engineering, (b) second phase endotaxial nanostructuring and (c) bond anharmonicity, we can achieve a maximum zT of ~1.1 at 635 K in $AgSbSe_2$-ZnSe (2 mol%), which is significantly higher than that of pristine $AgSbSe_2$. The above system, therefore, offers promise to replace traditional metal tellurides for mid-temperature power generation. We demonstrate a design strategy, which provides simultaneous enhancement of electrical transport through optimized doping, superior thermopower by the convergence of degenerate valence bands, and glass-like thermal conductivity due to the effective scattering of phonons by nanostructuring, bond anharmonicity, and a disordered cation sublattice.*

5.1 Introduction

Insertion of nanostructures of a foreign phase into the bulk matrix is an efficient way to scatter heat-carrying phonons, which significantly alters the thermoelectric performance of bulk narrow band gap semiconductors.[1–5] For example, as discussed in chapter 2, nanostructured alloys of GeTe rich (TAGS)[6] and PbTe rich (LAST-m)[7] with $AgSbTe_2$ showed astonishing *zT* values of ~1.5 at 750 K and ~1.8 at 800 K, respectively. The nanostructuring approach has been successfully implemented to numerous thermoelectric materials for reduction of lattice thermal conductivity.[8–12] A detailed discussion on the second phase nanostructuring approach has been given in the introduction part of the thesis (see page 18). Although, the effect of second phase nanostructuring[13,14] and spontaneously formed nanostructures due to cation ordering[15] on the thermoelectric performance of $AgSbTe_2$ have been investigated, but the effect of second phase nanostructuring on the thermoelectric properties of $AgSbSe_2$ have not been explored yet.

This chapter presents the extraordinary enhancement in the thermoelectric performance of *p*-type $AgSbSe_2$-ZnSe (x%) [x = 0-8 mol%] by the synergistic effect of carrier engineering, second phase nanostructuring, and bond anharmonicity. We have chosen ZnSe ($F4\bar{3}m$, a = 5.67 Å)[16] as the second phase in $AgSbSe_2$ ($Fm\bar{3}m$, a = 5.78 Å)[17] for two reasons. Firstly, at low concentrations of ZnSe in $AgSbSe_2$, a solid solution may be formed. Zn^{2+} can possibly dope into the Sb^{3+} cation sublattice and, from simple valence counting, will contribute one *p*-type carrier in $AgSbSe_2$. Secondly, slightly higher concentrations of ZnSe in $AgSbSe_2$ above the solid solution limit may give rise to phase separation of ZnSe nanostructures in the $AgSbSe_2$ matrix, which can act as effective phonon scattering centers. By varying the concentration of ZnSe in $AgSbSe_2$, it may be possible to tune the system from a solid solution to a phase separated system, which can have important effects on the electronic and phonon transport properties of $AgSbSe_2$. We have shown that at an optimum concentration of 2 mol% of ZnSe, Zn^{2+} acts as a *p*-type dopant and increases the hole concentration in the system, thereby enhancing the electrical conductivity. High *p*-type carrier doping accesses multiple flat valence band valleys of $AgSbSe_2$ with close energies and produces a high effective mass, which gives rise to a high thermopower. Transmission electron microscopy (TEM) investigation reveals the presence of coherent endotaxial nanoprecipitates (2 to 6 nm) in the $AgSbSe_2$

matrix at a second phase concentration of 2 mol% ZnSe. Upon increasing the ZnSe concentration up to 8 mol%, the nanoprecipitates become larger with semi-/incoherent interfaces. Changes in the interface relationship between the nanoparticles and the matrix with different ZnSe concentrations dramatically affect the electronic transport properties of the $AgSbSe_2$-ZnSe system. Suitable doping, size of the nanoprecipitates and the nanoprecipitate-matrix interface relationship have a significant role in altering the electronic transport to maximize the power factor in this system. Second phase nanostructuring and strong Sb-Se bond anharmonicity coupled with a disordered cation sublattice effectively scatter the heat carrying phonons, resulting in glass-like thermal conductivity in $AgSbSe_2$-ZnSe. Collectively, we show that by integrating different but synergistic concepts: (a) carrier engineering, (b) second phase endotaxial nanostructuring and (c) intrinsic bond anharmonicity, we can achieve a zT value of ~1.1 at ~635 K in $AgSbSe_2$-ZnSe (2 mol%), which is significantly higher than that of pristine $AgSbSe_2$. Integration of different but synergistic concepts to simultaneously tailor the interconnected thermoelectric parameters should be a general strategy for improving the thermoelectric performance of bulk semiconductors.

5.2 Methods

5.2.1 Synthesis

The following chemicals were purchased from Alfa Aesar and used for the synthesis without further purification: elemental silver (Ag, 99.9%, metal basis), elemental antimony (Sb, 99.9999%, metal basis), elemental zinc (Zn, 99.999%), elemental selenium (Se, 99.999%, metal basis).

Ingots (9 g) of $AgSbSe_2$-ZnSe (2-8%) and pristine $AgSbSe_2$ were synthesized by mixing appropriate ratios of high-purity starting materials of Ag, Sb, Zn and Se in a quartz tube. The tubes were sealed under high vacuum (10^{-5} Torr) and slowly heated up to 673 K over 12 h, then heated up to 1123 K in 4 h, soaked for 10 h, and subsequently, air quenched to room temperature. For electrical and thermal transport measurements the samples were cut and polished. In Figure 5.1(a), we show a photograph of an “as

synthesized" high-quality ingot of $AgSbSe_2$-ZnSe (2 mol%), with bar and coin shaped samples obtained after cutting and polishing such ingots.

5.2.2 Characterizations

Powder XRD for all the samples was recorded using Cu Kα (λ = 1.5406 Å) radiation on a Bruker D8 diffractometer. TEM imaging was performed using an aberration corrected FEI TITAN3TM 80-300 kV transmission electron microscope operating at 300 kV. Room temperature carrier concentration has been derived from Hall coefficient measurements using a PPMS. Detailed discussions on all the characterizations have been given in the introduction part of the thesis (page 31).

5.2.3 Thermoelectric measurements

Seebeck coefficient and electrical conductivity were measured under helium atmosphere by ULVAC-RIKO ZEM-3 instrument in 300-723 K temperature range. Thermal diffusivity, *D*, was directly measured by laser flash diffusivity method in a Netzsch LFA-457 under N_2 atmosphere range of 300-725 K. The total thermal conductivity, κ_{total}, of the samples was estimated to be in the temperature using the formula, $\kappa_{total} = DC_p\rho$, where *D* is the thermal diffusivity, C_p is the specific heat and ρ is the density of the sample. The thermal and electrical transport properties were measured along the same direction in the sample. Detailed discussions on thermoelectric measurements have been given in the introduction part of the thesis (page 41).

5.3 Results and discussion

5.3.1 Structural characterization

Powder X-ray diffraction patterns of pristine and 2 mol% ZnSe-containing $AgSbSe_2$ samples could be indexed to the $AgSbSe_2$ structure with the $Fm\bar{3}m$ space group, with no other second phase, observed within the detection limits of powder XRD (Figure 5.1(b)). Interestingly, upon increasing the ZnSe concentrations from 4 to 8 mol%, we observed the presence of extra low-intensity peaks in the PXRD patterns (Figure 5.1(b)), which can be indexed based on the cubic ZnSe structure ($F4\bar{3}m$). The lattice parameter initially contracted with an increase in ZnSe concentration from 0 to 2% and then remained nearly

constant upon further increase in ZnSe up to 8 mol%, and did not follow Vegard's law for solid solutions (Figure 5.1(c)). This indicates a phase separation rather than solid solution behavior at a ZnSe concentration beyond 2 mol%. We believe that up to ≤2 mol%, ZnSe forms a solid solution with the $AgSbSe_2$ and with further increase in ZnSe phase separation occurs.

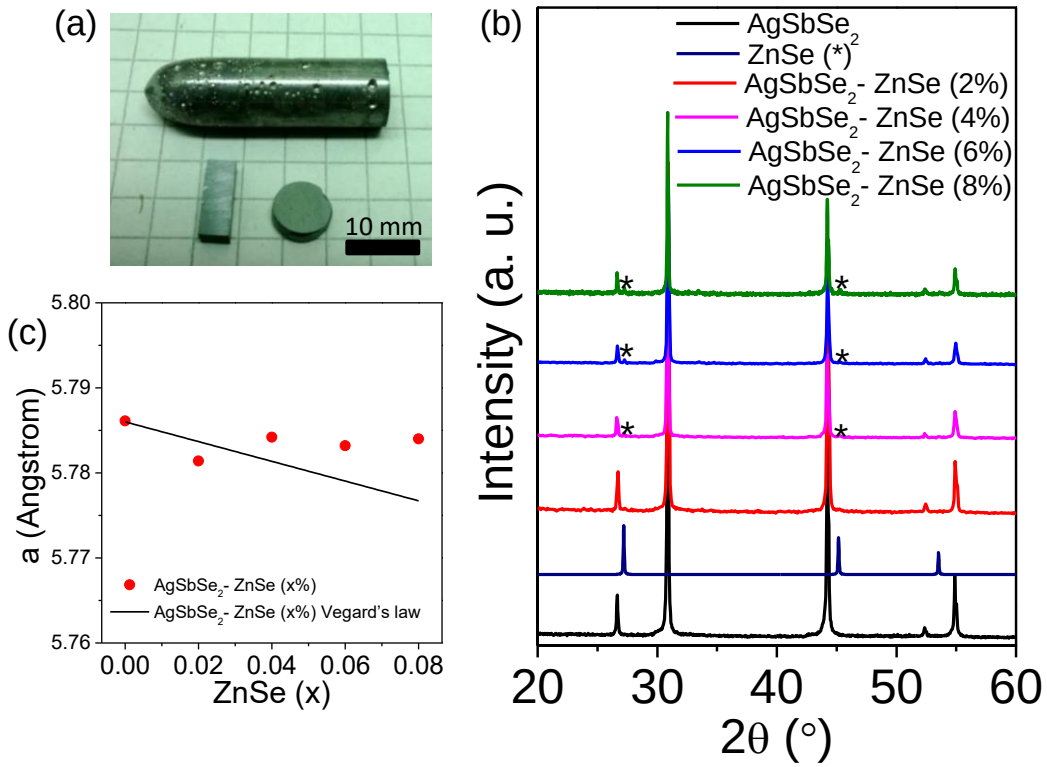

Figure 5.1 (a) Photograph of an as-synthesized ingot. Bar and coin-shaped samples are used for electrical and thermal transport measurements, respectively. (b) Powder XRD patterns of $AgSbSe_2$–ZnSe (x) [x = 0-8 mol%] samples. "*" indicates the ZnSe phase. (c) Lattice parameter (a) vs. ZnSe concentration in $AgSbSe_2$–ZnSe (x%) [x = 0-8 mol%]; the solid line indicates Vegard's law for the solid solution.

5.3.2 Nano/ Microstructure

In order to understand the phase separation behaviour and nanoscale architecture of $AgSbSe_2$-ZnSe (0-8 mol%), we performed a transmission electron microscopy (TEM) investigation on 2 mol% ZnSe and 8 mol% ZnSe containing $AgSbSe_2$ and controlled $AgSbSe_2$ samples. In Figure 5.2(a), we show a medium magnification TEM image of the $AgSbSe_2$-ZnSe (2 mol%) sample. It clearly reveals numerous spherical nanoprecipitates (~2 to 6 nm) embedded in the $AgSbSe_2$ matrix, which is otherwise not detectable by PXRD. In order to understand the interfacial relationship between the nanoprecipitate and the matrix, we performed high- resolution TEM (HRTEM) analysis of the 2 mol% ZnSe

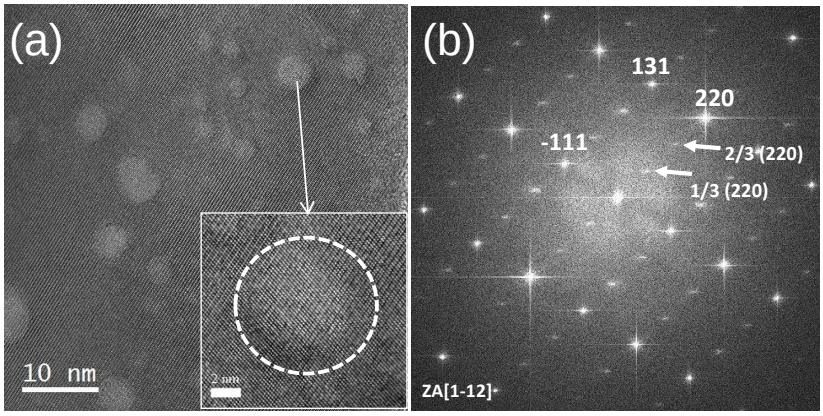

Figure 5.2 (a) Medium magnification TEM image of the $AgSbSe_2$-ZnSe (2 mol%) sample; inset is the magnified image from one of the coherent precipitates. (b) Fast Fourier transform (FFT) pattern of (a). Arrows in (b) show the weak superstructure spots.

containing sample (inset in Figure 5.2(a)). No dislocations were observed at the interface boundary (marked by dotted line), suggesting the presence of coherent interfaces in the case of small spherical nanoprecipitates. Strong spots in the fast Fourier transform (FFT) images could be indexed based on the cubic $AgSbSe_2$ structure ($Fm\bar{3}m$) (Figure 5.2(b)). Therefore, the small spherical nanoprecipitates with coherent interfaces are endotaxially placed in the $AgSbSe_2$ matrix when the concentration of ZnSe is as low as 2 mol%. Interestingly, we observed weak superstructure spots along the <220> direction (arrows in Figure 5.2(b)), which may be due to ordering of Ag and Sb atoms in $AgSbSe_2$. The similar ordering of cations in $AgSbTe_2$ has been predicted by first-principle calculations for the ground state structure,[18,19] and has also been observed in $AgPb_mSbTe_{2+m}$ by single crystal X-ray diffraction and most recently by inelastic neutron scattering, and TEM investigations in $AgSbTe_2$.[15,20] The electrical transport measurements and theoretical investigations on cubic $AgBiS_2$ nanocrystals also indicate the cation-ordering at room temperature.[21,22]

The size and shape of the nanoprecipitates change significantly with increasing ZnSe concentration. Although it is difficult to quantitatively determine the compositions of individual precipitates due to their overlap with the matrix, powder XRD of the $AgSbSe_2$-ZnSe (>2%) samples clearly shows peaks corresponding to the ZnSe phase ($F4\bar{3}m$, a = 5.67 Å), indicating that the second phase nanostructures are indeed ZnSe precipitates. The low magnification TEM image (Figure 5.3(a)) of the 8 mol% ZnSe containing sample shows the presence of oriented lamellar nanoprecipitates with a larger

size compared to the 2 mol% ZnSe containing sample. We also observed the presence of a few spherical nanoprecipitates (25-30 nm diameter) in the $AgSbSe_2$-ZnSe (8%) sample (inset in Figure 5.3(a)). Figure 5.3(b) and (c) show the HRTEM and magnified Fourier filtered images of the interface, respectively. In Figure 5.3(d), the inverse fast Fourier transform image with (111) planes reveals the presence of dislocations (indicated by dotted circles) at the interface between the precipitate and the matrix, confirming the incoherent interfaces in the case of larger nanoprecipitates.

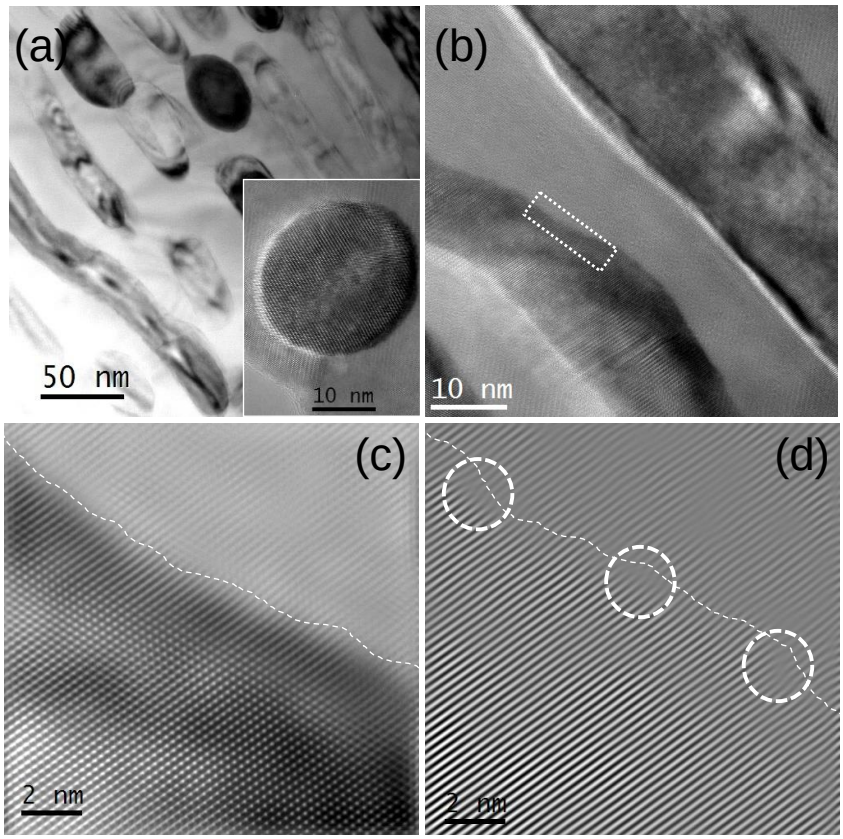

Figure 5.3 (a) Low magnification TEM image showing the presence of oriented lamellar nanoprecipitates, and the inset shows spherical nanoprecipitates in the $AgSbSe_2$-ZnSe (8 mol%) sample. (b) and (c) are the corresponding HRTEM and magnified Fourier filtered images at the precipitate matrix interface. (d) Inverse FFT of (111) planes showing the presence of misfit dislocation at the interface as marked with dotted circles.

From the above powder XRD and TEM analysis, we conclude that the $AgSbSe_2$-ZnSe system represents a solid solution below ZnSe concentrations of <2 mol%, while in the 2-8 mol% ZnSe concentration range phase separation occurs and the formation of nanostructures with different sizes and interfaces takes place. We claim that 2 mol% ZnSe in $AgSbSe_2$ sample is the optimized concentration, where the coexistence of a solid

solution and endotaxial nanoscale ZnSe precipitates occurs, which indeed simultaneously improve the electronic and thermal transport properties as elaborated below.

5.3.3 Thermoelectric properties

The temperature dependent electrical transport properties of $AgSbSe_2$-ZnSe (2-8 mol%) samples over the 300-723 K range are presented in Figure 5.4. Figure 5.4(a) shows the temperature dependent electrical conductivity (σ) of pristine $AgSbSe_2$ and $AgSbSe_2$-ZnSe (2-8 mol%) samples. Typically, the room temperature σ for the $AgSbSe_2$-ZnSe (2 mol%) sample was ~61 S cm^{-1}, which remained almost the same up on increasing the temperature up to ~630 K, and then decreases to ~34 S cm^{-1} at ~705 K. A rise of σ at room temperature was observed with increasing ZnSe concentrations from 0 to 6 mol%, and then the σ fell with further increase in ZnSe concentration to 8 mol% (Figure 5.4(b)). The room temperature Hall coefficients, R_H, for pristine and selected ZnSe containing $AgSbSe_2$ samples are positive, which indicates *p*-type conduction in this system. The measured carrier concentrations are ~5×10^{18}, ~5×10^{19} and ~5.3×10^{19} carriers cm^{-3} for the pristine, 2 mol% and 6 mol% ZnSe containing $AgSbSe_2$ samples, respectively (Table 5.1). An increase in the hole concentration indicates that Zn^{2+} dopes into the Sb^{3+} cation sublattice and, from simple valence counting, contributes one *p*-type carrier. At the optimized ZnSe concentration of 2 mol% in $AgSbSe_2$, the system presents coexistence of a solid solution and nanoscale precipitates. In the $AgSbSe_2$-ZnSe (2 mol%) sample, most of the ZnSe may dissolve in the matrix while the remaining small amount of ZnSe precipitates into coherent endotaxial nanocrystals (2 to 6 nm). When the ZnSe concentration is increased to 8 mol%, only ≤2 mol% Zn^{2+} forms a solid solution, while the remaining large amount of ZnSe forms large incoherent lamellar nanoprecipitates. The increase in the room temperature σ value with the increase of the ZnSe concentration from 0 to 6 mol% can be attributed to the combined effect of increase in carrier concentration to an optimum value and the presence of more coherent endotaxial nanoprecipitates, which does not alter the carrier transport in $AgSbSe_2$. On the other hand, the larger incoherent nanoprecipitates scatter the hole carriers significantly, decreasing the σ value in the case of the 8 mol% ZnSe containing $AgSbSe_2$ sample. The room temperature hole mobilities, defined as $\mu = \sigma/ne$, for the pristine $AgSbSe_2$, 2 mol%

ZnSe and 6 mol% ZnSe containing $AgSbSe_2$ samples are ~7, ~9 and ~11 $cm^2\ V^{-1}\ s^{-1}$, respectively (Table 5.1).

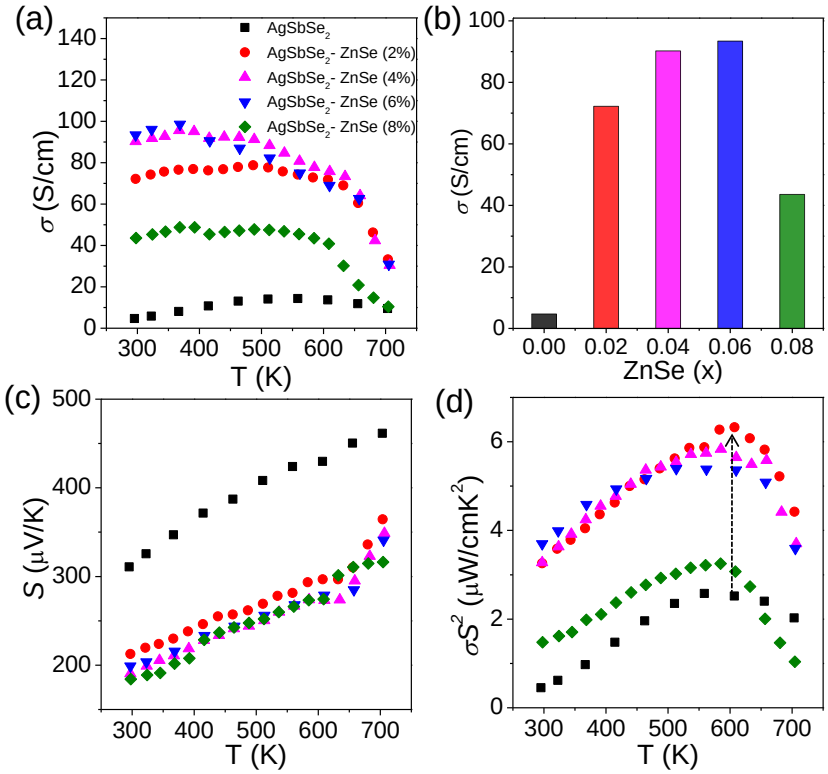

Figure 5.4 (a) Temperature dependent electrical conductivity (σ) of $AgSbSe_2$-ZnSe (x%) [x = 0-8 mol%] samples. (b) Room temperature σ values with increasing the ZnSe concentration in $AgSbSe_2$. (c) and (d) Temperature dependent Seebeck coefficient (S) and power factor (σS^2), respectively. The dotted arrow shows the enhancement of σS^2. The same symbol notation and colors for the samples are used in all panels.

Table 5.1 Carrier concentration (n), electrical conductivity (σ), carrier mobility (μ) and effective mass (m^*) of pristine $AgSbSe_2$ and selected $AgSbSe_2$-ZnSe samples at room temperature.

Sample	n (cm^{-3})	σ (S cm^{-1})	μ ($cm^2\ V^{-1}\ s^{-1}$)	m^*/m_0
$AgSbSe_2$	5×10^{18}	5	7	1.2
$AgSbSe_2$-ZnSe (2%)	5×10^{19}	72	13	1.95
$AgSbSe_2$-ZnSe (6%)	5.3×10^{19}	94	22	2.08

Figure 5.4(c) presents the temperature dependent Seebeck coefficients (S) of pristine $AgSbSe_2$ and ZnSe containing $AgSbSe_2$ samples. The positive values of S confirm the p-type conduction in the system, which is in agreement with the Hall coefficient data. The room temperature S value generally decreases with increasing ZnSe concentration, because of the increasing carrier concentration of the system. Typically, in

the case of the $AgSbSe_2$-ZnSe (2 mol%) sample, the room temperature *S* value is ~215 μV K^{-1} which increases to ~365 μV K^{-1} at ~705 K. Similar high *S* value was found the Pb and Cd-doped $AgSbSe_2$.[23,24] The high density of states effective mass (*m**) is responsible for the high *S* values in this compound. Assuming a single parabolic band model with acoustic phonon scattering, we have estimated the *m** using equations ((3.1)-(3.3)) (page 110; chapter 3) using the measured *S* and Hall carrier concentrations (*n*). Calculated values of *m** for $AgSbSe_2$-ZnSe (2 mol%) and $AgSbSe_2$-ZnSe (6 mol%) samples are 1.95m_0 and 2.08m_0 respectively, which is higher than pristine $AgSbSe_2$ (Table 5.1). Zn^{2+} doping increases the number of *p*-type carriers which can access the multiple valence band valleys of $AgSbSe_2$ with close energies, thus resulting in an increase in *m** value with increasing carrier concentration. Similar high *m** values (1.2 to 1.8m_0) have also been observed in Pb- and Bi-doped $AgSbSe_2$.[23] An increase in the population of carriers in the multiple flat valence bands at high temperature produces higher *m**, which in turn increases *S* above ~600 K (Fig. 4(c)), as *S* is directly related to *m** by equation (3.4) (page 111; Chapter 3).[23,25,26] We have observed that these materials have comparatively low hole mobilities (μ), which is due to the presence of heavy holes (Table 5.1). It is probable that the increase in *m** at high temperatures further decreases the hole mobility, thus resulting in a decrease in the electrical conductivity above ~600 K for the $AgSbSe_2$-ZnSe samples (Fig. 5(a)). Similar behavior in temperature dependent σ and *S* near ~600 K has also been observed in Pb/Bi-doped $AgSbSe_2$.[23]

Interestingly, we have observed that the μ value does not decrease with the addition of ZnSe (2-6 mol%) in $AgSbSe_2$ (Table 5.1). This may be due to the following reasons: (a) the electronic performance of thermoelectric materials depends on the weighted mobility, $\mu(m^*/m_0)^{3/2}$.[25,27] However, μ is low for bands with heavy mass, m_b^* (the band-mass of a single valley or single pocket). When the charge carriers are predominantly scattered by acoustic phonons, it is expected that $\mu \propto 1/m_b^{*5/2}$. Therefore, increasing the band-mass should decrease the carrier mobility. In contrast, the convergence of many charge carrier band valleys has virtually no detrimental effects.[25] Multiple degenerate valleys have the effect of producing large *m** without explicitly reducing m. A valley degeneracy, N_v, has the effect of increasing *m** by a factor of $N_v^{2/3}$. The density of states effective mass is given by $m^* = N_v^{2/3} m_b^*$,[25,27] where N_v includes

orbital degeneracy and m_b* is, more specifically, the average (single valley) density of states effective mass of the degenerate valleys.[25,27] The mobility is nominally unaffected by N_v. Zn^{2+} doping increases the number of *p*-type carriers which can access the multiple valence band valleys of $AgSbSe_2$ with close energies, and offers unaffected carrier mobility in the samples. (b) A low concentration of ZnSe (2-6 mol%) gives rise to coherent endotaxial nanocrystals (2 to 6 nm) which do not alter carrier transport in $AgSbSe_2$. Thus, μ is remains unaffected or is even slightly improved. Similar results have been observed in the endotaxial nanostructured PbTe-SrTe system.[9,10]

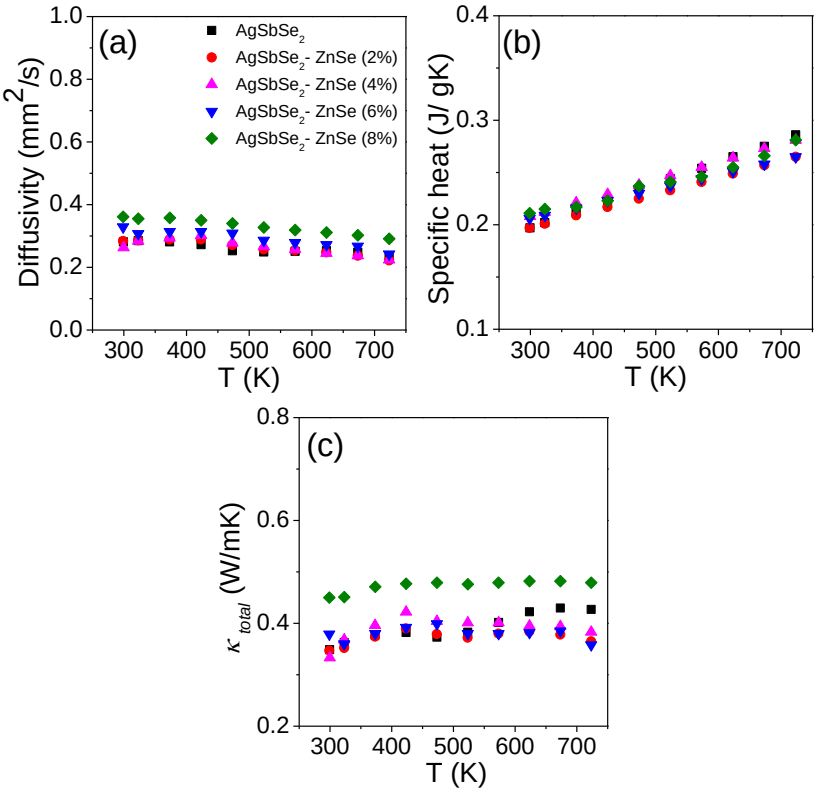

Figure 5.5 Temperature dependent (a) thermal diffusivity, (b) specific heat and (c) total thermal conductivity (κ_{total}) of $AgSbSe_2$-ZnSe (x%) [x = 0-8 mol%].

Figure 5.4(d) shows the temperature dependent power factors (σS^2) for the pristine and $AgSbSe_2$-ZnSe (2-8 mol%) samples. Typically, at room temperature, the σS^2 value for $AgSbSe_2$-ZnSe (2 mol%) is ~3.3 μW cm^{-1} K^{-2} which rises to a maximum of ~6.3 μW cm^{-1} K^{-2} at 605 K and then falls to ~4.4 μW cm^{-1} K^{-2} at ~705 K. The smooth electrical transport due to the presence of coherent endotaxial nanoprecipitates and high *S* value in $AgSbSe_2$-ZnSe (2-6 mol%) samples result in markedly higher σS^2 compared to

that of the $AgSbSe_2$-ZnSe (8 mol%) sample, where the carrier transport is significantly affected by the presence of large incoherent nanostructures (Figure 5.3(c)).

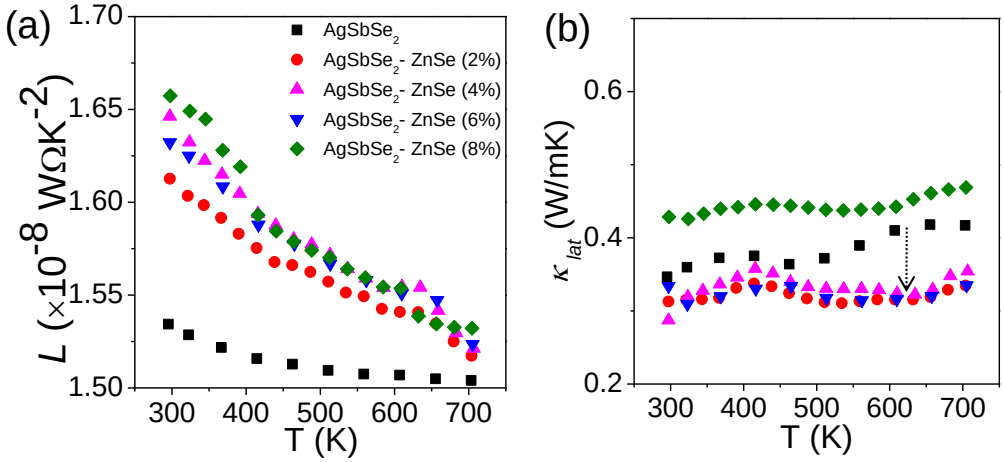

Figure 5.6 Temperature dependent (a) calculated Lorenz numbers, (b) lattice thermal conductivity (κ_{lat}) of $AgSbSe_2$-ZnSe (x%) [x = 0-8 mol%] samples.

The total thermal conductivity, κ_{total}, of all the samples was estimated in the temperature range of 300-725 K using the formula $\kappa_{total} = DC_p\rho$, where D is the thermal diffusivity (Figure 5.5(a)), C_p is the specific heat (Figure 5.5(b)) and ρ is the density of the sample. A κ_{total} value of ~0.34 W m^{-1} K^{-1} was measured at room temperature for the $AgSbSe_2$-ZnSe (2%) sample, which remains almost the same over the 300-725 K range (Figure 5.5(c)). The lattice thermal conductivity, κ_{lat}, was estimated after subtracting the electronic part, κ_{el}, from the κ_{total}. The electronic thermal conductivities ($\kappa_{el} = L\sigma T$) were extracted based on the fitting of the respective Seebeck values to estimate the reduced chemical potential (η) from which the Lorenz number, L, can be obtained (Figure 5.6(a)) as discussed in chapter 3. This assumes a parabolic band model and energy independent scattering time. Typically, the $AgSbSe_2$-ZnSe (2%) sample exhibits an ultra-low glass-like κ_{lat} value of ~0.3 W m^{-1} K^{-1} in the temperature range of 300-650 K (Figure 5.6(b)). This value is 30% lower compared to that of pristine $AgSbSe_2$. Similar low values of κ_{lat} have been observed recently in bulk AgBiSeS[28] and nanostructured $AgBiSe_2$.[29] This decrease in κ_{lat} can be attributed to the additional scattering of heat-carrying phonons by the small (2-6 nm) nanoprecipitates embedded in the $AgSbSe_2$ matrix, in addition to the intrinsic effect of bond anharmonicity and effective phonon scattering by the highly disordered Ag/Sb lattice at high temperature.

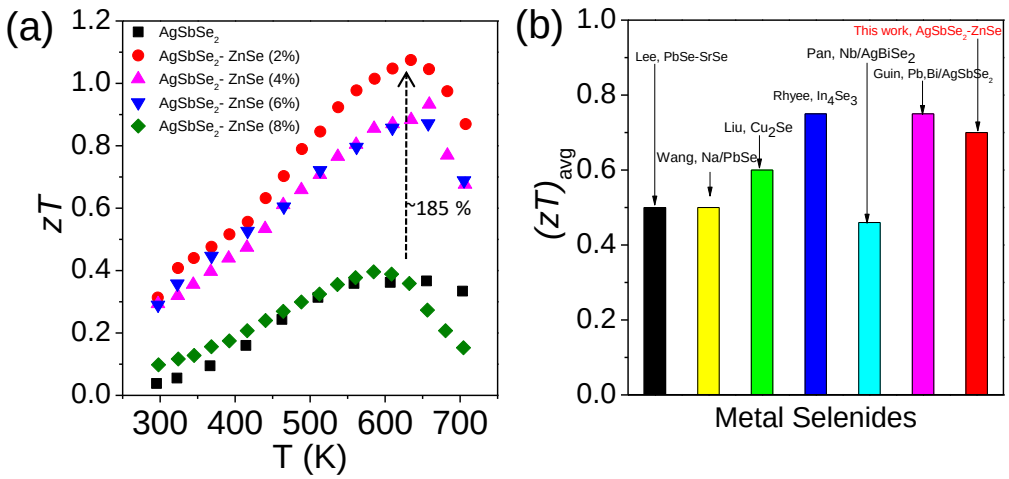

Figure 5.7 (a) Temperature dependent thermoelectric figure of merit (*zT*) of $AgSbSe_2$-ZnSe (x%) [x = 0–8 mol%]. The dotted line shows the 185% enhancement in *zT* compared to pristine $AgSbSe_2$, (b) Average *zT* of the present $AgSbSe_2$-ZnSe (2%) and leading polycrystalline metal selenides reported in the literature, considering a hot side temperature of 690 K and cold side temperature of 350 K.

Figure 5.7(a) presents the *zT* values as a function of temperature for different $AgSbSe_2$-ZnSe (2–8%) and control $AgSbSe_2$ samples. The highest *zT* value of ~1.10 at ~635 K was achieved for $AgSbSe_2$-ZnSe (2%), which is 185% higher than that of the pristine $AgSbSe_2$ sample. With such high *zT* value in this Te-free material, we can expect an average zT_{avg} value of ~0.7 (considering a hot side temperature of 640 K and cold side temperature of 350 K), which is in line with other leading high performance metal selenide-based thermoelectric materials in the mid-temperature range (Figure 5.7(b)).[23,30–34] The 4 and 6 mol% ZnSe containing samples have also shown reasonably high *zT* values of ~0.9 at ~640 K.

5.4 Conclusions

In conclusion, we have shown a simultaneous improvement in the interdependent thermoelectric parameters of *p*-type $AgSbSe_2$ by adopting second phase nanostructuring accompanied by carrier engineering. We demonstrate that by integrating carrier engineering and second phase endotaxial nanostructuring coupled with an intrinsic high degree of bond anharmonicity, we can achieve a promising *zT* value of ~1.1 at ~635 K in $AgSbSe_2$-ZnSe (2 mol%), which is 185% higher than that of the pristine $AgSbSe_2$ sample. Zn^{2+} at an optimum concentration (2 mol%) acts as an effective *p*-type dopant in $AgSbSe_2$, thereby enhancing the electrical transport. High-density *p*-type carriers can

access the multiple degenerate valence band valleys of $AgSbSe_2$ and produce high effective mass, which in turn gives rise to high thermopower and hence a superior power factor. Small (2 to 6 nm) coherent endotaxial nanoprecipitates in the 2-6 mol% ZnSe containing samples do not alter carrier transport in $AgSbSe_2$, and function exclusively as phonon scattering centers to reduce the lattice thermal conductivity, especially at high temperatures. Optimum doping, the size of the nanoprecipitates and the interfacial relationship between the nanoprecipitates and the matrix each play a significant role in altering the electronic transport to maximize the power factor in this system. Second phase nanostructuring and intrinsic strong Sb-Se bond anharmonicity with a disordered cation sublattice allow effective phonon scattering, which leads to a glass-like κ_{lat} of the $AgSbSe_2$-ZnSe system. This boost in zT to a highly promising value in the case of this Te-free material highlights the role of-and need for-integrating different but synergistic concepts to simultaneously tailoring the interdependent thermoelectric parameters for the improvement of the thermoelectric performance of bulk semiconductors.

References

[1] J. R. Sootsman, D. Y. Chung, M. G. Kanatzidis, *Angew. Chemie - Int. Ed.* **2009**, *48*, 8616–8639.

[2] G. Tan, L.-D. Zhao, M. G. Kanatzidis, *Chem. Rev.* **2016**, *116*, 12123–12149.

[3] M. G. Kanatzidis, *Chem. Mater.* **2010**, *22*, 648–659.

[4] K. Nielsch, J. Bachmann, J. Kimling, H. Böttner, *Adv. Energy Mater.* **2011**, *1*, 713–731.

[5] C. J. Vineis, A. Shakouri, A. Majumdar, M. G. Kanatzidis, *Adv. Mater.* **2010**, *22*, 3970–3980.

[6] S. H. Yang, T. J. Zhu, T. Sun, J. He, S. N. Zhang, X. B. Zhao, *Nanotechnology* **2008**, *19*, 245707.

[7] K. F. Hsu, S. Loo, F. Guo, W. Chen, J. S. Dyck, *Science* **2004**, *303*, 818–821.

[8] K. Biswas, J. He, G. Wang, S.-H. Lo, C. Uher, V. P. Dravid, M. G. Kanatzidis, *Energy Environ. Sci.* **2011**, *4*, 4675–4684.

[9] K. Biswas, J. He, Q. Zhang, G. Wang, C. Uher, V. P. Dravid, M. G. Kanatzidis, *Nat. Chem.* **2011**, *3*, 160–166.

[10] K. Biswas, J. He, I. D. Blum, C.-I. Wu, T. P. Hogan, D. N. Seidman, V. P. Dravid, M. G. Kanatzidis, *Nature* **2012**, *489*, 414–418.

[11] Y. Lee, S.-H. Lo, C. Chen, H. Sun, D.-Y. Chung, T. C. Chasapis, C. Uher, V. P. Dravid, M. G. Kanatzidis, *Nat. Commun.* **2014**, *5*, 3640.

[12] S. Il Kim, K. H. Lee, H. A. Mun, H. S. Kim, S. W. Hwang, J. W. Roh, D. J. Yang, W. H. Shin, X. S. Li, Y. H. Lee, et al., *Science* **2015**, *348*, 109–114.

[13] J. Xu, H. Li, B. Du, X. Tang, Q. Zhang, C. Uher, *J. Mater. Chem.* **2010**, *20*, 6138–6143.

[14] P. A. Sharma, J. D. Sugar, D. L. Medlin, *J. Appl. Phys.* **2010**, *107*, 113716.

[15] J. Ma, O. Delaire, F. May, C. E. Carlton, M. McGuire, L. H. VanBebber, D. L. Abernathy, G. Ehlers, T. Hong, A. Huq, et al., *Nat. Nanotechnol.* **2013**, *8*, 445–451.

[16] P. D. Lao, Y. Guo, G. G. Siu, S. C. Shen, *Phys. Rev. B* **1993**, *48*, 11701–11704.

[17] S. Geller, J. H. Wernick, *Acta Crystallogr.* **1959**, *12*, 46–54.

[18] K. Hoang, S. D. Mahanti, J. R. Salvador, M. G. Kanatzidis, *Phys. Rev. Lett.* **2007**,

99, 156403.

[19] S. V. Barabash, V. Ozolins, C. Wolverton, *Phys. Rev. Lett.* **2008**, *101*, 155704.

[20] E. Quarez, K. Hsu, R. Pcionek, N. Frangis, E. K. Polychroniadis, M. G. Kanatzidis, *J. Am. Chem. Soc.* **2005**, *127*, 9177–9190.

[21] S. N. Guin, S. Banerjee, D. Sanyal, S. K. Pati, K. Biswas, *Inorg. Chem.* **2016**, *55*, 6323–6331.

[22] S. N. Guin, K. Biswas, *Chem. Mater.* **2013**, *25*, 3225–3231.

[23] S. N. Guin, A. Chatterjee, D. S. Negi, R. Datta, K. Biswas, *Energy Environ. Sci.* **2013**, *6*, 2603–2608.

[24] S. N. Guin, A. Chatterjee, K. Biswas, *RSC Adv.* **2014**, *4*, 11811–11815.

[25] Y. Pei, X. Shi, A. LaLonde, H. Wang, L. Chen, G. J. Snyder, *Nature* **2011**, *473*, 66–69.

[26] G. J. Snyder, E. S. Toberer, *Nat. Mater.* **2008**, *7*, 105–114.

[27] Y. Pei, H. Wang, G. J. Snyder, *Adv. Mater.* **2012**, *24*, 6125–6135.

[28] Y.-L. Pei, H. Wu, J. Sui, J. Li, D. Berardan, C. Barreteau, L. Pan, N. Dragoe, W.-S. Liu, J. He, et al., *Energy Environ. Sci.* **2013**, *6*, 1750.

[29] C. Xiao, X. Qin, J. Zhang, R. An, J. Xu, K. Li, B. Cao, J. Yang, B. Ye, Y. Xie, *J. Am. Chem. Soc.* **2012**, *134*, 18460–18466.

[30] Y. Lee, S. Lo, J. Androulakis, C. Wu, L. Zhao, D. Chung, *J. Am. Chem. Soc.* **2013**, *135*, 5152–5160.

[31] J.-S. Rhyee, K. H. Lee, S. M. Lee, E. Cho, S. Il Kim, E. Lee, Y. S. Kwon, J. H. Shim, G. Kotliar, *Nature* **2009**, *459*, 965–968.

[32] H. Wang, Y. Pei, A. D. Lalonde, G. J. Snyder, *Adv. Mater.* **2011**, *23*, 1366–1370.

[33] H. Liu, X. Shi, F. Xu, L. Zhang, W. Zhang, L. Chen, Q. Li, C. Uher, T. Day, G. J. Snyder, *Nat. Mater.* **2012**, *11*, 422–425.

[34] L. Pan, D. Bérardan, N. Dragoe, *J. Am. Chem. Soc.* **2013**, *135*, 4914–4917.

Chapter 6

Promising thermoelectric performance in *n*- type $AgBiSe_2$: effect of aliovalent anion doping *

*Publication based on this work: *J. Mater. Chem. A* **2015,** *3,* 648

CHAPTER 6

Promising thermoelectric performance in *n*- type $AgBiSe_2$: effect of aliovalent anion doping

Summary. *Surprisingly, most of the available high-performance materials are p-type; but both n- and p-type materials are essential for a thermoelectric module. In this chapter, we present promising thermoelectric performance in halogen (Cl/Br/I) doped n-type bulk* $AgBiSe_2$*, which is a Pb-free material and consists of earth-abundant elements. Aliovalent halide ion doping (2-4 mol%) in the* Se^{2-} *sublattice of* $AgBiSe_2$ *significantly increases the n-type carrier concentration in* $AgBiSe_2$*, thus improving the temperature dependent electronic transport properties. Temperature dependent cation order-disorder transition tailors the electronic transport properties in* $AgBiSe_{1.98}X_{0.02}$ *(X = Cl, Br and I) samples. Bond anharmonicity and disordered cation sublattice effectively scatter heat carrying phonon in the high-temperature cubic phase of* $AgBiSe_{1.98}X_{0.02}$ *(X = Cl, Br and I), which limits the lattice thermal conductivity to a low value of ~0.27 W* m^{-1} K^{-1} *at ~810 K. The highest thermoelectric figure of merit, zT, value of ~ 0.9 at ~810 K has been achieved for the* $AgBiSe_{1.98}Cl_{0.02}$ *sample, which is promising among the n-type metal selenide based thermoelectric materials.*

6.1 Introduction

The performance of thermoelectric materials could be improved either through enhancing the power factor (σS^2) or through lowering the thermal conductivity or both at the same time.[1–4] In addition to high *zT*, it is also essential to search for both *p*- and *n*-type materials as both are required to construct a thermoelectric device. Unexpectedly, most of the existing high-performance materials are *p*-type. Intrinsically low thermal conducting and promising thermoelectric materials, like $AgSbSe_2$,[5,6] $AgSbTe_2$,[7,8] Ag_9TlTe_5,[9] $Ag_{0.95}GaTe_2$,[10] Cu_3SbSe_4,[11] $CsBi_4Te_6$,[12] InTe,[13] $CsAg_5Te_3$[14] are all *p*-type. To date, few compounds have evident *n*-type conduction with ultra-low thermal conductivity.[15,16] Among the I-V-VI_2 class of compound, $AgBiSe_2$ shows intrinsic *n*-type conduction in pristine bulk phase. Recently, a peak *zT* value of ~1 at 773 K has been achieved in $AgBiSe_2$ by *n*-type Nb doping.[17] Surprisingly, solution grown $AgBiSe_2$ nanocrystals show *p*-type conduction with promising thermoelectric performance.[18,19] Although, the effect of the cation doping on the thermoelectric property of $AgBiSe_2$ has been investigated, but the effect of anion substitution in this system is unexplored. Halide ion (Cl^-/ Br^-/I^-) can possibly aliovalently dope on the Se^{2-} sublattice and from simple valence counting, will contribute one *n*-type carrier in $AgBiSe_2$, which will improve the electronic transport property.

This chapter presents the synthesis and promising thermoelectric properties of high-quality bulk crystalline ingots of *n*-type Cl^-/ Br^-/I^- doped $AgBiSe_2$. We show that Cl^- acts as an effective *n*-type dopant and markedly increases the electrical conductivity up to ~340 S cm^{-1} at room temperature, which results in a large increase in the power factor (σS^2) of $AgBiSe_2$ over a wide temperature range. We could achieve a maximum *zT* of ~0.9 at ~810 K in the case of *n*-type $AgBiSe_{1.98}Cl_{0.02}$ crystalline ingot due to high power factor and intrinsically low thermal conductivity. We also report the comparison of the thermoelectric properties between Cl^-, Br^- and I^- doped $AgBiSe_2$ samples.

6.2 Methods

6.2.1 Synthesis

Elemental silver (Ag, 99.999%, metal basis), elemental bismuth (Bi, 99.9999%, metal basis), elemental selenium (Se, 99.999%, metal basis), bismuth chloride ($BiCl_3$, 99.999%, metal basis), bismuth bromide ($BiBr_3$, 99.999%, metal basis), bismuth iodide (BiI_3, 99.999%, metal basis) were purchased from Alfa Aesar and used for the synthesis without further purification.

Ingots (~9 g) of pristine $AgBiSe_2$ and $AgBiSe_{2-x}X_x$ (X = Cl/Br/I; x = 2-4 mol%) were synthesized by mixing appropriate ratios of high-purity starting materials of Ag, Bi, Se and BiX_3 (X = Cl/Br/I) in quartz tube. The tubes were sealed under high vacuum (10^{-5} Torr) and slowly heated up to 673 K over 12 h, then heated up to 1123 K in 4 h, soaked for 10 h, and subsequently slow cooled to room temperature over a period of 12 h.

6.2.2 Characterizations

Room temperature powder X-ray diffraction of the sample was recorded using a Cu Kα (λ = 1.5406 Å) radiation on a Bruker D8 diffractometer. Temperature-dependent X-ray diffraction measurements under N_2 flow were carried out with X-ray beam of E = 12.42 keV and λ = 0.998 Å, at BL-18B (Indian beamline), Photon Factory, KEK, Tsukuba, Japan. A Netzsch DSC 200F3DSC instrument was used for measurement. To probe optical energy gap of these compounds, optical diffuse reflectance measurement was performed on finely ground powder using a Perkin Elmer Lambda 900, UV/vis/NIR spectrometer. Room temperature carrier concentration of all the samples has been derived from Hall coefficient measurement by using PPMS. Elaborative discussions on the characterizations have been given in the introduction part of the thesis (page 31).

6.2.3 Thermoelectric measurements

Seebeck coefficient and electrical conductivity were measured under helium atmosphere by ULVAC-RIKO ZEM-3 instrument from room temperature to 823 K. The longer direction coincide with the direction in which the thermal conductivity was measured. Thermal diffusivity, D, was directly measured by laser flash diffusivity method in a Netzsch LFA-457 under N_2 atmosphere from room temperature to 823 K. The total thermal conductivity, κ_{total}, of the samples was estimated using the formula, κ_{total} =

$DC_p\rho$, where D is the thermal diffusivity, C_p is the specific heat and ρ is the density of the sample. Elaborative discussions on the thermoelectric measurements have been given in the introduction part of the thesis (page 41).

6.3 Results and discussion

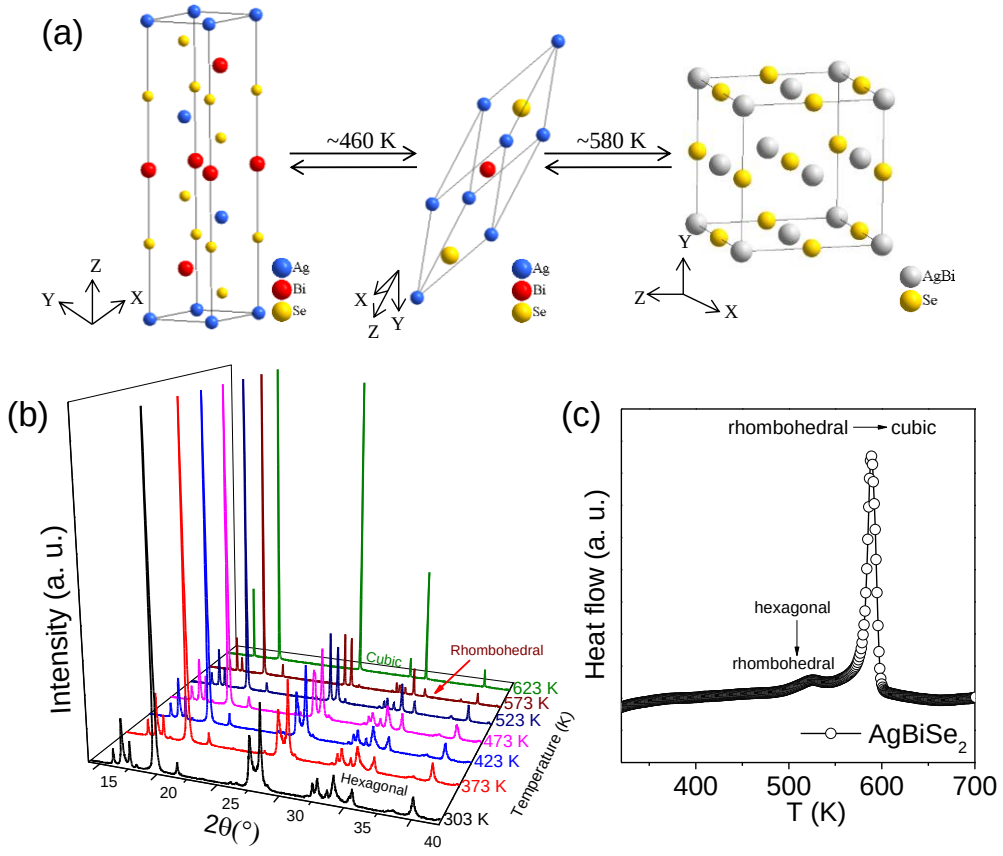

Figure 6.1 (a) Crystal structural evaluation among hexagonal, rhombohedral and cubic phase of $AgBiSe_2$ (b) Temperature dependent synchrotron (E = 12.42 KeV and λ = 0.998 Å) powder X-ray diffraction patterns of $AgBiSe_2$ (c) Differential scanning calorimetric data for pristine $AgBiSe_2$.

Silver bismuth selenide, $AgBiSe_2$, is a polymorphous semiconductor known to show fascinating temperature dependent structural phase transition (Figure 6.1(a)).[17,19] At room temperature, $AgBiSe_2$ crystallizes in a cento-symmetric ordered hexagonal phase (space group $P\bar{3}m1$; a = 4.194 Å, c = 19.65 Å). $AgBiSe_2$ undergoes two structural phase transitions at higher temperatures, at 460 K (hexagonal to rhombohedral) and 580 K (rhombohedral to cubic), respectively.[20] The intermediate rhombohedral phase belongs to the $R\bar{3}m$ space group with the lattice constant of a = 7.022 Å, having ordered Ag and

Bi atoms in the distinguishable positions, while in the high-temperature cubic phase (space group $Fm\bar{3}m$, a = 5.832 Å), the Ag and Bi atoms are disordered.[20] In order to understand the structural phase transition in the present samples, we have performed temperature dependent (300-623 K) synchrotron powder X-ray diffraction (PXRD) (E = 12.42 KeV and λ = 0.998 Å) of $AgBiSe_2$ (Figure 6.1(b)). Temperature dependent PXRD data clearly indicates a structural transition from rhombohedral to cubic phase above 573 K, but the hexagonal to rhombohedral phase transition was not properly differentiated. Similar observation of structural phase transitions has been recorded in solution grown $AgBiSe_2$ nanocrystal samples.[17,19] Differential scanning calorimetric (DSC) measurements (Figure 6.1(c)) clearly shows a peak at 585 K, which is due to rhombohedral to cubic phase transition in $AgBiSe_2$. An onset (T ~ 480 K) of a low-intensity peak has been evidenced, which is near to the hexagonal to rhombohedral phase transition temperature.[17]

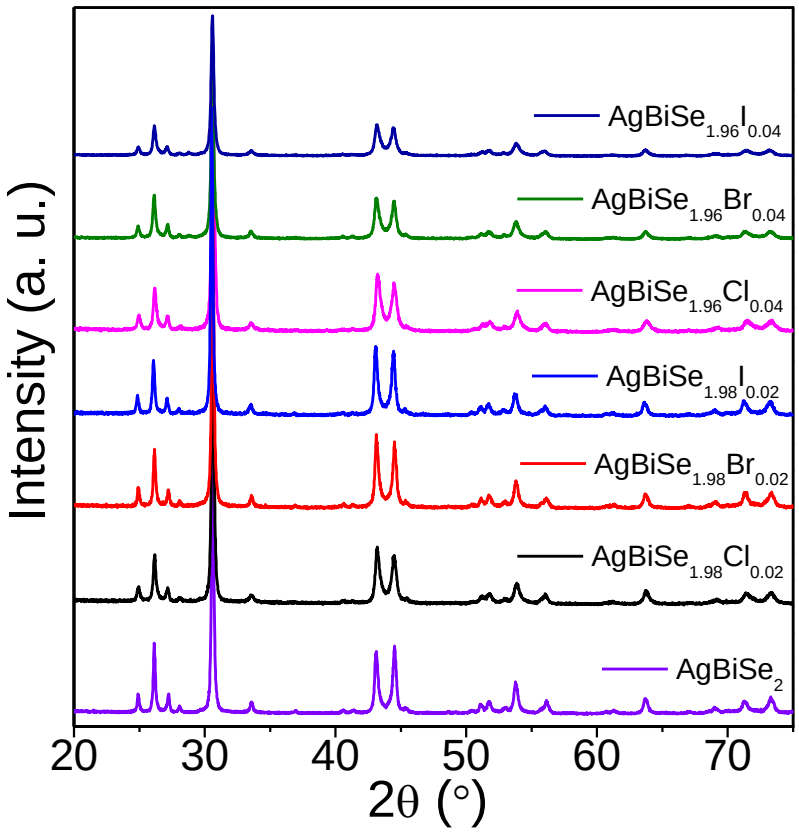

Figure 6.2 Room temperature powder XRD pattern of pristine $AgBiSe_2$ and $AgBiSe_{2-x}X_x$ (X = Cl, Br, I; x = 2-4 mol%) recorded at lab source (Cu Kα ;λ= 1.5406 Å).

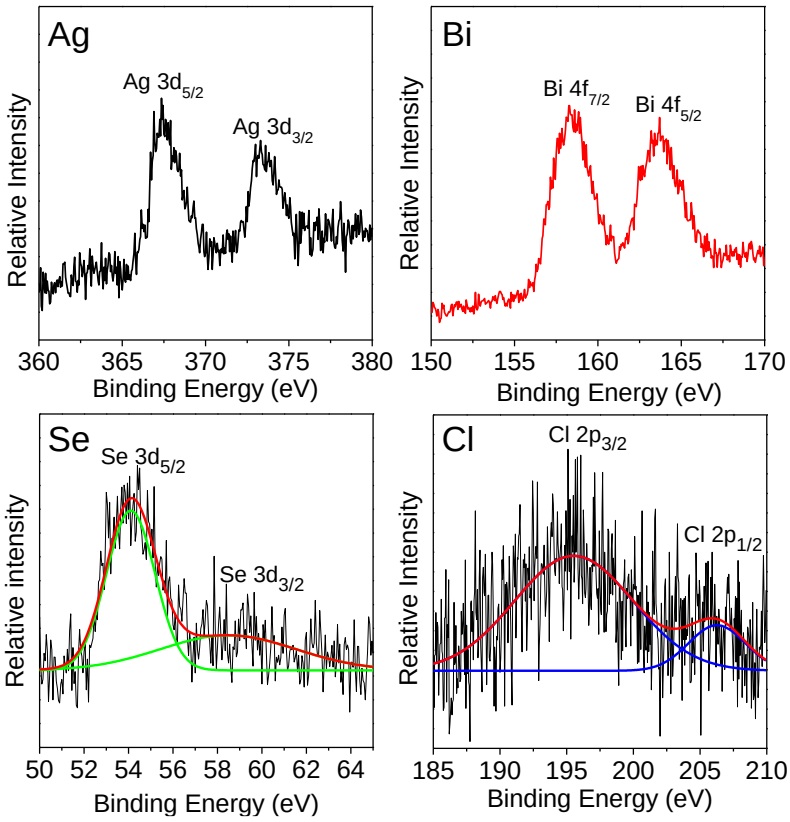

Figure 6.3 X-ray photoelectron spectra of as prepared $AgBiSe_{1.98}Cl_{0.02}$ (a) Ag 3d, (b) Bi 4f, (c) Se 3d and (d) Cl 2p spectra.

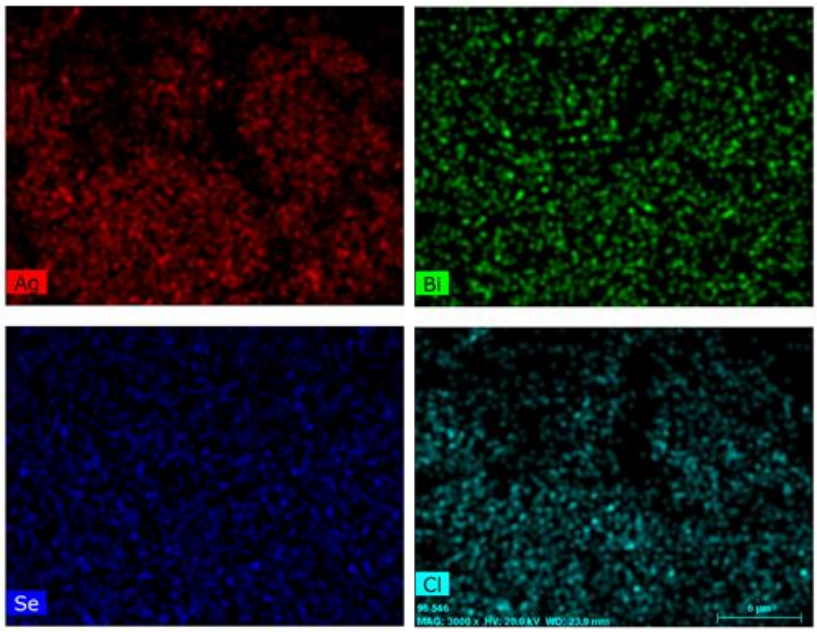

Figure 6.4 Energy dispersive X-ray elemental mapping of $AgBiSe_{1.98}Cl_{0.02}$ sample.

Room temperature powder XRD patterns of pristine $AgBiSe_2$ and $AgBiSe_{2-x}X_x$ (X = Cl, Br, I; x = 2-4 mol%) samples were measured in lab source (Cu Kα; λ = 1.5406 Å), which has been shown in Figure 6.2. The XRD patterns of the all the halogen doped samples could be indexed based on room temperature hexagonal phase of $AgBiSe_2$ (space group $P\bar{3}m1$), with no impurity phase being observed within the detection limits of powder XRD, which indicates successful substitution of halogen in the Se site of $AgBiSe_2$. Substitution of the halogen was further confirmed by X-ray photoelectron spectroscopy (Figure 6.3) and energy dispersive X-ray elemental mapping analysis (Figure 6.4) of the $AgBiSe_{1.98}Cl_{0.02}$ sample.

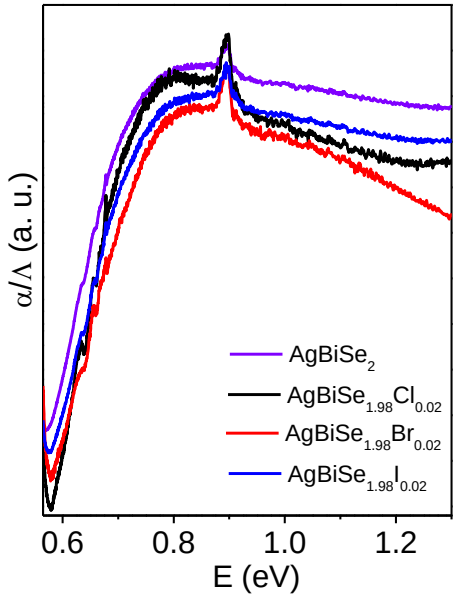

Figure 6.5 Optical absorption spectra of pristine $AgBiSe_2$ and $AgBiSe_{1.98}X_{0.02}$ (X = Cl, Br, I) samples.

In Figure 6.5 we have presented room temperature optical absorption spectra of pristine $AgBiSe_2$ and $AgBiSe_{1.98}X_{0.02}$ (X = Cl, Br and I) samples. The spectroscopically measured band gap of the pristine $AgBiSe_2$ is ~0.6 eV, which is typical of a narrow band gap semiconductor. Measured band gaps of $AgBiSe_{2-x}X_x$ (X = Cl, Br, I; x = 2 mol%) are slightly higher compared to that of pristine $AgBiSe_2$. The larger band gap in halogen doped samples is due to the higher electronegativity of the halogen (Cl = 3.16, Br = 2.96, I = 2.66 in Pauling scale) compared to that of selenium (2.55). Thus, the more ionic character of the metal-halogen bond than the metal-selenium bond results in widening the

band gap of $AgBiSe_{1.98}X_{0.02}$ (X = Cl, Br, I). These results also support successful substitution of halogens in the Se site of $AgBiSe_2$.

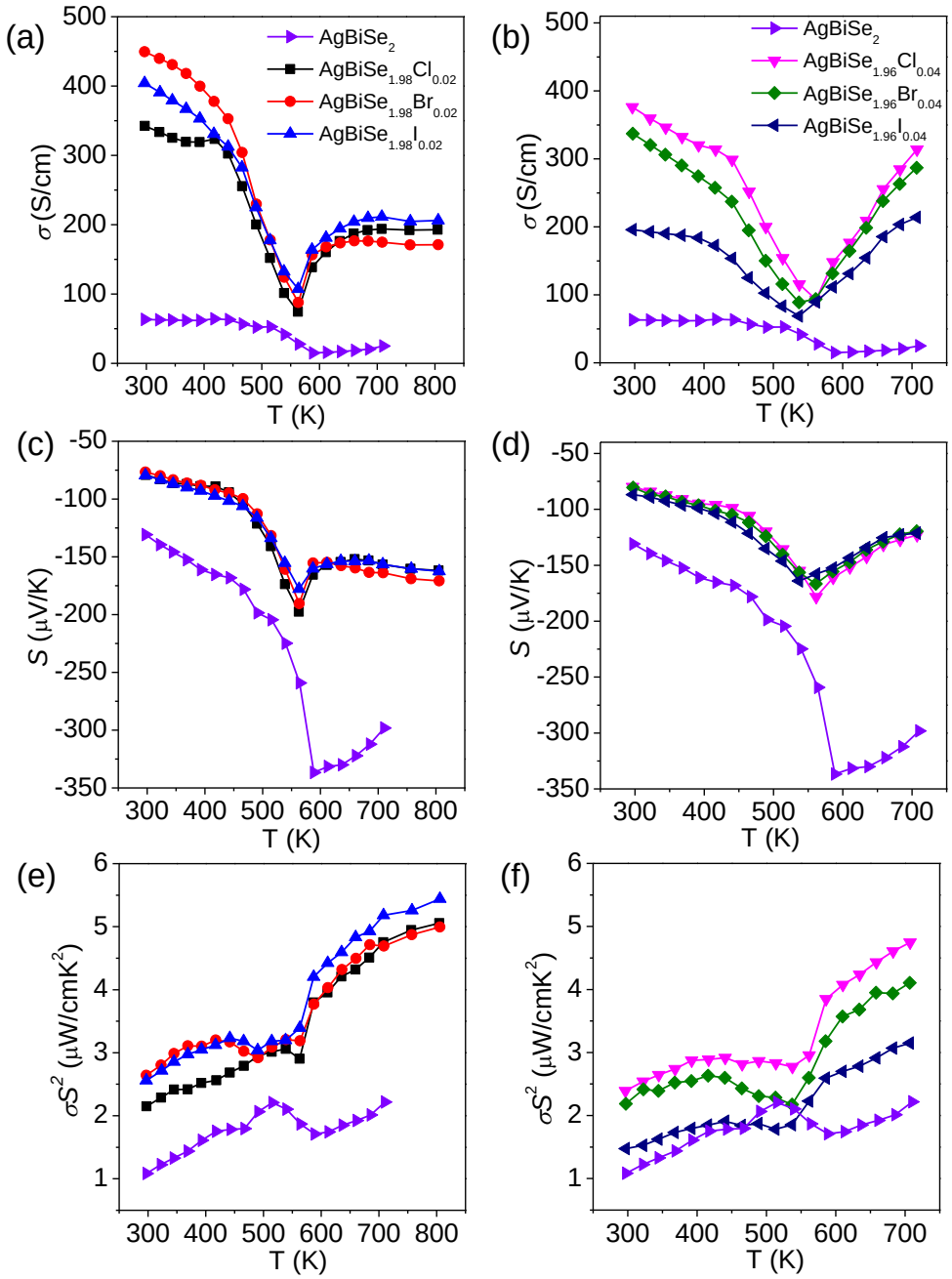

Figure 6.6 Temperature dependent electrical conductivity (σ), Seebeck coefficient (S) and power factor (σS^2). (a), (c) and (e) for $AgBiSe_{1.98}X_{0.02}$ (X = Cl, Br, I) and (b), (d) and (f) for $AgBiSe_{1.96}X_{0.04}$ (X = Cl, Br, I) with pristine $AgBiSe_2$.

Temperature dependent electronic transport properties of pristine $AgBiSe_2$ and $AgBiSe_{2-x}X_x$ (X = Cl/Br/I; x = 2-4 mol%) samples have been presented in Figure 6.6. In Figure 6.5(a), we show temperature dependent electrical conductivity (σ) of $AgBiSe_2$ and

$AgBiSe_{1.98}X_{0.02}$ (X = Cl, Br, I) samples. A σ value of ~63 S cm^{-1} has been measured at room temperature in the case of pristine $AgBiSe_2$, which remains almost flat up to ~460 K (hexagonal to rhombohedral phase transition temperature). In the rhombohedral phase (temperature range of 460-580 K), temperature dependent σ decreases continuously from 52 S cm^{-1} to 16 S cm^{-1} and behaves like a metallic phase. $AgBiSe_2$ transforms to cubic phase around 585 K, and then temperature dependent σ value increases to 24 S cm^{-1} at 708 K. σ of 2 mol% halogen doped samples are significantly higher compared to that of pristine $AgBiSe_2$ sample. Typically, the $AgBiSe_{1.98}Cl_{0.02}$ sample shows a σ of 343 S cm^{-1} at room temperature then decreases to 300 S cm^{-1} at 450 K (hexagonal to rhombohedral phase transition temperature). In the rhombohedral phase, temperature dependent σ decreases with increasing temperature and reaches a value of 73 S cm^{-1} at 562 K, indicating the metallic behavior. In the cubic phase of $AgBiSe_{1.98}Cl_{0.02}$, temperature dependent σ increases with increasing the temperature to reach a value of 193 S cm^{-1} at 810 K. Temperature dependent σ of $AgBiSe_{1.98}X_{0.02}$ (X = Cl, Br, I) samples show typical metal to semiconductor transition during rhombohedral to cubic phase transformation. The room temperature σ of 2 mol% Br-doped $AgBiSe_2$ sample is higher compared to that of 2 mol% Cl and I doped samples (see Table 6.1). The effective ionic radius of Cl^-, Br^-, I^- and Se^{2-} are 1.81, 1.96, 2.20 and 1.98 Å respectively.[21] Thus, higher σ value for $AgBiSe_{1.98}Br_{0.02}$ sample is due to the perfect substitution of Br^- ion in the Se^{2-} sublattice because of close matching of the ionic radius. Overall, the result indicates that halogen dopants can effectively enhance the electrical conductivity of $AgBiSe_2$ by doping electrons in the conduction band of $AgBiSe_2$. We have also investigated electronic transport properties of $AgBiSe_{1.96}X_{0.04}$ (X = Cl, Br, I) samples (Figure 6.6(b)). Room temperature σ for the 4 mol% Cl-doped samples is higher than that of 2 mol% Cl-doped $AgBiSe_2$ samples (Table 6.1), while the room temperature σ value of the 4 mol% Br/I doped samples is lower than that of 2 mol% Br/I doped $AgBiSe_2$ (Table 6.1).

The Hall coefficient, R_H, at room temperature is negative for pristine and halogen doped $AgBiSe_2$ samples, which indicates *n*-type conduction. Assuming parabolic bands and single band conduction process at 300 K, we have estimated the carrier concentration, *n*, from the formula: $n = 1/eR_H$, where *e* is the electronic charge. Measured

carrier concentrations and carrier mobilities of pristine and halogen doped samples are presented in Table 6.1. Carrier concentration (n) increases from 5.85×10^{18} cm^{-3} for the pristine $AgBiSe_2$ to 3.72×10^{19} cm^{-3} for the $AgBiSe_{1.98}Cl_{0.02}$ sample. Carrier mobility (μ) decreases slightly for the 2 mol% halogen doped samples compared to that of pristine $AgBiSe_2$. Thus, the increase in the σ in 2 mol% halogen doped $AgBiSe_2$ is primarily due to an increase in the carrier concentration after halogen doping. Although 4 mol% halogen doped $AgBiSe_2$ samples show increased carrier concentration compared to 2 mol% halogen doped $AgBiSe_2$ samples, μ is lower in the case of 4 mol% halogen doped samples. The decrease of μ in 4 mol% halogen doped samples is due to excess charge carrier scattering from the point defects created by solid solution halogen doping.

Table 6.1 Room temperature carrier concentration (n), electrical conductivity (σ), carrier mobility (μ) and effective mass (m^*) of pristine $AgBiSe_2$ and $AgBiSe_{2-x}X_x$ (X = Cl, Br, I; x = 2-4 mol%) samples.

Sample	n (cm^{-3})	σ (S cm^{-1})	μ (cm^2 V^{-1} s^{-1})	m^*/m_0
$AgBiSe_2$	5.85×10^{18}	63	67	0.25
$AgBiSe_{1.98}Cl_{0.02}$	3.72×10^{19}	343	57	0.46
$AgBiSe_{1.98}Br_{0.02}$	4.63×10^{19}	450	61	0.51
$AgBiSe_{1.98}I_{0.02}$	3.98×10^{19}	404	63	0.48
$AgBiSe_{1.96}Cl_{0.04}$	4.77×10^{19}	376	49	0.55
$AgBiSe_{1.96}Br_{0.04}$	4.60×10^{19}	337	46	0.54
$AgBiSe_{1.96}I_{0.04}$	4.65×10^{19}	196	26	0.59

In Figure 6.6(c), we present temperature dependent Seebeck coefficient (S) of $AgBiSe_2$ and $AgBiSe_{1.98}X_{0.02}$ (X = Cl, Br, I) samples. The negative sign of the S confirms the n-type conduction. The S value for pristine $AgBiSe_2$ is -131 μV K^{-1} at room temperature, which increases slowly with increasing temperature up to ~460 K, and then within the rhombohedral phase, S increases quickly with increasing temperature to reach a value of -338 μV K^{-1} at ~585 K. After the rhombohedral to cubic phase transition temperature, S reaches a value of -300 μV K^{-1} at ~710 K. Halogen doping in $AgBiSe_2$ has a significant effect on the temperature dependent thermopower. All the halogen doped samples show lower S values compared to that of pristine $AgBiSe_2$ (Figure 6.6(c) and 6.6(d)). The decrease in the S in halogen doped samples is due to increase in the carrier

concentration in the system as, according to Mott-Jones formula, S is inversely proportional to the carrier concentration (n) and can be estimated as $S \sim n^{-2/3}$.[3] Typically, $AgBiSe_{1.98}Cl_{0.02}$ sample shows a S value of -81 μV K^{-1} at room temperature, which slowly increases with increasing the temperature up to hexagonal to rhombohedral phase transition temperature (460 K) then increases rapidly to reach a value of -198 μV K^{-1} at ~562 K within the rhombohedral phase. In the cubic phase of $AgBiSe_{1.98}Cl_{0.02}$, temperature dependent S decreases initially after rhombohedral to cubic phase transition and then remains almost flat and shows a value of -163 μV K^{-1} at 810 K. Similar anomalies in the temperature dependent S have been observed in n-type Nb-doped $AgBiSe_2$ bulk ingot.[17] It must be mention that solution grown p-type $AgBiSe_2$ nanocrystals show interesting reversible p-n-p type conduction (thermopower) switching,[19] which we have not observed in the present case. We have estimated the carrier effective mass (m^*) values at room temperature using equations (3.1)-(3.3) given in chapter 3 (page 110). A detailed discussion on m^* calculation has been given in chapter 3. The calculated m^* values for all the samples have been presented in Table 6.1. Calculated m^* values for the $AgBiSe_{2-x}X_x$ (X = Cl, Br, I; x = 2-4 mol%) samples are higher compared to that of bulk n-type BiAgSeS (~0.36 m_o) with rock salt structure.[15]

Figure 6.6(e) represents the temperature dependent power factors (σS^2) of the pristine and $AgBiSe_{1.98}X_{0.02}$ (X = Cl, Br, I) samples. A maximum σS^2 of ~2.23 μW/cm K^2 at ~708 K has been achieved for the pristine sample. σS^2 values for the halogen doped samples are significantly higher than that of the pristine sample. Typically, the $AgBiSe_{1.98}I_{0.02}$ sample shows a σS^2 value of ~2.56 μW/cm K^2 at room temperature, which increases to a value of ~5.45 μW/cm K^2 at ~810 K. Superior electrical transport in the $AgBiSe_{1.98}X_{0.02}$ (X = Cl, Br, I) compared to the pristine $AgBiSe_2$ results in improved σS^2 in $AgBiSe_{1.98}X_{0.02}$ (X = Cl, Br, I) samples. The σS^2 values for the 4 mol% halogen doped samples are lower than that of 2 mol% halogen doped samples throughout the measured temperature range (Figure 6.6(f)), which is primarily due to low σ values at low temperatures and low S values at high temperature.

The total thermal conductivity, κ_{total}, of pristine and $AgBiSe_{1.98}X_{0.02}$ (X = Cl, Br, I) samples was estimated over the 300-823 K temperature range using the formula, $\kappa_{total} = DC_p\rho$, where D is the thermal diffusivity, C_p is specific heat and ρ is density of the

sample (Figure 6.7). The density of the pellets obtained was in the range ~98% of the theoretical density. Temperature dependent *D* was measured by laser flash diffusivity

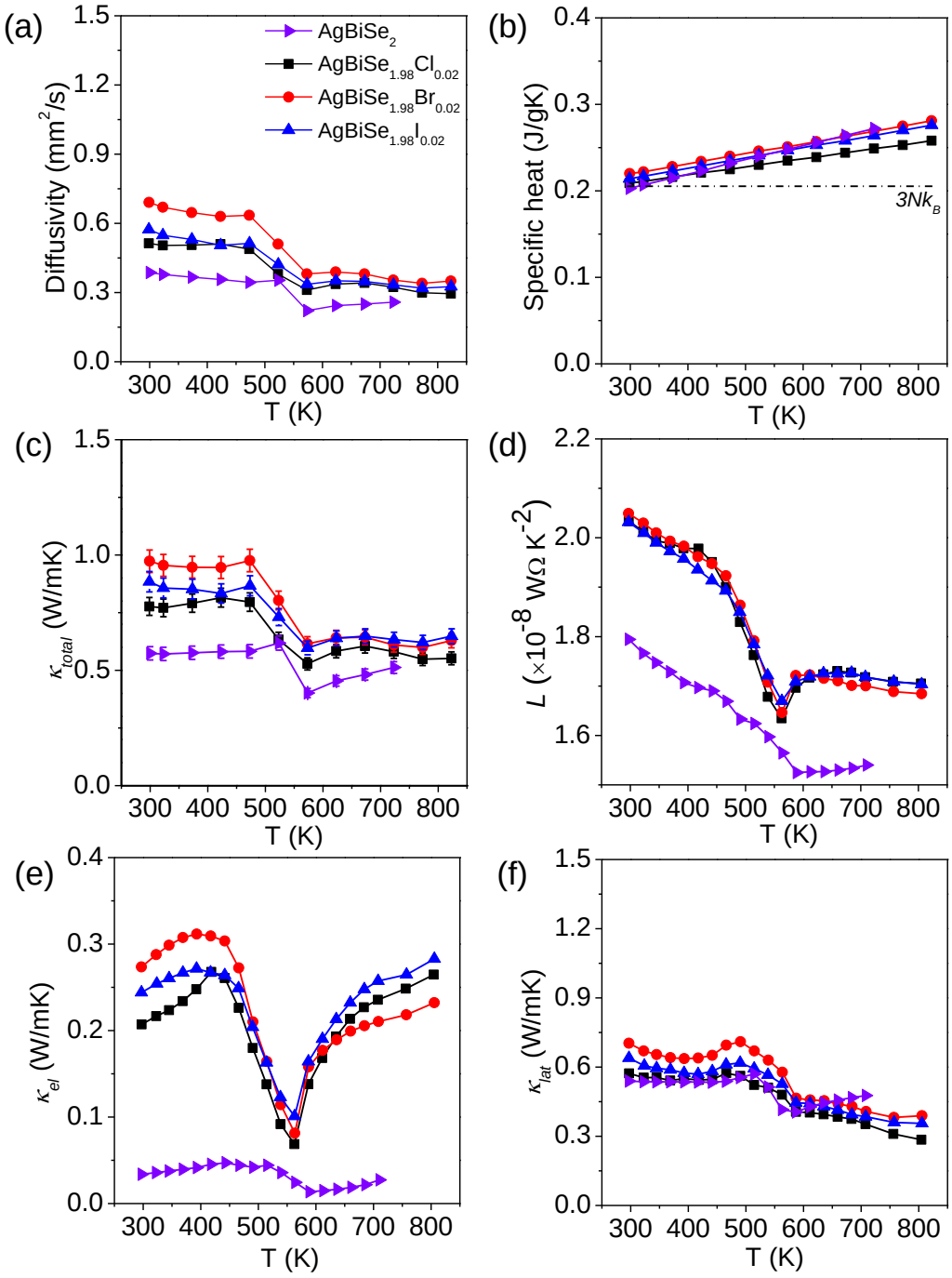

Figure 6.7 Temperature dependent (a) thermal diffusivity (*D*), (b) specific heat (C_p), (c) total thermal conductivity (κ_{total}) with 5% error bar (d) calculated Lorenz numbers (e) electronic thermal conductivity (κ_{lat}) and (f) lattice thermal conductivity (κ_{lat}) of $AgBiSe_2$ and $AgBiSe_{1.98}X_{0.02}$ (X = Cl, Br and I) samples.

technique over 300-823 K range (Figure 6.7(a)). Temperature dependent C_p was derived during diffusivity measurement were plotted with Dulong-Petit C_p value in Figure 6.7(b). C_p values are consistent with the previously reported values of Nb-doped $AgBiSe_2$.[17] At room temperature, a κ_{total} value of ~0.77 W m^{-1} K^{-1} was measured for $AgBiSe_{1.98}Cl_{0.02}$, which remains almost same up to ~470 K (Figure 6.7(c)). With further increase in temperature, within the rhombohedral phase, κ_{total} decreases with increasing temperature to reach a minimum value of ~0.52 W m^{-1} K^{-1} at 570 K. Above the rhombohedral to cubic phase transition temperature (575 K), κ_{total} of $AgBiSe_{1.98}Cl_{0.02}$ remains almost the same up to ~823 K. We have observed similar trend in the temperature dependent κ_{total} in Br/I doped $AgBiSe_2$ samples.

Table 6.2 Measured room temperature κ_{total} and κ_{lat} value of present samples in comparison with the previously reported samples of $AgBiSe_2$.

Sample	κ_{total} (W m^{-1} K^{-1}) at 300 K	κ_{lat} (W m^{-1} K^{-1}) at 300 K
$AgBiSe_2$ (present work)	~0.58	~0.54
$AgBiSe_2$[22]	~0.63	~0.58
$AgBiSe_{1.98}Cl_{0.02}$ (present work)	~0.77	~0.57
$Ag_{0.98}Nb_{0.02}BiSe_2$[22]	~0.77	~0.58

The electronic thermal conductivity has been estimated using Wiedemann-Franz law: $\kappa_{el} = L\sigma T$, where Lorenz number, L, was extracted based on the fitting of the respective S values that estimate the reduced chemical potential (Figure 6.7(d) and (e)). The lattice thermal conductivity, κ_{lat}, was obtained by subtracting the electronic thermal conductivity, κ_{el}, from the κ_{total} and plotted in Figure 6.7(f). At room temperature, a κ_{lat} value of ~0.57 W m^{-1} K^{-1} was measured for $AgBiSe_{1.98}Cl_{0.02}$, which remains almost the same up to ~470 K (Figure 6.7(f)). With further increase in the temperature to ~810 K, κ_{lat} decreases to reach a value of ~0.27 W m^{-1} K^{-1}. κ_{total} and κ_{lat} values of the present samples are comparable to the values reported in previous literature (Table 6.2).[17,23] Low value of κ_{lat} above the order-disorder phase transition (rhombohedral -cubic) temperature (~570 K) is due to (a) phonon softening owing to a high degree of anharmonicity of Bi-Se bonds caused by the stereochemically active lone pair ($6s^2$) on Bi and (b) effective phonon scattering by the disordered Ag/Bi lattice in the cubic phase of

$AgBiSe_2$. Thermal transport properties of 4 mol% doped samples have been presented in Figure 6.8. All the 4 mol% halogen doped samples also exhibit reasonably low κ_{total} values throughout the measured temperature range.

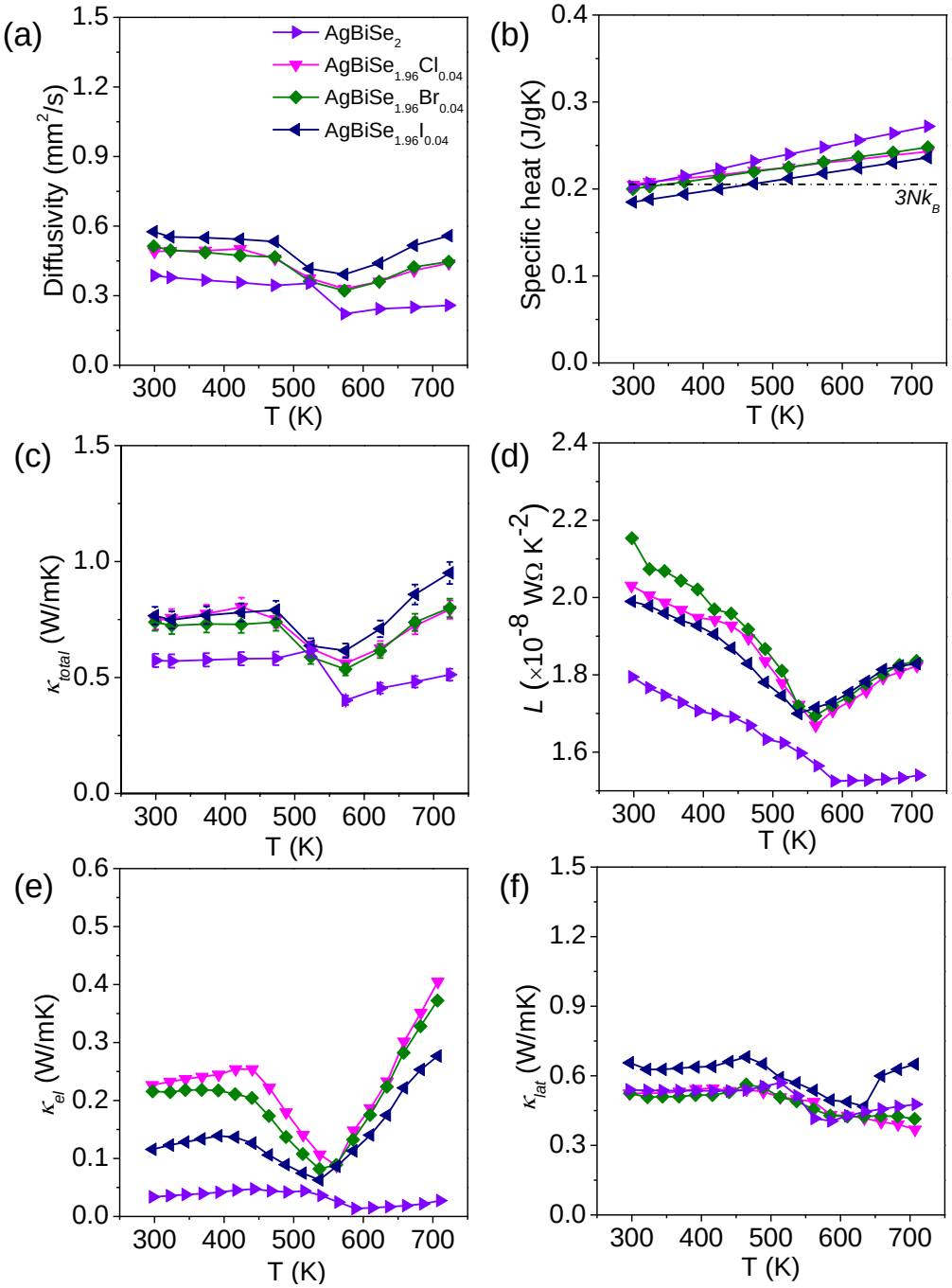

Figure 6.8 Temperature dependent (a) thermal diffusivity (D), (b) specific heat (C_p), (c) total thermal conductivity (κ_{total}) with 5% error bar (d) calculated Lorenz numbers (e) electronic thermal conductivity (κ_{lat}) and (f) lattice thermal conductivity (κ_{lat}) of $AgBiSe_2$ and $AgBiSe_{1.96}X_{0.04}$ (X = Cl, Br and I) samples.

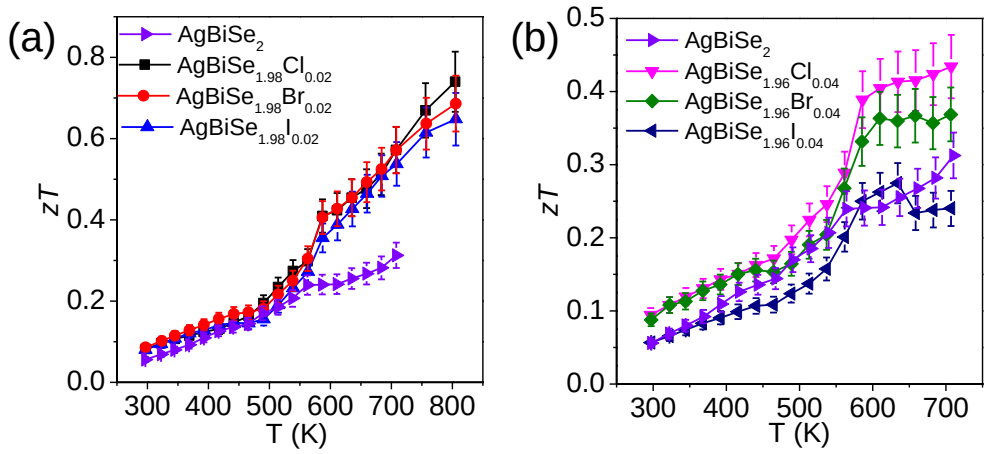

Figure 6.9 Temperature dependent thermoelectric figure merit, zT of (a) $AgBiSe_{1.98}X_{0.02}$ (X = Cl, Br and I) and (b) $AgBiSe_{1.96}X_{0.04}$ (X = Cl, Br and I) with pristine $AgBiSe_2$. 10% error bar is shown for zT estimation.

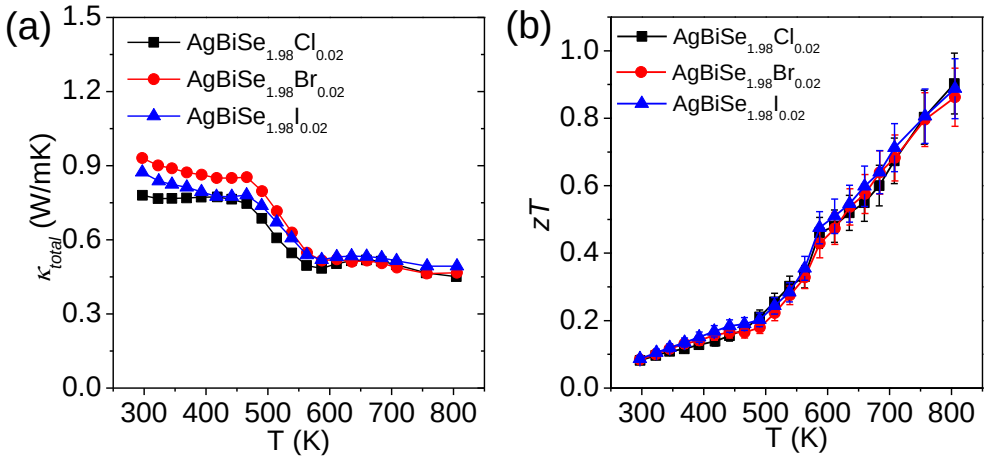

Figure 6.10 Temperature dependent (a) total thermal conductivity (κ_{total}) using Dulong-Petit C_p, and (b) zT of $AgBiSe_{1.98}X_{0.02}$ (X = Cl, Br and I) samples estimated using Dulong-Petit C_p. 10% error bar is shown for zT estimation.

Temperature dependent thermoelectric figure of merit, zT, has been estimated from the measured electrical and thermal transport data in 300-810 K range for pristine and $AgBiSe_{2-x}X_x$ (X = Cl, Br, I; x = 2-4 mol%) samples (Figure 6.9). A peak zT value of ~0.31 at ~708 K has been achieved for pristine $AgBiSe_2$. Among the halogen-doped samples, $AgBiSe_{1.98}Cl_{0.02}$ shows the highest zT value with a peak zT of ~0.75 at ~810 K. In the case of *n*-type bulk Nb-doped $AgBiSe_2$ samples, Dulong-Petit C_p was used for the calculation of temperature dependent zT.[17] In order to compare the present zT of halogen doped $AgBiSe_2$ with the zT of previously reported Nb-doped $AgBiSe_2$ samples, we have also estimated the zT of the $AgBiSe_{1.98}X_{0.02}$ (X = Cl, Br, I) sample using Dulong-Petit C_p, which has been presented in Figure 6.10(b). A peak zT value of ~0.9 at ~810 K has been

achieved for the $AgBiSe_{1.98}Cl_{0.02}$ sample, which is comparable to the performance of previously reported Nb-doped $AgBiSe_2$ samples.[17] Thus, the present study indicates that high thermoelectric performance in *n*-type $AgBiSe_2$ can be achieved by aliovalent anion doping.

6.4 Conclusions

In conclusion, high-quality crystalline ingots of *n*-type $AgBiSe_2$ and $AgBiSe_{2-x}X_x$ (X = Cl, Br, I; x = 2-4 mol%) were grown by the simple melting of elemental metal and chalcogen followed by cooling to room temperature. Carrier concentrations in *n*-type $AgBiSe_2$ could be optimized by doping of a small amount of halogen in the Se sublattice of $AgBiSe_2$ to achieve superior electrical conductivity compared to the pristine sample. Halide ion ($Cl^-/Br^-/I^-$) aliovalently dopes on the Se^{2-} sublattice, and from simple valence counting, contributes one *n*-type carrier in $AgBiSe_2$, which gives rise to improved electronic transport property. Metal to semiconductor type transition is evidenced during rhombohedral to cubic phase transformation in halogen doped $AgBiSe_2$. The combination of enhanced electrical conductivity and a reasonably high Seebeck coefficient results in high power factor values peaking at a high temperature of ~810 K. A high degree of anharmonicity in the Bi-Se bond, and effective phonon scattering by the disordered Ag/Bi lattice gives rise to ultra-low κ_{lat} in the cubic phase of $AgBiSe_2$. A peak zT value of ~0.9 at ~810 K has been achieved for the $AgBiSe_{1.98}Cl_{0.02}$ sample, which makes it a promising *n*-type thermoelectric material for mid-temperature applications.

References

[1] J. R. Sootsman, D. Y. Chung, M. G. Kanatzidis, *Angew. Chemie - Int. Ed.* **2009**, *48*, 8616–8639.

[2] G. Tan, L.-D. Zhao, M. G. Kanatzidis, *Chem. Rev.* **2016**, *116*, 12123–12149.

[3] G. J. Snyder, E. S. Toberer, *Nat. Mater.* **2008**, *7*, 105–114.

[4] W. G. Zeier, A. Zevalkink, Z. M. Gibbs, G. Hautier, M. G. Kanatzidis, G. J. Snyder, *Angew. Chemie - Int. Ed.* **2016**, *55*, 6826–6841.

[5] S. N. Guin, A. Chatterjee, D. S. Negi, R. Datta, K. Biswas, *Energy Environ. Sci.* **2013**, *6*, 2603–2608.

[6] S. N. Guin, K. Biswas, *J. Mater. Chem. C* **2015**, *2*, 10415–10421.

[7] F. D. Rosi, E. F. Hockings, N. E. Lindenblad, *RCA Rev.* **1961**, *22*, 82–121.

[8] H. Wang, J.-F. Li, M. Zou, T. Sui, *Appl. Phys. Lett.* **2008**, *93*, 202106.

[9] K. Kurosaki, A. Kosuga, H. Muta, M. Uno, S. Yamanaka, *Appl. Phys. Lett.* **2005**, *87*, 61919.

[10] A. Yusufu, K. Kurosaki, A. Kosuga, T. Sugahara, Y. Ohishi, H. Muta, S. Yamanaka, *Appl. Phys. Lett.* **2011**, *99*, 61902.

[11] X.Shi, *J. Mater. Chem. A* **2014**, *2*, 13527.

[12] D.-Y. Chung, T. Hogan, P. Brazis, M. Rocci-lane, C. Kannewurf, M. Bastea, C. Uher, M. G. Kanatzidis, *Science* **2000**, *287*, 1024–2027.

[13] M. K. Jana, K. Pal, U. V. Waghmare, K. Biswas, *Angew. Chemie - Int. Ed.* **2016**, *55*, 7792–7796.

[14] H. Lin, G. Tan, J. N. Shen, S. Hao, L. M. Wu, N. Calta, C. Malliakas, S. Wang, C. Uher, C. Wolverton, et al., *Angew. Chemie - Int. Ed.* **2016**, *55*, 11431–11436.

[15] Y.-L. Pei, H. Wu, J. Sui, J. Li, D. Berardan, C. Barreteau, L. Pan, N. Dragoe, W.-S. Liu, J. He, et al., *Energy Environ. Sci.* **2013**, *6*, 1750.

[16] D. Wu, Y. Pei, Z. Wang, H. Wu, L. Huang, L. D. Zhao, J. He, *Adv. Funct. Mater.* **2014**, *24*, 7763–7771.

[17] L. Pan, D. Bérardan, N. Dragoe, *J. Am. Chem. Soc.* **2013**, *135*, 4914–4917.

[18] C. Xiao, J. Xu, B. Cao, K. Li, M. Kong, Y. Xie, *J. Am. Chem. Soc* **2012**, *134*, 7971–7977.

[19] C. Xiao, X. Qin, J. Zhang, R. An, J. Xu, K. Li, B. Cao, J. Yang, B. Ye, Y. Xie, *J.*

Am. Chem. Soc. **2012**, *134*, 18460–18466.

[20] S. Geller, J. H. Wernick, *Acta Crystallogr.* **1959**, *12*, 46–54.

[21] R. D. Shannon, *Acta Crystallogr. Sect. A* **1976**, *32*, 751–767.

[22] L. Pan, D. Be, N. Dragoe, *J. Am. Chem. Soc.* **2013**, *135*, 4914–4917.

[23] M. D. Nielsen, V. Ozolins, J. P. Heremans, *Energy Environ. Sci.* **2013**, *6*, 570–578.

Chapter 7

Kinetically stabilized rocksalt $AgBiS_2$ nanocrystals : temperature induced order-disorder phase transition and associated anomalous thermoelectric properties *

*Publication based on this work: (1) *Chem. Mater.* **2013,** *25,* 3225; (2) *Inorg. Chem.* **2016,** *55,* 2323.

CHAPTER 7

Kinetically stabilized cubic $AgBiS_2$ nanocrystals: temperature induced order-disorder transition and associated anomalous thermoelectric properties

Summary: *High temperature rock salt phases of $AgBiS_2$ and $AgBiS_{2-x}Se_x$ (x = 0.05-0.1) have been kinetically stabilized at room temperature in the form of nanocrystal (~11 nm) by simple solution-based synthesis. Experimental evidence for cubic nanocrystals derives from variable temperature powder X-ray diffraction (XRD), band gap measurement, X-ray photoelectron spectroscopy (XPS), transmission electron microscopy (TEM), and electron diffraction analysis. The existence of fascinating order-disorder type transition in these nanocrystals was evidenced by temperature dependent electrical conductivity, thermopower, and heat capacity measurements. Disordered cation sublattice and nanoscale grain boundaries coupled with strong Bi-S bond anharmonicity allow effective phonon scattering, which leads to low lattice thermal conductivity of the nanocrystalline $AgBiS_2$. The origin of order-disorder phase transition and the associated anomalous change of thermopower in $AgBiS_2$ nanocrystals was investigated by using a combined experimental, density functional theory based first-principles calculation and ab initio molecular dynamics simulations. Positron annihilation spectroscopy indicates the presence of higher numbers of Ag vacancies in the nanocrystal compared to that of the bulk cubic counterpart at room temperature. Furthermore, temperature-dependent two-detector coincidence Doppler broadening spectroscopy and Doppler broadening of the annihilation radiation (S-parameter) indicate that the Ag vacancy concentration increases abruptly during the order-disorder transition in nanocrystalline $AgBiS_2$. At high temperature, an Ag atom shuttles between the vacancy and interstitial sites to form a locally disordered cation sublattice in the nanocrystal, which is facilitated by the formation of more Ag vacancies during the phase transition. This process increases the entropy of the system at higher vacancy concentration, which, in turn, results in the unusual rise in thermopower.*

7.1 Introduction

Phase transition in inorganic solids is a commonly identified phenomenon that can occur because of the effect of physical perturbations like temperature, voltage, pressure, etc.[1,2] The discovery or design of a new polymorphic material and physical understanding of its phase transitions are important for fundamental structure-property correlations. The physical and physicochemical properties of the material can be tuned significantly by tailoring their chemical composition, crystal structure, electronic structure, and particle size or morphology. Hence, apart from the solid-state high-temperature synthesis techniques, different low-temperature synthesis methods like the seeded growth method, polyol process, solvothermal method, and hot injection have been explored for the synthesis of materials with different size and shape. Bottom-up wet chemical synthesis of various thermoelectric nanomaterials, such as $Bi_xSb_{2-x}Te_3$,[3–5] $Bi_2Te_xSe_{3-x}$,[6] $Cu_2ZnGeSe_4$,[7] $Cu_2ZnSnSe_4$,[8] $Cu_2CdSnSe_4$,[9] $Ag_2S_xSe_{1-x}$[10] and Cu_2ZnSnS_4[11] followed by densification into nanostructured bulk materials provides an efficient route for decreasing the thermal conductivity, and thus tune the thermoelectric figure of merit.

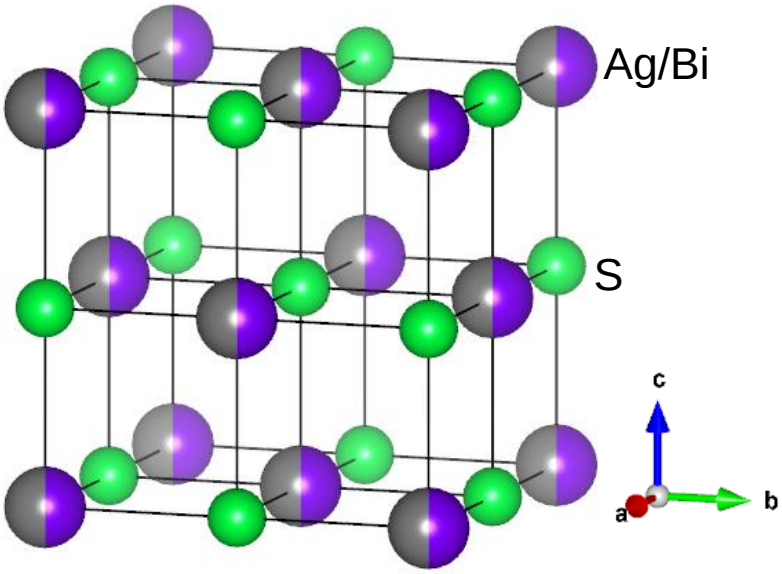

Figure 7.1 Crystal structure of the high temperature cubic phase of $AgBiS_2$ with disordered Ag/Bi positions.

Ternary silver bismuth sulfide, $AgBiS_2$, is a typical member of I-V-VI_2 family (where I = Cu, Ag, Au; V = As, Sb, Bi; and VI = S, Se, Te). It is a polymorphic semiconductor and shows structural phase transition as a function of the temperature. In

the bulk phase, $AgBiS_2$ crystallizes in a hexagonal crystal structure (space group, $P\bar{3}m1$) at room temperature, which transforms to a cation disordered rock salt structure (space group, $Fm\bar{3}m$) at ~473 K (Figure 7.1).[12] Although the cubic I-V-VI_2 compound crystallizes in cation disordered structure, Mahanti and coworkers predicted several plausible low-energy ordered structures using theoretical calculations.[13] Recently, transmission electron microscopy studies also support the theoretical prediction and evidence the local cation orderings in bulk cubic I-V-VI_2 compounds.[14,15] For example, in bulk $AgSbTe_2$, a tendency of ordering of Ag and Sb in nanoscale leads to the formation of spontaneous nanostructures in the $AgSbTe_2$ matrix.[14] However, stabilization of the pure-phase ordered cubic structure in I-V-VI_2 compounds was not known in the literature.

Here, we present a solution-based bottom-up synthesis of *n*-type $AgBiS_2$ and $AgBiS_{2-x}Se_x$ (x = 0.05-0.1) nanocrystals with cubic rock salt structure, which is otherwise stable only above 473 K in the bulk phase. Thermoelectrically important kinetic cubic phases have been stabilized at room temperature by solution-based synthesis along with the size reduction to the nanoscale. We highlight the structural, optical, electronic charge and thermal transport properties of the nanocrystals. The existence of astonishing order-disorder type transition in these nanocrystals was evidenced for the first time by temperature dependent σ, S and heat capacity measurements. Strong phonon scattering by the disordered cation sublattice, bond anharmonicity and nanoscale grain boundaries minimize the κ_{lat} to as low as 0.4-0.5 W m^{-1} K^{-1} in 290-830 K range.

We also shed light on the origin of such order-disorder phase transition and the associated anomalous change of thermopower in $AgBiS_2$ nanocrystals by using a combined experimental, density functional theory (DFT)-based first principles calculation and *ab- initio* molecular dynamics (AIMD) simulations. Raman spectroscopic analysis and theoretical investigation indicate the existence of different structure and bonding characteristics in nanocrystal and bulk $AgBiS_2$. The nanocrystal prefers the Ag/Bi ordered structure at room temperature, whereas the bulk phase adopts the disordered structure. Shuttling of Ag atom between the vacant and interstitial sites at higher temperatures leads to a transition from cation ordered structure to a thermodynamically stable locally disordered structure in nanocrystalline $AgBiS_2$.

Positron annihilation spectroscopy reveals the formation of a larger number of Ag vacancies in $AgBiS_2$ nanocrystals compared to its bulk counterpart at high temperatures, which eventually provide the path for Ag-ion shuttling. Additionally, a synergistic increase in the entropy due to Ag-ion shuttling triggered by Ag vacancy formation during the phase transition and a change in the entropy due to charge-carrier transport resulted in a sudden enchantment in temperature dependent thermopower in nanocrystalline $AgBiS_2$ at 610 K.

7.2 Methods

7.2.1 Synthesis

Bismuth(III) acetate (Alfa Aesar, 99%), anhydrous silver acetate (Alfa Aesar, 99%), sulfur powder (Alfa Aesar, 99.999%), selenium powder (Aldrich, 99.5+%), oleic acid (Sigma-Aldrich, 90%), elemental silver (Ag; Alfa Aesar, 99.999%, metal basis), elemental bismuth (Bi; Alfa Aesar, 99.9999%, metal basis), and elemental sulfur (S; Alfa Aesar, 99.999%) were used for synthesis.

7.2.1.1 Synthesis of cubic $AgBiS_2$ nanocrystals. We have synthesized cubic $AgBiS_2$ nanocrystals using bottom-up soft chemical synthesis. At first, silver acetate (50 mg, 0.30 mmol), bismuth acetate (116 mg, 0.30 mmol), and oleic acid (10 mL) were combined in a round-bottom flask and the mixture was heated to 100 °C for 2 h with stirring in N_2 atmosphere. The resulting clear pale yellow metal oleate solution was transferred to a 25 mL Teflon-lined stainless steel autoclave and sulfur powder (19.2 mg, 0.60 mmol) was added inside an N_2-filled glovebox. Then the autoclave was placed in a preheated hot air oven for 2 h at 180 °C. The reaction was suddenly quenched by immersing the hot autoclave in ice-cold water. The black color nanocrystals of $AgBiS_2$ were precipitated out from the reaction mixture by adding excess ethanol and followed by centrifugation. $AgBiS_2$ nanocrystals were washed several times with a mixture of *n*-hexane and ethanol mixture and finally dried under vacuum at 60 °C for 2 h.

7.2.1.2 Synthesis of cubic $AgBiS_{2-x}Se_x$ (x = 0.05-0.1) nanocrystals. In a typical synthesis of $AgBiS_{1.92}Se_{0.08}$, silver acetate (50 mg, 0.30 mmol), bismuth acetate (116 mg, 0.30 mmol), and oleic acid (10 mL) were taken in a round-bottom flask and the mixture

was heated to 100 °C for 2 h with stirring under N_2 atmosphere. In addition to that, clear Se/S precursor solution was made by the reaction of 18.46 mg (0.576 mmol) S and 1.9 mg (0.024 mmol) Se powder in oleic acid at 130 °C for 2 h under N_2 atmosphere. Then the S/Se precursor solution was transferred into a 50 mL Teflon-lined stainless steel autoclave and silver/bismuth oleate precursor solution was added to it inside an N_2- filled glovebox. Then the autoclave was placed in preheated hot air oven for 2 h at 180 °C. The black color nanocrystals were precipitated out from the reaction mixture by centrifugation and were washed several times with n-hexane and ethanol and finally dried under vacuum at 60 °C for 2 h.

7.2.1.3 Capping agent removal and densification. In order to measure the electrical transport properties, the organic capping ligands from the surface of the nanocrystals were removed by treating the nanocrystals with *n*-hexane and a hydrazine solution (85% v/v) under vigorous stirring at room temperature. The hydrazine-treated nanocrystals were then pressed at room temperature into rectangular bars ($2 \times 2 \times 8$ mm^3) and disks (2 mm thick and 8 mm diameter) shaped samples. The rectangular and disk-shaped samples were sealed in a quartz tube under vacuum (10^{-5} Torr) and then sintered at 450 °C for 2 h. The density of the pellet used for the measurement was ∼92% of the theoretical density.

7.2.1.4 Synthesis of bulk cubic $AgBiS_2$. Bulk ingot (∼7 g) of bulk cubic $AgBiS_2$ was synthesized by mixing appropriate ratios of high-purity Ag, Bi, and S in an evacuated quartz tube. The tube was sealed under high vacuum (10^{-5} Torr), slowly heated to 723 K for 12 h, then heated to 1123 K in 4 h, annealed for 10 h, and, subsequently, ice-water quenched to trap the high-temperature cubic phase at room temperature. We cut and polished the bulk ingot to a parallelepiped ($2 \times 2 \times 8$ mm^3) for electronic transport measurement.

7.2.2 Characterizations

Room temperature and temperature dependent powder X-ray diffraction (XRD) of the sample was recorded using a Cu Kα (λ = 1.5406 Å) radiation on a Bruker D8 diffractometer. In addition, room temperature synchrotron powder XRD measurement was carried out with an X-ray beam of λ = 1.0279 Å, at BL-18B (Indian beamline), Photon Factory, KEK, Tsukuba, Japan. To probe optical energy gap optical diffuse reflectance measurement was performed on powder sample using a Perkin Elmer Lambda

900, UV/vis/NIR spectrometer. XPS measurements were performed with a Mg- *Kα* (1253.6 eV) X-ray source on an Omicron nanotechnology instrument. FESEM imaging has been performed using a NOVA NANO SEM 600 (FEI, Germany). Energy dispersive X-ray spectroscopy (EDX) analysis was performed with an EDAX Genesis instrument attached to the SEM column. TEM experiment was done using a JEOL (JEM3010). Elaborative discussions on all the characterizations have been given in the introduction part of the thesis (page 31).

7.2.3 Thermoelectric measurements

Seebeck coefficient and electrical conductivity were measured under helium atmosphere by ULVAC-RIKO ZEM-3 instrument from room temperature to 823 K. Thermal diffusivity, *D*, was directly measured by laser flash diffusivity method in a Netzsch LFA-457 under N_2 atmosphere from room temperature to 823 K. The longer direction coincides with the direction in which the thermal conductivity was measured. The total thermal conductivity, κ_{total}, was calculated using the formula, $\kappa_{total} = DC_p\rho$, where ρ is the density of the sample, measured using the sample dimension and mass, C_p is specific heat. Elaborative discussions on the thermoelectric measurements have been given in the introduction part of the thesis (page 41).

7.2.4 Positron annihilation spectroscopy

The positron annihilation lifetimes were measured with a fast-fast coincidence assembly consisting of two constant fraction differential discriminators (Fast ComTech; model 7029A).[16] The detectors were 25 mm length × 25 mm width tapered to 13-mm-diameter (truncated-conical) BaF_2 scintillators optically coupled to Philips XP2020Q photomultiplier tubes. The resolving time (full width at half-maximum, fwhm), measured with a ^{60}Co source and with the proper energy window (700-1320 keV for the start channel and 300-550 keV for the stop channel) of the fast-fast coincidence assembly, was 220 ps. For positron annihilation studies, a 10 μCi ^{22}Na source of positrons (enclosed between ~1.5 μm thin Ni foils) was sandwiched between two identical samples. Lifetime measurement was done at room temperature. For each sample, a total of 5×10^6 coincidence counts were recorded. The computer program PATFIT-8832[17] was used along with the necessary source corrections to evaluate all of the measured positron

lifetime spectra. For the temperature-dependent (300-750 K) Doppler broadening of positron annihilation radiation (DBPAR) measurement, a single HPGe detector (efficiency, 12%; type, PGC 1216sp of DSG) having an energy resolution of 1.1 keV at 514 keV of 85Sr was used. The source sample sandwich was kept in a vacuum-sealed heating oven with a temperature accuracy of ±2 K. The DBPAR spectrum was recorded in a dual ADC-based multiparameter data acquisition system (MPA-3 of FAST ComTec). The Doppler broadening of the annihilation 511 keV γ-ray spectrum was analyzed by evaluating the conventional line-shape parameters (S-parameter).[18,19] The S-parameter was calculated as the ratio of the counts in the central area of the 511 keV photopeak ($|511\ \text{keV} - E\gamma| \leq 0.85$ keV) and the total area of the photopeak ($|511\ \text{keV} - E\gamma| \leq 4.25$ keV). The S-parameter represents the fraction of positrons annihilating with the lower momentum electrons with respect to the total electrons annihilated. For the coincidence Doppler broadening (CDB) measurement, two identical HPGe detectors (efficiency, 12%; type, PGC 1216sp of DSG) having an energy resolution of 1.1 keV at 514 keV of 85Sr were used as two 511 keV γ- ray detectors, while the CDB spectra were recorded in a dual ADC-based multiparameter data acquisition system (MPA-3 of FAST ComTec) having an energy per channel of 144 eV. The peak to background ratio of this CDB measurement system with ±ΔE selection was $\sim 10^5$:1.[20] The CDB spectrum was analyzed by evaluating the ratio curve analysis.

7.2.5 Vacancy formation and structural dynamics

This part has been done in collaboration with Prof. Swapan K. Pati's group in JNCASR. DFT-based first-principles calculations were carried out with Perdew-Burke-Ernzerhof functional[21] and augmented-wave[22,23] methods with the inclusion of DFT-D2 dispersion correction, as implemented in the Vienna *ab initio* simulation package (VASP).[24–26] An energy cutoff of 540 eV was used for the plane-wave basis set expansion. 5 × 5 × 5 (tetragonal) k meshes were used to sample Brillouin zone integration for structural optimization.[26,27] To compute the formation energy of the vacancy of the respective elements (Ag, Bi, and S), we relaxed the atomic configuration maintaining the symmetry of the crystal. The Brillouin zone was sampled by a dense 10 × 10 × 10 k-point mesh for electronic structure calculation on relaxed geometries. *ab initio* molecular dynamics simulations (AIMD) (NVT; 300 K) was based on quantum DFT

using the same protocol as that used for structural optimization. The length and time scales achieved in this study were 20 ps and 1 fs, respectively. A Nosé−Hoover[28–30] type thermostat was applied as the temperature bath.

7.3 Results and discussion

Rocksalt $AgBiS_2$ and $AgBiS_{2-x}Se_x$ (x = 0.05-0.1) nanocrystals (~11 nm) were synthesized by the reaction of oleate of Ag and Bi with S/Se precursor in oleic acid at 180 °C for 2 h followed by quenching of the reaction mixture in ice-cold water. Acetate salts of Ag^+ and Bi^{3+} were used as metal precursors, and elemental S/Se dissolved in oleic acid, as the S/Se source. In the synthesis, the acetate salts converted into clear pale yellow solutions of metal oleates upon heating the reaction mixtures to 100 °C under N_2 flow for 2 h. Low temperature, solution-based synthesis was followed by sudden quenching along with the size reduction to the nanoscale stabilizes kinetic rocksalt phase of $AgBiS_2$ at room temperature. Similar phenomena are rare and have been observed only in a few semiconductors where a metastable kinetic polytype is accessed on the nanoscale, as for example in $Pb_{2-x}Sn_xS_2$[31] wurzite MnSe,[32] Cu_2SnSe_3,[33] $CuInS_2$[34] and orthorhombic MnAs[35].

Powder XRD (Figure 7.2(a)) of the as-synthesized nanocrystals could be indexed on the cubic $AgBiS_2$ structure (space group, $Fm\bar{3}m$). It also shows the powder XRD of cubic bulk $AgBiS_2$ for comparison, which is synthesized by vacuum-sealed tube reaction at 1123 K followed by quenching in water to stabilize the high temperature phase. Lattice parameter was obtained by Rietveld profile matching (Figure 7.2(b)). Linear expansion in the lattice parameter with increasing Se concentration in $AgBiS_{2-x}Se_x$ (x = 0.05-0.1) (Figure 7.2(c)) follow the Vegard's law for the solid solution. As larger Se^{2-} anions are introduced in the place of smaller S^{2-}, the unit cell undergoes a systematic expansion, leading to increase in lattice parameter. This gradual expansion of lattice parameter indicates an isomorphic substitution of smaller S^{2-}position by bigger Se^{2-}, forming a single-phase solid solution rather than phase separation. We have also performed high temperature powder XRD of nanocrystalline $AgBiS_2$ in the 300-673 K range, which

clearly shows no structural change (Figure 7.3). All temperature XRD data can be indexed on cubic $AgBiS_2$ structure (space group, $Fm\bar{3}m$).

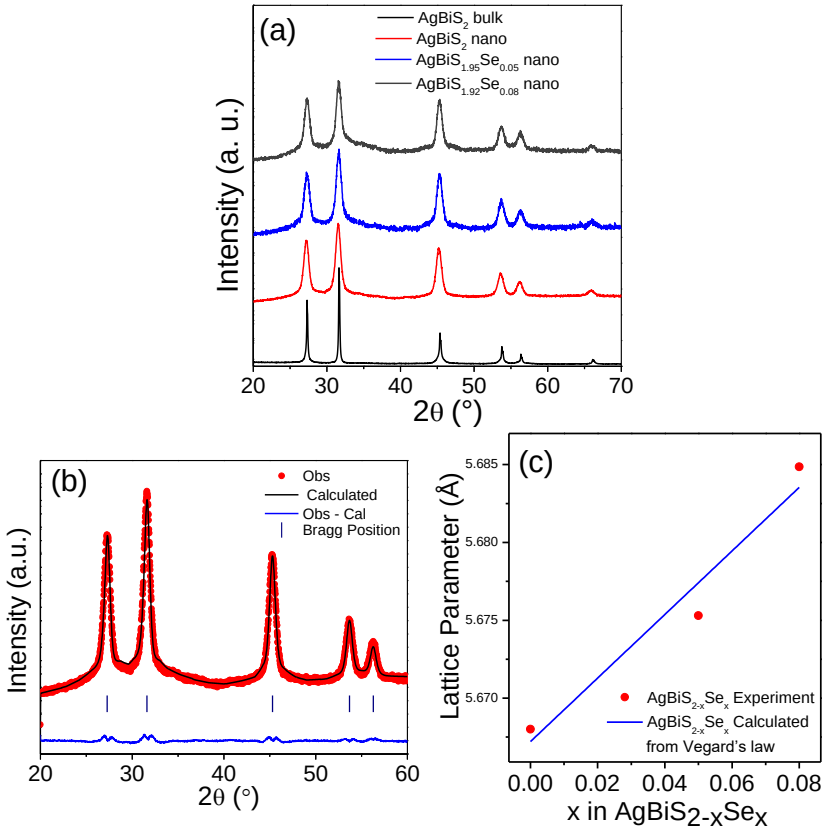

Figure 7.2 (a) Powder XRD patterns of as prepared $AgBiS_2$ and $AgBiS_{2-x}Se_x$ nanocrystals along with cubic bulk $AgBiS_2$, (b) Rietveld refinement profile for $AgBiS_2$ nanocrystals. (c) Lattice parameter (*a*) vs. Se concentration in $AgBiS_{2-x}Se_x$ and solid line indicates the Vegard's law for solid solution.

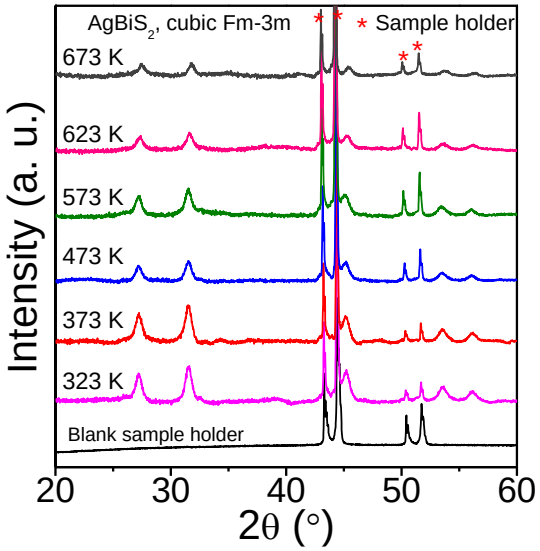

Figure 7.3 High temperature powder XRD of nanocrystalline $AgBiS_2$ in the 323-673 K range, which clearly shows no structural change. All temperature XRD data can be indexed on cubic $AgBiS_2$ structure (space group, $Fm\bar{3}m$).

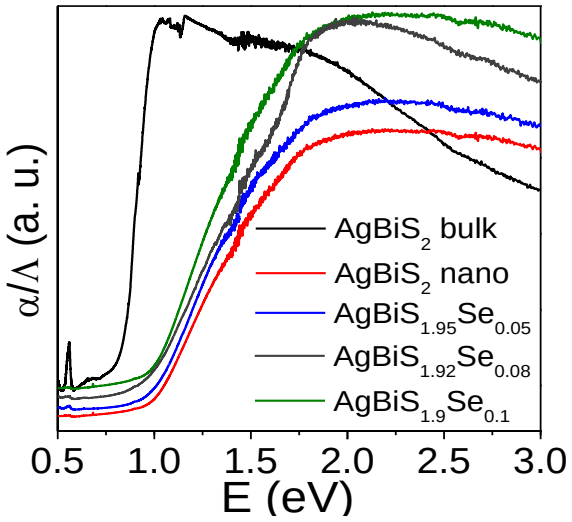

Figure 7.4 Electronic absorption spectra of as prepared $AgBiS_2$ and $AgBiS_{2-x}Se_x$ nanocrystals along with cubic bulk $AgBiS_2$.

As-synthesized cubic nanocrystals and the bulk samples exhibit well-defined band gap energies in the near-IR region (Figure 7.4). The spectroscopically measured band gap of the bulk cubic $AgBiS_2$ is ~0.8 eV, while the band gap for nanocrystalline $AgBiS_2$ is measured to be ~1.0 eV. An increase in the band gap in the case of nanocrystals compar-

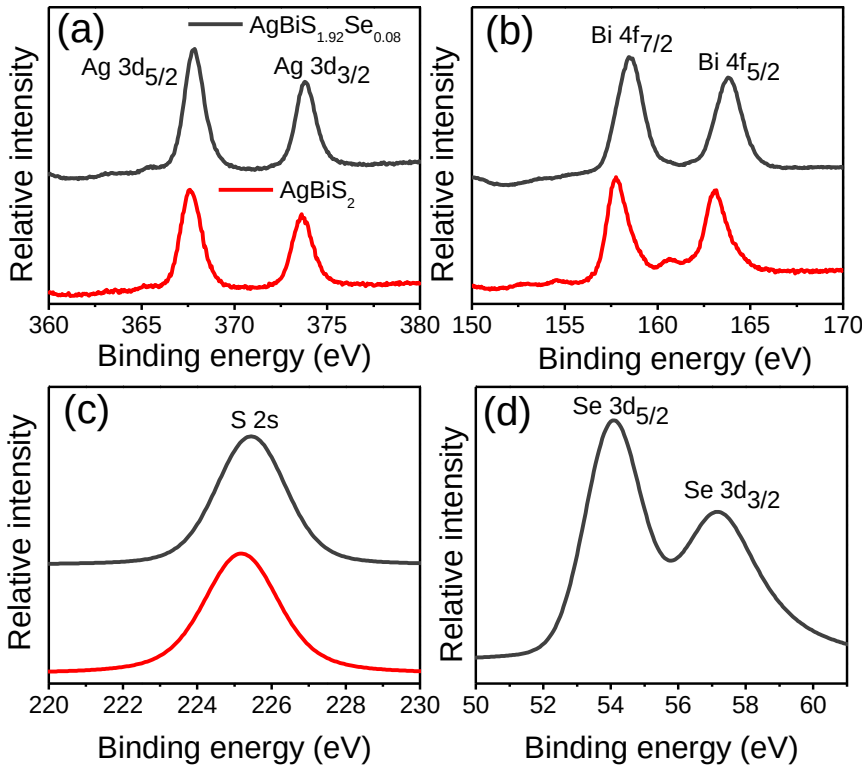

Figure 7.5 XPS spectra of as prepared $AgBiS_2$ and $AgBiS_{1.92}Se_{0.08}$ nanocrystals. (a) Ag 3d, (b) Bi 4f, (c) S 2s, and (d) Se 3d spectra.

ed to the bulk is due to the quantum confinement effect. Systematic lower energy shift of the band gap in $AgBiS_{2-x}Se_x$ nanocrystals compared to pristine nanocrystalline $AgBiS_2$ was observed with increasing the Se concentration (Figure 7.4), which supports the successful Se substitution in S sublattice of $AgBiS_2$.

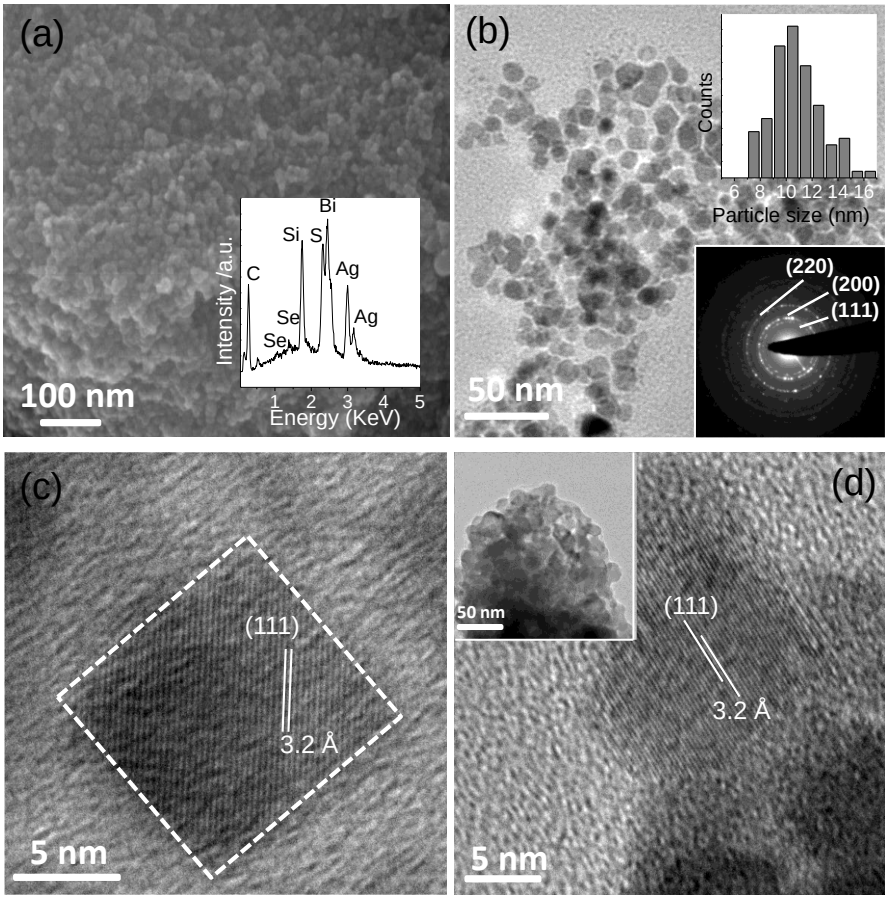

Figure 7.6 (a) FESEM image of nanocrystalline $AgBiS_2$; the lower inset shows the EDX spectra of $AgBiS_{1.92}Se_{0.08}$. (b) TEM image of $AgBiS_2$ nanocrystals; the upper inset shows the size distribution histogram of $AgBiS_2$ nanocrytals and lower inset shows the indexed SAED pattern. (c) HRTEM image of a cubic $AgBiS_2$ nanocrystal. (d) TEM (inset) and HRTEM images of $AgBiS_2$ nanocrystals after surface cleaning and densification.

In order to confirm the presence of Se in solid solution nanocrystals, we have measured the X-ray photoelectron spectra of nanocrystalline $AgBiS_2$ and $AgBiS_{1.92}Se_{0.08}$ (Figure 7.5). Two strong peaks at 367.8 and 373.7 eV (Figure 7.5(a)) with a peak splitting of 5.9 eV were observed due to Ag $3d_{5/2}$ and Ag $3d_{3/2}$, which is consistent with the standard Ag(I). The peaks at 158.3 and 163.7 eV were corresponded to Bi $4f_{7/2}$ and Bi $4f_{5/2}$ (Figure 7.5(b)). The binding energy of S 2s located at 225.3 eV (Figure 7.5(c)).

Peaks at 54.1 and 57.1 eV assigned to Se $3d_{5/2}$ and Se $3d_{3/2}$ (Figure 7.5(d)), respectively, suggest the incorporation of Se in the S sublattice of $AgBiS_2$.

As-prepared $AgBiS_2$ nanocrystals are nearly monodisperse as can be seen from the field emission scanning electron microscopy (FESEM) image (Figure 7.6(a)). Energy dispersive X-ray (EDX) spectra of nanocrystalline $AgBiS_{1.92}Se_{0.08}$ sample also confirm the presence of Se in the sample (lower inset, Figure 7.6(a)). To investigate the microstructure, transmission electron microscopy (TEM) and electron diffraction experiments were carried out. A typical TEM image of the as-synthesized $AgBiS_2$ nanocrystals is shown in Figure 7.6(b). A particle size distribution histogram generated from the TEM images is plotted in the upper inset of Figure 7.6(b). The average particle size was estimated to be ~11 nm. The selected area electron diffraction (SAED) pattern of the 11 nm nanocrystal can be indexed based on cubic rock salt $AgBiS_2$ (inset, Figure 7.6(b)). The high-resolution TEM (HRTEM) image shows clear lattice spacing of 3.2 Å corresponding to (111) interplanar distances of cubic $AgBiS_2$ (Figure 7.6(c)).

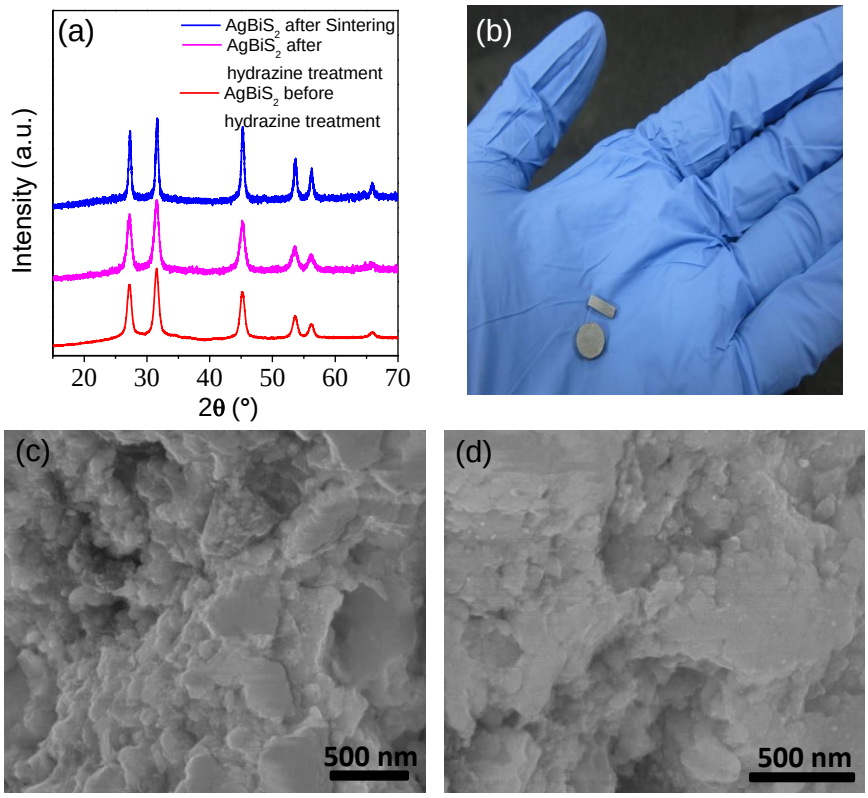

Figure 7.7 (a) Powder XRD patterns of capped, surfactant cleaned and sintered AgBiS2 nanocrystals. (b) Photograph of bar and pellet shaped samples were used for thermoelectric measurements. (c) and (d) SEM image of surface cleaned and compacted nanocrystalline $AgBiS_2$ and $AgBiS_{1.92}Se_{0.08}$.

For the electronic and thermal transport measurements, we have carefully removed the organic capping agent by treating as-synthesized nanocrystals with *n*-hexane and hydrazine solution (85% v/v) under vigorous stirring, followed by densification through pressing and sintering in a vacuum (10^{-5} Torr) sealed quartz tube at 450 °C for 2 h. We have not observed any structural change in the surface cleaned densified nanocrystals, as can be confirmed from the powder XRD patterns (Figure 7.7(a)) and HRTEM analysis (Figure 7.6(d)). The sample became much more compact, and the adjacent nanoscale grains are closely attached to each other with slight an increase in the grain size, as can be seen from TEM (inset, Figure 7.6(d)) and SEM (Figure 7.7(c), (d)).

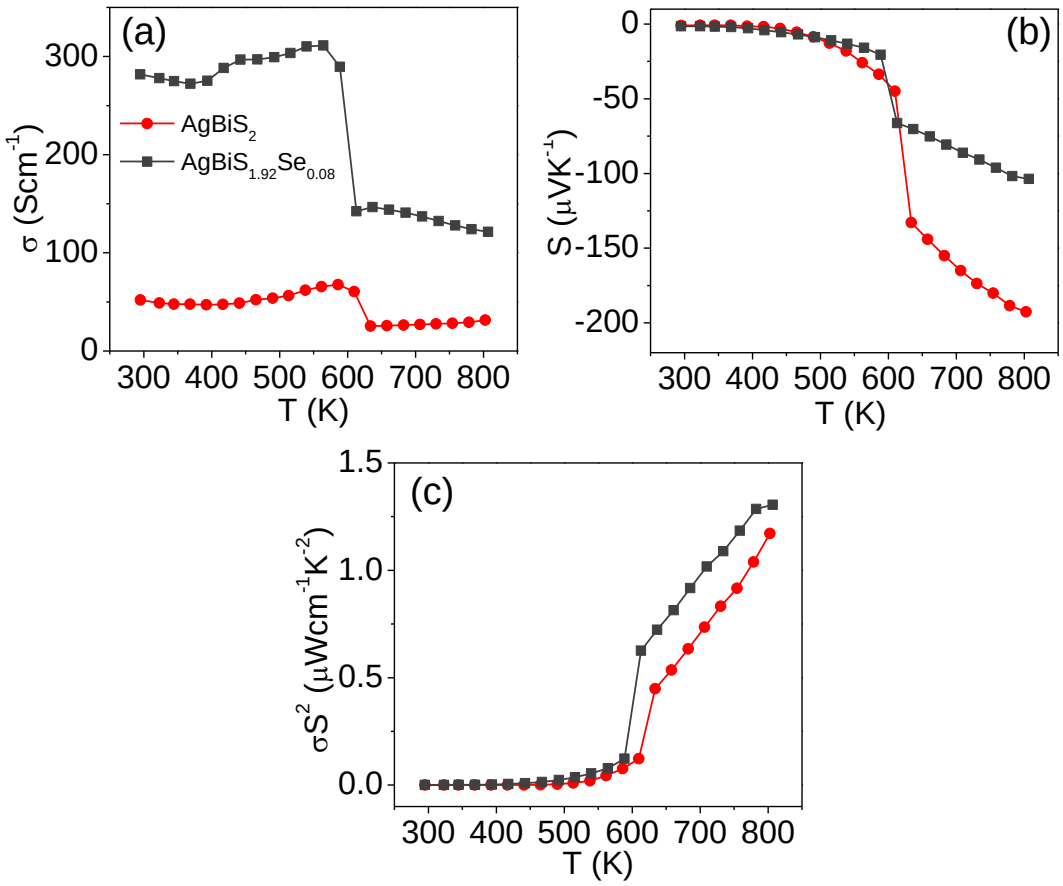

Figure 7.8 Temperature dependent (a) electrical conductivity (σ), (b) Seebeck coefficient (S), (c) power factor (σS^2) of nanocrystalline $AgBiS_2$ and $AgBiS_{1.92}Se_{0.08}$ sample.

The temperature dependent electrical and thermal transport properties of nanocrystalline $AgBiS_2$ and solid solution $AgBiS_{1.92}Se_{0.08}$ samples in the 300-830 K range are presented in Figure 7.8. Typically, the nanocrystalline $AgBiS_2$ has σ of ~52 S cm^{-1} at 300 K, which rapidly falls to ~26 S cm^{-1} at ~630 K and stays almost flat in the

625-810 K range, reaches a value of ~32 S cm^{-1} at ~810 K (Figure 7.8(a)). We also observed similar sudden decrease in σ from 310 S cm^{-1} to 145 S cm^{-1} at ~610 K in the case of $AgBiS_{1.92}Se_{0.08}$ sample. An abrupt decrease (~50%) in σ at ~600 K indicates an enhanced disordering in the arrangement of Ag and Bi atoms in the face centered cubic lattice of nanocrystalline $AgBiS_2$ above 600 K. We attribute this sharp decrease in σ at this transition temperature due to an additional scattering of charge carriers by the highly disordered Ag/Bi lattice. Such anomaly in the temperature dependent σ is very rare and is found only in few bulk crystals such as $Cu_{0.5}NbS_2$, $Ag_{0.5}NbS_2$,[36,37] and Cu_2Se[38] at their order-disorder transition temperatures. As the high-temperature powder XRD data in the 300-673 K range for nanocrystalline $AgBiS_2$ shows no structural change (Figure 7.3), transition found in transport measurement of $AgBiS_2$ nanocrystals is solely attributed to the enhanced disordering of the cations.

The negative sign of *S* indicates *n*-type conduction in nanocrystalline $AgBiS_2$ and $AgBiS_{1.92}Se_{0.08}$ (Figure 7.8(b)). Formation of chalcogen vacancies during the chemical synthesis may be responsible for electron carriers, which gives rise to *n*-type behavior. Typically, over 300-500 K range, the nanocrystalline $AgBiS_2$ has a very low value of *S* up to -10 μV K^{-1}, which sharply increases to ~-135 μV K^{-1} at ~630 K, and reaches a value of ~-195 μV K^{-1} at ~810 K. A similar rapid increase in *S* is also observed in the $AgBiS_{1.92}Se_{0.08}$ sample at ~610 K, but the overall thermopower value is lower compared to pristine $AgBiS_2$ nanocrystals, which may be due to the presence of a greater number of charge carriers in the solid solution sample. This remarkably sharp enhancement in S at ~600 K may be ascribed to a sudden increase in the entropy of the system,[39] which also suggests a transition to highly disordered cation arrangement in $AgBiS_2$ nanocrystals above 610 K. On the basis of the temperature dependent σ and *S*, maximum power factors, σS^2, were estimated to be 1.2 and 1.3 μW cm^{-1} K^{-2} at 810 K for $AgBiS_2$ and $AgBiS_{1.92}Se_{0.08}$ samples, respectively (Figure 7.8(c)).

The total thermal conductivity, κ_{total}, of the samples was estimated in the temperature range of 300-823 K using the formula $\kappa_{total} = DC_p\rho$. Interestingly, we find a λ- type transition in the temperature dependent C_p in 500-620 K range (Figure 7.9(b)), which confirms an order-disorder type transition in nanocrystalline $AgBiS_2$. Similar λ-

type transitions have been found in $AgCrSe_2$[40] and Ag_2Se,[10] where cation rearrangement is responsible for the same.[2,41]

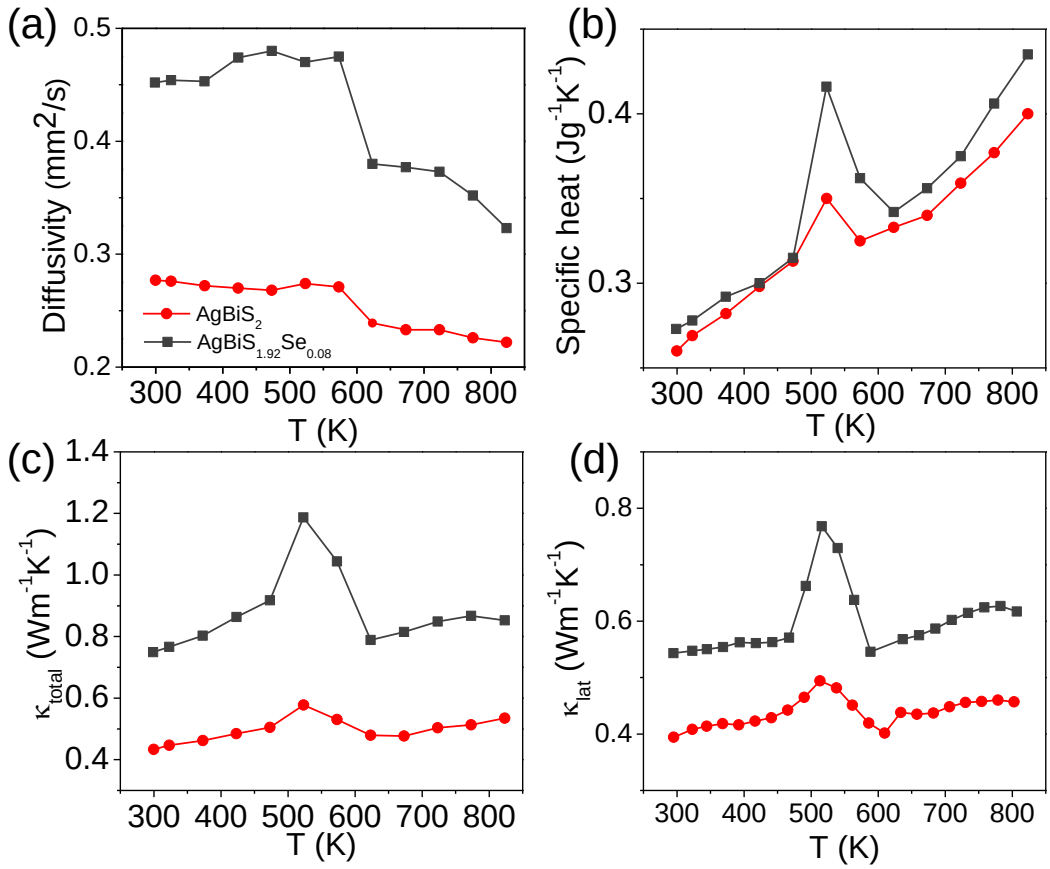

Figure 7.9 Temperature dependent (a) thermal diffusivity (D), (b) specific heat (C_p), (c) total thermal conductivity (κ_{total}), and (d) lattice thermal conductivity (κ_{lat}) of nanocrystalline $AgBiS_2$ and $AgBiS_{1.92}Se_{0.08}$ sample.

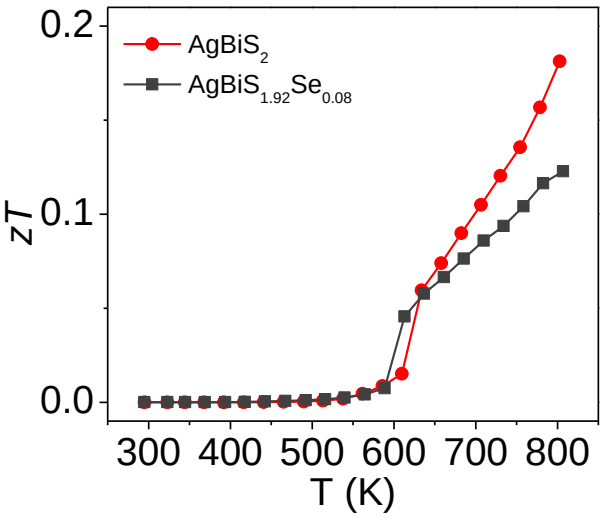

Figure 7.10 Temperature dependent thermoelectric figure of merit (zT) of of nanocrystalline $AgBiS_2$ and $AgBiS_{1.92}Se_{0.08}$ sample.

Nanocrystalline $AgBiS_2$ has very low κ_{total} values (~0.43-0.57 W m^{-1} K^{-1}) in 300-825 K range (Figure 7.9(c)). Interestingly, we have observed slightly higher values of κ_{total} in the case of $AgBiS_{1.92}Se_{0.08}$. A strong anomaly in the temperature dependent κ_{total} also indicates disordering of Ag/Bi cation above 550 K. The electronic thermal conductivity ($\kappa_{el} = L\sigma T$, where L is the Lorenz number) was estimated based on L value of 2.44×10^{-8} $W\Omega K^{-2}$. The lattice thermal conductivity, κ_{lat}, was calculated by subtracting the κ_{el} from the κ_{total} and plotted in Figure 7.9(d). Typically, $AgBiS_2$ has κ_{lat} values of ~0.4-0.5 W m^{-1} K^{-1} in 300- 825 K range. This extremely low κ_{lat} was observed due to three possible reasons: (a) a high degree of anharmonicity in the Bi-S bonds, which gives rise to strong phonon-phonon interactions; (b) effective phonon scattering by the highly disordered Ag/Bi lattice above the transition temperature; and (c) strong phonon scattering at the nanoscale grain boundaries present in $AgBiS_2$ samples. Temperature-dependent zT for the samples are plotted in Figure 7.10. Maximum zT was achieved to be ~0.2 at 810 K for $AgBiS_2$ nanocrystals, which is indeed promising and comparable or higher than that in the case of any solution grown sulfide nanocrystals.

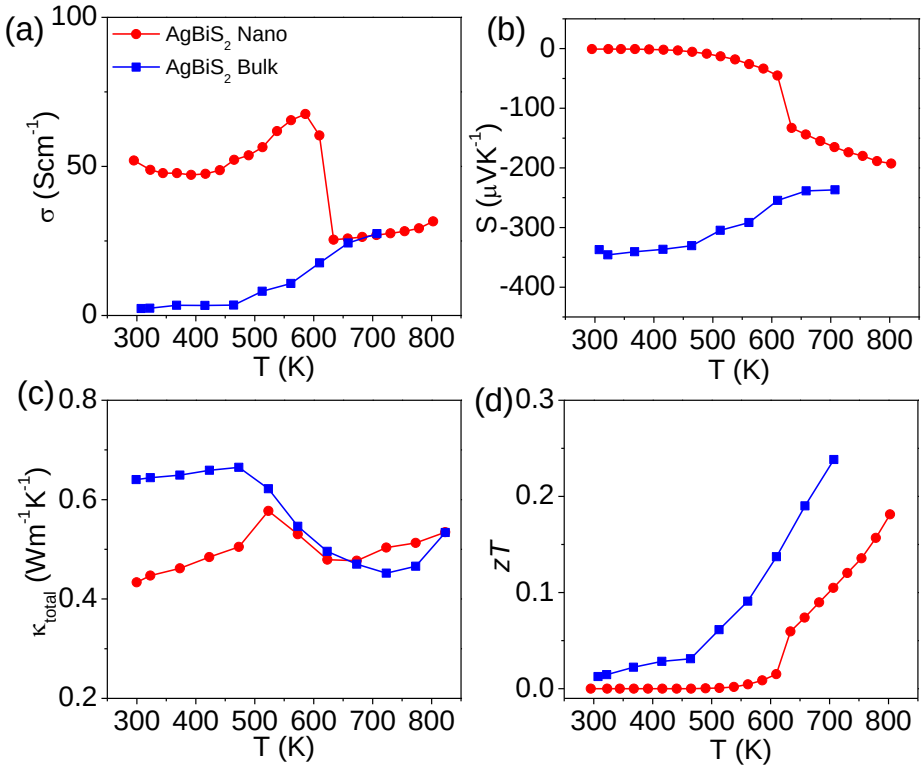

Figure 7.11 Comparison of the temperature dependent (a) electrical conductivities (σ), (b) Seebeck coefficients (S), (c) total thermal conductivities (κ_{total}) and (d) thermoelectric figure of merit (zT) between cubic nanocrystalline and bulk $AgBiS_2$ sample.

In order to compare the transport properties of the cubic nanocrystalline $AgBiS_2$ with the cubic bulk $AgBiS_2$, we have measured thermoelectric properties of the bulk sample (Figure 7.11). Typically, the bulk $AgBiS_2$ has σ of ~3 S cm^{-1} at 300 K, which slowly increases to ~28 S cm^{-1} at 705 K, indicating the semiconductor-like conduction. The negative sign of *S* indicates *n*-type carriers in bulk sample similar to the nanocrystals. The room temperature *S* for the bulk sample is ~-337 μV K^{-1}, which decreases to ~-237 μV K^{-1} at 710 K. Observation of higher thermopower values in bulk sample than those of the nanocrystalline sample suggests the presence of a lesser number of *n*-type carriers in bulk $AgBiS_2$. Interestingly, we have not observed any sharp transition in the temperature dependent σ as well as *S* data in the case of bulk $AgBiS_2$. At room temperature, κ_{total} of the bulk sample shows a value of ~0.65 W m^{-1} K^{-1} which remains flat up to 480 K and then decreases to ~0.45 W m^{-1} K^{-1} at 725 K. Room temperature κ_{total} value of the bulk sample is higher than that of the nanocrystalline sample, while the high temperature κ_{total} values are comparable between bulk and nanocrystalline phases. The decrease in κ_{total} at 480 K in the case of bulk $AgBiS_2$ may be due to the extra phonon scattering by the disordered Ag/Bi lattice at high temperature. In the case of bulk $AgBiS_2$, the maximum *zT* value was achieved to be ~0.23 at 705 K, which is comparable to that of the nanocrystalline sample.[11]

To understand the mechanism of the order-disorder phase transition and associated unusual change of thermopower in nanocrystalline $AgBiS_2$, we have done further experimental and theoretical investigations. To understand the structure of $AgBiS_2$ nanocrystals, we have performed synchrotron powder XRD and Raman spectroscopy. It is expected to observe weak superstructure reflections in powder XRD of nanocrystals because ordering in a crystal lattice can cause superstructure reflections. Synchrotron powder XRD is a powerful technique to envisage such weak reflections. Thus, to understand the room temperature structure of $AgBiS_2$ nanocrystals, we performed synchrotron powder XRD (Figure 7.12(a)). However, no superstructure reflection was observed in the synchrotron powder XRD pattern. Previous attempts to locate superstructure peaks due to local ordering in the bulk samples of I-V-VI_2 were also not successful.[42] Here, we anticipate that broad peaks in powder XRD of nanocrystals hinder the presence of weak superstructure reflection.

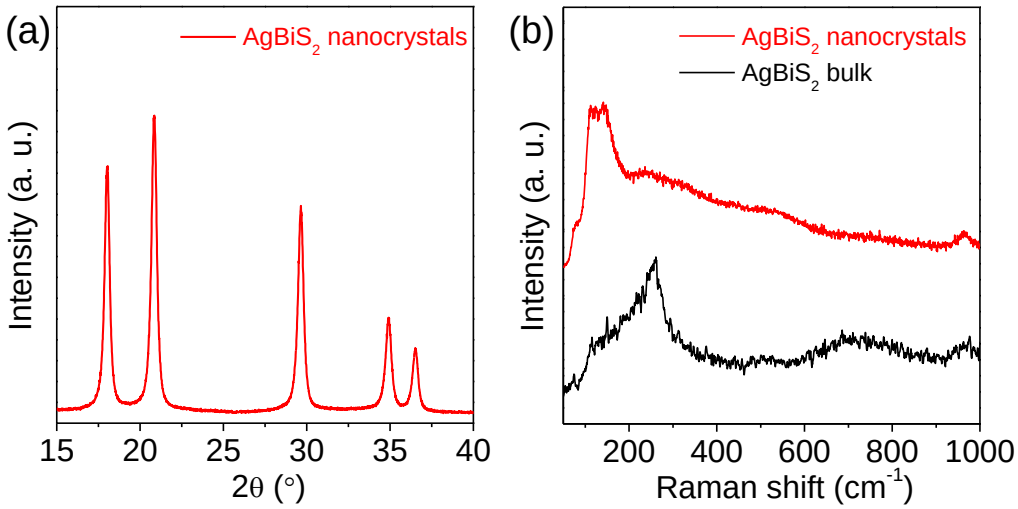

Figure 7.12 (a) Room temperature synchrotron powder XRD pattern of $AgBiS_2$ nanocrystals (λ = 1.0279 Å). (b) Room temperature Raman spectra of quenched bulk and nanocrystalline $AgBiS_2$.

Raman spectroscopy is an effective tool for structural characterization because it provides information related to the chemical bonding and symmetry of the structure. The room temperature Raman spectra for quenched bulk and nanocrystalline $AgBiS_2$ are presented in Figure 7.12(b). The Raman spectra of bulk and nanocrystalline samples are significantly different, which indicates that the nature of bonding is different in nanocrystals compared to that in the bulk. In the case of bulk $AgBiS_2$, the peak at 117 cm^{-1} and three broad peaks centered at 260, 705, and 968 cm^{-1} are consistent with Bi-S bond vibrations.[43] In contrast, for the nanocrystalline sample, peaks below ~100 cm^{-1} and a peak at 147 cm^{-1} are due to Ag lattice vibrations. A broad peak at ~238 cm^{-1} is due to Ag-S bond vibration.[44] The other peaks at ~124, 141, 316, 436, 509, and 963 cm^{-1} are consistent with Bi-S bond vibrations.[43] This result indicates that the structure of the nanocrystal is different from that of the bulk counterpart.

Defect formation can play an important role in the structural phase transition. Thus, to investigate the type of defect, we performed positron annihilation spectroscopy on both bulk and nanocrystalline $AgBiS_2$. Positron annihilation is well-known for defect characterization and identification.[18,19] It is possible to identify the chemical nature of the vacancies by proper analysis of the CDB spectrum.[16] Room temperature lifetime spectroscopy, CDB spectroscopy, and temperature-dependent (300-750 K) one-detector DBPAR line-shape spectroscopy were used to identify the defects and its role for structural changes in the nanocrystalline $AgBiS_2$ samples.

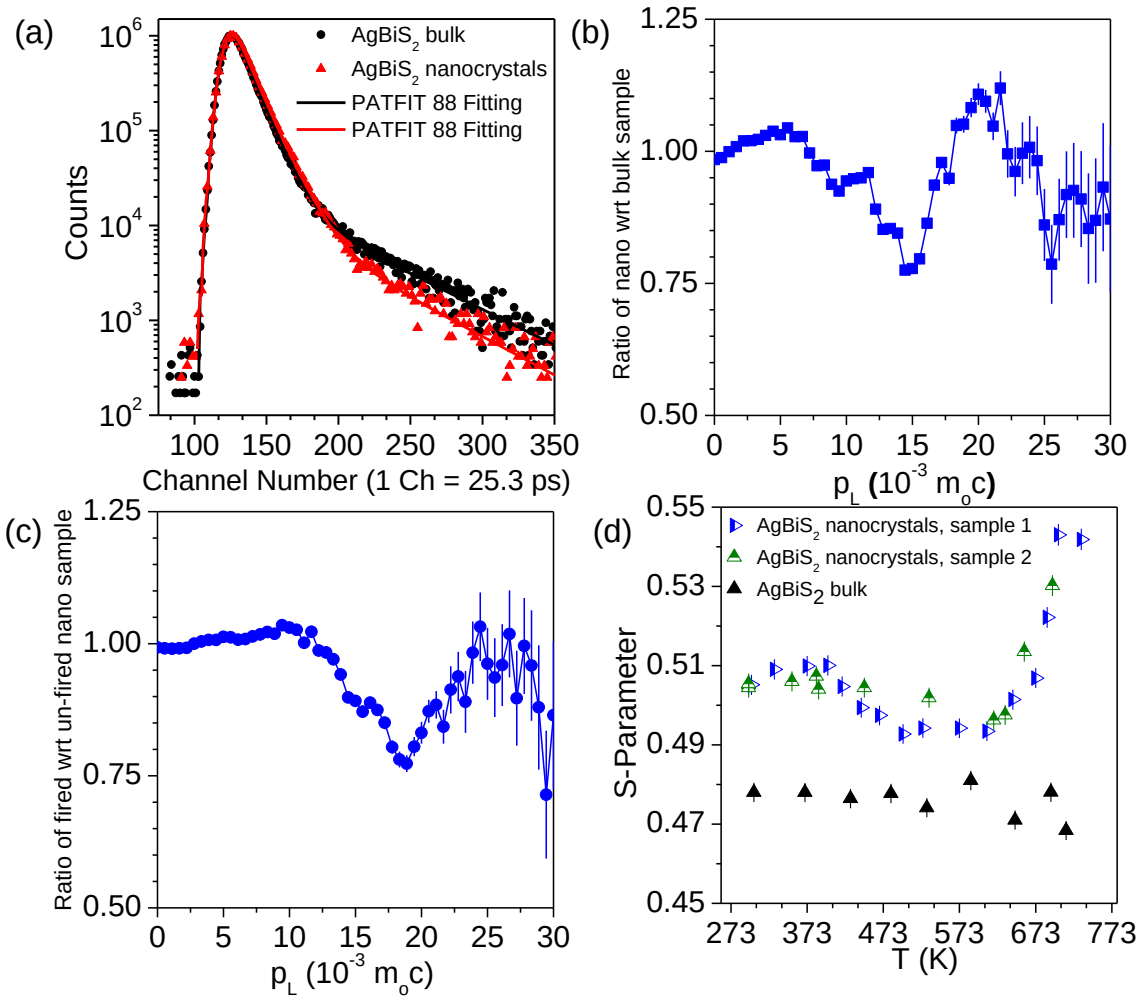

Figure 7.13 (a) Positron annihilation lifetime spectra for bulk and nanocrystalline $AgBiS_2$. (b) Area normalized ratio between the CDB spectrum of nanocrystalline and bulk $AgBiS_2$. (c) Ratio curve of nanocrystalline $AgBiS_2$ quenched from 750 K with respect to unannealed nanocrystalline $AgBiS_2$. (d) Temperature-dependent Doppler broadening S-parameter of nanocrystalline and bulk $AgBiS_2$.

Figure 7.13(a) presents the positron annihilation lifetime spectra for the bulk and nanocrystalline $AgBiS_2$ samples. The lifetime spectrum was analyzed by the PATFIT-88 program. The best fit of the spectrum was obtained with a three-lifetime component fitting (Table 7.1), with a long lifetime of ~1.5 ns for the bulk sample, which decreases to ~1.3 ns for the nanocrystalline sample. The shortest lifetime component is the free annihilation of positron,[19] while the intermediate component is due to positron annihilation at the defect site, which here is the Ag vacancy.[45,46] The long lifetime component originates from the formation of positronium at the sample surface or at the large voids inside the sample.[19] Table 7.1 indicates that the intensity of the lifetime component associated with Ag vacancies increases in nanocrystalline $AgBiS_2$ compared

to that in the bulk, which suggests the existence of a higher number of Ag vacancies in the nanocrystalline sample.

Table 7.1 Positron lifetime components of bulk and nanocrystalline $AgBiS_2$.

Sample	τ_1 (ps)	I_1 (%)	τ_2 (ps)	I_2 (%)	τ_3 (ps)	I_3 (%)
Bulk	155 ± 3	31 ± 1	340 ± 3	65 ± 1	1483 ± 24	4 ± 0.1
Nanocrystalline	164 ± 2	13 ± 1	332 ± 3	84 ± 1	1330 ± 37	3 ± 0.1

In order to identify the specific nature of the defect, we carried out two-detector CDB spectroscopy measurement at room temperature. The CDB data were analyzed by area normalized ratio curve analysis.[16,20] Figure 7.13(b) shows the area normalized ratio between the CDB spectrum of nanocrystalline $AgBiS_2$ and the same for bulk $AgBiS_2$. The ratio curve shows a dip in the momentum value at 15×10^{-3} m_0c corresponding to an E_{kin} value of 57 eV, which is close to the binding energy of Ag 4p (60 eV). Thus, this indicates less annihilation of positrons with a higher momentum core electron of Ag. This proves the presence of more Ag vacancies in the nanocrystalline $AgBiS_2$ sample compared to its bulk counterpart. The positron lifetime value also supports the trapping of the positron in the Ag vacancy-type defects in nanocrystalline $AgBiS_2$ (Table 7.1).

Figure 7.13(c) shows the typical ratio curve of annealed (24 h) and quenched nanocrystalline $AgBiS_2$ (750 K) with respect to as-synthesized nanocrystalline $AgBiS_2$. Here one can find two significant dips in the momentum values of 15×10^{-3} and 19×10^{-3} m_0c. We have used the virial approximation (in the atom, the expectation value of the kinetic energy of an electron, E_{kin}, is equal to the binding energy of the electron) for calculation of E_{kin} using $p_L = (2m_0E_{kin})^{1/2}$, along with considering that positrons are thermalized before annihilation. Here, p_L is the longitudinal component of electron momentum p along the detector axis, and m_0 is the rest mass of an electron. The dip positions in the ratio curves correspond to E_{kin} values of 57 and 92 eV, respectively. The value of E_{kin} is very close to the binding energies of the Ag 4p (60 eV) and 4s (97 eV) core electrons. This result clearly indicates that a large number of Ag vacancies are uniformly distributed in the nanocrystalline $AgBiS_2$ sample when it is annealed at 750 K followed by quenching to room temperature. In summary, (a) nanocrystalline $AgBiS_2$ contains more Ag vacancies compared to the bulk counterpart at room temperature and

(b) the Ag vacancy concentration increases in high temperatures in nanocrystalline samples, as confirmed from the above annealing and quenching experiment.

Temperature-dependent Doppler broadening of the annihilation radiation reflects the momentum distribution of annihilating electrons, which has provided more information about the change in the Ag vacancy concentration during the order-disorder phase transition in $AgBiS_2$ nanocrystals. The Doppler broadening spectra were analyzed by evaluating the S-parameter defined by the ratio of the counts in the central area of the annihilation photo peak and the total area of the photo peak. Variation of the S-parameter with temperature (273-750 K) for nanocrystalline $AgBiS_2$ shows a sharp increase above 610 K, which is absent for bulk $AgBiS_2$ (Figure 7.13(d)). The onset of the S-parameter for the nanocrystalline sample at high temperatures indicates the formation of a vacancy-like defect and its subsequent recovery after the transition. We also verified the trend of the S parameter in different batches of the nanocrystalline sample (Figure 7.13(d)), which reproduces similar results. In contrast, the cubic phase of bulk $AgBiS_2$ does not show such an increase in the S-parameter at high temperatures (Figure 7.13(d)). Nanocrystalline $AgBiS_2$ possesses a kinetic ordered cubic structure, which transforms to a thermodynamically stable disordered cubic phase at 610 K. Temperature-dependent S-parameter variation indicates that the order-disorder phase transition in nanocrystalline $AgBiS_2$ is actually triggered by the abrupt increase in the Ag vacancy concentration.

The microscopic picture of the inherent defect chemistry was also investigated by first-principles calculations based on DFT and AIMD. At first, the structural optimizations were carried out through quantum mechanical calculations and the most stable configuration (Figure 7.14) for $AgBiS_2$ has been used to study the thermodynamic feasibility of defects/vacancies.[47] A finite-sized supercell model (Figure 7.14) was used to calculate the formation energy of various types of defects including Ag, Bi, and S vacancies, as well as the occupancy at the interstitial site. We found that the formation of an Ag vacancy is the energetically most favorable among all possible defects discussed above (Table 7.2). This suggests that the Ag vacancy is the native defect in nanocrystalline $AgBiS_2$. Additionally, the defect attributed to S and Bi is also unfavorable because the formation energy is highly positive for either vacancy or interstitial occupation. Thus, the Ag vacancy in the system can only be a spontaneous and

thermodynamically driven defect process at the nanoscale, which clearly supports the results of positron annihilation spectroscopy.

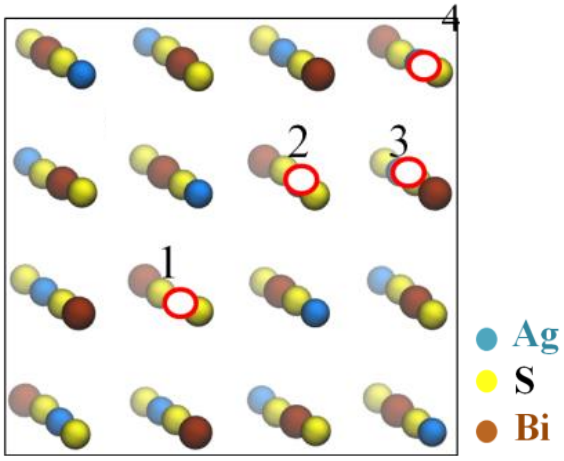

Figure 7.14 Optimized structural configuration for cubic $AgBiS_2$ nanocrystals. Color notation: cyan, Ag; violet, Bi; yellow, S. In panel c, numbers 1-4 indicate the Ag vacancy with the position of the vacancies at 1,2 (A type: nearest neighbor), 1,3 (B type: next-nearest neighbor), and 1,4 (C type: next to the next-nearest neighbor).

Table 7.2 Formation Energy (E_f^v, eV/vacancy) of different types of defects in the nanocrystalline cubic $AgBiS_2$.

Type of defect	E_f^v	IPr
V_{Ag}	-0.09, +0.01, -0.06, -0.06	0.28, -0.12, -0.12, -0.12
$Interstitial_{Ag}$	0.025	0.71
V_S	1.32	0.19
$Interstitial_S$	0.42	0.82
V_{Bi}	4.50	-0.05

Four values for V_{Ag} denote the Ag vacancies with single, A, B, and C type, from left to right. IPr due to the defect is in units of GPa/fu.

Furthermore, we have investigated the effect of Ag vacancies and the order-disorder transition on the anomalous change of thermopower in $AgBiS_2$ nanocrystals. Thermopower is the electric potential generated by a temperature gradient in a material, and physically it is the ratio of entropy carried out by moving charges to the charge transported. It is known from the Kubo formalism that the thermopower can be divided into two parts:[48,49]

$$S = -\frac{1}{k_B T}\frac{J_{qe}}{J_{ee}} - \frac{1}{e}\frac{\mu}{T} \tag{7.1}$$

where, k_B is Boltzmann's constant, T is temperature, e is the elementary charge, μ is chemical potential, J_{qe} and J_{ee} are transport integrals representing the heat transport per electron and the current transported per electron respectively.[49] In this equation, the first term is defined as "*transport thermopower*," $S_{transport}$, which originates from the manner in which charge is transported. The second term is called "*presence thermopower*", $S_{presence}$, which is the contribution from the entropy change when a carrier is added to the system, irrespective of the means by which it was transported.[49] $S_{presence}$ can be expressed as μ/eT = α*/e, $\alpha^* = \left(\frac{\partial S'}{\partial N}\right)_U$ where S' is entropy, e is electron charge, N is number of carriers and U is internal energy. α* is related to degeneracy by $k\ln(G_S \cdot G_C)$, where G_S and G_C are the spin and configuration degeneracy, respectively.[39] In the absence of magnetic field and magnetic ions, the spin degeneracy will be remained invariant. Thus, change in entropy will be solely driven by the configurational entropy term. It has been previously observed that a significant increase in thermopower may be obtained if entropy change of a phase transition coupled to carrier transport.[49] Hence, a significant change of thermopower in a system can be observed if there is any change in either of the way of charge transport or entropy-factor when a carrier is added to the system.

Figure 7.15(a) shows snapshot from the *ab initio* molecular dynamics (AIMD) trajectory of the $AgBiS_2$. We found that the Ag vacancy alters the Ag-S bonding motif and results in shuttling of Ag atom in the interstitial region (Figure 7.15(a)). The introduction of the Ag vacancy into the system can give rise to a transition from an ordered to a locally disordered state. This process maximizes at a critical value of 12.5-18.75% of the Ag vacancy. Beyond this vacancy concentration, the process becomes thermodynamically infeasible (Figure 7.15(b)). Shuttling of Ag ion through the Ag vacancy at elevated temperature plays a crucial role in the order-disorder transition. Additionally, electrostatic interaction between the charge carrier and Ag ion present in the vacant or interstitial site affects charge transport in the system. The formation of large Ag vacancies during the transition (~610 K) triggers shuttling of the partially positively charged Ag atom and results in predominant phonon-electron (hole) interaction, which affects the manner of charge transport. Hence, phonons will force electrons toward one end of the material, giving rise to enhancement of *S* transport, which contributes to the

effective increment in the thermopower value. On the other hand, alteration of the Ag vacancy results in alteration of the charge-carrier concentrations in the system, and it is important to note that the increase in the Ag-vacancy concentration results in a finite rate of entropy production per unit volume of $AgBiS_2$ nanocrystals (see Figure 7.15(c)). Hence, a significant change of thermopower can be observed in the system when there is any change in the carrier concentration through vacancy creation. This effect contributes to the $S_{presence}$ component of thermopower. Thus, the coupling between the charge carrier and lattice vibration associated with the movement of an Ag atom results in additional phase entropy, which gives rise to an increase in the $|S|$ value at higher Ag vacancy concentration.

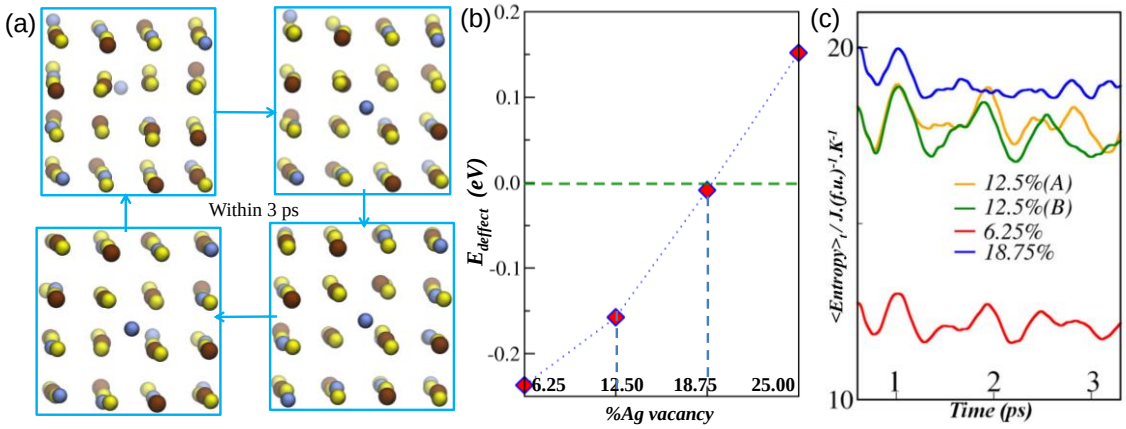

Figure 7.15 (a) Snapshot from the AIMD trajectory of the $AgBiS_2$ cubic cell with 62 atoms in the presence of 12.5% of the Ag vacancy in the optimize structure (Figure 7.14), showing Ag-atom shuttling in the interstitial position. Color notation: cyan, Ag; violet, Bi; yellow, S. (b) Different Ag vacancy concentrations versus defect formation energies. (c) Entropy originating due to the Ag vacancy for a thermally equilibrated system at 300 K. Various concentrations and types of Ag vacancies have been considered in the nanocrystalline optimize structure.

Notably, changes from single to dual vacancy (6.25% to 12.50% of the Ag vacancy) result in drastic changes in the entropy factor due to the presence of the shuttling of Ag atoms at the interstitial site as explained above (Figure 7.15(c)). We emphasize that, at a lower concentration of vacancy (6.25%), Ag atoms shuttle between the vacant lattice point and the interstitial site. However, at a higher extent of vacancy, the time scale spent by an Ag atom at the interstitial site is much longer, which results in a longer mean free path. This increases the entropy of the system at higher vacancy concentration (Figure 7.15(c)), which, in turn, results in an unusual rise in thermopower (contributed by both $S_{transport}$ and $S_{presence}$). It is also important to note that a further

(>18.75%) increase in the vacancy concentration reaches the thermodynamic limit and does not change the characteristic feature anymore (Figure 7.15(c)). A similar result of the coupling of the structural entropy with electronic thermopower was previously observed in superionic Cu_2Se.[49]

7.4 Conclusions

In summary, high temperature rocksalt phases of $AgBiS_2$ and $AgBiS_{2-x}Se_x$ (x = 0.05-0.1) have been kinetically stabilized at room temperature in nanocrystals (~11 nm) by rapid and scalable solution-based synthesis. Fascinating anomalies in the temperature dependent σ, S, and C_p were observed at ~610 K due to novel order-disorder type transition, which indeed optimizes the electronic charge transport in these nanocrystals. Disordered cation sublattice and nanoscale grain boundaries coupled with strong Bi-S bond anharmonicity allow effective phonon scattering, which leads to minimal κ_{lat} of the nanocrystalline $AgBiS_2$. Optimization of thermoelectric performance through a combined phonon scattering approach is expected to be applicable to other nanocrystals with disordered cation/anion sublattice. We also established a fundamental understanding of the order-disorder transition and associated abrupt change in thermopower in $AgBiS_2$ nanocrystals. The nanocrystalline cubic phase of $AgBiS_2$ prefers a cation ordered structure, whereas bulk cubic $AgBiS_2$ prefers a disordered structure. Positron annihilation spectroscopy indicates the Ag vacancy as the native defect in $AgBiS_2$. The concentration of the Ag vacancy is higher in the nanocrystal compared to that in the bulk at room temperature. A significant rise in the Ag vacancy concentration was evidenced during the order-disorder phase transition at 610 K in nanocrystalline $AgBiS_2$. Shuttling of an Ag atom in a vacant or an interstitial site at higher temperatures due to the formation of more Ag vacancies plays a key role in the transition from an ordered to a locally disordered structure in nanocrystalline cubic $AgBiS_2$. This indeed increases the entropy of the system at higher vacancy concentration, which, in turn, results in an unusual rise in thermopower (contributed by both $S_{transport}$ and $S_{presence}$). Synthesis of a new metastable phase in the nanoscale, mechanistic understanding of the order-disorder phase transition, and associated unusual properties not only enrich the fundamental solid-state inorganic

chemistry but also should assist chemists in understanding the exotic properties associated with the phase transition.

References

[1] C. N. R. Rao, J. Gopalakrishnan, *New Directions in Solid State Chemistry*, Cambridge University Press, **1997**.

[2] A. West, *Solid State Chemistry and Its Applications, 2nd Edition, Student Edition*, **2014**.

[3] R. J. Mehta, Y. Zhang, C. Karthik, B. Singh, R. W. Siegel, T. Borca-Tasciuc, G. Ramanath, *Nat. Mater.* **2012**, *11*, 233–240.

[4] J. S. Son, M. K. Choi, M. K. Han, K. Park, J. Y. Kim, S. J. Lim, M. Oh, Y. Kuk, C. Park, S. J. Kim, et al., *Nano Lett.* **2012**, *12*, 640–647.

[5] M. Scheele, N. Oeschler, I. Veremchuk, K.-G. Reinsberg, A.-M. Kreuziger, A. Kornowski, J. Broekaert, C. Klinke, H. Weller, *ACS Nano* **2010**, *4*, 4283–4291.

[6] A. Soni, Y. Zhao, L. Yu, K. A. M. Khor, M. S. Dresselhaus, Q. Xiong, *Nano Lett.* **2012**, *12*, 1203–1209.

[7] M. Ibáñez, R. Zamani, A. LaLonde, D. Cadavid, W. Li, A. Shavel, J. Arbiol, J. R. Morante, S. Gorsse, G. J. Snyder, et al., *J. Am. Chem. Soc.* **2012**, *134*, 4060–4063.

[8] F. J. Fan, Y. X. Wang, X. J. Liu, L. Wu, S. H. Yu, *Adv. Mater.* **2012**, *24*, 6158–6163.

[9] F. J. Fan, B. Yu, Y. X. Wang, Y. L. Zhu, X. J. Liu, S. H. Yu, Z. Ren, *J. Am. Chem. Soc.* **2011**, *133*, 15910–15913.

[10] C. Xiao, J. Xu, K. Li, J. Feng, J. Yang, Y. Xie, *J. Am. Chem. Soc.* **2012**, *134*, 4287–4293.

[11] H. Yang, L. A. Jauregui, G. Zhang, Y. P. Chen, Y. Wu, *Nano Lett.* **2012**, *12*, 540–545.

[12] S. Geller, J. H. Wernick, *Acta Crystallogr.* **1959**, *12*, 46–54.

[13] K. Hoang, S. D. Mahanti, J. R. Salvador, M. G. Kanatzidis, *Phys. Rev. Lett.* **2007**, *99*, 156403.

[14] J. Ma, O. Delaire, a F. May, C. E. Carlton, M. a McGuire, L. H. VanBebber, D. L. Abernathy, G. Ehlers, T. Hong, a Huq, et al., *Nat. Nanotechnol.* **2013**, *8*, 445–51.

[15] L. Aggarwal, J. S. Sekhon, S. N. Guin, A. Arora, D. S. Negi, R. Datta, K. Biswas, G. Sheet, *Appl. Phys. Lett.* **2014**, *105*, 0–5.

[16] A. Sarkar, M. Chakrabarti, S. K. Ray, D. Bhowmick, D. Sanyal, *J. Phys. Condens.*

Matter **2011**, *23*, 155801.

[17] M. Kirkegaard, P. Pedersen, N. J. Eldrup, *Rep. Riso Natl. Lab* **1989**.

[18] C. Hautojarvi, P. Corbel, *Positron Spectroscopy of Solids*, IOS Press: Amsterdam, The Netherlands, **1995**.

[19] R. Krause-Rehberg, H. S. Leipner, *Positron Annihilation in Semiconductors*, **1999**.

[20] M. Chakrabarti, D. Sanyal, a Chakrabarti, *J. Phys. Condens. Matter* **2007**, *19*, 236210.

[21] J. P. Perdew, K. Burke, M. Ernzerhof, *Phys. Rev. Lett.* **1996**, *77*, 3865–3868.

[22] J. R. Blöchl, N. Adelstein, B. S. Mun, H. L. Ray, P. N. Ross, J. B. Neaton, L. C. De Jonghe, R. J. L. Andon, J. F. Counsell, H. McKerrell, et al., *Phys. Rev. B. Condens. Matter* **1994**, *50*, 17953–17979.

[23] G. Kresse, *Phys. Rev. B* **1999**, *59*, 1758–1775.

[24] G. Kresse, J. Hafner, *Phys. Rev. B* **1994**, *49*, 14251–14269.

[25] G. Kresse, J. Furthmüller, *Comput. Mat. Sci.* **1996**, *6*, 15–50.

[26] G. Kresse, J. Furthmüller, *Phys. Rev. B* **1996**, *54*, 11169–11186.

[27] J. Marx, D. Hutter, *Modern Methods and Algorithms of Quantum Chemistry*, John Von Neumann Institute For Computing: Juelich, Germany, **2000**.

[28] S. Nosé, *J. Chem. Phys.* **1984**, *81*, 511.

[29] W. G. Hoover, *Phys. Rev. A* **1985**, *31*, 1695–1697.

[30] G. J. Martyna, M. L. Klein, M. Tuckerman, *J. Chem. Phys.* **1992**, *97*, 2635–2643.

[31] R. B. Soriano, C. D. Malliakas, J. Wu, M. G. Kanatzidis, *J. Am. Chem. Soc.* **2012**, *134*, 3228–33.

[32] I. T. Sines, R. Misra, P. Schiffer, R. E. Schaak, *Angew. Chemie - Int. Ed.* **2010**, *49*, 4638–4640.

[33] M. E. Norako, M. J. Greaney, R. L. Brutchey, *J. Am. Chem. Soc.* **2012**, *134*, 23–26.

[34] D. Pan, L. An, Z. Sun, W. Hou, Y. Yang, Z. Yang, Y. Lu, *J. Am. Chem. Soc.* **2008**, 5620–5621.

[35] K. Senevirathne, R. Tackett, P. R. Kharel, G. Lawes, K. Somaskandan, S. L. Brock, *ACS Nano* **2009**, *3*, 1129–1138.

[36] M. Bouwmeester, D. Lee, *Phys. Rev. B* **1991**, *43*, 9431–9435.

[37] R. Pfalzgraf, B. W. Spreckels, H. Paulus, W. Schollhorn, *J. Phys. F Met. Phys.* **1987**, *17*, 857–863.

[38] H. Liu, X. Shi, F. Xu, L. Zhang, W. Zhang, L. Chen, Q. Li, C. Uher, T. Day, G. J. Snyder, *Nat. Mater.* **2012**, *11*, 422–425.

[39] Y. Wang, N. Rogado, R. J. Cava, N. P. Ong, *Nature* **2003**, *423*, 425–428.

[40] F. Gascoin, A. Maignan, *Chem. Mater.* **2011**, *23*, 2510–2513.

[41] C. N. R. Rao, *Acc. Chem. Res.* **1984**, *17*, 83–89.

[42] M. D. Nielsen, V. Ozolins, J. P. Heremans, *Energy Environ. Sci.* **2013**, *6*, 570–578.

[43] X. Q. Zuo, X. Yang, L. Zhou, B. Yang, G. Li, H. B. Tang, H. J. Zhang, M. Z. Wu, Y. Q. Ma, S. W. Jin, *RSC Adv.* **2014**, *4*, 57412–57418.

[44] I. Martina, R. Wiesinger, M. Schreiner, *e-Preservation Sci.* **2012**, *9*, 1–8.

[45] S. N. Guin, J. Pan, A. Bhowmik, D. Sanyal, U. V. Waghmare, K. Biswas, *J. Am. Chem. Soc.* **2014**, *136*, 12712–12720.

[46] C. Xiao, X. Qin, J. Zhang, R. An, J. Xu, K. Li, B. Cao, J. Yang, B. Ye, Y. Xie, *J. Am. Chem. Soc.* **2012**, *134*, 18460–18466.

[47] S. N. Guin, S. Banerjee, D. Sanyal, S. K. Pati, K. Biswas, *Inorg. Chem.* **2016**, *55*, 6323–6331.

[48] R. Kubo, M. Y. Kubo, Ryogo, *J. Phys. Soc. Japan* **1957**, *12*, 570–586.

[49] D. R. Brown, T. Day, K. A. Borup, S. Christensen, B. B. Iversen, G. J. Snyder, *APL Mater.* **2013**, *1*, 52107.

Chapter 8

Nanoscale stabilization of non-equilibrium rock salt AgBiSeS and its temperature driven unusual phase transformation *

* *unpublished*

CHAPTER 8

Nanoscale stabilization of non-equilibrium rock salt AgBiSeS and its temperature driven unusual phase transformation

Summary. *Stabilization of metastable phases of inorganic solids at ambient condition is an art in synthetic chemistry. This chapter presents stabilization of a non-equilibrium rock salt phase of AgBiSeS in the nanocrystalline form. High symmetry rock salt nanocrystals upon thermal treatment undergo an unusual irreversible phase transition to a low symmetry trigonal structure. To get fundamental insights into such unusual finding we have performed temperature dependent synchrotron powder X-ray diffraction, positron annihilation spectroscopy and structural energy and phonon modes investigations. We found, passivation of the uncoordinated surface atoms by chemically bound ligands (oleic acid) results in the stabilization of metastable rock salt AgBiSeS. Here we also establish the origin of structural phase stability and phase transition.*

8.1 Introduction

The paradigm shifts in the research area of energy, environmental and technologically relevant disciplines in recent decades have emerged library of new functional inorganic materials. The majority of them has been synthesized using high-temperature solid state method.[1–6] Although synthesis of materials using high-temperature method is an excellent process and leads to the formation of the thermodynamically stable product, but it often leaves very little room for kinetic modifications.[1–5] The plenteous structural chemistry and exotic chemical, physicochemical properties of kinetic phases are precious for a better understanding of fundamental solid state chemistry and technological prospect.[1,2,4,7,8] The crystal symmetry is an important parameter to tune electronic structure of material and hence it is desirable to synthesize the metastable or kinetic structures. In this regards, it is essential to increase the reactant diffusion rate for kinetic modifications so that activation energy barrier of the reaction can be lowered to avoid the thermodynamic path. In this context, metal flux, and molten salt techniques has been explored successfully for the synthesis of many novel materials from oxides,[3] chalcogenides,[2,4,5] intermetallics,[1,9] and pnictides[10] family with new structure types.

Apart from the solid-state methods, the chemistry in nanoscale shaped a great scope for tuning of the materials properties. The control of crystal structures, size and morphology resulted in many technologically relevant properties in the nanoscale material.[11–15] Seeded-growth, polyol, solvothermal, hot injection methods are well explored for the synthesis of nanocrystals with tailored composition, size, shape and crystal structure.[11–15] The advantage of solution based synthesis is the high diffusion rate as precursors are generally exist as soluble form in a suitable solvent. Thus, like molten salt and flux methods, in low temperature solution-based synthesis can also stabilize new metastable phases in nanoscale. High surface energy, surface stress in nano-dimension along with reaction temperature, solvent, ligands, surfactants and precursor source play crucial role for the determination of crystal structure and dynamics of phase transition.[8,16–18] In other word, at low-temperature solution phase synthesis, the reaction is often controlled kinetically rather than thermodynamically.[19] Hence, thermodynamic phase stability of the material can reverse in nano-dimension and sometimes unusual high energy metastable structural phases can stabilize at ambient condition. Although

stabilization of metastable phases is quite challenging and uncommon, but was observed in $Pb_mSb_{2n}Te_{m+3n}$,[14] $Pb_mBi_{2n}Te_{3n+m}$,[20] $Pb_{2-x}Sn_xS_2$,[21] Co- nanoparticle,[19] wurtzite-type MnSe (γ-MnSe),[22] $CuInSe_2$,[23] Cu_2SnSe_3,[24] Cu_2ZnSnS_4,[25,26] tetragonal-type Ag_2Se (β-Ag_2Se),[27] orthorhombic-type MnAs,[28] and bixbyite type V_2O_3[17].

AgBiSeS is an interesting material form of I-V-VI_2 family (where I = Cu, Ag, Au; V = As, Sb, Bi; and VI = S, Se, Te) gained significant attention recently for thermoelectric applications.[29,30] In bulk phase, this material is known to crystalizes in a disordered rock salt cubic structure (space group Fm-3m) at high temperature.[29–31] We found that AgBiSeS is a polymorphic material, shows a reversible phase transition from trigonal structure to a rock-salt cubic structure above 250 ^{0}C (Figure 8.2). First-principles total energy calculations also reveal that trigonal system is more stable than rock salt structure at room temperature (will be discussed later). These finding direct that the rock salt structure is a high-temperature polymorphic form of AgBiSeS. To date, all the studies on AgBiSeS are mainly focused on the bulk sample. However, we emphasized that size reduction to nanoscale has impact on the crystal structure and property of the material. Therefore, it would be worthy to explore the phase stability of the AgBiSeS in nano-dimension.

In this chapter, we present stabilization of non-equilibrium AgBiSeS with rock salt structure in nanocrystalline form. We found the rock salt nanocrystals upon thermal treatment undergoes an irreversible phase transition to a low symmetry trigonal structure. To get insights into such unusual finding we have performed temperature dependent synchrotron powder X-ray diffraction, positron annihilation spectroscopy and first principles calculation. Temperature dependent synchrotron PXRD shows rock salt to trigonal transition takes place at ~230 ^{0}C. Positron annihilation spectroscopy study indicates the formation of a large amount of Ag vacancies during rock salt to trigonal transition might assist the transition. Density Functional Perturbation Theory (DFPT) based calculations confirms nanocrystalline cubic AgBiSeS has three imaginary phonon modes at Γ -point, which implies the metastable nature of the cubic nanocrystalline phase. The passivation of the uncoordinated surface atoms by chemically bound ligands result in the stabilization of metastable cubic AgBiSeS. Finally, we establish the origin of

structural phase stability and /or transition, which relies on the dimensionality of AgBiSeS sample.

8.2 Methods

8.2.1 Synthesis

Silver acetate anhydrous (Alfa Aesar, 99%), bismuth neodecenate (90%, Alfa Aesar), sulfur powder (S; 99.999%, Alfa Aesar) and selenium powder (Se, Aldrich, 99.5+%), oleic acid (Sigma-Aldrich, 90%) were used for synthesis of nanocrystalline AgBiSeS. For bulk AgBiSeS synthesis, bismuth (Bi; 99.9999%, Alfa Aesar), silver shot (Ag; 99.999%, Sigma-Aldrich), selenium shot (Se; 99.999%, Alfa Aesar), sulfur (S; 99.999%, Alfa Aesar) were used. All the chemicals were used as purchased for the synthesis.

8.2.1.1 Synthesis of AgBiSeS nanocrystals. We have synthesized cubic AgBiSeS nanocrystals using a bottom-up soft chemical synthesis. At first, silver acetate (50 mg, 0.2995 mmol), and oleic acid (8 mL) were taken in a round-bottom flask and the mixture was heated to 100 °C for 1/2 h with stirring in N_2 atmosphere. The resulting clear solution cooled down to room temperature and in the solution bismuth neodecenate (216.83 mg, 0.2995 mmol), selenium powder (23.69 mg, 0.2995 mmol) and sulfur powder (9.62 mg, 0.2995 mmol) were added. The reaction mixture was then heated rapidly to 220 °C, holds for 2 h. Afterward, the solution of the reaction mixture was cooled to room temperature. The black color nanocrystals of AgBiSeS were precipitated out from the reaction mixture by adding excess ethanol and n-hexane (1:1) and followed by centrifugation. AgBiSeS nanocrystals were washed several times with n-hexane and ethanol and finally dried under vacuum at 60 °C for 2 h.

8.2.1.2 Synthesis of bulk cubic AgBiSeS. Ingots (7g) of bulk cubic AgBiSeS was synthesized by mixing 0.0162 mol (1.7509g) silver, 0.0162 mol (3.384g) bismuth, 0.0162 mol (1.279g) selenium, 0.0162 mol (0.52g) sulfur in a quartz tube. The tube was flame sealed under high vacuum (10^{-5} Torr) and slowly heated up to 400 ^{0}C over 12 h, then heated up to 850 ^{0}C in 4 h, soaked for 10 h, and subsequently ice water quenched to trap the high-temperature cubic phase at room temperature.

8.2.1.3 Synthesis of bulk trigonal AgBiSeS. Ingots (7g) of bulk trigonal AgBiSeS was synthesized by mixing appropriate ratios of the highly pure starting materials i.e.

(1:1:1:1) as like bulk cubic AgBiSeS in a quartz tube. The tube was slowly heated up to 400 ^{0}C over 12 h, then heated up to 850 ^{0}C in 4 hrs, soaked for 10 h, and slowly cooled to room temperature in a period of 15 h to get the trigonal phase of AgBiSeS.

8.2.2 Characterizations

Room temperature powder X-ray diffraction of the sample was recorded using a Cu Kα (λ = 1.5406 Å) radiation on a Bruker D8 diffractometer. Temperature-dependent X-ray diffraction measurements under N_2 flow were carried out with X-ray beam of E = 12.42 keV and λ = 0.9543 Å, at BL-18B (Indian beamline), Photon Factory, KEK, Tsukuba, Japan. A Netzsch DSC 200F3 DSC instrument was used for measurement. To probe optical energy gap of these compounds, optical diffuse reflectance measurement was performed on finely ground powder using a Perkin Elmer Lambda 900, UV/vis/NIR spectrometer. FESEM imaging has been performed using a NOVA NANO SEM 600 (FEI, Germany). TEM experiment has been done using a JEOL (JEM3010) and also using a FEI TECNAI^{G2} T20 TEM. EDX elemental mapping was performed during STEM imaging. ICP-AES measurements were carried out using a Perkin-Elmer Optima 7000DV instrument. XPS measurements were performed with a Mg- Kα (1253.6 eV) X-ray source on an Omicron nanotechnology instrument. Elaborative discussions on the characterizations have been given the introduction part of the thesis (page 31).

8.2.3 Positron annihilation study

Positron annihilation experiments were done with a ^{22}NaCl source of strength about 10 μCi sealed in a 1.5 μm (micro-meter) thick nickel foil. The sealed source was placed in between two identical plane faced samples (8 mm diameter × 1 mm thick pellet). The positron annihilation lifetime was measured with a conventional fast-fast coincidence assembly consisting of two gamma ray detectors (25 mm long and 25 mm tapered to 13 mm diameter BaF_2 scintillator optically coupled with XP2020 Q photomultiplier tube) and two constant fraction differential discriminators (Fast ComTech; model 7029A) having time resolution (full width at half maximum) of ~ 220 ps measured by the prompt gamma ray of ^{60}Co source.[32] About five million coincidence counts were recorded in a multichannel analyzer. The recorded lifetime spectrum was analyzed by the computer code PATFIT-88[33] with proper source corrections.

To identify the chemical nature of the defect the coincidence Doppler broadening (CDB) measurement with ± ΔE selection was used. The CDB setup consisting of two identical HPGe detectors [33] (model number PGC 1216sp of DSG, Germany of 12 % efficiency and having energy resolution of 1.15 keV at 514 keV of ^{85}Sr) has a very high peak to background ratio (better than 10^5:1). About 2×10^7 counts were recorded in a dual ADC based multiparameter data acquisition system (Model number MPA-3 of FAST ComTec, Germany). The CDB spectrum of the nanocrystalline AgBiSeS sample was analyzed by constructing the ratio curve [33,34] with the area normalized CDB spectrum of the bulk AgBiSeS sample.

The temperature dependent (30 ^{o}C to 350 ^{o}C) Doppler broadening of positron annihilation radiation (DBPAR) measurement was carried out with a single HPGe detector (*Efficiency*: 12 %; *Type*: PGC 1216sp of DSG, Germany) having energy resolution of 1.1 keV at 514 keV of ^{85}Sr. In this particular measurement, the source sample sandwich has been kept in a vacuum sealed heating oven with a temperature accuracy of ± 2 ^{o}C. The DBAR spectrum was recorded in a dual ADC based - multiparameter data acquisition system (MPA-3 of FAST ComTec, Germany). The Doppler broadening of the annihilation 511 keV γ-ray spectrum was analyzed by evaluating the conventional line-shape parameters (S-parameter).[34] The S-parameter is calculated as the ratio of the counts in the central area of the 511 keV photo peak ($|$ 511 keV - E_γ $| \leq$ 0.85 keV) and the total area of the photo peak ($|$ 511 keV - E_γ $| \leq$ 4.25 keV). The S-parameter represents the fraction of positrons annihilating with the lower momentum electrons with respect to the total electrons annihilated.

8.2.4 Structural stability analysis

This part of the work has been done in collaboration with Prof. Swapan K. Pati's group, JNCASR. Density functional theory based first-principles calculations of the trigonal and cubic phases of AgBiSeS have been carried out with a general gradient approximation (GGA (PBE))[35] method as implemented in Quantum Espresso package.[36] On-site electron correlations of d-electrons of Ag atom were modeled with Hubbard U parameter (5 eV). Plane-wave basis was truncated with energy cut-offs of 60 and 480 Ry in the representation of wave functions and density, respectively. 7 × 7 × 3 (trigonal), and 7 × 7 × 7 (cubic) k-meshes are used to sample Brillouin zone integration. To understand the

structural stability, we have determined vibrational density of states (VDOS) at high symmetry point (Γ) using density-functional perturbation theory (DFPT).[37] To study the effect of nanoscale, we have used a 48 atom (trigonal) and 32 atom (cubic) supercell by considering different crystallographic directions, such as, [100, 010, 001, 111] axes for termination of the periodicity of the 3D crystal lattice that eventually mimic the effect of low dimensionality. Cell parameter of the simulation box is taken to be the average of the experimental cell parameters of $AgBiS_2$ and $AgBiSe_2$ crystallizing in the trigonal structure and that of the cubic structure. The structural optimizations are performed using the Broyden–Fetcher–Goldfarb–Shanno (BFGS) algorithm. Convergence threshold is set at 10^{-3} Ry $bohr^{-1}$ for force. We have checked that these conditions give good convergence of the total energy within 10^{-4} Ry per atom.

8.3 Results and discussion

Nanocrystalline rock salt phase of AgBiSeS was synthesized using a simple solution-phase method in oleic acid medium. Silver acetate and bismuth neodecenate were used for Ag^+ and Bi^{3+} sources. The elemental power of selenium and sulfur were used as anionic source. In the synthesis, silver acetate was converted into Ag- oleate. The resulting Ag- oleate, bismuth neodecenate, Se and S powder were then heated to 220 °C for 2 hrs and then quickly cooled down to room temperature. The solution based low-temperature synthesis and size reduction to nanoscale stabilize kinetic rocksalt phase of AgBiSeS at room temperature. The experimental evidence for this was acquired from powder X-ray diffraction (XRD), X-ray photoelectron spectroscopy (XPS), energy dispersive X-ray analysis (EDAX), scanning and transmission electron microscopy (FESEM/TEM), inductively coupled plasma atomic emission spectroscopy (ICP-AES) and selected area electron diffraction analysis (SAED). Bulk AgBiSeS with cubic and trigonal symmetry were synthesized using an elemental melting reaction at 850 °C by mixing the appropriate ratios of high-purity Ag, Bi, Se and S in evacuated quartz tube. To trap the high-temperature cubic phase at room temperature, reaction tube was quenched in ice water bath. The room temperature trigonal phase of the material was obtained by slow cooling of the tube to room temperature.

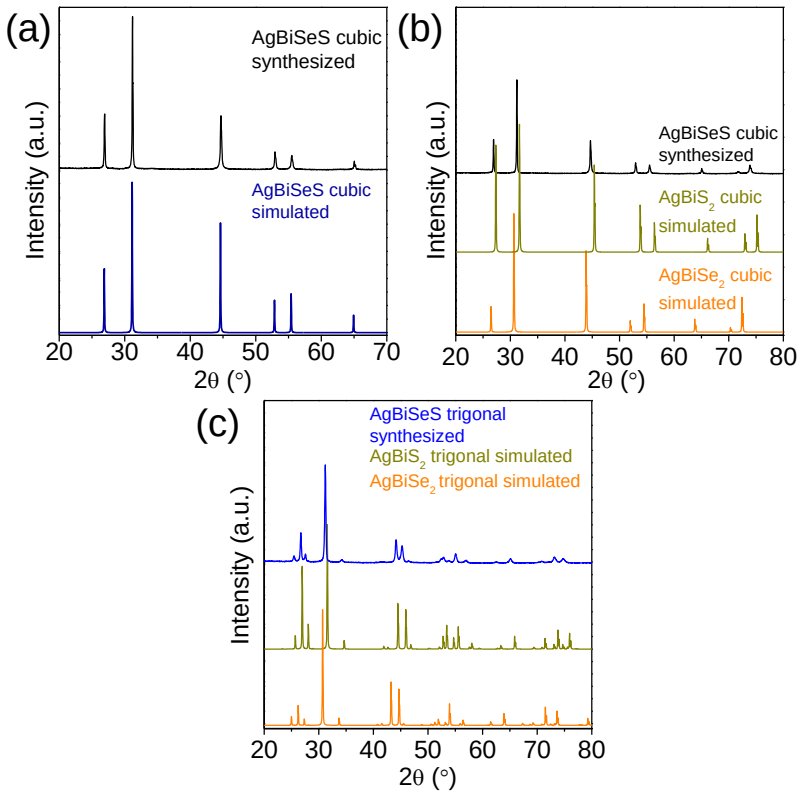

Figure 8.1 Powder XRD pattern for bulk AgBiSeS: (a), (b) cubic and (c) trigonal bulk AgBiSeS with simulated patterns (λ = 1.5406 Å).

In Figure 8.1 we present power XRD patterns of bulk trigonal and cubic AgBiSeS samples with simulated patterns. All the peaks of the ice water quenched sample could be index based on the simulated cubic AgBiSeS pattern (Figure 8.1(a)). The 2θ positions for the cubic sample were located exactly in the middle of cubic $AgBiSe_2$ and $AgBiS_2$ phases (Figure 8.1(b)). We would like to note that for trigonal phase no simulated PXRD pattern reported. However, it is expected that as like cubic phase, the 2θ peak positions for trigonal phase will be located in middle of that for trigonal phases of $AgBiSe_2$ and $AgBiS_2$. The comparison pattern shows the peaks for the slow cooled sample are located exactly in the middle of trigonal $AgBiSe_2$ and $AgBiS_2$ phases indicate the trigonal structure of the compound at room temperature (Figure 8.1(c)). Rietveld profile refinement using trigonal symmetry model also indicates the trigonal structure of slow cooled sample (Figure 8.2(a)). Temperature dependent structural evolution study using synchrotron PXRD indicates bulk trigonal AgBiSeS undergoes a reversible trigonal to cubic phase transition ~250 ^{0}C (Figure 8.2(b)). The above discussions conclude that the

cubic phase of bulk AgBiSeS is a high-temperature phase, which transforms reversibly to a trigonal structure upon cooling to room temperature.

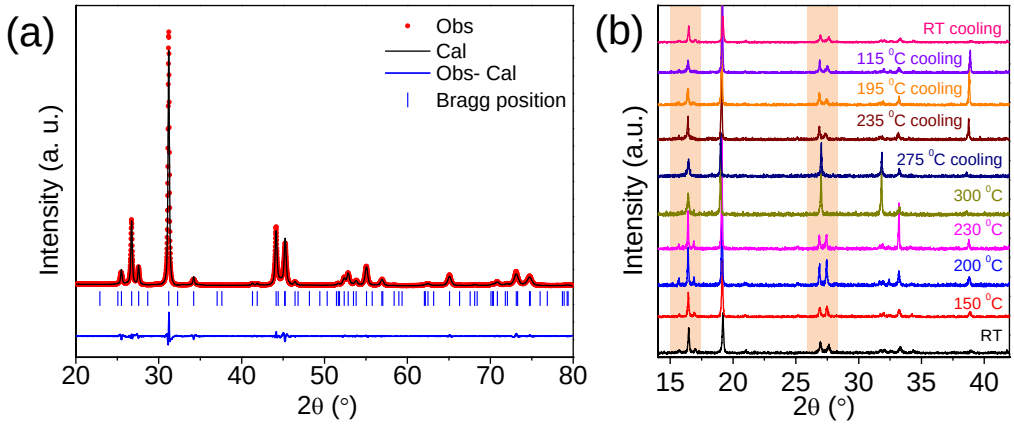

Figure 8.2 (a) Rietveld-refined powder XRD patterns of as-synthesized slow cooled bulk AgBiSeS with trigonal model (Space group: $P\bar{3}m1$). Rietveld R-factors: R_p: 9.64, R_{wp}: 11.1, R_{exp}: 3.97, Chi^2: 7.84. (b) Temperature dependent (RT–300 ^{0}C) heating–cooling cycle synchrotron (λ= 0.9543 Å) powder X-ray diffraction pattern of bulk trigonal AgBiSeS.

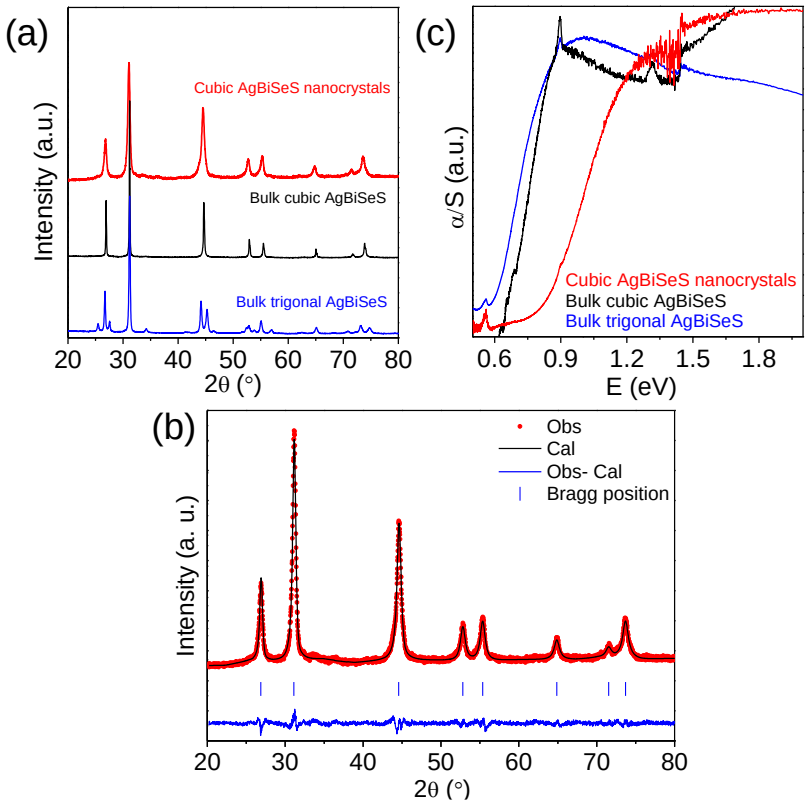

Figure 8.3 (a) Powder XRD pattern of as synthesized AgBiSeS nanocrystals. (b) Optical absorption spectra of cubic AgBiSeS nanocrystals with bulk cubic and trigonal AgBiSeS. (c) Rietveld-refined powder XRD pattern of as-synthesized nanocrystalline AgBiSeS with cubic model (Space group: $Fm\bar{3}m$). Rietveld R-factors: R_p: 15.0, R_{wp}: 13.4, R_{exp}: 10.55, Chi^2: 1.61.

In Figure 8.3(a) we represent the room temperature PXRD pattern of as-synthesized nanocrystals with bulk trigonal and cubic AgBiSeS. All the peaks in PXRD pattern could be indexed based on the cubic phase AgBiSeS, indicates the cubic rock salt structure of the as-synthesized nanocrystals. Rietveld profile refinement also indicates the cubic structure of the nanocrystals (Figure 8.3(b)). The low-temperature soft chemical synthesis and size reduction to nanoscale lead to the formation of cubic phase of AgBiSeS. The as-synthesized nanocrystals exhibit well defined optical band gap ~0.8 eV, which is blue shifted than bulk cubic (~0.65 eV) and trigonal (~0.6 eV) AgBiSeS (Figure 8.3(c)).

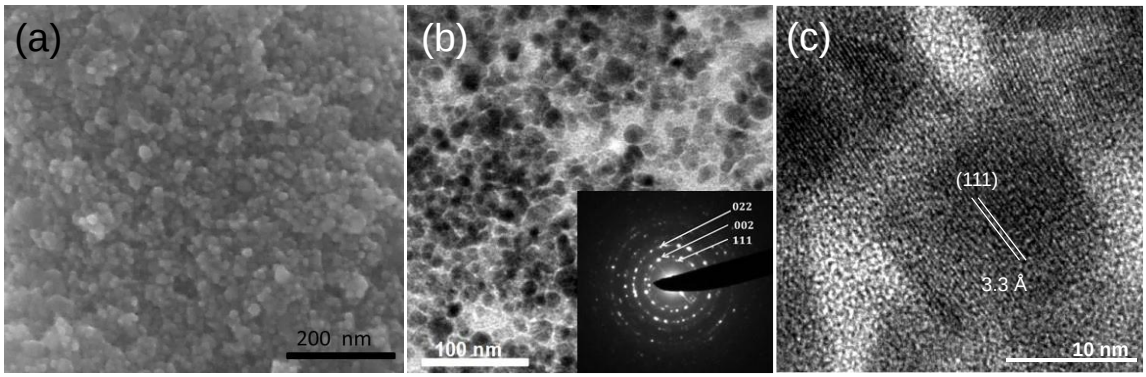

Figure 8.4 (a) FESEM image of nanocrystalline AgBiSeS. (b) TEM image of AgBiSeS nanocrystals; the lower inset shows the indexed SAED pattern. (c) High-resolution TEM image of as-synthesized nanocrystalline cubic AgBiSeS.

The as-synthesized AgBiSeS nanocrystals are nearly monodisperse in nature can be seen from field emission scanning electron microscopy (FESEM) image (Figure 8.4(a)). Transmission electron microscopy (TEM) and electron diffraction experiments were carried out for further structural investigation (Figure 8.4(b)). The size of the nanocrystals ranges from 8 to 12 nm. Selected area electron diffraction (SAED) collected from the nanocrystals clearly shows that the Bragg diffractions correspond to the rock salt structure type (inset of Figure 8.4(b)). High-resolution TEM (HRTEM) image shows a clear lattice spacing of 3.3 Å, which is corresponding to (111) interplanar distance of cubic AgBiSeS (Figure 8.4(c)). X-ray photoelectron spectroscopy study on the nanocrystals indicate the present of all the elements in the nanocrystals (Figure 8.5). The composition of the nanocrystals obtained from ICP-AES measurement indicates stoichiometry in close to the nominal composition. The EDX compositional mapping

over the group of nanocrystals also indicates the single-phase homogeneity of the AgBiSeS nanocrystals (Figure 8.6).

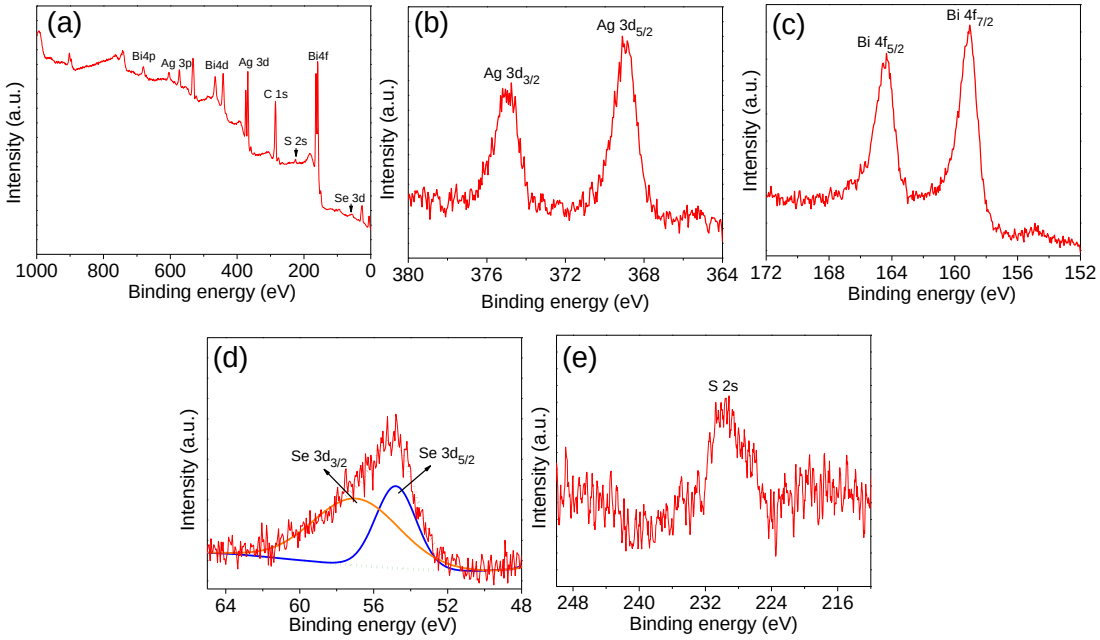

Figure 8.5 XPS spectra of as prepared AgBiSeS (a) total survey scan, (b) Ag 3d, (c) Bi 4f, (d) Se 3d (e) S 2s spectra.

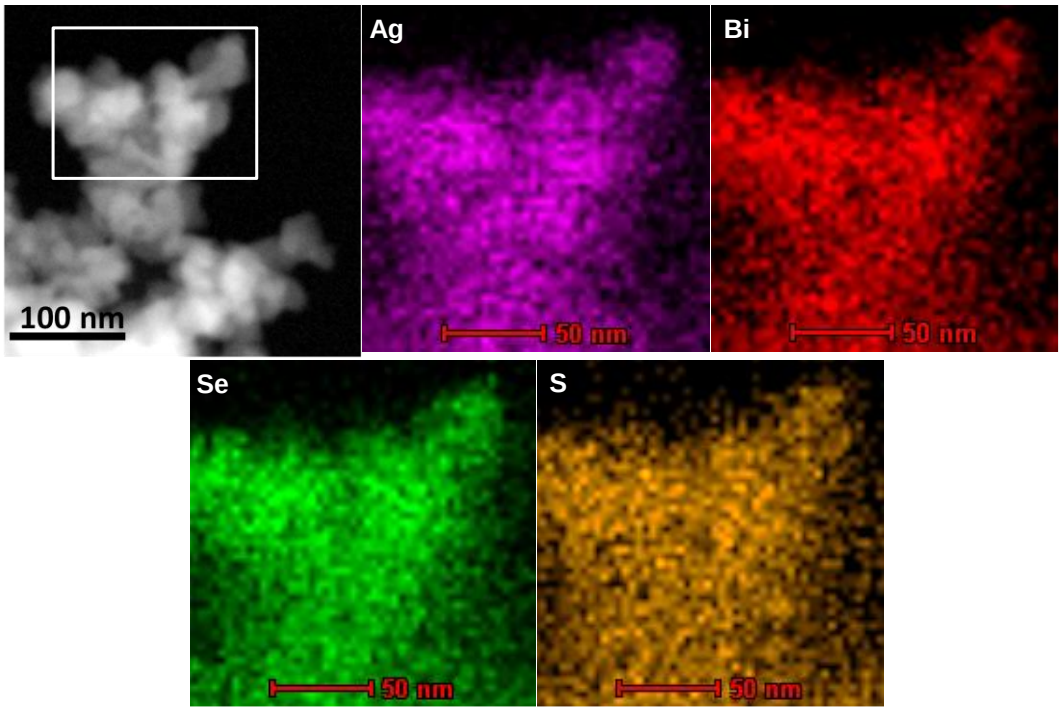

Figure 8.6 STEM image of and STEM-EDX compositional mapping over a group of nanocrystals (from the highlighted portion of the STEM image).

In ordered to understand the structural evolution in nanocrystalline samples, we have performed variable temperature synchrotron PXRD during heating- cooling cycle (Figure 8.7(a)). We observed that nanocrystalline rocksalt AgBiSeS remain unchanged below 200 ^{0}C, which specifies the nanocrystals are stable up to this temperature. The onset of the transformation occurs at ~200 °C and further increase of temperature results in the transformation to trigonal structure (marked with black arrow in the Figure 8.7(a)). Notably, the phase transition is irreversible in nature for nanocrystals, as the trigonal structure does not revert back to cubic during cooling cycle. A similar result was found on thermal annealing of the nanocrystalline sample at high temperature (Figure 8.7(b)). We would like to note that the nanocrystals were exclusively transformed to trigonal AgBiSeS without any phase separation to trigonal $AgBiSe_2$ and $AgBiS_2$ (Figure 8.7(c)). All these observations imply kinetic arrest of the rock salt metastable phase at nano-dimension, which transform to thermodynamic cubic phase on heating.

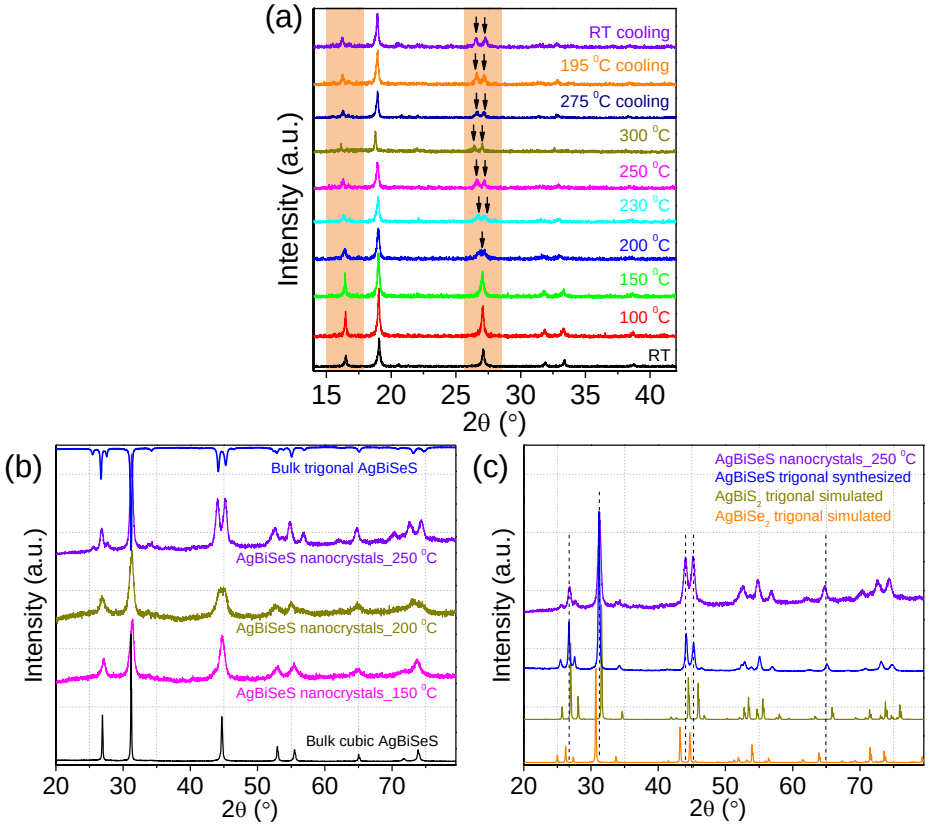

Figure 8.7 (a) Temperature dependent (RT–300 ^{0}C) heating–cooling cycle synchrotron (λ= 0.9543 Å) PXRD pattern of nanocrystalline AgBiSeS; shaded region and black arrows indicate the splitting of PXRD peaks. (b) PXRD of nanocrystals with different annealing temperature with bulk cubic and trigonal pattern. (c) PXRD pattern of 250 ^{0}C annealed sample with trigonal $AgBiSe_2$, AgBiSeS and $AgBiS_2$ patterns. Black dotted line in the figure (c) indicates the peak position is matching solely with trigonal AgBiSeS.

To acquire better insight of structural change during phase transition we have looked into the type of defect present in the system as it can play an important role in the structural phase transition. Positron annihilation spectroscopy is a unique tool for characterization and identification of defect in material. In the present study, we have used room temperature lifetime spectroscopy, CDB spectroscopy, and temperature-dependent (RT- 300 ^{0}C) one-detector DBPAR line-shape spectroscopy to identify the type of defects and its role during the structural phase transformation.

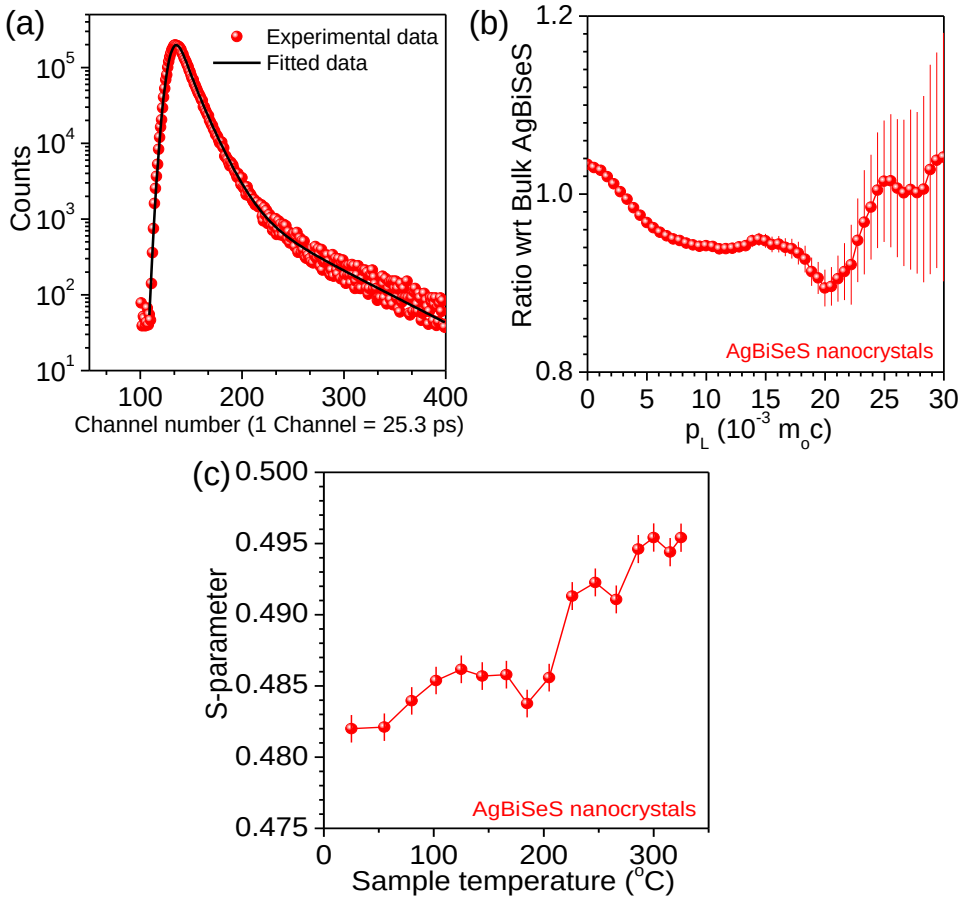

Figure 8.8 (a) Positron annihilation lifetime spectra for cubic nanocrystalline AgBiSeS. (b) Area normalized ratio between the CDB spectrum of nanocrystalline and bulk cubic AgBiSeS. (c) Temperature dependent Doppler broadening S-parameter of AgBiSeS nanocrystals.

In Figure 8.8(a) we present the positron annihilation lifetime spectrum for the nanocrystalline AgBiSeS sample. The best fit (variance of fit is less than 1 per channel) of the spectrum obtained with three-lifetime component fitting. The lifetime components are τ_1 (166 ± 1 ps), τ_2 (344 ± 4 ps) and τ_3 (1606 ± 70 ps) with relative Intensities I_1 (25 ± 1), I_2 (72 ± 1) and I_3 (3 ± 0.2) respectively. The shortest lifetime component, τ_1 is the free

annihilation of positrons while the intermediate lifetime, τ_2 due annihilation of positrons at the defect site.[38,39] The τ_2 value indicates the presence of Ag vacancy-type defect in AgBiSeS sample.[32,40,41] The long lifetime component τ_3 (1606 ± 70 ps) is due to the formation of positronium in the voids or surface of the sample.

To understand the specific nature of defect in the system we have performed coincidence Doppler broadening (CDB) measurement. In Figure 8.8(b) we represent the area normalized ratio between the CDB spectrum of nanocrystalline AgBiSeS and the same for bulk cubic AgBiSeS. The ratio curve shows a dip in the momentum with minimum centroid at 20×10^{-3} $m_o c$. The dip in the ratio curve in the higher momentum region (centroid at 28×10^{-3} $m_o c$) indicates less annihilation of positrons with core electrons of atom. The chemical nature of the defect site can be identified by estimating the kinetic energy (E_{kin}) of the electrons corresponding to that momentum value. Assuming positrons are thermalized before annihilation and using Virial theorem approximation (in the atom the expectation value of the kinetic energy of an electron, E_{kin}, is equal to the binding energy of the electron), we have calculated, E_{kin} using the formula, $p_L = (2\ m_0 E_{kin})^{1/2}$, where, m_0 is the rest mass of an electron and p_L is the longitudinal component of electron momentum p along the detector axis. From the calculation we found the momentum value of 20×10^3 $m_o c$ corresponds to E_{kin} of 102 eV, which is very close to the binding energy of Ag 4s (97 eV) core electrons. Thus, the ratio curve indicates the presence of higher concentration of Ag vacancy (V_{Ag}) in the nanocrystalline AgBiSeS sample with respect to the bulk AgBiSeS sample.

Figure 8.8(c) presents the temperature dependent (RT to 350 ^oC) variation of Doppler broadening of positron annihilation line shape parameter (S-parameter) for the nanocrystalline AgBiSeS. It clearly shows a step-like increase of S-parameter beyond 210 ^oC heating of the sample. The increase of S-parameter at higher temperature suggests positrons are annihilating more with the open volume defects, which is V_{Ag} in the present case. This observation gives a hint that increase in the Ag vacancy concentration plays a vital role during cubic- trigonal phase transformation.

To get insights into the structural feasibility and associated phase transition we have carried out DFT and DFPT based first-principles calculations. From the thermodynamic analysis, we found that cubic phase is less stable with respect to the

trigonal phase at both the nano and bulk scale, while, they have an equal difference in enthalpies (Figure 8.9). The analysis of Γ -point phonon modes for nanocrystalline phases of AgBiSeS indicates that particularly the cubic nanocrystals possess three imaginary phonon modes, V_1, V_2, V_3 (Figure 8.9(a)). Such instability arises due to the stretching and shear modes mainly form the coordinatively unsaturated surface atoms of nanocrystal, thus impart the metastable nature of the nanocrystalline cubic phase. However, instability due to surface strain can be relieved by specific synthesis condition.[8,16,18] In nanodimension the passivation of the uncoordinated surface atoms by chemically bound ligands can result in stabilization of uncommon phases *i.e.* oleic acid in present study. Consequently, cubic phase at nano-dimension appears to be a kinetically trapped state due to specific synthesis condition and effect of the nanoscale regime. Γ -point phonon analysis of trigonal nanocrystals indicates that all the vibrational modes have positive frequencies, thus a thermodynamically stable phase at nanodimension.

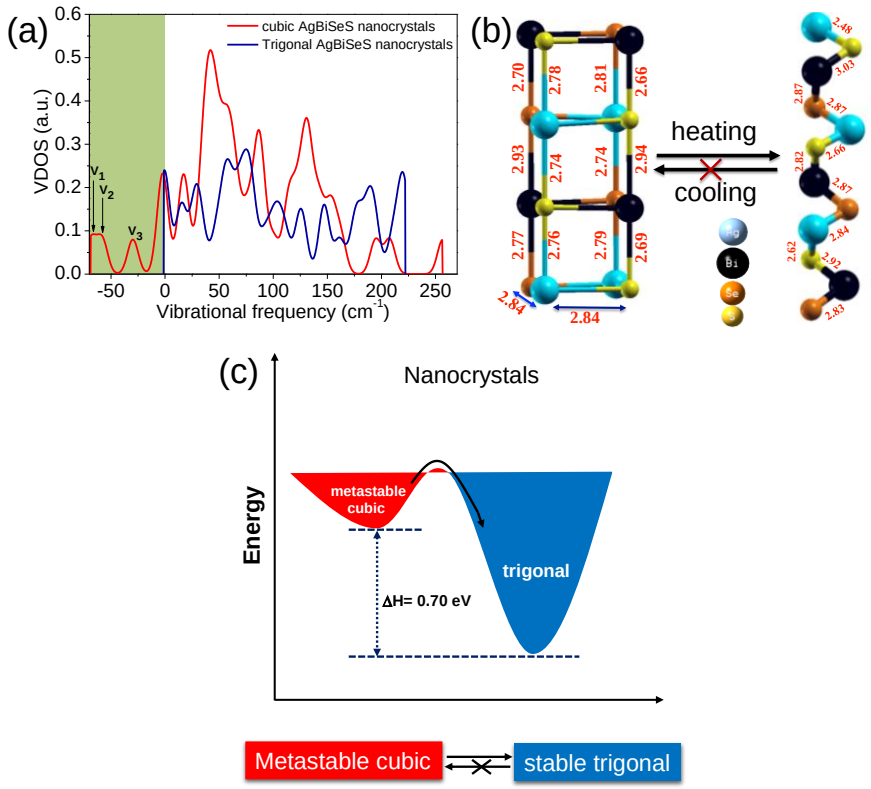

Figure 8.9 (a) Γ -point phonon modes for nanocrystalline cubic and trigonal phases of AgBiSeS; V_1, V_2 and V_3 indicate imaginary phonon mods for cubic AgBiSeS nanocrystals (b) The crystals structural evolution among nanocrsyaltalline cubic and trigonal AgBiSeS. The numerical value in the picture indicate the bond distances (in Å unit). (c) Energy diagram for nanocrystalline AgBiSeS.

In Figure 8.9(b) we show the crystal structural evolution among nanocrystalline cubic and trigonal AgBiSeS. It is clearly seen that in cubic phase the Ag-S and Ag-Se bonds at the surface are in similar range to that at the interior (Figure 8.9(b)). On the other hand, for trigonal nanocrystal, surface bonds are shorter with respect to the interior to a large extent. Thus, room for structural deformation is less for cubic phase compares to trigonal phase because of the symmetry constraint. Consequently, the cubic phase in nano-dimension cannot release the strain through bond deformation, which gives rise to unstable modes of vibration due to the stretching, and shear modes involving mainly the surface atoms. In contrast, structural relaxation stabilizes the trigonal phase and results in high surface tension. A change of 1.28-2.17 GPa pressure during cubic to trigonal phase transformation in nanocrystals also indicate a large relaxation of strain in the system after phase transformation. Therefore, during thermal treatment of metastable nanocrystalline phase, while it reaches the thermodynamically stable trigonal phase it does not revert back to cubic phase. Notably, the Γ -point phonon analysis of the bulk cubic and trigonal AgBiSeS does not show any imaginary modes, indicate both the structures have stable minima and are inter-convertible depending on the temperature (not shown in thesis). In fact, the variation of pressure for trigonal to cubic at bulk phase transition is zero. Accordingly, trigonal-cubic phase transition in bulk phase is reversible in nature. This result suggest that surface strain prevails in nanocrystal has a strong influence on the phase transition. For a better visualization of phase transition process, we have shown schematic of energy diagram for nanocrystalline AgBiSeS in Figure 8.9(c).

Theoretical investigations reveal that metastable cubic to stable trigonal phase transition at nanoscale occurs via a transient rhombohedral intermediate structure, and the process can be expressed as, cubic →rhombohedral→ trigonal. The first step *i.e.* cubic→ rhombohedral transformation takes place *via* Ag-Bi exchange which is alleviated by a large increase in the Ag vacancy, as confirmed through positron annihilation study. In the second step the transient rhombohedral phase transform into stable trigonal phase by two successive steps: (a) bond stretching/shortening without any bond dissociation and reformation; (b) reorientation of the bond angles and dihedrals. However, the reverse process involving trigonal→ rhombohedral →cubic in nano-dimension is not feasible. In spite of the fact that Ag-vacancy is an intrinsic defect present in AgBiSeS system, which

ensures the second step, *i.e.* rhombohedral→cubic facile, but the cubic phase cannot be recovered from the trigoal phase. This is because the first step (trigonal →rhombohedral) transformation appears to be the rate-limiting factor at nano-dimension due to the contribution of huge strain.

8.4 Conclusions

In summary, we have synthesized rock salt phase of AgBiSeS nanocrystals by a low-temperature solution-based synthesis. The metastable rock salt structure is stabilized due to specific synthesis condition and effect of the nanoscale regime. The irreversible cubic-trigonal phase transition in nanocrystal goes via a transient rhombohedral phase that is facilitated by the formation of a large number of Ag vacancies at high temperature. We found nanocrystalline AgBiSeS remained in trigonal phase thermal treatment and does not revert back to rocksalt phase upon cooling. The surface strain prevails in nanocrystal has a substantial influence on the cubic to trigonal phase transition. The trigonal- cubic transition is locked in nanoscale, as the formation of transient rhombohedral phase from trigonal nanocrystals is not feasible in nano-dimension. Our study leaves a message that, the stabilization of metastable phases of materials in ambient condition, understanding of their phase stability would be important for desired technological application and fundamental solid-state chemistry.

References

[1] M. G. Kanatzidis, R. Pottgen, W. Jeitschko, *Angew. Chemie - Int. Ed.* **2005**, *44*, 6996–7023.

[2] D. P. Shoemaker, D. Y. Chung, J. F. Mitchell, T. H. Bray, L. Soderholm, P. J. Chupas, M. G. Kanatzidis, *Proc. Natl. Acad. Sci. U. S. A.* **2014**, *111*, 10922–10927.

[3] S. J. Mugavero, W. R. Gemmill, I. P. Roof, H. C. zur Loye, *J. Solid State Chem.* **2009**, *182*, 1950–1963.

[4] M. G. Kanatzidis, *Chem. Mater.* **1990**, *2*, 353–363.

[5] C. Graf, A. Assoud, O. Mayasree, H. Kleinke, *Molecules* **2009**, *14*, 3115–3131.

[6] M. Jansen, *Angew. Chemie - Int. Ed.* **2002**, *41*, 3746–3766.

[7] Y. Yin, A. P. Alivisatos, *Nature* **2005**, *437*, 664–670.

[8] C.-Chun Chen, A. B. Herhold, C. S. Johnson, A. P. Alivisatos, *Science* **1997**, *276*, 398–401.

[9] P. C. Canfield, Z. Fisk, *Philos. Mag. Part B* **1992**, *65*, 1117–1123.

[10] T. C. Ozawa, S. M. Kauzlarich, *Inorg. Chem.* **2003**, *42*, 3183–3186.

[11] A. P. Alivisatos, *Science* **1996**, *271*, 933–937.

[12] A. N. Goldstein, C. M. Echer, A. P. Alivisatos, *Science* **1992**, *256*, 1425–1427.

[13] C. B. Murray, C. R. Kagan, M. G. Bawendi, *Annu. Rev. Mater. Sci* **2000**, *30*, 545–610.

[14] R. B. Soriano, I. U. Arachchige, C. D. Malliakas, J. Wu, M. G. Kanatzidis, *J. Am. Chem. Soc.* **2013**, *135*, 768–774.

[15] S. Mourdikoudis, L. M. Liz-Marzán, *Chem. Mater.* **2013**, *25*, 1465.

[16] K. Jacobs, J. Wickham, A. P. Alivisatos, *J. Phys. Chem. B* **2002**, *106*, 3759–3762.

[17] D. J. M. A. Bergerud, R. Buonsanti, J. L. Jordan-Sweet, *Chem. Mater.* **2010**, *25*, 3172–3179.

[18] S. Singh, M. Brandon, P. Liu, F. Laffir, W. Redington, K. M. Ryan, *Chem. Mater.* **2016**, *28*, 5055–5062.

[19] D. Dinega, M. Bawendi, *Angew. Chemie Int. Ed.* **1999**, *38*, 1788–1791.

[20] A. Chatterjee, K. Biswas, *Angew. Chemie - Int. Ed.* **2015**, *54*, 5623–5627.

[21] R. B. Soriano, C. D. Malliakas, J. Wu, M. G. Kanatzidis, *J. Am. Chem. Soc.* **2012**,

134, 3228–33.

[22] I. T. Sines, R. Misra, P. Schiffer, R. E. Schaak, *Angew. Chemie - Int. Ed.* **2010**, *49*, 4638–4640.

[23] M. E. Norako, R. L. Brutchey, *Chem. Mater.* **2010**, *22*, 1613–1615.

[24] M. E. Norako, M. J. Greaney, R. L. Brutchey, *J. Am. Chem. Soc.* **2012**, *134*, 23–26.

[25] A. Singh, H. Geaney, F. Laffir, K. M. Ryan, *J. Am. Chem. Soc.* **2012**, *134*, 2910–2913.

[26] X. Lu, Z. Zhuang, Q. Peng, Y. Li, *Chem. Commun.* **2011**, *47*, 3141–3143.

[27] J. Wang, W. Fan, J. Yang, Z. Da, X. Yang, K. Chen, H. Yu, X. Cheng, *Chem. Mater.* **2014**, *26*, 5647–5653.

[28] K. Senevirathne, R. Tackett, P. R. Kharel, G. Lawes, K. Somaskandan, S. L. Brock, *ACS Nano* **2009**, *3*, 1129–1138.

[29] D. Wu, Y. Pei, Z. Wang, H. Wu, L. Huang, L. D. Zhao, J. He, *Adv. Funct. Mater.* **2014**, *24*, 7763–7771.

[30] Y.-L. Pei, H. Wu, J. Sui, J. Li, D. Berardan, C. Barreteau, L. Pan, N. Dragoe, W.-S. Liu, J. He, et al., *Energy Environ. Sci.* **2013**, *6*, 1750.

[31] S. Geller, J. H. Wernick, *Acta Crystallogr.* **1959**, *12*, 46–54.

[32] S. N. Guin, S. Banerjee, D. Sanyal, S. K. Pati, K. Biswas, *Inorg. Chem.* **2016**, *55*, 6323–6331.

[33] A. Sarkar, M. Chakrabarti, D. Sanyal, D. Bhowmick, S. Dechoudhury, A. Chakrabarti, T. Rakshit, S. K. Ray, *J. Phys. Condens. Matter* **2012**, *24*, 325503.

[34] M. Chakrabarti, A. Sarkar, S. Chattapadhayay, D. Sanyal, A. K. Pradhan, R. Bhattacharya, D. Banerjee, *Solid State Commun.* **2003**, *128*, 321–324.

[35] J. P. Perdew, K. Burke, M. Ernzerhof, *Phys. Rev. Lett.* **1996**, *77*, 3865–3868.

[36] P. Giannozzi, S. Baroni, N. Bonini, M. Calandra, R. Car, C. Cavazzoni, D. Ceresoli, G. L. Chiarotti, M. Cococcioni, I. Dabo, et al., *J. Phys. Condens. Matter* **2009**, *21*, 395502.

[37] S. Baroni, S. De Gironcoli, A. Dal Corso, P. Giannozzi, *Rev. Mod. Phys.* **2001**, *73*, 515–562.

[38] D. Sanyal, D. Banerjee, R. Bhattacharya, S. K. Patra, S. P. Chaudhuri, B. N.

Ganguly, U. De, *J. Mater. Sci.* **1996**, *31*, 3447–3451.

[39] D. Sanyal, D. Banerjee, U. De, *Phys. Rev. B* **1998**, *58*, 15226.

[40] S. N. Guin, J. Pan, A. Bhowmik, D. Sanyal, U. V. Waghmare, K. Biswas, *J. Am. Chem. Soc.* **2014**, *136*, 12712–12720.

[41] S. N. Guin, D. Sanyal, K. Biswas, *Chem. Sci.* **2016**, *7*, 534–543.

Chapter 9

Summary

CHAPTER 9

Summary

This chapter discusses the overall summary of the thesis. Decoupling of electronic and phonon transport is a key issue in thermoelectric. Chapter 2 demonstrates the concept of designing solid state inorganic compound with two different substructures, which actually decouples the electronic and phonon transports. Intrinsically low thermal conductivity in solid state inorganic compound is essential for high thermoelectric performance. We have discovered the effect of lone pair of group V elements in I-V-VI_2 (I = Cu, Ag, Au or alkali metal; V = Sb, Bi; and VI = S, Se) compounds (Chapter 3-6), which creates bond anaharmonicity, thereby ultralow thermal conductivity. We have also presented high thermoelectric performance in Te-free compounds and discovered new *n*-type halogen doped $AgBiSe_2$. Stabilization of non-equilibrium phases of inorganic solids is an art in synthetic chemistry. In the last two chapter, we show the role kinetic controlled synthesis for stabilization of metastable nanocrystalline phases with unusual structural phase transition and anomalous electronic transport properties.

In chapter 2A we have shown that a crystalline semiconducting noble metal sulfide, AgCuS, exhibits a sharp temperature-dependent reversible *p*-*n*-*p* type conduction switching, along with a colossal change in the thermopower (ΔS of ~1757 μV K^{-1}) at the superionic phase transition (T ~364 K). Moreover, AgCuS exhibits ultra-low thermal conductivity. We have developed a fundamental understanding of the phase transition and *p*-*n*-*p* type conduction switching in AgCuS through temperature dependent synchrotron powder X-ray diffraction, heat capacity, Raman spectroscopy, positron annihilation spectroscopy measurements and DFT-based first-principles calculations. We found that Ag vacancy is responsible for *p*-type conduction in β-AgCuS at room temperature and acts as an effective path for the movement of Ag atoms during (β-α) phase transition, whereas Cu-S bonds remain intact. An intermediate semimetallic state, constituting of hybridized Cu-S orbitals, arises from reshuffling of electronic orbitals contributing to valence and conduction bands during the orthorhombic to hexagonal

phase transition, which is responsible for the *p-n-p* conduction switching in AgCuS. Electronic density of states and phonon dispersion reveal that the rigid sulfur sublattice is primarily responsible for the electronic charge transport, whereas soft vibrations and mobility of Ag/Cu ions are responsible for the ultralow thermal conductivity in AgCuS. Thus decoupled electron and phonon transport is evident in AgCuS. In chapter 2B we have shown that order- disorder phase transition and thermoelectric properties of bulk AgCuS can be tuned further by reducing the size to the nanoscale. Temperature dependent Seebeck coefficient measurement indicates that the nanocrystalline AgCuS does not display *p-n-p* type conduction switching property due (a) higher band gap of AgCuS nanocrystals than that of the bulk counterpart (b) absence of hybridized Cu-S states during the (β-α) transition, which were otherwise responsible for the creation of an intermediate semimetallic state, (c) more Ag vacancies and (d) Ag leaching from AgCuS nanocrystals at elevated temperature.

In Chapter 3 to 5, we have discussed ultra-low thermal conductivity and high thermoelectric performance of Te-free $AgSbSe_2$. We have shown that large anharmonicity in Sb-Se bond due to $5s^2$ lone pair on Sb and disordered cation sub-lattice results in low thermal conductivity in $AgSbSe_2$. In Chapter 3 to 4, we have shown the hole transport property in $AgSbSe_2$ can be tuned by the addition of optimum concentrations of effective *p*-type metal ion dopants (Pb, Bi, Cd) or through controlling of Sb stoichiometry rather the addition of any foreign cation dopant. The significant increment in the electrical conductivity and superior thermopower by the convergence of degenerate valence bands resulted in a large increase in the power factor in $AgSbSe_2$. The superior electronic transport and ultra-low thermal conductivity, result in a maximum *zT* values of more than unity in cation doped $AgSbSe_2$ and $AgSb_{1-x}Se_2$ system. In Chapter 5, we have shown a large improvement in the thermoelectric properties of the $AgSbSe_2$-ZnSe system by integrating different but synergistic concepts: (a) carrier engineering, (b) second phase endotaxial nanostructuring and (c) bond anharmonicity.

In addition to high *zT*, it is also essential to search for both *p*- and *n*-type materials as both *n*- and *p*-type materials required to construct a thermoelectric device. However, most of the available high-performance materials are *p*-type. In Chapter 6, we have shown promising thermoelectric performance in halogen (Cl/Br/I) doped *n*-type bulk

$AgBiSe_2$. Aliovalent halide ion doping (2-4 mol%) in the Se^{2-} sublattice of $AgBiSe_2$ significantly increases the *n*-type carrier concentration and improves the electronic transport properties. The improved electronic transport and low thermal conductivity results in a peak *zT*, value of near unity for the $AgBiSe_{1.98}Cl_{0.02}$ sample, which is significant among the *n*-type metal selenide based thermoelectric materials.

In Chapter 7 we have demonstrated the low-temperature soft chemical synthesis of kinetic cubic phases of $AgBiS_2$ and $AgBiS_{2-x}Se_x$ (x = 0.05-0.1) in the form of nanocrystals at ambient condition. We have discovered an existence of anomalous order-disorder type transition in $AgBiS_2$ nanocrystals which was evidenced by temperature dependent electrical conductivity, thermopower, and heat capacity measurements. The fundamental understanding of the origin of order-disorder phase transition and the associated anomalous change of thermopower in $AgBiS_2$ nanocrystals has been developed using positron annihilation spectroscopy measurement, density functional theory based first-principles calculation, and *ab-initio* molecular dynamics simulations. We found, shuttling of the Ag atoms in vacant or an interstitial site at higher temperatures due to the formation of more Ag vacancies plays a key role in the transition from an ordered to a locally disordered structure in nanocrystalline cubic $AgBiS_2$ which increases the entropy of the system at higher vacancy concentration and results in an unusual rise in thermopower.

In Chapter 8 synthesis of a non-equilibrium rock salt phase of AgBiSeS nanocrystals has been demonstrated. Rock salt nanocrystals upon thermal treatment undergo an irreversible phase transition to a low symmetry trigonal phase. We have developed the fundamental understanding of the origin for such uncommon finding by using temperature dependent synchrotron powder X-ray diffraction, positron annihilation spectroscopy, and first principles calculation.

Overall, the work presented in this thesis can be summarized based on the below three categories:

(1) Decoupling of electronic and phonon transport in super-ionic noble metal chalcogenides. We have shown channelization of electronic and phonon transport through two different substructures in a single compound for the first time. The rigid sulfur sublattice is responsible for the electronic charge transport, whereas soft vibrations

of Ag/Cu ions are responsible for the ultralow thermal conductivity in AgCuS. Hence, it could be a useful strategy to tune the thermoelectric properties of solids with two different type substructures.

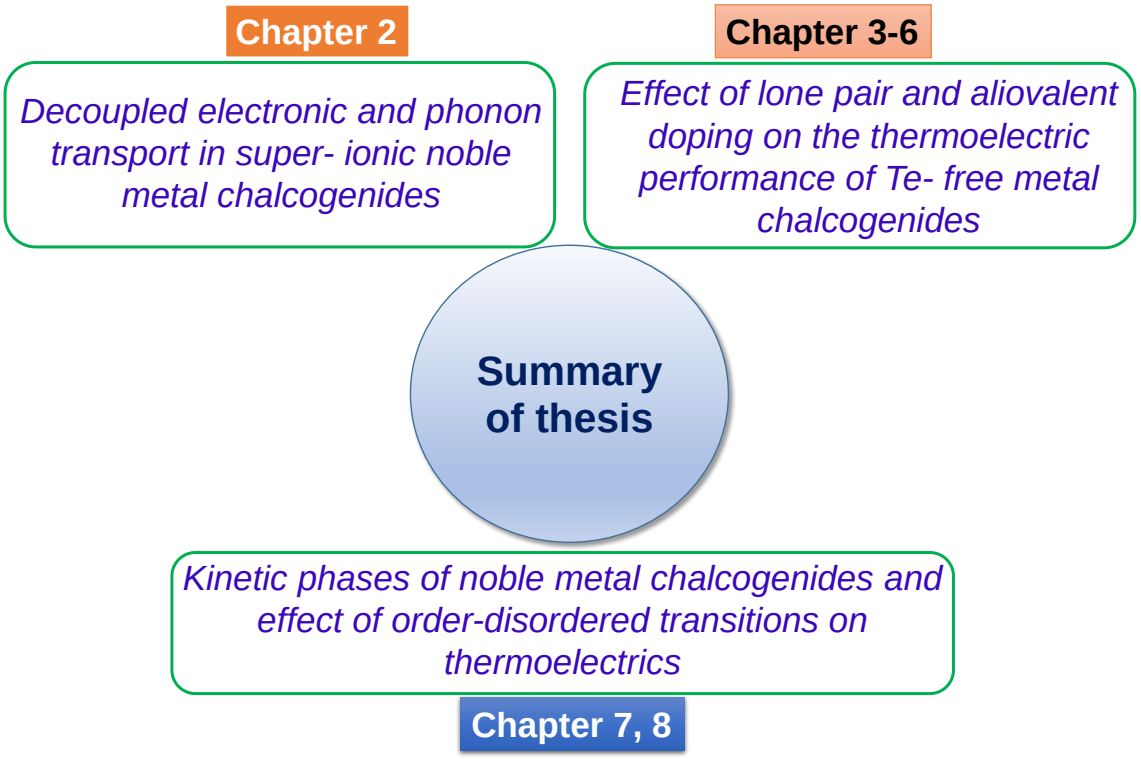

Scheme 9.1 Representation of types of work presented in the thesis.

(2) Effect of lone pair and aliovalent doping on the thermoelectric properties of Te- free I-V-VI_2 metal chalcogenides has been discussed in detail. Most of the high-performance materials are Te based and Te is expensive and rare; thus, it is desirable to develop high-performance Te- free materials. Here, we have understood the effect of the lone pair to reduce the thermal conductivity of $AgSbSe_2$ and $AgBiSe_2$ system. We have developed high-performance *p* and *n*-type materials from I-V-VI_2 class of compounds by implementing suitable *p* and *n*-type aliovalent doping strategy, vacancy doping and nano-structuring approach. The fundamental understanding of lone pair effect and material design strategy adopted here will be useful for exploration and development of next generation materials.

(3) Stabilization of kinetic phases of I-V-VI_2 metal chalcogenides, phase transition and its effect on their thermoelectric properties are also discussed in detailed. The synthesis of a

new metastable phase in the nanoscale, understanding their phase stability, phase transition, and associated unusual properties not only enrich the fundamental solid-state chemistry but also it will assist the chemists for the synthesis of new metastable phases of different structure types with exotic properties.

List of publications

- **Included in thesis**

1. **S. N. Guin,** S. Banerjee, D. Sanyal, S. K. Pati and K. Biswas, "Origin of the order–disorder transition and the associated anomalous change of thermopower in $AgBiS_2$ nanocrystals: A combined experimental and theoretical study" *Inorg. Chem.* **2016**, *55*, 6323-6331.

2. **S. N. Guin,** D. Sanyal and K. Biswas, "The effect of order-disorder phase transition and band gap evolution on the thermoelectric properties of AgCuS nanocrystals" *Chem. Sci.* **2016**, *7*, 534–543.

3. **S. N. Guin** and K. Biswas, "Sb deficiencies control hole transport and boost the thermoelectric performance of *p*-type $AgSbSe_2$" *J. Mater. Chem. C* **2015**, *3*, 10415–10421.

4. **S. N. Guin** and K. Biswas, "Temperature driven *p-n-p* type conduction switching materials: Current trends and future direction" *Phys. Chem. Chem. Phys.* **2015**, *17*, 10316–10325 (Perspective article).

5. **S. N. Guin,** V. Srihari and K. Biswas, "Promising thermoelectric performance in n-type $AgBiSe_2$: Effect of aliovalent anion doping" *J. Mater. Chem. A* **2015**, *3*, 648–655.

6. **S. N. Guin,** J. Pan, A. Bhowmik, D. Sanyal, U. V. Waghmare and K. Biswas, "Temperature dependent reversible *p-n-p* type conduction switching with colossal change in thermopower of semiconducting AgCuS" *J. Am. Chem. Soc.* **2014**, *136*, 12712–12720.

7. **S. N. Guin,** D. S. Negi, R. Datta and K. Biswas, "Nanostructuring, carrier engineering and bond anharmonicity synergistically boost the thermoelectric performance in *p*-type $AgSbSe_2$-ZnSe" *J. Mater. Chem. A* **2014**, *2*, 4324–4331.

8. **S. N. Guin,** A. Chatterjee and K. Biswas, "Enhanced thermoelectric performance in *p*-type $AgSbSe_2$ by Cd-doping" *RSC Advances* **2014**, *4*, 11811–11815.

9. **S. N.Guin,** A. Chatterjee, D. S. Negi, R. Datta and K. Biswas, "High thermoelectric performance in tellurium free *p*-type $AgSbSe_2$" *Energy Environ. Sci.* **2013**, *6*, 2603–2608.

10. **S. N. Guin** and K. Biswas, "Cation disorder and bond anharmonicity optimize the thermoelectric properties in kinetically stabilized rocksalt $AgBiS_2$ nanocrystals" *Chem. Mater.* **2013**, *25*, 3225–3231.

- **Not included in thesis**

11. M. Samanta, **S. N. Guin** and K. Biswas, "Ultrathin few layer oxychalcogenide BiCuSeO nanosheets" *Inorg. Chem. Front.* **2017**, *4*, 84-90.

12. R. Vincent, P. Malavi, Y. Sharma, Y. Sorb, U. Dutta, **S. N. Guin,** B. Joseph, S. K. Pati, S. Karmakar, K. Biswas and C. Narayana, "Pressure induced structural, electronic topological and semiconductor to metal transition in $AgBiSe_2$" *Appl. Phys. Lett.* **2016**, *109*, 171903.

13. S. R. Suryawanshi, **S. N. Guin,** A. Chatterjee, V. Kashid, M. A. More, D. J. Late and K. Biswas, "Low frequency noise and photo-enhanced field emission from ultrathin $PbBi_2Se_4$ nanosheets" *J. Mater. Chem. C* **2016**, *4*, 1096–1103.

14. S. Roychowdhury, S. Ghara, **S. N. Guin,** A. Sundaresan and K. Biswas, "Large linear magnetoresistance in topological crystalline insulator $Pb_{0.6}Sn_{0.4}Te$" *J. Solid State Chem.* **2016**, *233*, 199–204.

15. **S. N. Guin,** S. Kundu and K. Biswas, "Effect of aliovalent chlorine doping on the thermoelectric properties of *n*-type $AgBi_{0.5}Sb_{0.5}Se_2$" *Soc. Mater. Chem. Bulletin* **2015**, *6*, 30–36.

16. L. Aggarwal, J. S. Sekhon, **S. N. Guin,** A. Arora, D. S. Negi, R. Datta, K. Biswas and G. Sheet, "Direct evidence of strong local ferroelectric ordering in a thermoelectric semiconductor" *Appl. Phys. Lett.* **2014**, *105*, 113903. arXiv:1405.2766.

17. A. Chatterjee, **S. N. Guin** and K. Biswas, "Ultrathin septuple layered $PbBi_2Se_4$ nanosheets" *Phys. Chem. Chem. Phys.* **2014**, *16*, 14635–14639.

Book chapter

1. **S. N. Guin**, A. Banik and K. Biswas, "Thermoelectric energy conversion in layered metal chalcogenides" in the book "2-D Inorganic Materials beyond Graphene", Eds. C. N. R. Rao and U. V. Waghmare, World Scientific (Singapore), 2017 (*accepted for publication*).

Biography

Satya Narayan Guin was born on May 2, 1989 in a small village Barahatty, West Bengal (India). He received his B.Sc. (2009) and M.Sc. (2011) degree in Chemistry from University of Kalyani, Kalyani, West Bengal, India. He joined as a Ph.D student at New Chemistry Unit of Jawaharlal Nehru Centre for Advanced Scientific Research (JNCASR), Bangalore, India in August 2012 under the guidance of Dr. Kanishka Biswas. His research work is focused on thermoelectric materials based on metal chalcogenides and superionic metal chalcogenides, exploratory synthesis of inorganic solids and their structure property correlation. He is also a recipient of best poster award in "17th CRSI National Symposium in Chemistry" of CRSI, India and Carl Storm International Diversity Award from Gordon Research Conference on "Solid State Chemistry 2016" New London, NH, United States.